2019

Advanced Materials for Rechargeable Batteries

Haipeng Guo
University of Wollongong

UNIVERSITY
OF WOLLONGONG
AUSTRALIA

Advanced Materials for Rechargeable Batteries

Haipeng Guo

This thesis is presented as part of the requirement for the conferral of the degree:
Doctor of Philosophy

The University of Wollongong
Institute of Superconducting and Electronic Materials
Australia Institute of Innovation Materials

March, 2019

Certification

I, *Haipeng Guo*, declare that this thesis submitted in fulfilment of the requirements for the conferral of Doctor of Philosophy, in the Institute for Superconducting and Electronic Materials, Australia Institute for Innovative Materials, Faculty of Engineering and Information Sciences, the University of Wollongong, is wholly my own work unless otherwise referenced or acknowledged. This document has not been submitted for qualifications at any other academic institution.

_____

Haipeng Guo
6th February 2019

Acknowledgments

This thesis work was conducted with the support of everyone in the Institute for Superconducting and Electronic Materials (ISEM), Australian Institute for Innovative Materials (AIIM) at the University of Wollongong in Australia.

Firstly, I wish to express my utmost gratitude to my supervisors, Professor Hua Kun Liu, Professor Jiazhao Wang, and Assoc. Professor Shulei Chou, for their professional supervision, invaluable guidance, great support, endless encouragement, and precious advice throughout the whole course of my PhD study. Their encyclopedic knowledge, wisdom, persistence, enthusiasm, and love for research are highly contagious. They encouraged me to solve every research problem that I encountered and inculcated the necessity to be persistent to fulfill any goal. Here, I express my greatest respects and convey my gratitude to my supervisors.

Furthermore, I wish to express my appreciation to Dr. Wenbin Luo, for his kind discussion and guidance.

I would like to convey my appreciation to my colleagues, Dr. Lili Liu, Dr. Lei Zhang, Dr. Boyang Ruan, Dr. Chao Han, and Mr. Zhi Zheng, for spending their valuable time on helpful discussions and collaboration in research. I am grateful to my colleagues, Dr. Chaozhu Shu (Chengdu University of Technology) and Dr. Nengfei Yu (Nanjing University of Technology), who have been very helpful, sharing their experience, knowledge, and suggestions. I would also like to thank Dr. Tania Silver for her critical reading of my manuscripts.

Moreover, many thanks to Dr. Jun Wang, Dr. Qiannan Liu, Dr. Yuhai Dou, Dr.

Xuanwen Gao, Dr. Zhijia Zhang, Dr. Jiantie Xu, Dr. Jianqiu Deng, Dr. Li Wang, Dr. Haifeng Feng, Dr. Yajie Liu, Dr. YunxiaoWang, Dr. Wenbin Qiu, Dr. Zhixin Tai, Dr. Long Zhang, Mr. Xiaowei Wang, Mr. Zhe Hu, Mr. Weihong Lai, Mr. Jicheng Jiang, Mr. Chang Wu, Mr. Mingzhe Chen, Mr. Binwei Zhang, Mr. Zichao Yan, Mr. Qining Fan, Mr. Viet Pham, Mr. Qi Zhang, Mr. Long Ren, Mr. Liang Wang, Mr. Yaru Liang, Mrs. Fang Li, Miss Enhui Wang, Miss Yueyu Tong, Miss Qian Zhou, Miss Yang Li, Miss Qiuran Yang, and other staff members and students at AIIM for their kindly help and valuable advice during my PhD research.

I would like to express my gratitude for the technical assistance that I received in the University of Wollongong, including from Dr. Germanas Pelekis (XRD), Dr. Kosta Konstantinov (BET and TGA), Dr. Dongqi Shi (XPS), Mr. Tony Rome (SEM), Dr. Gilberto Casillas Garcia and Dr. David Mitchell (TEM and STEM), and Dr. Patricia Hayes (Raman). My thanks are extended to Mrs. Crystal Login, Mrs. Narelle Badger, Mrs. Naomi Davies, Mrs. Joanne George, Dr. Candace Gabelish, and Mr. Robert Morgan for their help in official and laboratory matters.

I would like to express special thanks to my parents and my wife Mrs. Huixi Li, who always stood by me, encouraged me to pursue my dream, and provided moral support during the whole course of my PhD study. Their selfless dedication and unwavering belief have been and will always be the strong support behind my life.

Finally, I would like to thank everyone who has helped, supported, and cared for me during my PhD study in the University of Wollongong. This thesis would not have been possible without the inspiration and support of their kindly help.

Abstract

As the most successful energy storage system, lithium ion batteries (LIBs) have been utilized in many different fields, such as electric vehicles, smart phones, digital cameras, laptop computers, and so on. Even though enormous efforts have been devoted to improving the performance of these batteries, they still suffer from some intrinsic problems, including poor cycling stability, insufficient rate performance, and active materials aggregation. Therefore, it is important to develop advanced materials with outstanding performance for next-generation batteries. In particular, the anode material, as an important component of the battery, is critical for the improvement of its performance and is currently attracting great research interests. In this thesis, a Ge@N-doped carbon-nanotubes (Ge@N-CNTs) composite with Ge nanoparticles uniformly distributed in the N-CNTs and a yolk-shell Si@carbon composite are synthesized and utilized as promising anode materials for LIBs.

Owing to their high theoretical energy density, low charge overpotential, and stable reaction intermediates, rechargeable sodium oxygen batteries (SOBs) have been considered as a promising energy storage system and received enormous attention during the past several years. Their charge overpotential, rate capability, discharge/charge capacity, and cycling stability are significantly affected by their electrocatalysts. Even though many different kinds of electrocatalysts have been developed as cathode catalysts for SOBs, it is still a big challenge to develop low-cost and efficient electrocatalysts with low charge overpotential and long cycling stability for SOBs. In this thesis, phosphorus and nitrogen dual-doped carbon (PNDC) and holey two-dimensional (2D) Ni_3Fe nitride nanosheets have been fabricated and characterized as cathode catalysts for SOBs.

Germanium is a prospective anode material for LIBs, as it possesses large theoretical capacity, outstanding lithium-ion diffusivity, and excellent electrical conductivity. Ge suffers from drastic capacity decay and poor rate performance, however, owing to its low electrical conductivity and huge volume expansion during cycling processes. Herein, a novel strategy has been developed to synthesize a composite of Ge@N-doped carbon nanotubes (Ge@N-CNTs) with Ge nanoparticles uniformly distributed in the N-CNTs by using capillary action. This unique structure could effectively buffer the large volume expansion. When evaluated as anode material, the Ge@N-CNTs demonstrated enhanced cycling stability and excellent rate capabilities.

As an promising anode for LIBs, silicon has attracted remarkable research interest because of its ultra-high theoretical capacity (4200 mAh g^{-1}) and low discharge plateaus (0.5 V vs Li/Li^{+}). Silicon suffers, however, from the huge volume changes during discharge/charge processes, leading to severe pulverization and detachment of the active materials. Herein, a yolk-shell structured silicon@carbon composite with an extra thin carbon layer coated on the surfaces of the silicon nanoparticles has been prepared through a template method. When utilized as anode material for LIBs, the void provided by the yolk-shell structure could accommodate the dramatic volume changes, and the thin carbon layer could enhance the conductivity of the silicon, leading to excellent cycling performance and outstanding rate capability.

Among various kinds of metal oxygen batteries, sodium oxygen batteries have been regarded as the most promising energy storage devices due to their low charge overpotential and high energy density. It is still a big challenge, however, to develop good electrocatalysts to control the discharge products of the sodium oxygen batteries, which could affect the electrochemical performance of the batteries. Here, phosphorous

and nitrogen dual-doped carbon (PNDC) are synthesized and employed as the electrocatalyst for sodium oxygen batteries. In the air electrodes of sodium oxygen batteries with this electrocatalyst, NaO_2 nanoparticles could be generated as the discharge product and well preserved on the electrode, leading to a quite low overpotential (0.18 V) and long cycling stability for 120 cycles.

Exploring economically efficient electrocatalysts with high catalytic activity is of great importance for various electrochemical energy conversion and storage technologies. Ultrathin metallic nickel-based holey nitride nanosheets were designed as electrocatalysts for SOBs. The holey 2D Ni_3Fe nitride nanosheets exhibit excellent catalytic activity owing to the inherent advantages of their abundant active catalytic sites, resulting from the complete exposure of the atoms in the large lateral surfaces and in the edges of pore areas, together with an expanded lattice spacing distance. The thus-obtained three-dimensional conductive integral architecture can not only accelerate electron transportation by means of the highly orientated crystalline structure, but also facilitates the diffusion of intermediates and gases. The holey 2D Ni_3Fe nitride nanosheets exhibit excellent catalytic activity when evaluated as air cathode for SOBs.

Table of Contents

LIST OF FIGURES

LIST OF TABLES

LIST OF ABBREVIATIONS

Abbreviation	Full name
LIBs	Lithium ion batteries
SIBs	Sodium ion batteries
LOBs	Lithium oxygen batteries
SOBs	Sodium oxygen batteries
1D	One-dimensional
2D	Two-dimensional
3D	Three-dimensional
CNTs	Carbon nanotubes
SEI	Solid electrolyte interface
EVs	Electric vehicles
GNS	Graphene nanosheets
DLC	Diamond-like Carbon
OMC	Ordered mesoporous carbon
CP	Carbon paper
VACNTs	Vertically aligned carbon nanotubes
OER	Oxygen evolution reaction
ORR	Oxygen reduction reaction
DN	Donor number
DMC	Dimethyl carbonate
EC	Ethylene carbonate
DEC	Dimethyl carbonate
TEGDME	Tetraethylene glycol dimethyl ether
PPy	Polypyrrole

CTAB	Cetyltrimethylammonium bromide
PVP	Poly(vinylpyrrolidone)
DI water	Deionized water
PTFE	Polytetrafluoroethylene
XRD	X-ray diffraction
XPS	X-ray photoelectron spectroscopy
TGA	Thermogravimetric analysis
BET	Brunauer-Emmett-Teller
BJH	Barrett-Joyner-Halenda
AFM	Atomic Force Microscopy
SEM	Scanning electron microscopy
FE-SEM	Field-emission scanning electron microscopy
TEM	Transmission electron microscopy
STEM	Scanning transmission electron microscopy
SAED	Selected area electron diffraction
EELS	Electron energy loss spectroscopy
EDX	Energy dispersive X-ray
CV	Cyclic voltammetry
LSV	Linear sweep voltammetry
EIS	Electrochemical impedance spectroscopy
HAADF	High-angle annular dark-field
EDS	Element dispersive spectroscopy
RHE	Reversible hydrogen electrode
$NaSO_3CF_3$	Sodium trifluoromethanesulfonate
TTF	Tetrathiafulvalene
FePc	Iron phthalocyanine

DBBQ	2,5-di-tert-butyl-1,4-benzoquienone
NaI	Sodium iodine
DMSO	Dimethyl sulfoxide
EG	Ethylene glycol
LDH	Layered double hydroxide

LIST OF SYMBOLS

Symbol	Name	Unit
ΔG	Gibbs free energy	kJ mol^{-1}
ΔH	Enthalpy	kJ mol^{-1}
T	Absolute temperature	K
S	Entropy	J K^{-1}
E	Potential	V
F	Faraday constant	C mol^{-1}
I	Current	A
Q_s	Specific capacity	mAh g^{-1}
n	Electron number	-
η_e	Coulombic efficiency	%
P	Pressure	Pa
d	Lattice spacing	nm

LIST OF ORGANIZATIONS

Abbreviation	Full name
ISEM	Institute of Superconducting and Electronic Materials
AIIM	Australia Institute for Innovative Materials
UOW	University of Wollongong

Chapter 1 Introduction

1.1 Research Background

Due to the rapid increase in non-renewable energy consumption and continuous growth of ecological concerns, great efforts have been devoted to the development of highly efficient, environmentally friendly, and low-cost energy conversion and storage systems. Among the various energy conversion and storage systems, the rechargeable batteries, such as lithium ion batteries (LIBs), sodium ion batteries (SIBs), lithium oxygen batteries (LOBs), and sodium oxygen batteries (SOBs), are considered as the most promising candidates due to their high energy density. As the performance of these batteries greatly depends on the properties of their electrode materials, it is critical to develop advanced materials with enhanced mechanical and electrical properties for next-generation batteries. These materials still have problems, however, including low electrical conductivity, extreme volume change during cycling, and active material aggregation or destruction. Therefore, it is still a big challenge to develop new electrode materials with high energy density, excellent structural stability, and low cost.

During the past several decades, LIBs have been intensively studied and successfully utilized in many different fields. In the currently commercialized LIBs, carbon-based materials, such as graphite, are widely used as anode materials, although these materials suffer from low specific capacity (372 mAh g^{-1}) and poor rate performance, which are holding back their further application in high energy density LIBs. Germanium (Ge) and silicon (Si), therefore, are considered as the most promising anode materials to replace carbon-based materials as anode for LIBs, owing to their high specific capacities and low discharge potentials. Nevertheless, the same problems also need to be solved before further application, including low electronic conductivity

and huge volume change associated with dramatic capacity fading. To improve the electrochemical performance of Ge and Si based anode materials, many efforts have been devoted to address the above problems. Various nanostructures based on Ge or Si have been developed, such as nanotubes, nanowires, nanorods, nanospheres, and nanoparticles. Among these different nanocomposites, the Ge/carbon or Si/carbon composites are recognized as a quite promising approach for practical application, owing to the void spaces for volume change accommodation and enhanced electronic conductivity provided by the carbon materials.

With the theoretical specific energy of 3451 Wh kg^{-1}, SOBs are considered as a next-generation energy storage system for further applications. Rather than the intercalation or alloying mechanism found LIBs or SIBs, SOBs employ a precipitation/dissolution mechanism during the discharge/charge process just like LOBs. In addition, SOBs have a much lower charge overpotential and stable reaction intermediate compared with LOBs. As the electrocatalysts could significantly affect the electrochemical properties of metal-O_2 batteries, great efforts have been devoted to improving the performances of SOBs. More breakthroughs need to be achieved, however, before SOBs can be utilized for practical applications.

1.2 Objectives of the Research

Therefore, in this thesis, four different electrode materials were developed for rechargeable batteries that feature low-cost, high energy density, and long cycling life. Specifically, capillary action was utilized to synthesize a Ge@N-doped carbon nanotubes (Ge@N-CNTs) composite with Ge nanoparticles uniformly distributed in the N-CNTs. This unique structure could effectively buffer the large volume

expansion. When evaluated as anode material, the Ge@N-CNTs demonstrates enhanced cycling stability and excellent rate capabilities. In addition, yolk-shell Si@SiO_2/C@carbon nanospheres with interior core-shell structure Si@SiO_2/C as yolk were prepared through a template method. When utilized as anode material for LIBs, the void provide by the yolk-shell structure could accommodate the dramatic volume change and the thin carbon layer could enhance the conductivity of the silicon, leading to excellent cycling performance and outstanding rate capabilities. For the SOBs, phosphorous and nitrogen dual-doped carbon (PNDC) was synthesized and employed as an electrocatalyst for sodium oxygen batteries. As the air electrode for sodium oxygen batteries, the NaO_2 nanoparticle discharge product could be generated and well preserved on the electrode, leading to a quite low overpotential (0.18 V) and long cycling stability for over 120 cycles. Ultrathin metallic nickel-based holey nitride nanosheets were also fabricated as electrocatalysts for SOBs. The holey 2D Ni_3Fe nitride nanosheets exhibited excellent catalytic activity owing to the inherent advantages of their abundant active catalytic sites resulting on the complete exposure of the atoms in their large lateral surfaces and from the edges of pore areas, together with expanded lattice spacing. The holey 2D Ni_3Fe nitride nanosheets exhibited excellent catalytic activity when evaluated as air cathode for SOBs.

1.3 Thesis Structure

For the purpose of developing advanced electrode materials for rechargeable batteries, four different kinds of electrode materials with different fabrication methods were employed in this thesis. In addition, in order to study the electrochemical properties of these materials, detailed structural characterizations and electrochemical measurements have been conducted. The scope of this thesis work is briefly outlined as follows:

Chapter 1 introduces the background for the development of Lithium ion batteries and Sodium oxygen batteries, and the significance of this work for the development of advanced electrode materials for Lithium ion batteries and Sodium oxygen batteries with high energy density and low cost.

Chapter 2 presents a literature review on Lithium ion batteries and Sodium oxygen batteries, including their development histories, working principles, basic concepts, electrode materials, and electrolytes.

Chapter 3 includes the list of chemicals and detailed experiments used and conducted in this thesis work, including the electrode preparation, coin-cell assembly, and physical and electrochemical characterization techniques.

Chapter 4 presents a capillary action method to fabricate Ge@N-doped carbon nanotubes (Ge@N-CNTs) composite as an anode material for Lithium ion batteries with Ge nanoparticles uniformly distributed in the N-CNTs.

Chapter 5 introduces a facile method to synthesize yolk-shell $Si@SiO_2/C@$carbon nanospheres with interior core-shell structure, in which $Si@SiO_2/C$ serves as yolk, as an anode material for Lithium ion batteries.

Chapter 6 investigates the phosphorous and nitrogen dual doped carbon (PNDC) as electrocatalyst for Sodium oxygen batteries.

Chapter 7 presents the holey 2D Ni_3Fe nitride nanosheets as electrode materials for

Sodium oxygen batteries.

Chapter 8 summarizes the work in this thesis and provides some prospects for the synthesis of other advanced electrode materials for rechargeable batteries.

Chapter 2 Literature Review

2.1 Lithium-Ion Batteries

2.1.1 General Background

The development of efficient energy storage and conversion systems for the demands of our lifestyles has attracted enormous research interests for as long as the last two centuries. From the primary batteries, such as Zn-MnO_2, to secondary batteries, such as lead-acid and Ni-Cd, batteries have been recognized as the most useful energy storage systems, especially for the cheap and sustainable energy supply. Unfortunately, these older battery systems could not meet the demands of our modern lifestyles for portable electronic applications due to their low energy and power densities. Therefore, great research efforts have been devoted into the development of new energy storage system with high energy density and high power density.

With lithium the most electropositive and the lightest metal, lithium ion batteries (LIBs) have many merits compared with other above-mentioned traditional batteries, such as high energy density and high power density, as shown in **Figure 2.1**.[1, 2] In addition, LIBs have high working voltage (about 3.6 V), long cycling life, no "memory effect", and low self-discharge. Therefore, since they were first commercialized by Sony in 1991, LIBs have been utilized in various applications, such as mobile phones, laptops computers, cameras, and electric vehicles. Even though many breakthroughs have been achieved, the current commercial LIBs still cannot meet our society's rapidly increased demands. Further development are expected to expand the applications of LIBs with high electrochemical performances.

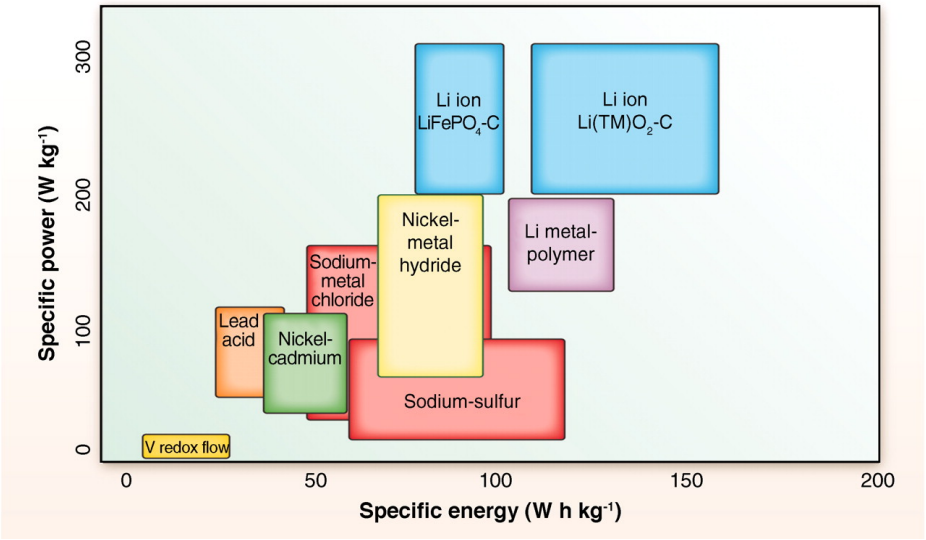

Figure 2.1 Comparison of gravimetric energy and specific power densities of different battery systems.[1]

2.1.2 Brief History

The development history of batteries is illustrated in **Figure 2.2**. In 1800, Alessandro Volta fabricated the first modern electrochemical cell. Then, different type of batteries were developed, such as lead-acid batteries, Ni-metal batteries, zinc-carbon batteries, and alkaline batteries. In the 1970s, primary lithium cells were developed and commercialized. Meanwhile, Whittingham proposed a rechargeable lithium battery with titanium sulfide (TiS_2) as anode and Li metal as anode. The commercialization of this battery unfortunately failed, however, due to the safety issues associated with the lithium dendrites during the continuous discharge/charge processes. In the 1980s, Goodenough discovered that layered structure $LiCoO_2$ could be used as the cathode material for batteries because lithium could be electrochemically inserted and de-inserted into/from the layered structure. Furthermore, a series of Li_xMO_2 (M = Co, Ni, or Mn) materials were studied as cathodes for batteries by Goodenough's group. In 1980, M. Armand proposed the concept of "Rocking Chair Batteries". Afterwards, the first commercial LIBs were developed by Sony in 1991 with $LiCoO_2$ as cathode and

graphite as anode, which could deliver an energy density as high as 180 Wh kg^{-1} at an average voltage of 3.6 V. In addition, the graphite anode could prevent the formation of lithium dendrites, resolving the safety problems caused by the short circuits. Henceforward, an enormous number of researchers have been working on this research field to improve the performance of LIBs. To meet the rapidly increasing demands of our society, it is a highly desirable to develop new electrode materials with high energy density, low cost, and long cycling life.

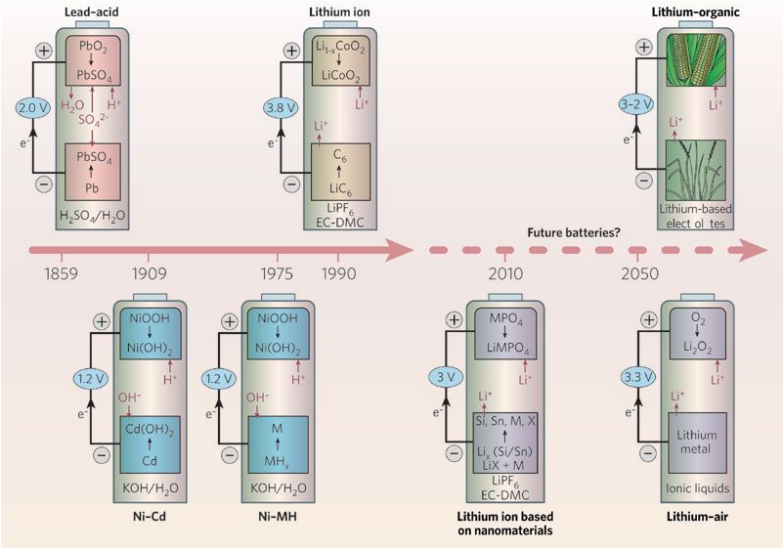

Figure 2.2 Schematic illustration of the development of batteries.[3]

2.1.3 Working Principles

In a typical LIB, there are four essential components, the cathode, the anode, the electrolyte, and the separator, as shown in **Figure 2.3**. The two electrodes have different chemical potentials, which are connected by an ionically conductive electrolyte. During discharge, an external device is used to connect the two electrodes and electrons are transferred from the anode to the cathode electrode. At the same time, lithium ions flow through the electrolyte to maintain the charge balance. Taking a

conventional LIB with $LiCoO_2$ as an cathode and graphite as an anode as example, lithium ions are transported from the graphite anode to the $LiCoO_2$ cathode through the electrolyte during discharging and transferred back to the graphite anode from the $LiCoO_2$ cathode when recharging with a higher voltage. The corresponding electrochemical reactions are shown below:

$$\text{Cathode: } LiCoO_2 \leftrightarrow Li_{1-x}CoO_2 + xLi^+ + xe^- \quad (2.1)$$

$$\text{Anode: } 6C + xLi^+ + xe^- \leftrightarrow Li_xC_6 \quad (2.2)$$

$$\text{Overall: } LiCoO_2 + 6C \leftrightarrow Li_{1-x}CoO_2 + Li_xC_6 \quad (2.3)$$

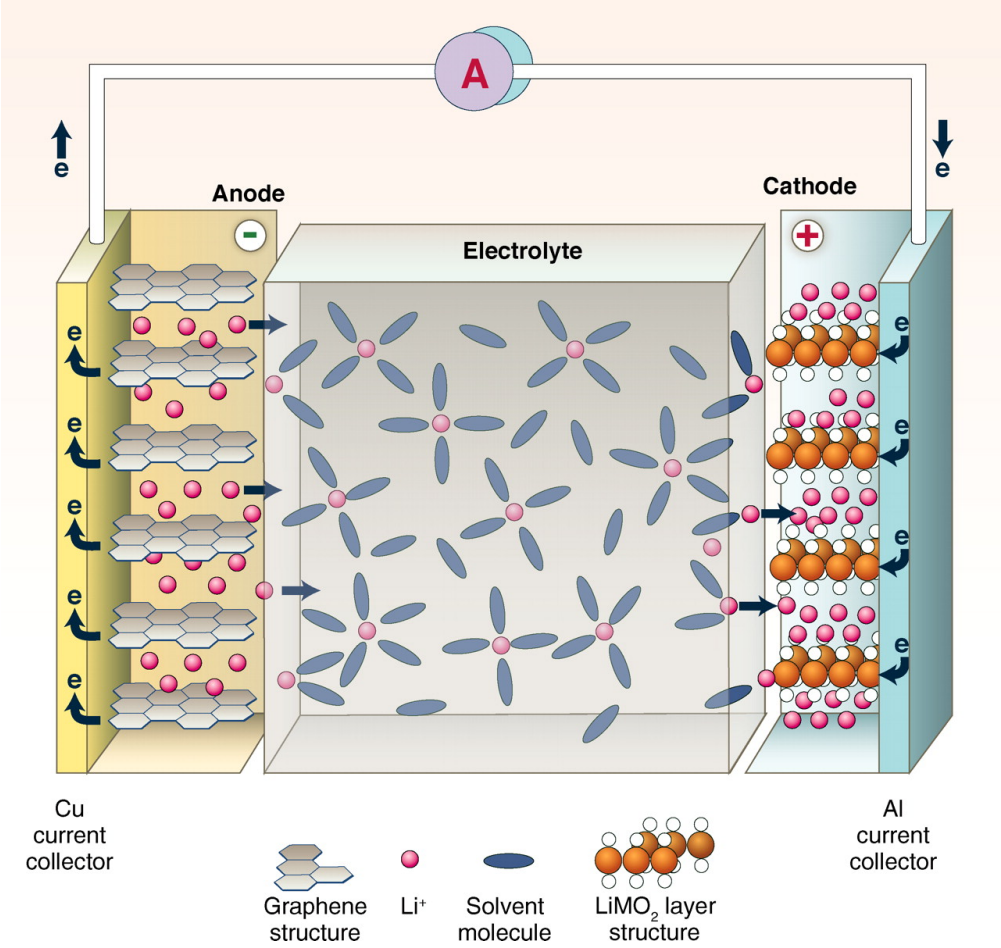

Figure 2.3 Schematic illustration of a rechargeable LIBs.[1]

2.1.4 Basic Concepts

The basic concepts and definitions for LIBs are discussed below:

Open circuit voltage (V_{oc}) is the voltage measured across the terminals of the battery without external current flow. V_{oc} is determined by the electrochemical potential difference between the anode and the cathode.

$$V_{oc} = (\mu_A - \mu_C) / (-nF) \quad (2.4)$$

where μ_A is the electrochemical potential of the anode; μ_C is the electrochemical potential of the cathode; n is the number of electrons involved; F is the Faraday constant (96485 C mol^{-1}).

The operating voltage could be defined as:

$$V = V_{oc} - IR \quad (2.5)$$

where I is the operating current and R is the internal resistance of the battery.

Capacity (Q) is the overall amount of electric charge in the battery for the redox reaction during charge/discharge.

$$Q = \int_{t1}^{t2} I(t)dt = nzF$$

where t represents the time; $I(t)$ is the current; n stands for the number of ions; z is the valence of the ions; F is the Faraday constant.

Specific capacity (Q_s) could be calculated as the gravimetric specific capacity (mAh g^{-1}) based on the capacity per unit weight of the active material or the volumetric specific capacity (mAh cm^{-3}) based on the capacity per unit volume of the active material.

Irreversible capacity represents the capacity loss of the active materials during one intercalation and deintercalation process. It is the capacity difference between the charge and discharge processes at the *n*th cycle.

Coulombic efficiency (η_e) represents the cycling stability of the battery, which is calculated from the ratio of the charge capacity to the discharge capacity at the *n*th cycle.

Energy density could be assessed in gravimetric (Wh kg^{-1}) or volumetric (Wh L^{-1}) terms, which represents the energy content in the cell.

Power density also could be assessed in gravimetric (W kg^{-1}) or volumetric (W L^{-1}) terms.

Charge/discharge rate (C-rate) is used to assess the transportation speed of lithium ions during charge or discharge processes. C stands for either the theoretical capacity or the nominal capacity of the battery.

2.1.5 Cathode Materials

Because they are essential for LIBs, cathode materials are critical for the development of advanced LIBs for portable electronics and electric vehicles.[4] There are mainly three kinds of cathode materials for LIBs: layered, spinel, and olivine structured oxides (**Figure 2.4**).

Layered structure $LiCoO_2$ is currently a widely used cathode materials in commercial LIBs, which has high energy density and good cycling performance.[6-8] Its layered structure features two-dimensional (2D) paths for lithium ion intercalation and deintercalation. Further applications of $LiCoO_2$ is hindered, however, by its low

specific capacity (only about 140 mAh g^{-1}), high cost, and toxicity. Another layered structured compound $LiNi_{1/3}Co_{1/3}Mn_{1/3}O_2$ has been considered as a promising candidate to replace $LiCoO_2$ due to its excellent electrochemical properties and structural stability.[9]

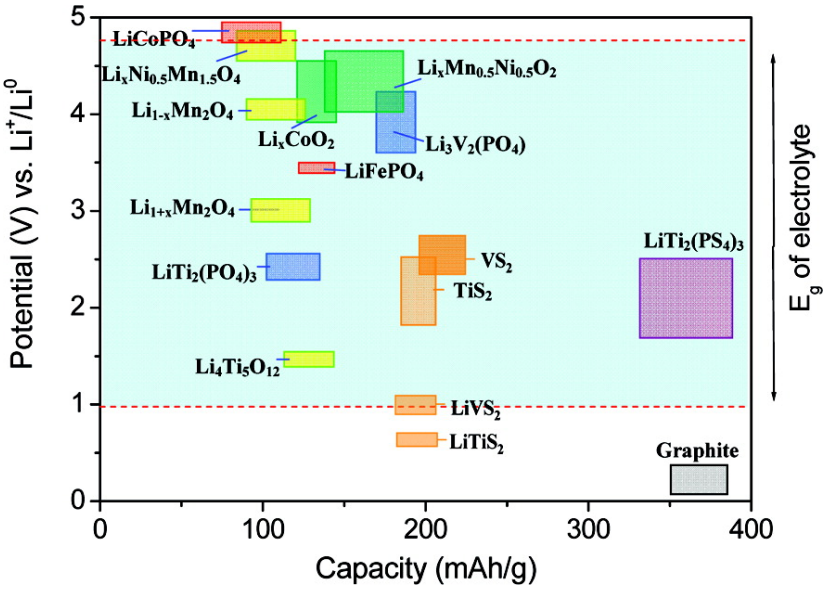

Figure 2.4. Voltage versus capacity for several electrode materials.[5]

Spinel structured $LiMn_2O_4$ is also receiving great research attention as an appealing cathode material for LIBs, owing to its abundant resources, high discharge potential, and better thermal stability compared with layered structure $LiCoO_2$.[10, 11] In addition, $LiMn_2O_4$ has three-dimensional (3D) framework structure for the diffusion of lithium ions, which could accommodate the volume changes during lithium ion intercalation and deintercalation compared to the 2D layered $LiCoO_2$, although $LiMn_2O_4$ also has some problems, such as low specific capacity (148 mAh g^{-1}), low power density, and unsatisfactory cycling stability, which could be attributed to the Jahn-Teller distortion of unstable Mn^{3+} ions.

Furthermore, olivine $LiFePO_4$ also is considered as a competitive cathode material for

LIBs.[12, 13] Even though $LiFePO_4$ suffers from low electronic conductivity, it has many merits for practical application, such as relatively high theoretical capacity (170 mAh g^{-1}), abundant raw materials, low cost, and safety. Apart from the above-mentioned three types of cathode materials, vanadium oxides also have been studied as cathode materials for LIBs. For example, V_2O_5 has been extensively explored owing to its high theoretical capacity (510 mAh g^{-1}).[14] Nevertheless, its low lithium diffusion rate and poor electronic conductivity are holding back its electrochemical performance, which needs to be resolved before further application.

2.1.6 Anode Materials

As the anode material could significantly affect the electrochemical performance of LIBs, it is important to choose excellent ones for high power and energy density LIBs.[15] To date, many different kinds of anode materials have been extensively studied, including carbonaceous materials, alloy materials, and metal oxides. Moreover, the ideal anode material should not only have high capacity, but also a stable structure and low potential.

2.1.6.1 Carbonaceous Materials

Due to its low cost, long cycle life, and low operating potential, graphite is widely used as the anode material for LIBs.[16, 17] Through forming LiC_6 at very low potential (0.1 V), graphite could deliver a theoretical capacity of about 372 mAh g^{-1}. Even though the graphite anode could reduce the safety issue for employing metallic lithium, its low theoretical capacity and low lithium diffusion coefficient are restricting its further application for high power density LIBs.

One-dimensional carbon materials also have received great research interest as promising anode materials for LIBs because of their high surface activity and giant surface-area-to-volume ratios, including carbon nanotubes (CNTs), carbon fibers, and carbon wires.[18, 19] Taking CNTs for example, the pseudo-graphitic layers of CNTs can be used to store lithium ions. In addition, the delocalization of electrons caused by strain on the planar bonds of the carbon hexagon could increase the electronegativity of the CNTs structure. As a result, CNTs could deliver a reversible capacity as high as 500 mAh g^{-1}.

Two-dimensional graphene nanosheets have attracted considerable attention as anode materials for LIBs due to their astonishing electrical conductivity, large surface area, excellent mechanical properties, and chemical stability.[20-22] Graphene nanosheets suffer from low initial coulombic efficiency, however, as well as rapid capacity decay, and large irreversible capacity. Furthermore, graphene nanosheets are extensively used in combination with other electrode materials to improve the electrochemical performance of the composites. In addition, the ultrathin graphene nanosheets could prevent the severe aggregation of nanoparticles and accommodate the huge volume change during the discharge/charge process. The anchored nanoparticles also could efficiently reduce the restacking of graphene nanosheets and preserve the high active surface area.

2.1.6.2 Alloy Materials

Group IVA elements (Si, Ge, and Sn) with the alloying reaction mechanism have been extensively explored.[23-25] These elements and their derived compounds have relatively

low voltages profiles and high theoretical capacity, thus making them promising anode materials for LIBs. The crystal structures of Group IVA elements are depicted in Figure 2.4 (a) and their gravimetric and volumetric capacities are shown in **Figure 2.5** (b).[26, 27] Even though these alloying materials possess higher specific capacities than the intercalation materials, their huge volume expansion during alloying/de-alloying results in severe capacity decay and poor cycling stability.

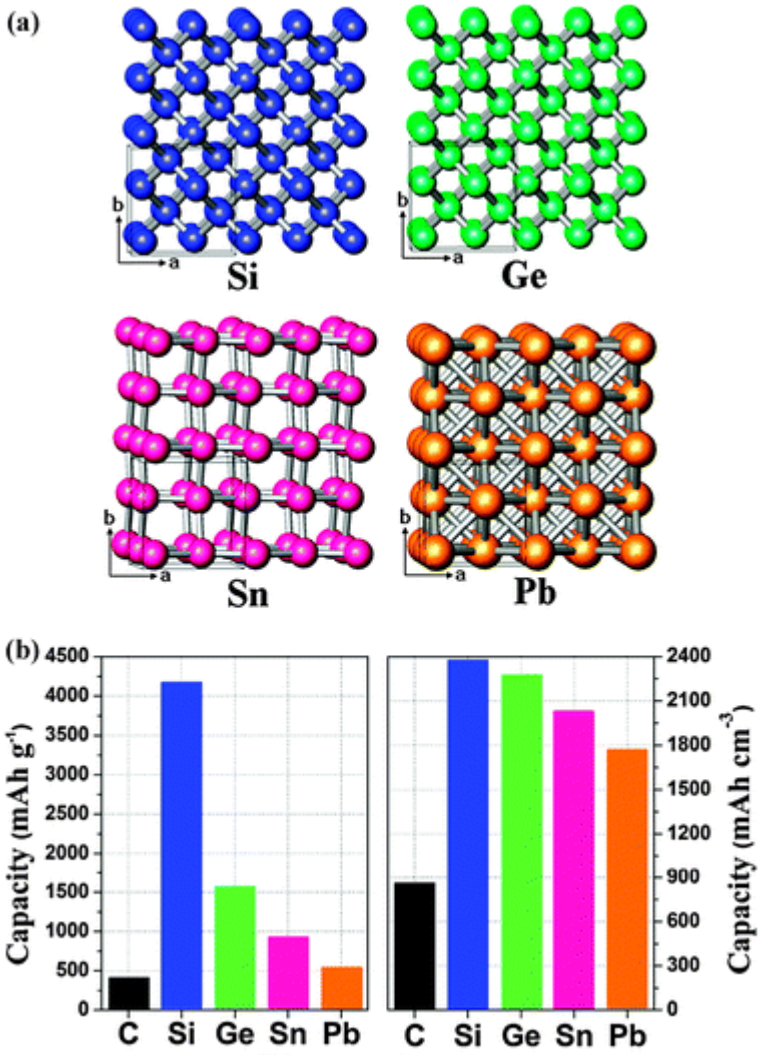

Figure 2.5. Crystal structures and capacities of Group IV elements. (a) Crystal structures of cubic Si (blue), cubic Ge (green), tetragonal Sn (red), and cubic Pb (orange). (b) Gravimetric and volumetric capacities of C (LiC_6), Si ($Li_{4.4}Si$), Ge ($Li_{4.25}Ge$), Sn ($Li_{4.25}Sn$), and Pb ($Li_{4.25}Pb$).[26]

Silicon has been considered as a potential candidate anode material for LIBs because of its abundance, low cost, low electrochemical potential, and ultrahigh theoretical capacity (4200 mAh g^{-1}).[28-30] During the alloying process, silicon can form different intermetallic compounds, including $Li_{12}Si_7$, Li_7Si_{13}, $Li_{13}Si_4$, and $Li_{22}Si_5$. Silicon anode always suffers from dramatic capacity decay, however, which severely obstructs its practical application in future LIBs. The reasons for the huge irreversible capacity for silicon anodes are listed below:

(a) Silicon particles are detached from the conductive carbon or the current collector because of the large volume changes and pulverization during cycling, which leads to the loss of active material[31-33];

(b) Unstable solid electrolyte interphase (SEI) film would be continuously formed on the freshly exposed active particle surfaces during volume expansion, which results in poor coulombic efficiency and short cycling life[34, 35];

(c) The aggregation of anode particles may cause an increase in the Li diffusion length and the trapping of SEI films in the particles, leading to irreversible capacity loss[36-38].

Compared with Si, Ge has a much lower gravimetric capacity of 1600 mA hg^{-1}, but it can take advantage of the better electrochemical kinetics associated with much higher lithium ion diffusivity (400 times faster than for Si) and better electrical conductivity (140 times higher than for Si).[39-41] With these favorable transport properties, it is expected that Ge will have a better rate capability than Si. Fast transport of both electrons and Li ions is highly desirable for achieving a high charging/discharging rate in LIBs. Unfortunately, like other alloy materials, Ge also has high initial irreversible

capacity and suffers from rapid capacity fade during cycling.

To achieve high specific capacity, good cycling performance, and high rate capability, several strategies have been investigated in the past decade. One approach to improve the cycling performance of Ge is to reduce the particles to nano-size, by such approaches as using nanoparticles[42-44], nanotubes[45, 46], and nanowires[47, 48]. Such improvement has been attributed to the facile strain accommodation and the short diffusion paths for electron and Li-ion transport in these nanostructured electrodes. For example, Park et al.[46] prepared ultra-long Ge nanotubes from core-shell Ge-Sb nanowires using the Kirkendall effect. The Ge nanotubes exhibited an exceptionally high rate capability, maintaining a reversible capacity of over 1000 mA hg^{-1} for over 400 cycles at 40 C (40 A g^{-1}). Another very common approach to solve these problems is using buffer layers such as carbon or graphene to improve the electrochemical performance of Ge anode, which has been proved to be an effective method to accommodate the volume expansion, improve contact between the active material and the current collector, and result in improved rate performance[49-52]. The most commonly used strategies to fabricate Ge and carbon composites are chemical vapor deposition[53], vapor or solution liquid-solid processes[54], and others. For instance, Xue et al.[54] used hybrid Ge/C core-shell nanoparticles with reduced graphene oxide as an anode material for LIBs. The material showed average coulombic efficiency higher than 99% for up to 50 cycles after the second cycle and an enhanced capacity of 380 mA hg^{-1} after 50 cycles under a high current density of 3600 mA g^{-1}, which can be compared with a capacity of 100 mA hg^{-1} for Ge/C nanoparticles under the same current and cycling conditions.

2.1.6.3 Metal Oxides

Metal oxides have received extensive attention for LIBs due to their high capacity (500-1000 mAh g^{-1}) and well-ordered structure.[55-61] Based on the reaction mechanism, metal oxide anodes could be divided into three types:

(1) Conversion reaction mechanism with the formation and decomposition of Li_2O during the reduction and oxidation of metal (M) oxides, such as Co_3O_4, Fe_2O_3, and NiO:[62-67]

$$M_xO_y + 2yLi^+ + 2ye^- \leftrightarrow xM + yLi_2O \quad (2.6)$$

(2) Insertion/extraction mechanism with insertion and extraction of lithium ions from the lattices of metal oxides, such as TiO_2:[68, 69]

$$MO_x + yLi^+ + ye^- \leftrightarrow Li_yMO_x \quad (2.7)$$

(3) Alloying reaction mechanism, such as in SnO_2:[70, 71]

$$M + xLi^+ + xe^- \leftrightarrow Li_xM \quad (2.8)$$

2.2 Sodium-Oxygen Batteries

2.2.1 General Background

To accommodate the rapid economic growth, the demand for energy has become a global challenge for human society. The fast utilization of nonrenewable fossil fuels, however, such as petroleum, coal, and natural gas, results in their exhaustion. In addition, the consumption of fossil fuels also causes severe environment pollution and leads to the greenhouse effect. Herein, new forms of energy based on low-cost and sustainable energy sources (solar, wind, and wave energy) are required to meet

development of modern society. In addition, efficient energy storage systems are necessary to store the variable and unreliable renewable energy. As the current state-of-the-art energy storage system, LIBs could not satisfy the requirement for extended application in electric vehicles (EVs), and further development of energy storage technology is necessary.

With their extremely high theoretical energy density, metal-O_2 batteries are considered as potential candidate for future applications, such as EVs. Among the various metal-O_2 batteries, sodium-oxygen batteries (SOBs) have attracted great research attention due to their high theoretical specific energy (3451 Wh kg^{-1}), low charge overpotential, and relatively stable reaction intermediate. Nevertheless, great efforts are still needed to improve the electrochemical performance of SOBs for practical application in EVs.

2.2.2 Brief History

During the past several years, enormous research attention has been devoted to the research on lithium oxygen batteries (LOBs). Unlike the structure of conventional LIBs, the cathode is exposured to the O_2 atmosphere, which makes LOBs research much more challenging and complicated. In 1996, Abraham et al. successfully fabricated the first rechargeable LOBs with porous carbon as air cathode. By using MnO_2 as cathode, Bruce and co-workers greatly improved the rechargeability of the Li_2O_2 electrode. Even though LOBs have the highest theoretical specific energy (11430 Wh kg^{-1}) of metal-O_2 batteries, they still have many disadvantages, such as unstable reaction intermediates, high charge overpotential, and poor cycle life. Therefore, Peled and co-workers investigated the first SOBs operating above the melting point of sodium metal (97.8 ºC), as an alternative to LOBs.[72] Later, Fu et al. fabricated the

first rechargeable SOBs, which could be operated at room temperature.[73] Since then, SOBs have attracted the interest of numerous researchers due to their high theoretical specific, low charge overpotential, and relatively stable reaction intermediates compared to LOBs, as shown in **Figure 2.6**.

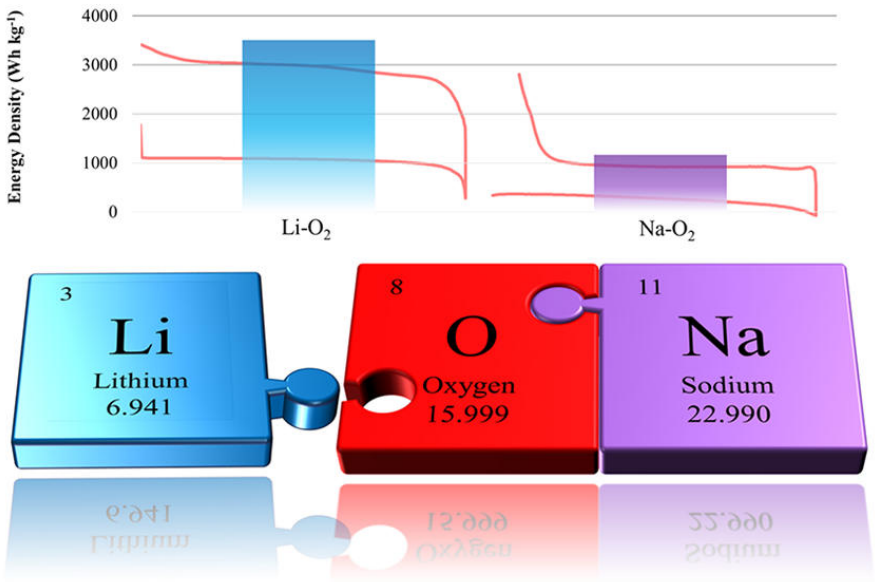

Figure 2.6. Comparison of the lithium oxygen battery and the sodium oxygen battery.[74]

2.2.3 General Principles

A typical structure for SOBs is shown in **Figure 2.7**, which is quite similar to that of LOBs. SOBs are open systems, since oxygen gas absorbed from the air works as the cathode active material, and sodium metal is employed as the anode material. Similar to LOBs, SOBs also undergo a dissolution/precipitation reaction during the discharge/charge processes. During the discharge process, the sodium metal is oxidized to form sodium ions and releases electrons to the external circuit. Meanwhile, sodium ions are transferred to the cathode electrode through the electrolyte and combined with the reduced oxygen molecules to generate sodium oxide products (NaO_2 or Na_2O_2) on the surface of the air cathode. The corresponding electrochemical reactions are shown below, with E^0 the standard potential:

Cathode: $O_2 + e^- \rightarrow O^{2-}$ (2.9)

Or $O_2 + 2e^- \rightarrow O_2^{2-}$ (2.10)

Anode: $Na \rightarrow Na^+ + e^-$ (2.11)

Overall: $Na + O_2 \rightarrow NaO_2$ $E^0 = 2.27$ V (2.12)

Or $2Na + O_2 \rightarrow Na_2O_2$ $E^0 = 2.33$ V (2.13)

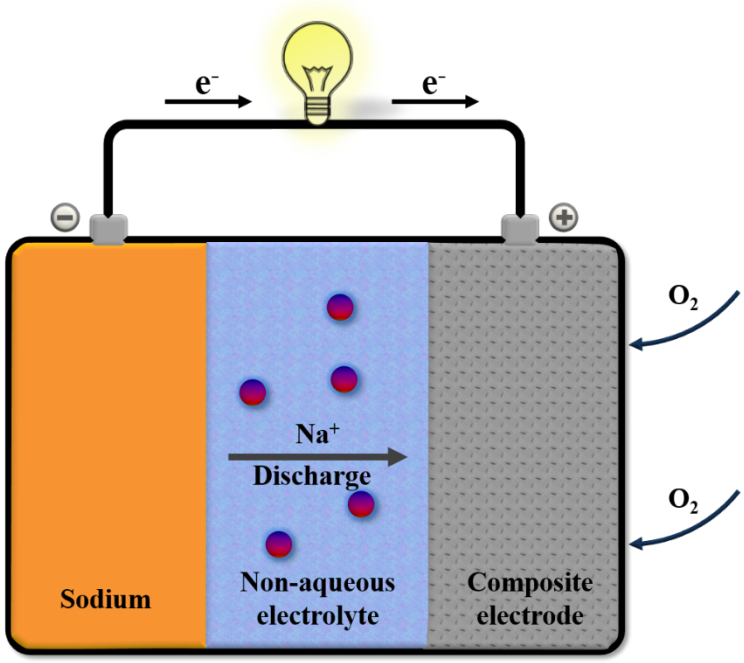

Figure 2.7. Schematic illustration of a Sodium oxygen battery.

Based on the hard and soft acid and base theory, sodium ions with relatively larger radii and higher polarizability than lithium ions could be considered as a soft Lewis acid, which could efficiently stabilize the soft Lewis base reaction of the intermediate superoxide ions. Therefore, sodium superoxide could be the final discharge product of SOBs, which is much more stable than lithium superoxide.

2.2.4 Basic Concepts

In order to better assess SOBs, more concepts are introduced as supplements to the

concepts based on the LIBs in section 2.1.4.

Potential (E) represents the electromotive force between the cathode and the anode electrodes, which could be calculated based on the Gibbs free energy (ΔG^0) as shown below:

$\Delta G^0 = \Delta H^0 - TS^0$

Where ΔH^0 is the enthalpy, T stands for absolute temperature (K), and S^0 represents the entropy.

When ΔG^0 is completely converted to electrical energy, the electrode potential can be calculated as follows:

$E = -\Delta G^0/nF$

Where ΔG^0 is the Gibbs free energy, n represents the number of electrons engaged in the reaction, and F stands for the Faraday constant.

Overpotential is the potential difference between the practical potential and the thermodynamic potential of a redox reaction. The overpotential is required because extra energy is needed to overcome the energy barriers to drive the reaction. Therefore, electrocatalysts are needed to decrease the energy barriers and reduce the overpotential of the reactions.

Round-trip efficiency is the ratio of the discharge to the charge voltage, which is highly dependent on the electrocatalytic activity of the catalyst used in the battery.

2.2.5 Cathode Materials

As the most important component of the SOBs, the cathode electrode could

significantly influence the electrochemical performance of the battery. During the discharge process, oxygen is reduced and reacts with sodium ions to form sodium oxides discharge products on the air electrode. In general, the air cathode should have excellent electrical conductivity, high specific surface area, adequate porosity and porous structure, chemical and electrochemical stability, and low cost. Excellent electrical conductivity is needed to accelerate the transport of electrons for the electrochemical reactions. As the air electrode needs to provide a three-phase zone for the oxygen reduction and evolution reactions, it should have a porous structure for the gas diffusion and accommodate the solid discharge products. Otherwise, the solid discharge products would block the gas diffusion paths and result in the death of the battery. Many publications have revealed that the electrochemical performance, in such aspects as the discharge capacity, overpotential, and cycling stability, is highly dependent on the efficiency of the air cathode.

Apart from the structure of the air cathode, an electrocatalyst also could reduce the overpotential and improve the cycling stability of the SOBs. To date, there has been much research interest devoted to the development of cathode catalysts for SOBs, such as carbonaceous materials, metal oxides, and soluble catalysts.

2.2.5.1 Carbonaceous Materials

To date, carbon-based air cathodes have been widely investigated for SOBs because of their outstanding electrical conductivity, large surface area, and tunable porous structure. As summarized in Table 2.1, various carbon-based materials have been researched as air cathodes for SOBs, such as graphene nanosheets (GNS), diamond-like carbon (DLC), carbon nanotubes (CNTs), and porous carbon spheres.

Table 2.1 Summary of various carbon-based air cathodes for SOBs.[75] BET: Brunauer-Emmett-Teller.

Air Cathode	BET Specific Surface Area	Specific Discharge Capacity	Discharge Current Density
Carbon Fiber (CF)	< 1m^2 g^{-1}	300 mAh g^{-1} (2.9 mAh cm^{-2})	12.3 mA g^{-1} (0.12 mA cm^{-2})
		12 mAh g^{-1} (0.11 mAh cm^{-2})	51.4 mA g^{-1} (0.50 mA cm^{-2})
Diamond-like Carbon (DLC)	-	3600 mAh g^{-1} (1.08 mAh cm^{-2})	1/60 C
		1884 mAh g^{-1} (0.56 mAh cm^{-2})	1/10 C
Heat-treated carbon black (CB)	1282 m^2 g^{-1}	2783 mAh g^{-1} (0.98 mAh cm^{-2})	75 mA g^{-1} (0.03 mA cm^{-2})
		1914 mAh g^{-1} (0.67 mAh cm^{-2})	300 mA g^{-1} (0.10 mA cm^{-2})
Ordered mesoporous carbon (OMC)	1544 m^2 g^{-1}	7987 mAh g^{-1} (1.57 mAh cm^{-2})	100 mA g^{-1} (0.02 mA cm^{-2})
Graphene nanosheets (GNSs)	83 m^2 g^{-1}	9368 mAh g^{-1}	200 mA g^{-1}
		1110 mAh g^{-1}	1000 mA g^{-1}
Nitrogen-doped graphene nanosheets (N-GNSs)	-	8600 mAh g^{-1} (3.6 mAh cm^{-2})	75 mA g^{-1} (0.03 mA cm^{-2})
		3980 mAh g^{-1} (1.7 mAh cm^{-2})	300 mA g^{-1} (0.12 mA cm^{-2})
Carbon nanotube (CNT) paper	-	7530 mAh g^{-1} (1.5 mAh cm^{-2})	500 mA g^{-1} (0.1 mA cm^{-2})
Vertically aligned carbon nanotubes (VACNTs)	80 m^2 g^{-1}	4500 mAh g^{-1} (6.3 mAh cm^{-2})	67 mA g^{-1} (0.09 mA cm^{-2})

CNT	215 $m^2 g^{-1}$	1530 mAh g^{-1} (4.22 mAh cm^{-2})	65 mA g^{-1} (0.2 mA cm^{-2})
CNT-CF	112 $m^2 g^{-1}$	800 mAh g^{-1} (4.37 mAh cm^{-2})	36 mA g^{-1} (0.2 mA cm^{-2})
CNT-CB	128 $m^2 g^{-1}$	530 mAh g^{-1} (2.30 mAh cm^{-2})	46 mA g^{-1} (0.2 mA cm^{-2})
Nitrogen doped carbon nanotube-carbon paper (NCNT-CP)	27 $m^2 g^{-1}$	1349 mAh g^{-1} (11.3 mAh cm^{-2}) 773 mAh g^{-1} (6.5 mAh cm^{-2})	12 mA g^{-1} (0.1 mA cm^{-2}) 60 mA g^{-1} (0.5 mA cm^{-2})

The application of GNS as air cathode for SOBs has been studied by many researchers due to their large theoretical surface area, excellent electrocatalytic activity, and high electrical conductivity. In addition, the unique morphology and three-dimensional (3D) structure assembled by the GNS could provide large space to accommodate the insoluble discharge products, resulting in high discharge capacity and good electrochemical performance. For example, Fu et al. developed a GNS air cathode electrode for SOBs, which exhibited a high discharge capacity of about 8268 mAh g^{-1} with the current density of 200 mA g^{-1}.[76] As shown in **Figure 2.8**, Sun and co-workers reported that the electrocatalytic activity of the GNS air cathode could be improved through nitrogen doping, and the nitrogen-doped graphene nanosheets (N-GNSs) exhibited a higher discharge capacity (8600 mAh g^{-1}) than that for the pure GNS air cathode (4350 mAh g^{-1}) with the current density of 75 mA g^{-1}.[77] The discharge plateaus of N-GNS air cathodes at various current densities are also higher than those of GNS air cathodes. The cyclic voltammetry (CV) curves reveal that the N-GNSs air cathode exhibits superior electrocatalytic activity towards both the oxygen evolution reaction (OER) with negatively shifted anodic peak and the oxygen reduction reaction (ORR) with positive onset potential when compared with the GNS air cathode.

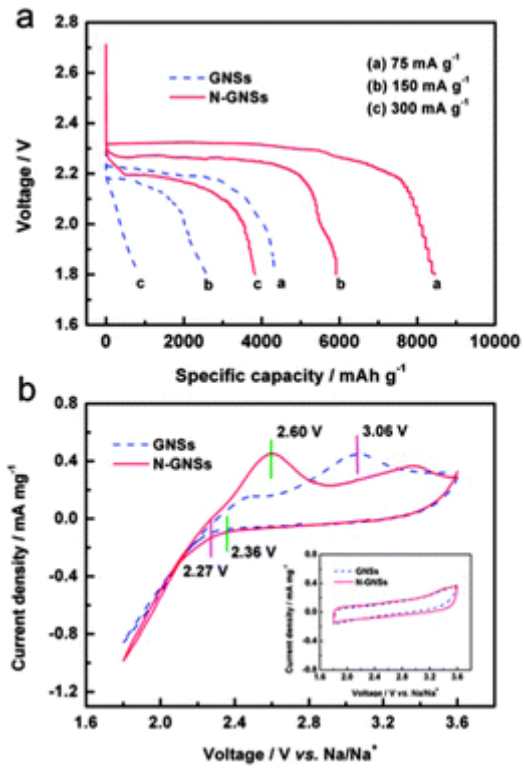

Figure 2.8. (a) Discharge curves at different current densities and (b) CV curves of GNS and N-GNS air cathodes.[77]

CNTs also have been studied as air cathode for the SOBs because of their high electrical conductivity, large surface area, and excellent corrosion resistance. Zhou and co-workers reported a CNT paper air cathode with large void spaces to store the discharge products, which could deliver a high discharge capacity of 7530 mAh g^{-1} under a current density of 500 mA g^{-1}.[78] Then, high surface-area vertically aligned carbon nanotubes (VACNTs) were reported with a capacity of 4200 mAh g^{-1} under the current density of 67 mA g^{-1}.[79] In addition, the VACNTs demonstrated excellent cycling stability with electrical energy efficiency of 90 % for 100 cycles when cycled with a limited capacity of 750 mAh g^{-1}. Sun et al. investigated the electrochemical performance of nitrogen doped carbon nanotubes on carbon paper (NCNT-CP) as air cathode for SOBs.[80] The NCNT-CP air cathode with high surface area and a unique 3D structure could significantly increase the capacity of the SOBs to 11.3 mAh cm^{-2},

which is 17 times higher than that of the bare carbon paper air cathode (**Figure 2.9**).

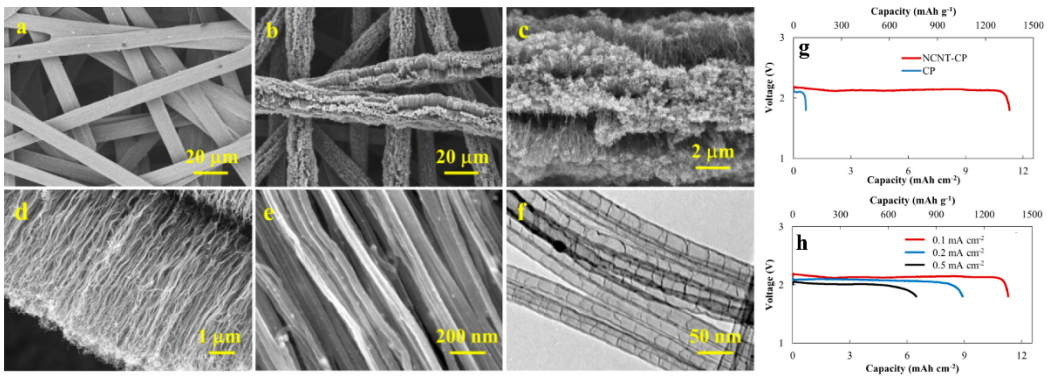

Figure 2.9. (a) Scanning electron microscopy (SEM) image of bare CP, (b–f) SEM and transmission electron microscopy (TEM) images of NCNT-CP air cathode, (g) discharge curves of bare CP and NCNT-CP air cathodes under a current density of 0.1 mA cm^{-2}, (h) discharge curves of NCNT-CP air cathode at various current densities.[80]

2.2.5.2 Metal Oxide

Metal oxides, such as $NiCo_2O_4$, α-MnO_2, Mn_2O_3, and $CaMnO_3$, are also being investigated in SOBs, and they already have been widely utilized to improve the electrochemical performance of LOBs. [81-85] Fu and co-workers fabricated a $NiCo_2O_4$ nanosheets/Ni foam composite as air cathode for SOBs, which could deliver a discharge capacity of about 1762 mAh g^{-1} under the current density of about 20 mA g^{-1}.[81] In addition, nanosheet discharge products composed of Na_2O_2 and Na_2CO_3 were obtained. Hintennach's group then synthesized α-MnO_2 nanowires by the microwave method for SOBs and the discharge capacity was about 2056 mAh g^{-1},[82] although the capacity faded to only 1215 mAh g^{-1} after 2 cycles. Porous $CaMnO_3$ microspheres/C were also reported with excellent electrocatalytic activity as air cathode compared to a Super P air cathode for SOBs.[83] As shown in **Figure 2.10**, this air cathode could deliver a discharge capacity as high as 9560 mAh g^{-1} under a current density of 100 mA g^{-1} in ether-based electrolyte. When the discharge capacity was limited to 1000

mAh g^{-1}, the $CaMnO_3$ microspheres/C air cathode could cycle for 80 cycles. In addition, NaO_2 and Na_2O_2 were detected as the discharge products of $CaMnO_3$ microspheres/C air cathode by using Raman spectroscopy and X-ray diffraction (XRD). In contrast, only Na_2O_2 was observed in the Super P air cathode.

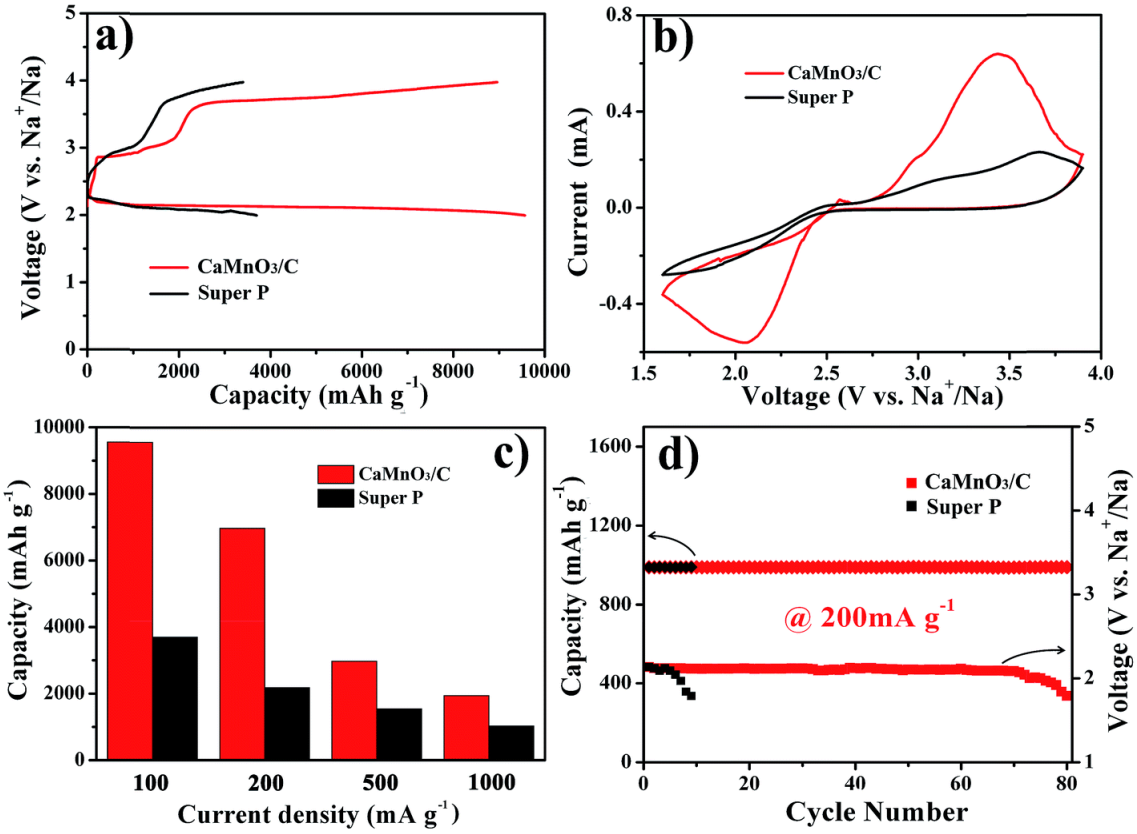

Figure 2.10. Electrochemical performance comparison of $CaMnO_3$/C and Super P air cathodes. (a) Discharge/charge curves of the two air cathodes at 100 mA g^{-1}, (b) CV curves with a scan rate of 0.1 mV s^{-1}, (c) Discharge capacities under various current densities, (d) Cycling performances of the two air cathodes.[83]

Moreover, other metal-based materials that also have excellent electrocatalytic activities can be used as air cathodes for the SOB, such as metals, metal phosphides, metal sulfides, and metal nitrides. For example, Liu et al. synthesized ultrathin heterostructured CoO/CoP nanosheets with a P-O interpenetrating interface as air cathode catalyst for SOBs (**Figure 2.11**).[86] The CoO/CoP nanosheets exhibited

excellent electrochemical performance due to the combination of CoP with high OER activity and CoO with high ORR activity. Therefore, CoO/CoP could not only deliver a high discharge capacity (12654 mAh g^{-1}), but could also exhibit good cycling stability for 65 cycles. Huang et al. reported Au-coated MnO_2 nanowires as air cathode for SOBs.[87] In-situ transmission electron microscopy (TEM) demonstrated that NaO_2 nanobubbles were formed on the surface of the Au-coated MnO_2 nanowires air cathode before they disproportionated to Na_2O_2 and O_2 gas during the discharge process.

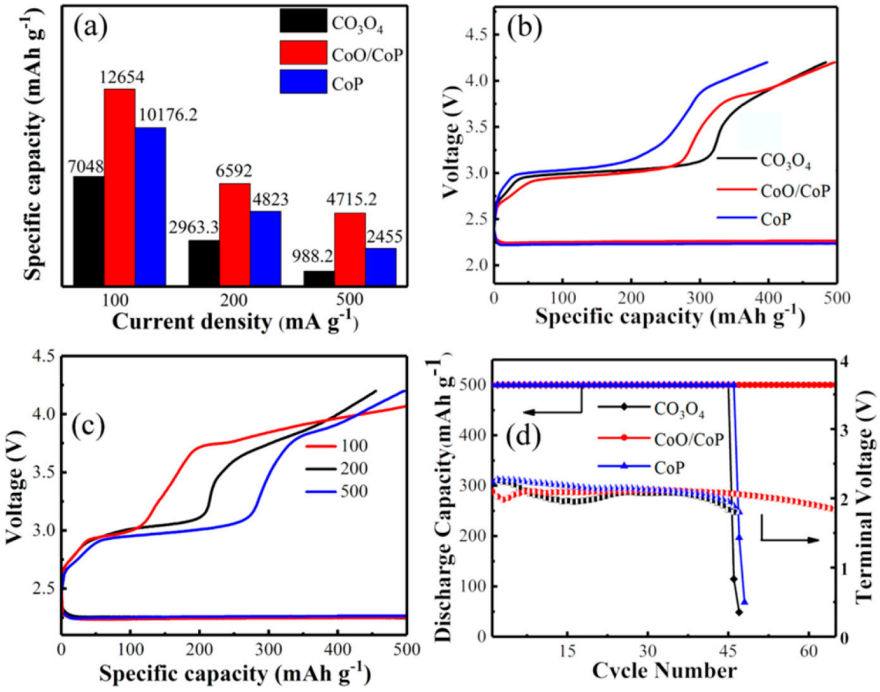

Figure 2.11. Electrochemical performance of Co_3O_4, CoO/CoP, and CoP nanosheets. (a) First discharge capacity under various current densities, (b) discharge/charge curves under a current density of 500 mA g^{-1}, (c) discharge/charge curves of CoO/CoP air cathode under various current densities, and (d) the cycling stability of Co_3O_4, CoO/CoP, and CoP nanosheets at a current density of 500 mA g^{-1}.[86]

2.2.5.3 Soluble Catalysts

Many soluble catalysts have already been used in LOBs, such as tetrathiafulvalene (TTF), iron phthalocyanine (FePc), lithium iodide (LiI), lithium bromide (LiBr), 2,5-

di-tert-butyl-1,4-benzoquienone (DBBQ), and 2,2,6,6-tetramethylpiperidinyloxyl (TEMPO), which could easily be conveyed in the electrolyte and act as redox mediators to accelerate the electrochemical reactions.[88-93] Therefore, soluble catalysts have attracted great research attention for SOBs

Soluble sodium iodide (NaI) catalyst was investigated for SOBs by Fu et al., which could operate for 150 cycles with a limited capacity of 1000 mAh g^{-1} at the current density of 500 mA g^{-1}.[94] As shown in **Figure 2.**12, soluble ferrocene catalyst was also explored to improve the electrochemical performance of SOBs, which could not only act as an electrocatalyst but also could participate in the electrochemical reactions.[95] Due to the dual catalytic activity towards the decomposition of the Na_2O_2 discharge product, an excellent cycling stability of 230 cycles with the limited capacity of 1000 mAh g^{-1} could be achieved.

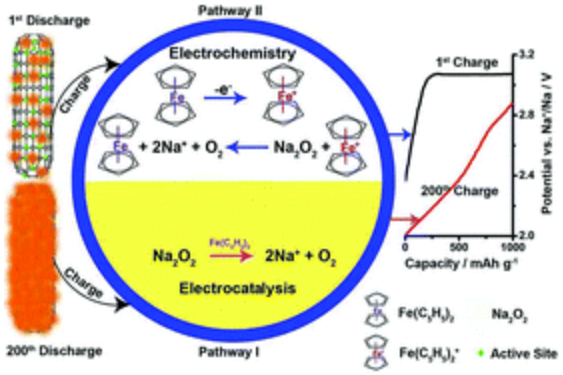

Figure 2.12. Schematic illustration of SOBs with soluble ferrocene catalyst.[95]

2.2.6 Anode Material

Sodium metal is used as the anode electrode for SOBs due to its high energy density and low potential. Its cycling stability and safety, however, are two big problems associated with the formation of dendrites on the sodium metal anode. The dendrites

could penetrate into the separator and cause a short circuit after reaching the cathode electrode, leading to poor cycling stability and severe safety issues. In addition, sodium metal also may be undermined by oxygen and moisture, which could crossover to the anode electrode from the air cathode.

Guo et al. also reported the sodium dendrite formation in SOBs.[96] With increased discharge capacity and cycle number, the surface of the sodium anode becomes rougher, as shown in **Figure 2.13**. Adelhelm and co-workers investigated the formation of sodium dendrites in SOBs.[97] After only 10 cycles, the dendrites penetrated the polymer separator. They also demonstrated that the formation of dendrites could then be suppressed by using solid electrolyte membranes. The ion-selective Nafion-Na^+ membrane separator could suppress the dendrite penetration, resulting in enhanced cycling stability for the SOBs.[98]

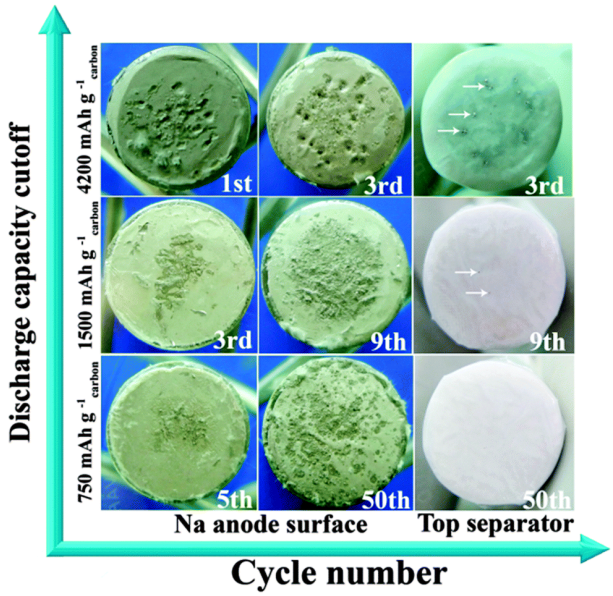

Figure 2.13. Photographs of the sodium anode and separator under various discharge conditions.[96]

In addition, the stability of sodium metal anode also could be improved through

forming a protective passivation film on the sodium anode (**Figure 2.14**).[99] The sodium fluoride-rich film could not only prevent the formation of sodium dendrites, but could also efficiently prevent oxygen crossover, leading to enhanced SOBs cycling stability for over 50 cycles with the limited discharge capacity of 1000 mAh g^{-1}. Janek et al demonstrated that utilizing sodium-metal-free sodiated carbon as anode also could efficiently prevent the formation of sodium dendrites.[100]

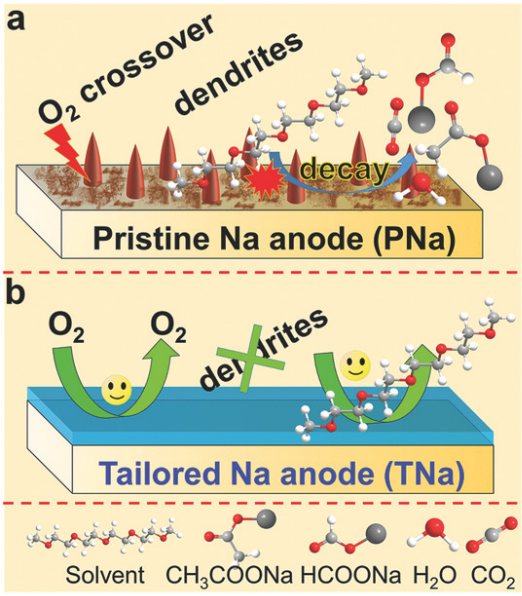

Figure 2.14. (a) Pristine sodium anode and (b) tailored sodium anode (TNa) against side reactions.[99]

2.2.7 Electrolyte

Similar to LOBs, the electrolytes for the SOBs also critically influence the formation mechanism of solid discharge products, thus affecting the maximum discharge capacity. [101-107] There are mainly two different discharge products (NaO_2 and Na_2O_2) associated with two different formation mechanisms during the discharging process as shown in Equations (2.12) and (2.13). As shown in **Figure 2.15**, high donor number (DN) solvents lead to the formation and removal of $[Na^+\text{-}O_2^-]_{(ads)}$, and facilitate the

generation of NaO_2, which exhibits lower charge overpotential.[107] Low DN solvents, however, could mainly yield Na_2O_2 because the solvation is weaker than that of high DN solvents.

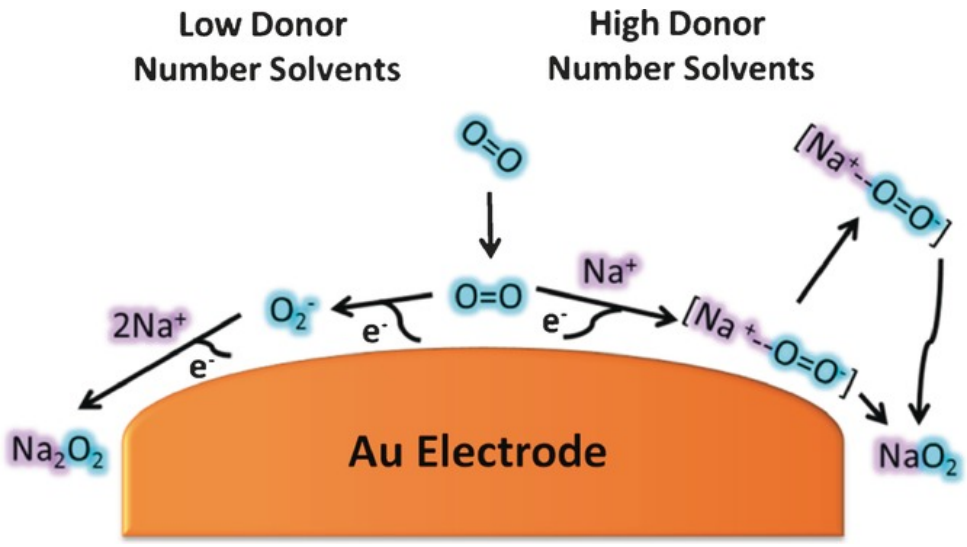

Figure 2.15. Schematic illustration of oxygen reduction mechanisms in non-aqueous solvents.[107]

In addition, the cycling stability of the SOBs is likely to be affected if the electrolyte is unstable and decomposes during cycling. The ideal electrolyte should have excellent physicochemical and electrochemical stability, which could guarantee the long cycling life and excellent electrochemical performance of non-aqueous SOBs. Therefore, a suitable electrolyte should meet the following requirements:

(1) High physicochemical stability, including low volatility or low vapor pressure, low moisture absorption, and non-flammability. As mentioned above, the SOBs should be open to the ambient atmosphere; therefore, non-aqueous solvents with low moisture absorption and low volatility are necessary and play a critical role in increasing cycling performance. **Figure 2.16** presents the solvent evaporation rate and moisture

absorption rate for various electrolytes. For example, the 1,2-dimethoxy ethane (DME) solvent evaporates quickly, and the pure solvent loses 87% of its initial weight, just by two days' storage inside a dry box at about 29 °C.[108] The cell will prematurely die because the electrolyte has dried out. Alternative solid-state electrolytes, ionic liquid-based electrolytes, and solid polymer electrolytes probably are beneficial for the cycling performance because batteries with these electrolytes could preserve their electrolyte for longer than batteries with conventional liquid organic electrolytes.

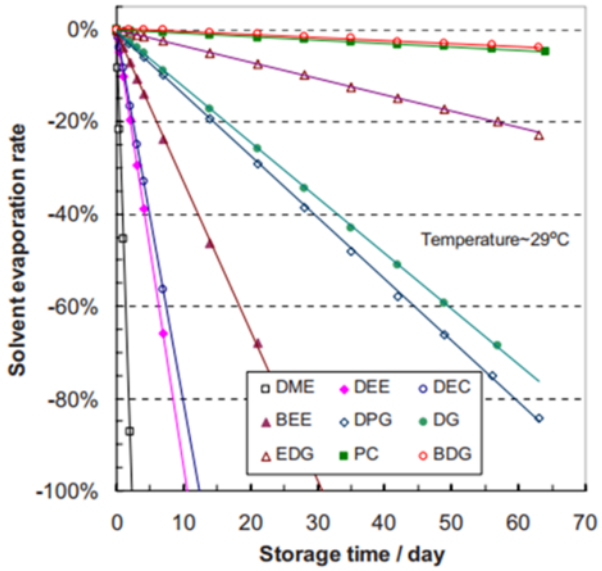

Figure 2.16. Solvent evaporation rates over time for various solvents.[108]

(2) Solid electrolyte interphase (SEI) formation. Sodium metal is an alkali metal and hence chemically reactive, rather electropositive, and quite susceptible to oxidation, especially in open atmosphere.[96-99] A stable SEI film, generated on the surface of the sodium metal via decomposition of the electrolyte, can impede the corrosion of sodium metal, but sodium deposition is usually associated with dendrite formation. Hence, it is also a big challenge to form a highly stable SEI layer by the use of different sodium salts, solvents, additives, and alternative sodium metal anodes.

(3) High oxygen solubility and diffusivity during the reaction process. Oxygen dissolution and diffusion in the interior of the cathode electrode, which is immersed in electrolyte, are the determining factors in oxygen availability. Therefore, besides high sodium ion conductivity, excellent oxygen dissolution and diffusion properties are necessary.

(4) High electrochemical stability and resistance to oxygen reduction intermediate species, such as superoxide radicals (O_2^-). The superoxide (O_2^-) intermediate is highly damaging to some electrolytes, and therefore, a suitable electrolyte should be quite stable against nucleophilic attack by the superoxide intermediate.

Although non-aqueous electrolytes have been studied for several years and successfully utilized in the current LOBs, the researches about electrolytes in SOBs are quite limited. There have been many publications regarding SOBs, but perfect non-aqueous electrolytes have not yet been found.[106, 107, 109-111] And the comparison of common electrolytes are listed in **Table 2.2**. Therefore, an ideal non-aqueous electrolyte for SOBs should satisfy the following demands:

(1) High physical stability, including low volatility, low moisture absorption, and non-flammability;

(2) Stable solid electrolyte interphase formation on the surface of the sodium metal anode;

(3) Outstanding oxygen solubility and diffusivity;

(4) Excellent chemical and electrochemical stability, especially in the presence of superoxide radicals (O_2^-).

Table 2.2. Comparison of some common electrolytes for Li-O_2 batteries.

	Electrolyte	molecular structure	Advantages	Disadvantages
Carbonate-based Electrolytes	Propylene carbonate (PC)	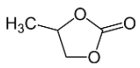	Low volatility, wide electrochemical window, and liquid-temperature range	Highly unstable towards O_2^- radical
	Ethylene carbonate (EC)			
	Dimethyl carbonate (DEC)	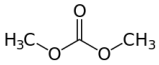		
Ether-based Electrolytes	1,2-dimethoxyethane (DME)	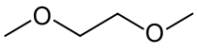	Low vapor pressure, non-flammability, and higher stability than carbonates	Unstable towards O_2^- radical
	Tetraethylene glycol dimethyl ether (TEGDME)	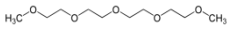		
	1, 3 dioxolane (DOL)			
	2-methyltetrahydrofuran (2-Me-THF)			
DMSO Electrolyte	Dimethyl sulfoxide (DMSO)	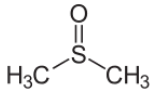	High conductivity and low viscosity	High vapor pressure and some side reactions
Ionic Liquids	*N*-methyl-*N*-propylpiperidinium TFSI ($PP_{13}TFSI$)	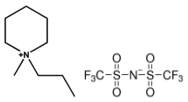	Wide electrochemical window, negligible vapor pressure, superior hydrophobicity, and low flammability	Low salt solubility and poor conductivity
Acetonitrile Electrolyte	Acetonitrile (MeCN)	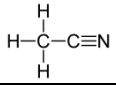	Stable towards O_2^- radical	High volatility

2.2.7.1 Carbonate-based Electrolytes

Organic carbonate-based electrolytes, such as cyclic (propylene carbonate (PC) (DN =

15.1) and ethylene carbonate (EC) (DN = 16.4)) and linear (dimethyl carbonate (DEC) (DN = 17.2)) carbonates, have been demonstrated to be dramatically unstable and not suitable as electrolyte in the oxygen-rich environment in the LOBs. It could be attributed to the presence of highly reactive superoxide radicals, with the major discharge products of Li_2CO_3 and RO-(C=O)-OLi rather than Li_2O_2, even though they have been widely applied in Li-ion battery systems due to their low volatility, wide electrochemical stability window, and wide liquid-temperature range.[112-120] Similarly, many different groups reported that Na_2CO_3 discharge product were obtained when using PC or EC/DMC as electrolytes due to the decomposition of the electrolytes.[73, 121-124]

2.2.7.2 Ether-based Electrolytes

Because of the low stability and severe decomposition of carbonate-based electrolytes during the operation of SOBs, ether-based solvents have come into consideration as organic electrolytes for SOBs.[85, 86, 99, 125-132] Ether-based solvents, such as linear (1,2-dimethoxyethane (DME) (DN = 20.0) and tetraethylene glycol dimethyl ether (TEGDME) (DN = 16.6)) and cyclic ethers (1, 3-dioxolane (DOL) (DN = 18.0) and 2-methyltetrahydrofuran (2-Me-THF) (DN = 18)), have relatively higher stability than carbonates with respect to superoxide.[120, 133]

The ether-based electrolytes exhibited good stability and excellent rate capability. Bryantsev et al. carried out density functional theory calculations to demonstrate that ether-based electrolytes are more suitable than carbonate-based ones through calculating the stability of a range of organic solvents against attack by the O_2^- radical.[134] The stability of TEGDME solvent was further investigated by Kang et al.,

and they confirmed that Na_2O_2 is the discharge product during the reaction with the TEGDME electrolyte.[135]

2.2.7.3 DMSO Electrolyte

Dimethyl sulfoxide (DMSO)-based electrolyte has also been paid considerable attention on account of its high conductivity and low viscosity.[106] DMSO (DN = 29.8) not only could form strongly-conducting solutions because of its excellent salt solubility as a polar versatile solvent, but also possesses high electrochemical reversibility for the O_2/O_2^- couple. [136] Wu et al. demonstrated the successful use of DMSO with concertrated sodium salt for the SOBs, which could cycle for 150 cycles.[106]

2.2.7.4 Ionic Liquids

Ionic liquids not only have a wide electrochemical window, but also have a negligible vapor pressure as well as superior hydrophobicity and low flammability. [124, 137-145] Ionic liquids have very low salt solubility and poor conductivity, however, which may hinder the formation of a SEI on lithium metal and limit the rate capacity. Ionic liquids have much higher viscosity and relatively lower O_2 diffusivity coefficients compared with DME and DMSO.

Many efforts have been devoted to researching the use of ionic liquid-based electrolytes in LOBs, such as (*N*-methyl-*N*-propylpyrrolidinium TFSI (P_{13}TFSI), *N*-methyl-*N*-propylpyrrolidinium bis(fluorosulfonyl)imide FSI (P_{13}FSI), *N*-methyl-*N*-propylpiperidinium TFSI (PP_{13}TFSI), *N*,*N*-diethyl-*N*-methyl-*N*-propyl-ammonium FSI

(N_{1223}FSI), 1-butyl-2,3-dimethyl-imidazolium TFSI (BdImTFSI), and *N*-methyl-*N*-butyl-pyrrolidinium TFSI (P_{14}TFSI)) by using DEMS.[146-151] They demonstrated that their LOBs with the ionic liquid electrolytes had a very stable electrolyte-electrode interface and extremely reversible charge/discharge cycling performance. However, when used in SOBs, the PP_{13}TFSI ionic liquid electrolyte suffers from severe decomposition with Na_2CO_3 and NaOH as discharge products.[124] Moreover, the low salt solubility and poor conductivity of ionic liquids are still obstructing their practical application.

2.2.7.5 Acetonitrile Electrolyte

Acetonitrile based electrolyte (CH_3CN (MeCN) (DN =14.1)) also has been studied as electrolyte due to its excellent stability towards the O_2^- radical intermediate.[107, 117, 136, 152, 153] By using surface enhanced Raman spectroscopy (SERS), Hardwick et al. reported that the Na_2O_2 was formed in CH_3CN-based electrolyte.[107] They also proved that a dense passivation Na_2O_2 film were generated with the increased Lewis acidity of sodium ion in the electrolyte. Even through the CH_3CN electrolyte is stable towards the superoxide intermediate and Na_2O_2, its high volatility and high reactivity towards sodium metal prevent its further use as a suitable electrolyte for SOBs.

2.2.7.6 Sodium Salts

Like solvents, sodium salts also could significantly affect the performance of the SOBs through influence the solvent viscosity, wettability, and oxygen solubility.[106, 109] An ideal salt should meet the following minimal requirements: (1) It should have higher solubility in aprotic solvent, and the solvated ions should have high mobility. (2) The

anions should have very high stability in the presence of superoxide radicals (O_2^-). (3) Both the cation and anion should be inert toward the other parts of the battery, such as the separators, current collectors, and shells. (4) It should promote the formation of stable SEI on the lithium metal anode.

Chapter 3 Experimental

3.1 General Procedure

The experimental procedures and techniques used in this thesis are presented in **Figure 3.1**. Electrode materials were fabricated by various methods and characterized through different physical techniques to investigate their physical and electrochemical properties. Ex-situ techniques were also employed to study their morphology and structural changes after electrochemical reactions.

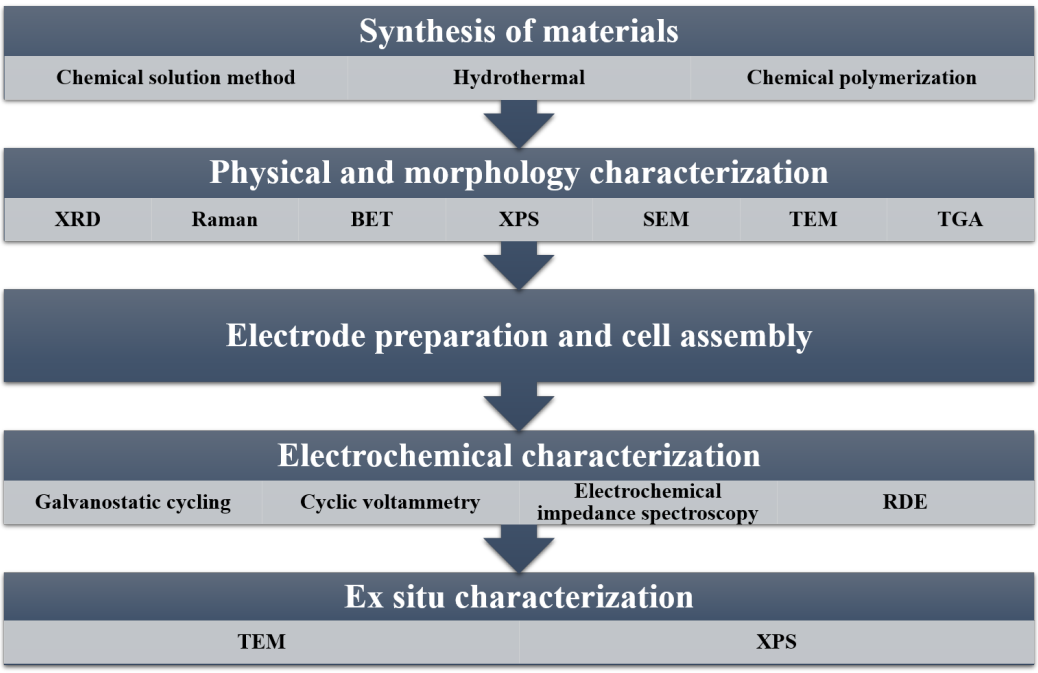

Figure 3.1 Illustration of experimental procedures and techniques utilized in this doctoral thesis.

3.2 List of Chemicals and Materials

The chemicals and materials utilized in this thesis are summarized and listed in Table 3.1.

Table 3.1 Summarized details of the chemicals and materials utilized in this thesis.

Chemicals/Materials	Formula	Purity	Supplier
Methyl orange	$C_{14}H_{14}N_3NaO_3S$	85 %	Sigma Aldrich
Iron chloride	$FeCl_3$	99.9 %	Sigma Aldrich
Pyrrole	C_4H_5N	98 %	Sigma Aldrich
Germanium dioxide	GeO_2	99.99%	Sigma Aldrich
Polyvinylpyrrolidone Mw = 10,000	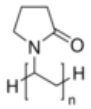	n/a	Sigma Aldrich
Hydrochloric acid	HCl	37 %	Chem-Supply
Sodium hydroxide	NaOH	98 %	Sigma Aldrich
Carbon black	C	Super P	Timcal Belgium
Sodium carboxymethyl cellulose	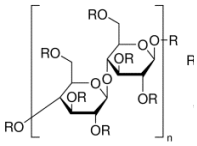	n/a	Sigma Aldrich
Lithium foil	Li	99.9 %	Sigma Aldrich
Hydrogen/Argon	H_2/Ar	n/a	BOC Gas
Copper foil	Cu	n.a	Vanlead Tech
Lithium hexafluorophosphate	$LiPF_6$	99.99 %	Sigma-Aldrich
Ethylene carbonate	$C_3H_4O_3$	99 %	Sigma Aldrich
Diethyl carbonate	$(C_2H_5O)_2CO$	99 %	Sigma

Dimethyl carbonate	$(CH_3O)_2CO$	99 %	Aldrich Sigma Aldrich
Cetyltrimethylammonium bromide	$C_{19}H_{42}BrN$	99 %	Sigma Aldrich
Silicon nanoparticles	Si	99 %	Sigma Aldrich
Ethanol	C_2H_5OH	100 %	Sigma Aldrich
3-Aminophenol	$H_2NC_6H_4OH$	98 %	Sigma Aldrich
Formaldehyde solution	HCHO	37 %	Sigma Aldrich
Ammonia solution	$NH_3 \cdot H_2O$	30 %	Sigma Aldrich
Acetone	CH_3COCH_3	99.9 %	Sigma Aldrich
Toray Carbon paper 060	C	n/a	Fuel Cell Store
Pt on Vulcan XC-72	Pt/C	20 wt. %	Fuel Cell Store
Nafion 117 solution	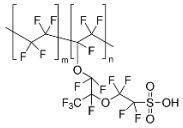	5 % in a mixture of lower aliphatic alcohols and H_2O	Sigma Aldrich
Tetraethylene glycol dimethyl ether	$CH_3O(CH_2CH_2O)_4CH_3$	99 %	Sigma Aldrich
Sodium trifluoromethanesulfonate	CF_3SO_3Na	98 %	Sigma Aldrich
Isopropyl alcohol	$(CH_3)_2CHOH$	99.7 %	Sigma Aldrich

Polytetrafluoroethylene preparation		60 wt.% dispersion in H2O	Sigma Aldrich
Iron (III) nitrate nonahydrate	$Fe(NO_3)_3 \cdot 9H_2O$	99.95 %	Sigma Aldrich
Nickel (II) chloride	$NiCl_2$	99.99 %	Sigma Aldrich
Urea	$CO(NH_2)_2$	99.5 %	Sigma Aldrich
Sodium citrate dehydrate	$Na_3C_6H_5O_7$	99 %	Sigma Aldrich
Sodium hypophosphite monohydrate	NaH_2PO_2	99 %	Sigma Aldrich
Nickel (II) nitrate hexahydrate	$Ni(NO_3)_2 \cdot 6H_2O$	98.5 %	Sigma Aldrich
Cobalt (II) nitrate hexahydrate	$Co(NO_3)_2 \cdot 6H_2O$	98 %	Sigma Aldrich
Ethylene glycol	$HOCH_2CH_2OH$	99.8 %	Sigma Aldrich
Sodium nitrate	$NaNO_3$	99.0 %	Sigma Aldrich
Ammonium fluoride	NH_4F	99.99 %	Sigma Aldrich
Manganese (II) nitrate tetrahydrate	$Mn(NO_3)_2 \cdot 4H_2O$	97 %	Sigma Aldrich
Hydrogen peroxide solution	H_2O_2	30 wt % in H2O	Sigma Aldrich

3.3 Materials Preparation

3.3.1 Chemical Polymerization

Chemical polymerization could combine one or several kinds of monomer units into polymer with long chains or even three-dimensional (3D) networks.[154] Due to functional and steric effects groups of the reacting compounds, chemical polymerization could occur by different mechanisms. For alkenes with σ-bonds, polymers could form through direct radical reactions with straightforward chemical polymerization. For monomers with carbonyl groups, relatively complex reactions are required, depending on the way to substitute carbonyl groups during molecule polymerization.

When monomers have heteroatoms, such as nitrogen or oxygen, they would require step-growth polymerization through stepwise reactions between functional groups of monomers. In contrast, chain-growth polymerization occurs for unsaturated monomers with extra internal double or triple carbon-carbon bonds. Polymers could be divided into homopolymers and copolymers based on the types of monomers used during polymerization. As shown in Equation (3.1), homopolymers are polymers that consist of units of the same monomer formed into repeated long chains or 3D structures, such as polyvinyl chloride (PVC). Whereas, copolymers are polymers that consist of two or more molecules (Equation 3.2), such as acrylonitrile butadiene styrene (ABS).

$$\text{Homopolymers: } A + A + A \cdots \rightarrow AAA\cdots \tag{3.1}$$

$$\text{Copolymers: } A + B + A \cdots\rightarrow ABA \cdots \tag{3.2}$$

In Chapters 4 and 6, homopolymer polypyrrole (PPy) nanotubes were fabricated through the chemical polymerization method. Methyl orange was added in deionized water, and then was dissolved form a solution. Then, pyrrole monomer was added dropwise and dissolved into the mixture. The solution was stirred for 24 h at room

temperature. The thus-formed PPy nanotubes were washed with ethanol and deionized water several times. In Chapter 5, the copolymer 3-aminophenol/formaldehyde resin (3-AFR) was also synthesized via the chemical polymerization method. Cetyltrimethylammonium bromide (CTAB) and Si nanoparticles was added into a solution with a volume ratio of $V_{(ethanol)}/V_{(DI\ water)}$ = 1:2. 3-aminophenol was then dissolved into the solution, followed by adding formaldehyde solution. Then ammonia aqueous solution was added into the mixture as catalyst. After reacting for 30 min, acetone was added into the solution to remove the interior part of the 3-AFR. Finally, the Si@3-AFR was obtained after washing three times with ethanol and water.

3.3.2 Chemical Solution Method

The chemical solution method is one of the most widely used chemical reactions because components of the solution could homogeneously mix to form a single phase. The solvation process is affected by the chemical polarity of the substances. There are two components of a solution: the solvent and the solute. A solvent is a substance that can dissolve other substances to form a solution. The substance dissolved into the solvent is called the solute. In addition, a solution could have many different kinds of solutes. After dissolving into the solvent, the solute could form molecules, chemical species, or ions in the solvent. Hence, the reactants in the solution could undergo uniform and stable chemical reactions with rapid reaction rates because the reactants in the solution could make intimate contact with each other. The chemical solution method is a very useful strategy to synthesize various products with controllable structure, morphology, and composition.

In Chapters 4 and 7, the chemical solution method was utilized to synthesize the Ge@N-CNTs, Ni_3Co-layered double hydroxides (LDH) nanosheets, and Ni_3Mn-LDH

nanosheets. To fabricate Ge@N-CNTs, PPy nanotubes were first added into deionized water, followed by ultrasonication for 1.5 h to form a suspension. Meanwhile, GeO_2 was dissolved in NaOH solution. After stirring for 1.5 h, the two solutions were mixed together, and then vigorously stirred for 20 min. The pH of the solution was slowly adjusted to 7 with dilute HCl. Then, poly(vinylpyrrolidone) (PVP) (molecular weight, MW=10,000) was added into the solution. After drying out, the sample was annealed at 650 °C in a tube furnace with a heating rate of 5 °C min^{-1} in argon atmosphere. When the temperature reached 650 °C, the argon gas was replaced by H_2 gas, and the reaction proceeded for 4 h. Finally, the sample was left to cool down to room temperature and then washed with ethanol and deionized water (DI water) several times. To prepare Ni_3Co-LDH nanosheets, $Ni(NO_3)_2 \cdot 6H_2O$, $CO(NH_2)_2$, and $Co(NO_3)_2 \cdot 6H_2O$ were dispersed into DI water to form a mixture with a volume ratio of $V_{(ethylene\ glycol)}/V_{(DI\ water)}$ = 3:1. After refluxing for 3 h at 90 ˚C, the product was collected after washing three times with ethanol and DI water. For the Ni_3Mn-LDH nanosheets, $Ni(NO_3)_2 \cdot 6H_2O$, $NaNO_3$, NH_4F, and $Mn(NO_3)_2 \cdot 4H_2O$ were added into the DI water with vigorous stirring under N_2 atmosphere. After 30 min, H_2O_2 was added dropwise into the solution. The NaOH solution was then dispersed dropwise into the above solution. After stirring for 12 h at room temperature, the product was collected after washing three times with ethanol and DI water.

3.3.3 Hydrothermal Method

The hydrothermal method is an efficient and low-cost technique to fabricate nanomaterials within sealed aqueous-based solutions at high temperature (100 - 1000 ºC) and high vapor pressure (1 MPa - 1 GPa). The autoclave used in this thesis is shown in Figure 3.2, which has a polytetrafluoroethylene (PTFE) vessels and a stainless steel

protector. The autoclaves are normally used in a conventional oven with a programmed temperature and duration of time. In order to ensure safety, the maximum volume of the precursor is 2/3 of the volume of the PTFE vessel with operating temperature below 250 ºC and pressure less than 1900 psi. Due to the high temperature and high pressure, many unique structures or composites, such as nanosheets and nanotubes, could be obtained through the hydrothermal method, which are difficult to synthesize with conventional chemical methods.

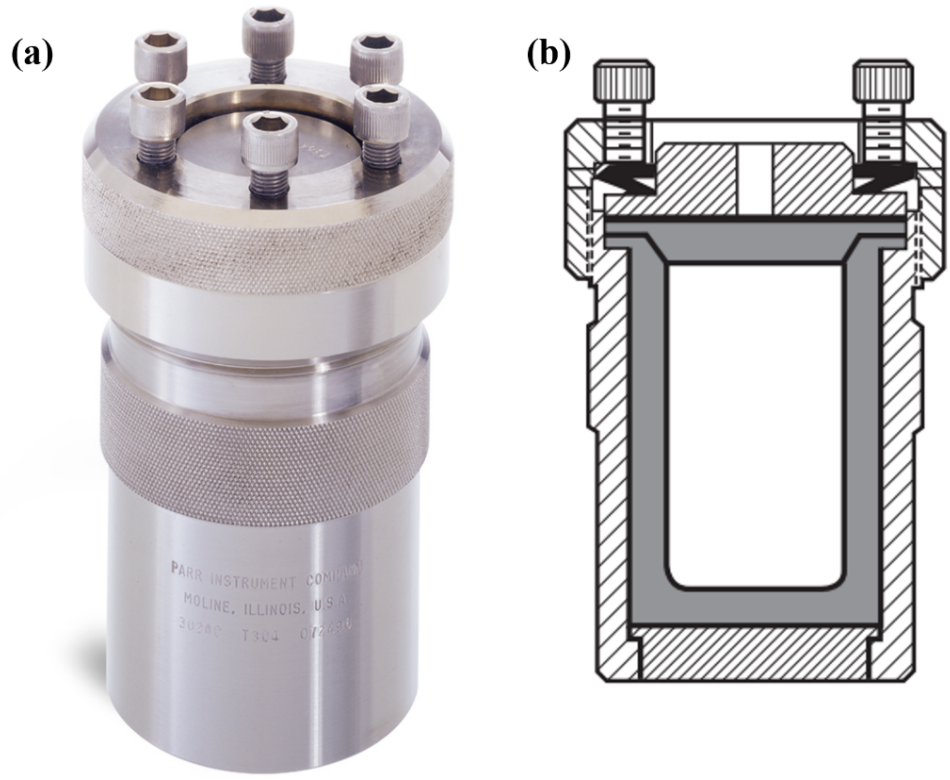

Figure 3.2. (a) Photograph and (b) cross-sectional view of hydrothermal autoclave (Acid Digestion Bombs 4748) from Parr Instruments.

In Chapter 7, the hydrothermal method was used to synthesize the Ni_3Fe-LDH nanosheets. Typically, $Fe(NO_3)_3 \cdot 9H_2O$ and $NiCl_2$ were dispersed into deionized (DI) water under vigorous stirring for 10 min, followed by adding urea and $Na_3C_6H_5O_7$. After another 10 min, the reaction proceeded for 24 h in a Teflon-lined autoclave at

150 ˚C. The Ni_3Fe-LDH was obtained after washing three times with ethanol and DI water.

3.4 Structure and physical characterization

3.4.1 X-Ray Diffraction

X-ray diffraction (XRD) is a straightforward and powerful technique used to identify the crystallographic structures and phases of materials. XRD also could be used to determine the crystallite/grain size and the preferred orientation of materials. The principle of XRD is demonstrated in Figure 3.3.

Because every crystalline substance features a unique set of *d*-spacings, the X-ray wavelengths will be scattered with unique angles. The patterns of the scattered X-rays have a functional relationship with the crystal structure of the material, which could be determined by Bragg's law:

$$n \lambda = 2d \sin \theta \tag{3.3}$$

where n represents any integer, λ stands for the X-ray wavelength of the incident beam, d is the spacing between the lattice planes, and θ is the incidence angle.

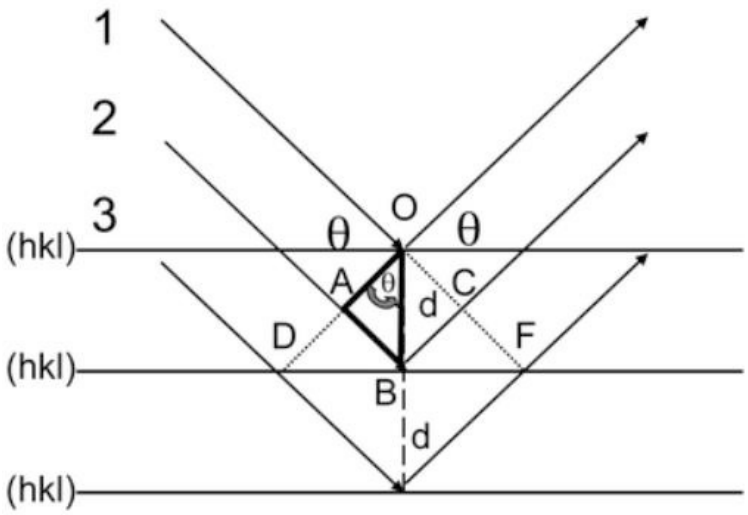

Figure 3.3 Principle of X-ray diffraction.

In this thesis work, XRD were carried out with a GBC MMA powder X-ray diffractometer (GBC Scientific Equipment LLC, USA) with Cu Kα radiation (λ = 1.5406 Å), which was operated at the voltage of 40 kV and current of 25 mA. The powdered sample was finely ground before pasting it onto a disk holder, which could be positioned on the axis of the diffractometer.

3.4.2 Raman Spectroscopy

Raman spectroscopy is a useful characterization technique to study the rotational, vibrational, and other low frequency modes in the structure of a sample, which could provide a structural fingerprint to identify molecules. In Raman spectroscopy, inelastic scattering of monochromatic light could interact with molecular vibrations, phonons or other excitations, leading to an energy shift of the laser photons. These energy shifts provide information on the vibrational modes of specific chemical bonds and symmetry region of molecules. Therefore, the molecules could be easily identified through the fingerprint provided by Raman spectroscopy. In this thesis work, the Raman spectroscopy was carried out by using a JOBIN YVON HR 800 Horiba Raman

spectrometer with the laser wavelength at 632.8 nm.

3.4.3 X-Ray Photoelectron Spectroscopy

X-ray photoelectron spectroscopy (XPS) is a surface-sensitive quantitative spectroscopic method to investigate the elemental composition, chemical states, empirical formula, and electronic state of a material. It can not only identify elements within a sample, but also can provide information about the valence states. XPS spectra are collected through measuring the kinetic energy and number of electrons escaping from the surface of a material (down to 10 nm) when it is irradiated with X-rays. XPS spectra could be utilized to investigate inorganic compounds, metal alloys, polymers, catalysts, and many other materials. In this thesis study, XPS analysis was conducted on a PHOIBOS 100 Analyzer system (SPECS) using Al Kα X-ray radiation with photon energy of 1486.6 eV under 12 kV and 120 W, which is kept under a high vacuum conditions ($P < 10^{-8}$ mbar). XPS data was analyzed with the commercial CasaXPS 2.3.15 software package. In addition, the spectra were calibrated by C 1s = 284.6 eV.

3.4.4 Thermogravimetric Analysis

Thermogravimetric analysis (TGA) is a powerful technique to measure the weight changes with increasing temperature under different atmospheres. It could be used to study the physical and chemical characterizations of material through the weight changes associated with decomposition, oxidation, or loss of volatiles (such as moisture) with increasing temperature. In this thesis work, a TGA instrument (Mettler-Toledo, Switzerland) was utilized to evaluate the carbon contents in the composite

materials. The temperature was heated to 800 ºC at a rate of 10 ºC min^{-1} in air.

3.4.5 Brunauer-Emmett-Teller (BET) Analysis

The Brunauer-Emmett-Teller (BET) method is an essential analysis technique to reveal the physical adsorption of gas molecules on a solid surface, which could be used to determine the specific surface area and pore size distribution of a material. It is carried out at liquid nitrogen temperature (77 K) under various pressures. The pore size distribution can then be calculated through the Barrett-Joyner-Halenda (BJH) method. In this thesis study, the specific surface areas were investigated using a Quantachrome Instruments Autosorb iQ2 through N_2 adsorption at -196 °C, based on the Brunauer-Emmett-Teller (BET) method. The vacuum pressure was kept under 10^{-4} Pa to degas the samples at 100 °C. The mean value was calculated after obtaining three measurements for each sample.

3.4.6 Atomic Force Microscopy

Atomic force microscopy (AFM) is a very useful type of scanning probe microscopy, which has a very high resolution of approximately one nanometer. The data is collected through touching the surface of the material with a sharp tip. AFM has three major functions: imaging, force measurement, and manipulation. In this thesis work, an atomic force microscope (MPF-3D, Asylum Research, Santa Barbara, USA) was used to harvest topographic information and estimate the thickness of atomically holey nanosheet materials.

3.4.7 Scanning Electron Microscopy

The scanning electron microscope (SEM) is a type of microscope that can scan and produce images of a specimen through a high-energy electron beam. It is a widely utilized technique to characterize the morphology and structure of materials. The high-energy beam of electrons interact with atoms of sample, providing various signals from the sample. After collecting by the detector, topographical and composition information on the sample's surface could be obtained. In this thesis work, the morphologies of materials were characterized with a field-emission scanning electron microscopy (FE-SEM, JEOL JSM-7500FA).

3.4.8 Transmission Electron Microscopy and Scanning Transmission Electron Microscopy

Transmission electron microscopy (TEM) is a microscopy technique using an electron beam that is transmitted through and interacts with a very thin specimen. TEM microscopes are able to image at a significantly higher resolution than SEM microscopes. TEM is normally used to investigate the morphology, crystal structure, lattice spacing, and electronic structure of a material. Selected area electron diffraction (SAED) is a crystallographic experimental technique that could be used as part of the TEM equipment. It is capable of identifying crystal structures and enabling the study of crystal defects in a quite small area several hundred nanometers in size. Scanning transmission electron microscopy (STEM) is a type of TEM, in which the electron beam is focused to a fine spot to scan over the specimen in a raster illumination system. Therefore, various analytical techniques can be used that are associated with STEM, such as electron energy loss spectroscopy (EELS) and spectroscopic mapping by energy dispersive X-ray spectroscopy (EDX). In this doctoral work, the TEM

observations were carried out using a JEOL 2011 TEM (200 keV) and a JEOL ARM-200F TEM (200 keV).

3.5 Electrode Preparation and Coin Cell Assembly

3.5.1 Electrodes for Lithium Ion Cells

2032-type coin-cells were used to test the electrochemical performance, as shown in Figure 3.4. The electrodes were prepared by mixing the active material (80 wt. %), Super P carbon black (10 wt. %), and sodium carboxymethyl cellulose (10 wt. %) in deionized water. The slurry was then cast on Cu foil and dried at 80 °C for 12 h in a vacuum oven. The working electrodes were prepared by punching the Cu film into discs 0.97 cm in diameter, and the loading mass of the active material for all the electrodes was at least 1.1 mg cm^{-2}. The coin-cells were assembled in an argon-filled glove box (Mbraun, Germany) with the prepared active material on Cu foil as working electrode, lithium foil as counter electrode, microporous polyethylene (Celgard 2400) as the separator, and 1 M $LiPF_6$ in a mixture of ethylene carbonate (EC), diethylcarbonate (DEC), and dimethyl carbonate (DMC) (3:4:4 by volume) as electrolyte. The assembly process was carried out in an argon-filled glove box with the oxygen and humidity levels under 0.1 ppm (Mbraun, Germany).

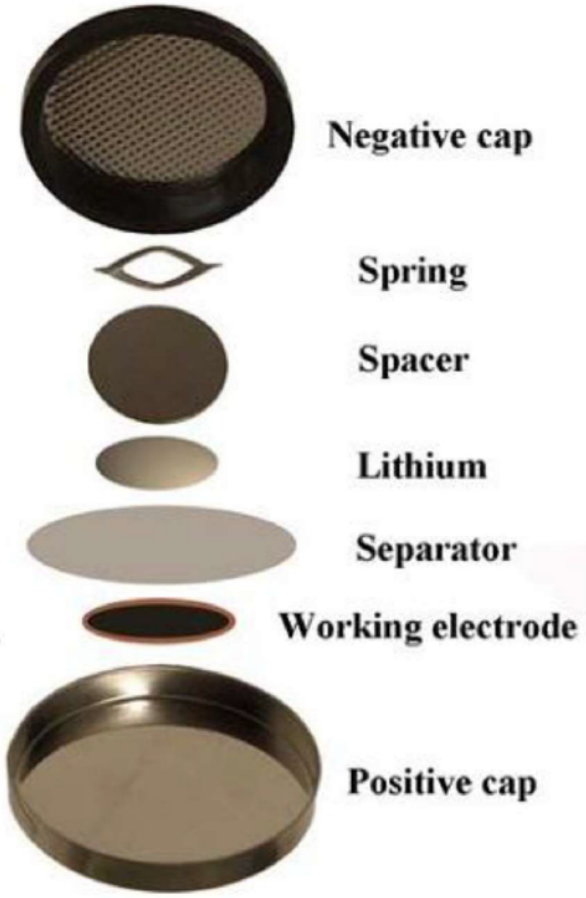

Figure 3.4 Illustration of the coin-cell.[155]

3.5.2 Electrodes for Sodium-Oxygen Cells

The electrochemical properties were measured using CR2032-type coin cells with holes in the cathode part. To prepare the oxygen cathodes, the active materials and poly(tetrafluoroethylene) (PTFE) solution were mixed in the ratio of 90:10 in isopropyl alcohol as catalyst slurry. The slurry was then pasted onto carbon paper and dried in a vacuum oven at 120 °C for 12 h. The typical loading of cathode active materials was 0.3 mg cm^{-2}. Tetraethylene glycol dimethyl ether (TEGDME) solvent was purified by rotary evaporation and stored with 4 Å activated molecular sieves for two weeks before use. Sodium trifluoromethanesulfonate ($NaSO_3CF_3$) was dried at 120 °C for 24 h under

vacuum. The electrolyte, consisting of 0.5 m sodium triflate in TEGDME, was prepared in an argon-filled glovebox. The cells were assembled in an argon-filled MBRAUN glove box (H_2O level <0.1 ppm and O_2 level <0.1 ppm). A piece of sodium cut from a sodium cube served as the anode and glass microfiber was used as separator.

3.6 Electrochemical Characterization Methods

3.6.1 Cyclic Voltammetry

Cyclic voltammetry (CV) is a widely utilized electrochemical technique to investigate electrochemical redox reactions. It could be used to measure the stability of reaction products, the presence of redox reaction intermediates, electron transfer kinetics, the analyte diffusion coefficient, and reaction reversibility. In CV, the electrode potential changes linearly over time in cyclical phases, and the change rate is known as the scan rate. There are normally three electrodes: the working electrode, the reference electrode, and the counter electrode. The potential is determined between the working electrode and the reference electrode, while the current is determined between the working electrode and the counter electrode. CV also can be used to investigate the adsorbed species on the electrode surface. In this thesis work, CV measurements were carried with a Biologic VMP-3 electrochemical workstation on Princeton 2273 and 636 instruments (Princeton Applied Research).

3.6.2 Linear Sweep Voltammetry

Linear sweep voltammetry (LSV) is a voltammetric method to measure the working

electrode current when the potential is swept linearly over time between the working electrode and the reference electrode. When the species begins to be oxidized or reduced, a current peak at the potential would be revealed in the curve. LSV can be used to identify unknown species and estimate the concentration of solutions. In this thesis work, the LSV technique was carried out to determine the ORR and OER activities of the materials in the base electrolyte.

3.6.3 Galvanostatic Charge and Discharge Measurements

Galvanostatic discharge/charge tests were carried out to investigate the capacity, rate performance, and cycling stability of the lithium ion batteries and sodium oxygen batteries within a given voltage window or specific capacity. The charge or discharge capacity is equivalent to the total electron charge (Q) in the corresponding discharge or charge process. It could be calculated based on the applied current (I) and the total time (t) consumed during the charge or discharge process ($Q = I \times t$). In this thesis work, all the galvanostatic charge/discharge tests were carried out on battery testers (Land CT 2001 and Neware) at room temperature.

3.6.4 Electrochemical Impedance Spectroscopy

Electrochemical impedance spectroscopy (EIS) is a powerful technique to investigate the frequency response of batteries, including the charge transfer, double layer capacitance, and ohmic resistance. EIS could be used to study the reaction mechanism of an electrochemical process and identify the rate-limiting step with the frequency response. Typically, an EIS impedance spectrum has a semicircle at high frequency and a linear tail at low frequency. The high frequency semicircle is ascribed to the

charge transfer resistance and the double layer capacitance. The low frequency linear tail is attributed to the diffusion of ions from the electrolyte into the electrode materials. In this thesis work, EIS data were collected on a Princeton 2273 workstation (Princeton Applied Research) with a Biologic VPM3 electrochemical workstation.

Chapter 4 Capillary induced Ge Uniformly Distributed in N-doped Carbon Nanotubes with Enhanced Li-Storage Performance

4.1 Introduction

Lithium ion batteries (LIBs), as the most advanced energy storage device, have been widely applied in electrical vehicles, portable electronics, and smart grids.[1, 156] The commercialized graphite anodes, however, cannot satisfy the demand for high energy next-generation batteries because of the low theoretical specific capacity (372 mAh g^{-1}) of graphite.[157] Therefore, anode materials with high capacity have been introduced, such as Si, Ge, and Sn.[158, 159] Among these, germanium has attracted considerable attention as a superior anode material owing to its excellent electrical conductivity, outstanding lithium-ion diffusivity, and large theoretical capacity.[40, 160-162] Similar to other anode materials (like silicon and tin), however, Ge also suffers from drastic capacity decay and poor rate performance owing to the severe volume changes (about 300 %) during repeated charge/discharge processes.[163] One approach to improving the electrochemical performance is to use nanosized materials, especially one-dimensional (1D) nanotube or nanowire structures, due to their short lithium ion diffusion length and excellent electrical conductivity.[46, 164-169] Many strategies have been developed to synthesize 1D structured materials, such as the hydrothermal,[167, 168] chemical-vapor deposition,[48, 170-173] electrospinning, [174] and chemical polymerization[175] methods. Another method is to use the carbon matrix, which could accommodate the volume changes, enhance the electrical conductivity of the electrode and serve as an active material for lithium storage.[176-179] In particular, nanoparticles encapsulated in carbon nanotubes represent the most desirable structure, which could not only benefit from the

advantages of 1D structure, but also provide void spaces to buffer the volume changes of active materials.[180-183] For example, Chu and co-workers prepared peapod-like Ge/CN_x with Ge incorporated in CN_x layers by using the chemical polymerization method to coat a polypyrrole layer on the surfaces of GeO_2 nanowires.[180] Yu and co-workers synthesized carbon-nanofiber-encapsulated Ge nanoparticles through the electrospinning method.[183] The active material nanoparticles were not very uniformly distributed within the carbon nanotubes, however, which may mean that the void spaces cannot be fully utilized to accommodate the volume changes. Therefore, it is extremely attractive to design a novel strategy to synthesize 1D structured materials with uniformly distributed active materials.

Capillary action is a facile strategy to synthesize novel 1D structured materials through filling the hollow cavities of nanotubes with the chosen materials.[184] Numerous efforts have been devoted to drawing different foreign materials in the liquid or molten phase into the hollow inner cavities by using capillary action to synthesize 1D structured materials.[185-190] The surface tension of the foreign materials, however, is the most important parameter for successful filling, which should be less than 200 mN m^{-1}.[191] Hence, only materials with low surface tension could be introduced into the hollow cavities by using capillary action. Therefore, it is still a big challenge to introduce high surface tension materials into the inner hollow cavities to fabricate 1D structured materials, which are expected to provide breathtaking opportunities for practical applications and fundamental research.

In this Chapter, we present a feasible strategy to synthesize core-shell GeO_2/NaCl@polypyrrole nanotubes by utilizing capillary action, which could be further transformed into 1D Ge@N-doped carbon nanotubes (Ge@N-CNTs)

composite with Ge nanoparticles uniformly distributed in the N-CNTs. The successful fabrication of Ge nanoparticles uniformly encapsulated in N-CNTs lies in two key aspects. First, as a high surface tension material, GeO_2 (250 mN m^{-1}) could not be directly introduced into the hollow cavities in the molten phase by using capillary action.[192] Even after it is dissolved in NaOH solution to form a liquid phase, the surface tension of the solution is still larger than the cut-off value, which also cannot be introduced into the hollow cavities by using capillary action. The surface tension could be decreased, however, through adding poly(vinylpyrrolidone) (PVP), and then the solution could be induced into the robust PPy nanotubes to form the core-shell GeO_2/NaCl@polypyrrole (PPy) nanotubes composite by utilizing capillary action. Second, through reducing GeO_2 to Ge and removing NaCl with a further annealing and centrifuging treatment, a composite of Ge nanoparticles uniformly distributed in the N-CNTs could be obtained. The uniformly distributed Ge nanoparticles could effectively utilize the void spaces provided by the unique 1D structure during cycling, which could preserve the original structure of the Ge@N-CNTs and achieve prolonged cycling stability. When investigated its lithium storage performance, the Ge@N-CNTs demonstrated enhanced cycling stability and excellent rate capacity.

4.2 Experimental Section

Synthesis of PPy nanotubes: PPy nanotubes were synthesized using a previously reported method.[193] In a typical synthesis process, methyl orange (0.25 mM) was added in deionized water (100 mL), and then $FeCl_3$ (1.35 g) was dissolved to the solution. Then, pyrrole monomer (5 mM) was dissolved into the mixture dropwisely. The solution was stirred for 24 h at room temperature. The thus-formed PPy nanotubes were washed with ethanol and deionized water several times. Then, PPy nanotubes

with an inner cavity about 100 nm in diameter were obtained.

Synthesis of Ge@N-CNTs: PPy nanotubes (50 mg) were first added into deionized water (50 mL), followed by ultrasonic for 1.5 h to form a suspension. Meanwhile, GeO_2 (144 mg) were dissolved in NaOH solution (100 mL). After stirring for 1.5 h, the two solutions were mixed together, and then vigorously stirred for 20 min. The pH of the solution was slowly adjusted to 7 with dilute HCl. Then, poly(vinylpyrrolidone) (PVP) (MW=10,000) (8 mg) was added into the solution. After drying out, the sample was annealed to 650 °C in a tube furnace at a rate of 5 °C min^{-1} in argon atmosphere. When the temperature reached 650 °C, the argon gas was replaced by H_2 gas, and the reaction proceeds for 4 h. Finally, the sample was left to cool down to room temperature and then washed with ethanol and deionized water several times. To synthesize Ge/N-CNTs, the same method is used, but without adding PVP.

Materials characterization: The crystalline structures of the samples were analyzed by powder X-ray diffraction (XRD, GBC MMA) using Cu Kα radiation. Raman spectra were carried out by using JOBIN YVON HR800 Confocal system. Thermogravimetric analysis (TGA) tests were collected with a TGA instrument (Mettler-Toledo, Switzerland) from room temperature to 800 °C at a rate of 10 °C min^{-1} in air. The morphologies of the materials were investigated by scanning electron microscopy (JSM-7500FA, JEOL) and transmission electron microscopy (JEM-ARM200F, JEOL).

Electrochemical measurement: 2032-type coin-cells were used to test the electrochemical performance. The electrodes were prepared by mixing the active material (80 wt. %), Super P (10 wt. %), and sodium carboxymethyl cellulose (10 wt. %)

in deionized water. The slurry was then cast on Cu foil and dried at 80 °C for 12 h in a vacuum oven. The working electrodes were prepared by punching the Cu film into discs 0.97 cm in diameter, and the loading mass of the active material for all the electrodes was at least 1.1 mg cm^{-2}. The coin-cells were assembled in an argon-filled glove box (Mbraun, Germany) with the prepared active material on Cu foil as working electrode, lithium foil as counter electrode, microporous polyethylene (Celgard 2400) as the separator, and 1 M $LiPF_6$ in a mixture of ethylene carbonate (EC), diethylcarbonate (DEC), and dimethyl carbonate (DMC) (3:4:4 by volume) as electrolyte. The assembly process was carried out in an argon-filled glove box with the oxygen and humidity levels under 0.1 ppm (Mbraun, Germany). The galvanostatically discharge and charge processes were carried out on a Land battery tester between 0.01-1.5 V vs. Li^+/Li. Cyclic voltammetry was conducted with a Biologic VMP-3 electrochemical workstation.

4.3 Results and Discussion

4.3.1 Structure and morphology

The synthesis process to fabricate the Ge@N-CNTs and Ge/N-CNTs composites is illustrated in **Figure 4.1**. First, uniform PPy nanotubes with a hollow inner cavity and open tips, which are favorable for capillary action, are synthesized through the polymerization method in a relatively large quantity. Second, the PPy nanotubes are mixed with a GeO_2 and NaOH aqueous solution, followed by adjusting the pH of the solution to 7 with diluted HCl. Then, PVP is added into the solution, which can decrease the surface tension and thus increase the effect of capillary action to fill the inner hollow cavities with GeO_2/NaCl in an aqueous solution.[194] Therefore, by

utilizing capillary action, a core-shell GeO_2/NaCl@PPy nanotubes composite is formed through inducing GeO_2/NaCl into the inner hollow cavities after drying at 60 °C. Finally, the unique 1D structured Ge@N-CNTs composite with Ge nanoparticles uniformly encapsulated in N-CNTs is obtained through a carbonization and annealing process in H_2 atmosphere, followed by the removal of NaCl by centrifuging.

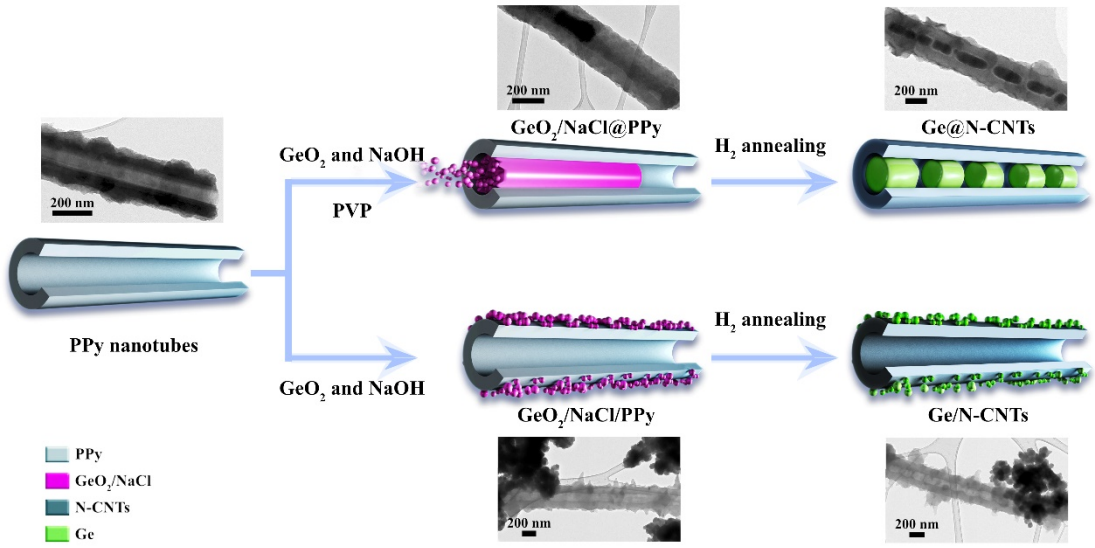

Figure 4.1. Illustration of the synthesis processes for the Ge@N-CNTs and Ge/N-CNTs composites.

As shown in the transmission electron microscope (TEM) images (Figure 4.1) and the scanning electron microscope (SEM) images (**Figure 4.2**), the PPy nanotubes with an inner cavity diameter of about 100 nm and open tips can be directly used for capillary action without any further treatment. The successful synthesis of core-shell GeO_2/NaCl@PPy nanotubes could be further confirmed by the elemental mapping images (**Figure 4.3**), which reveal that GeO_2 and NaCl are completely filled into the hollow inner cavity and uniformly distributed along the axial direction of a nanotube. The GeO_2/NaCl could not be induced into the hollow cavities of PPy nanotubes,

however, without adding PVP. This was because the surface tension of GeO_2/NaCl solution is too high to draw GeO_2/NaCl into the inner hollow cavities. All of the GeO_2/NaCl nanoparticles are dispersed on the outside of the PPy nanotubes instead of filling the hollow cavities. Therefore, Ge/N-CNTs with Ge nanoparticles aggregated on the outside of the N-CNTs could be obtained after further annealing and centrifugal treatment (Figure 4.1 and **Figure 4.4**). This implies that the PVP could increase the effect of capillary action through decreasing the surface tension. Moreover, the distribution of the nanoparticles in the composite could be easily tuned by adjusting the surface tension. During the heating process, the N-CNTs content was totally burned out, and the Ge was oxidized into GeO_2 with increasing temperature. Therefore, based on the weight of GeO_2, the content of Ge can be calculated. By using this method, the Ge contents are determined to be 70.5 wt. % and 72.5 wt. % in the Ge/N-CNTs and Ge@N-CNTs, respectively, according to the thermogravimetric analysis data (**Figure 4.5**).

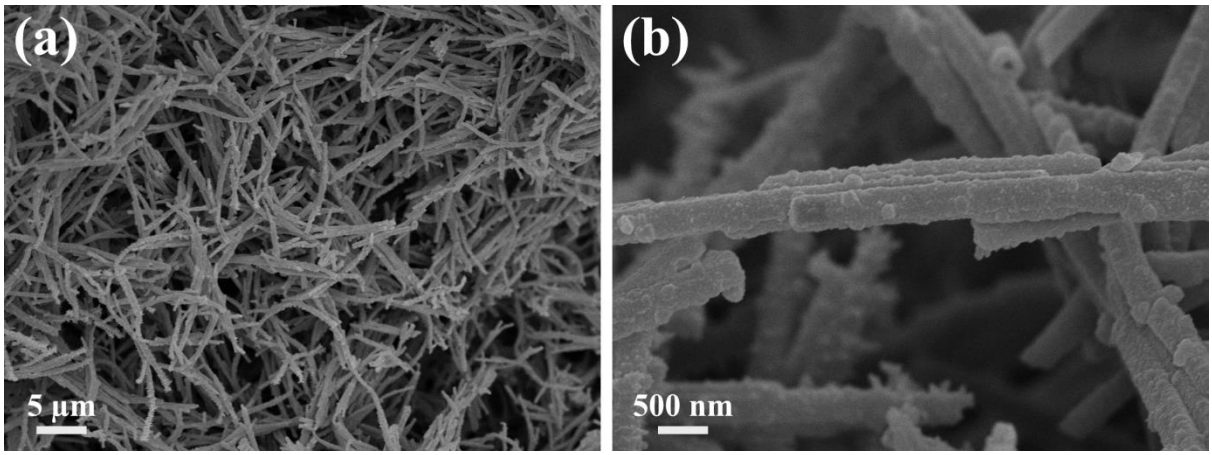

Figure 4.2**.** SEM images of PPy nanotubes.

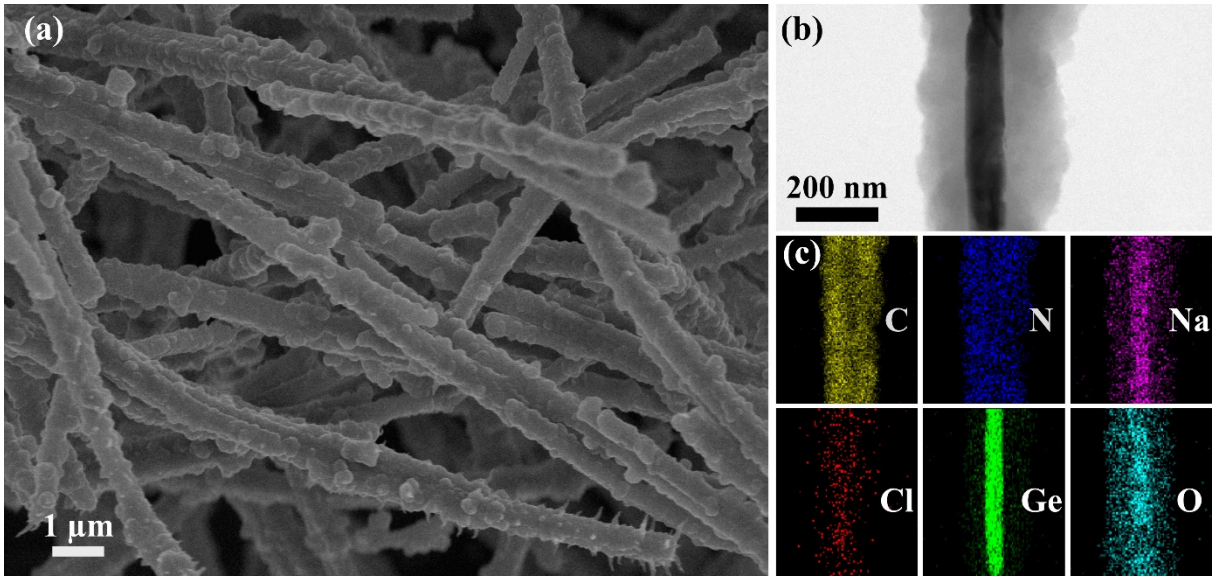

Figure 4.3. SEM image (a), TEM image (b), and corresponding elemental mapping images (c) of core-shell GeO_2/NaCl@PPy nanotubes.

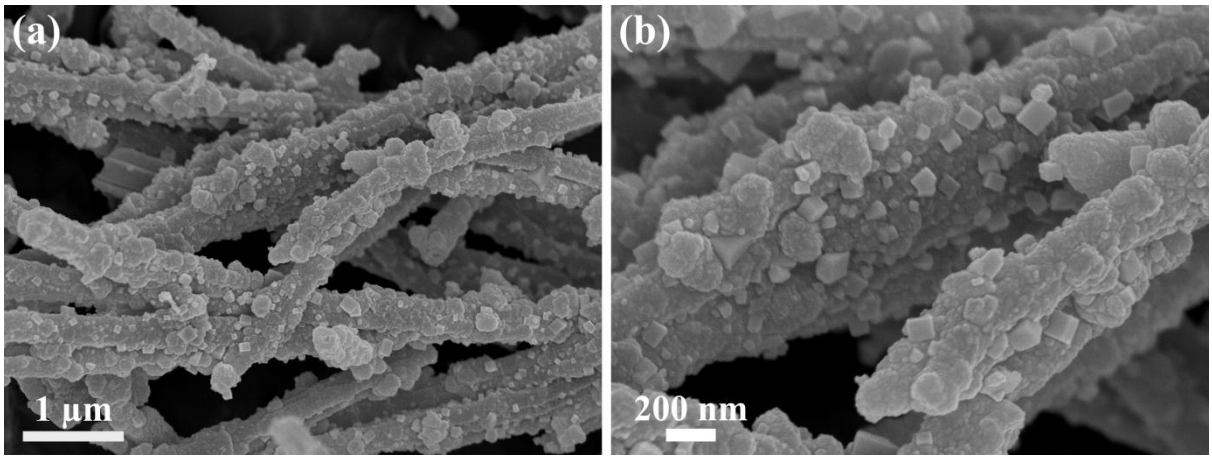

Figure 4.4. SEM images of Ge/N-CNTs.

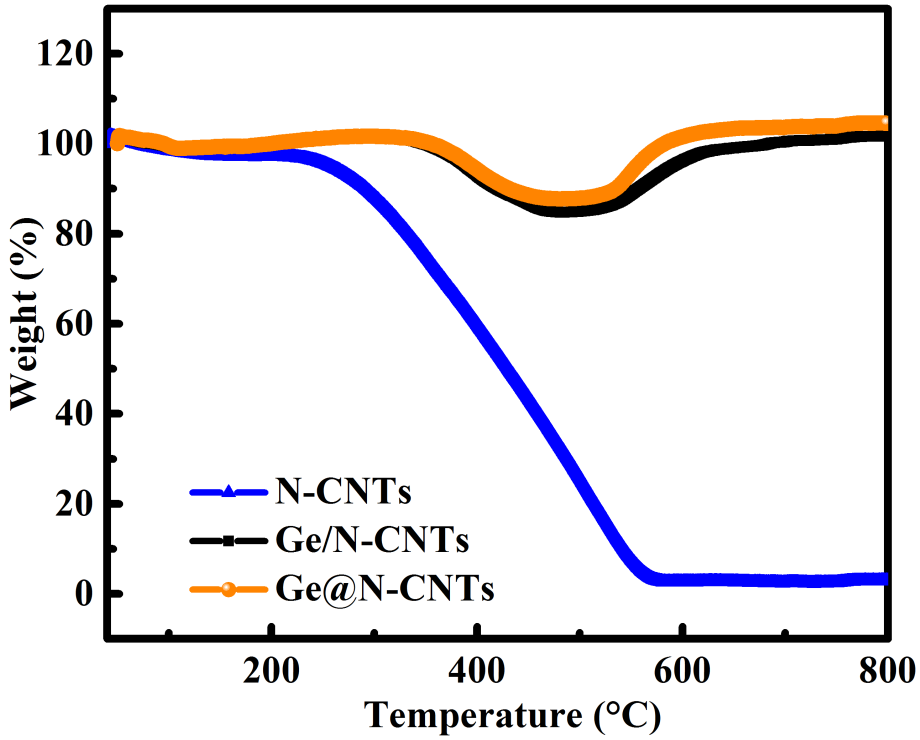

Figure 4.5. TGA curves of N-CNTs, Ge/N-CNTs, and Ge@N-CNTs in air with a heating rate of 10 °C min^{-1}.

The X-ray diffraction (XRD) patterns are manifested in **Figure 4.6**a. The XRD peaks of the Ge@N-CNTs and Ge/N-CNTs could be assigned to the cubic Ge (JCPDS No. 04-0545) without any impurity, demonstrating that the GeO_2 has been successfully reduced to Ge and that the NaCl has been fully removed. In addition, no obvious carbon diffraction peak can be detected because of the amorphous nature of the N-CNTs. The Raman spectra are shown in Figure 4.6b. For pure Ge, the peak centered at 300 cm^{-1} could be assigned to metallic Ge. As for the pure N-CNTs, peaks located at 1350 and 1580 cm^{-1} can be indexed to the D and G bands, respectively. Therefore, three peaks appeared at 300, 1350, and 1580 cm^{-1} for the Ge@N-CNTs and Ge/N-CNTs, which can be attributed to metallic Ge, the D and G bands of N-CNTs, respectively. It is worth to mention that $FeCl_3$ could be easily washed away after centrifugal treatment with ethanol and deionized water during the synthesis process of PPy nanotubes. In addition,

there is no peak of residual Fe in the XRD patterns and Raman spectra, indicating that there is no Fe in the final product.

As can be observed from the SEM image (Figure 4.6c), a large quantity of Ge@N-CNTs composite generally inherits the uniform tubular structure and diameter of the core-shell GeO_2/NaCl@PPy nanotubes. The TEM image (Figure 4.6d) further shows the details of the unique Ge@N-CNTs composite. The dark inner Ge cores are homogeneously encapsulated by the N-CNTs shells, and there are some void spaces not only between the individual Ge nanoparticles, but also between the Ge core and the N-CNTs shells. These uniformly distributed Ge nanoparticles could effectively use these void spaces to accommodate the large volume expansion during the cycling processes, thus preventing the agglomeration of the electrode materials. It is notable that these void spaces are generated not only from the reduction treatment of GeO_2 in H_2 gas, but also from the removal of NaCl after centrifuge treatment. The elemental mapping results for C, N, and Ge further demonstrate that the Ge nanoparticles are uniformly distributed along the axial direction of the tube (Figure 4.6e-g). Moreover, the N doping in the CNTs could improve the electrical conductivity, which additionally contributes to the enhanced electrochemical performance. In addition, as shown in Figure 4.6h, the element mapping for oxygen is negligible, indicating that the GeO_2 has been completely reduced to Ge during the annealing treatment. This maybe because the PPy nanotubes have open ends, which could allow the hydrogen gas flow into the cavities and reduce the GeO_2. All of these data demonstrate the successful fabrication of this unique Ge@N-CNTs structure with Ge nanoparticles uniformly encapsulated in the N-CNTs.

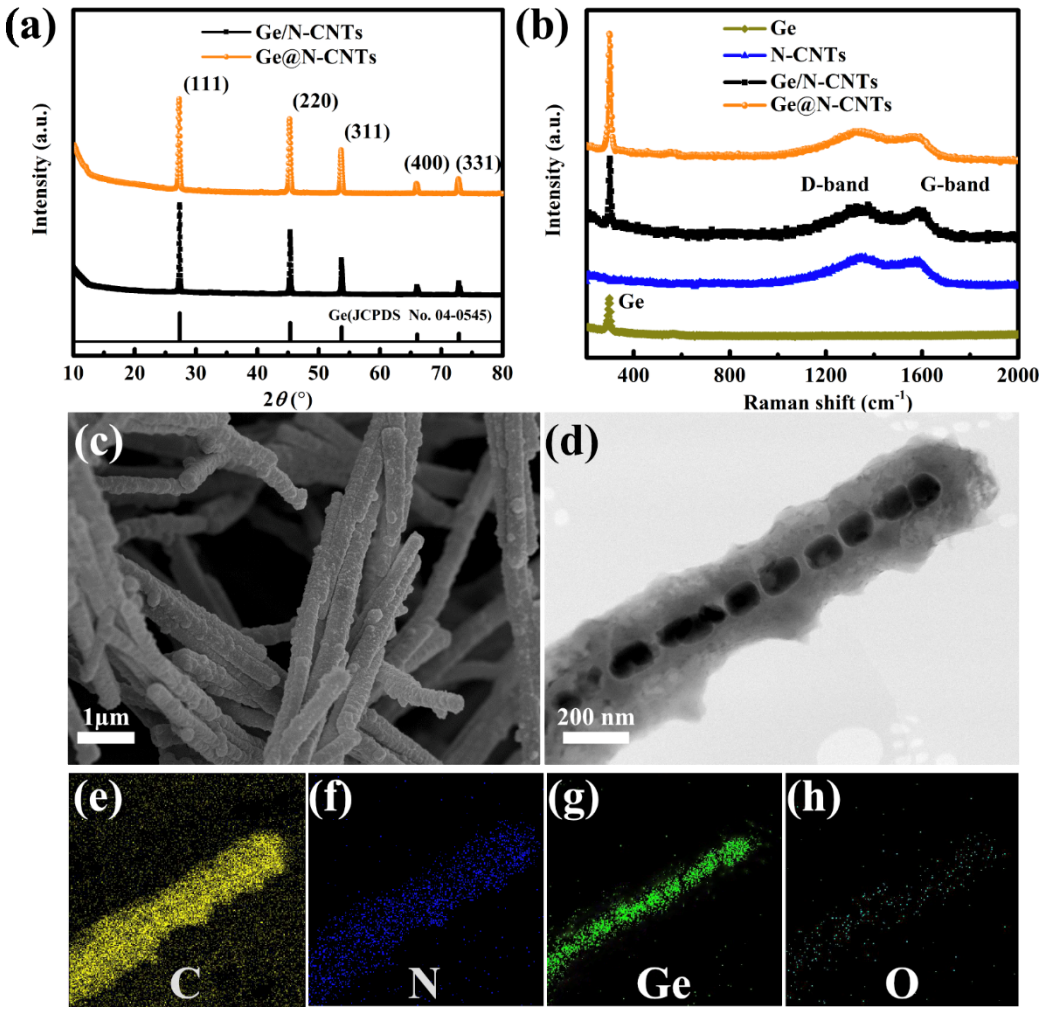

Figure 4.6. (a) XRD patterns of Ge/N-CNTs and Ge@N-CNTs. (b) Raman spectra of Ge, N-CNTs, Ge/N-CNTs, and Ge@N-CNTs. (c) SEM and (d) bright-field TEM images of Ge@N-CNTs. Elemental mapping images of C (e), N (f), Ge (g), and O (h) of an individual Ge@N-CNTs nanotubes.

4.3.2 Electrochemical characterizaiton

To demonstrate the structural advantages of the Ge@N-CNTs, the electrochemical performances of both the Ge@N-CNTs and the Ge/N-CNTs composites were investigated. The specific capacity was calculated using both N-CNTs and Ge composite. **Figure 4.7**a presents the first cycle discharge/charge curves of the Ge@N-CNTs and Ge/N-CNTs composites at a current density of 100 mA g^{-1} in the potential

range of 0.01-1.5 V versus Li/Li^+. The Ge/N-CNTs exhibits initial discharge and charge capacities of 1737 and 900 mAh g^{-1}, respectively, with a coulombic efficiency of 52 %. On the other hand, the Ge@N-CNTs composite shows a higher initial coulombic efficiency of 68 %, and its initial discharge and charge capacities are 1725 and 1176 mAh g^{-1}, respectively. The lithium storage mechanism of the Ge@N-CNTs was investigated by using cyclic voltammetry (CV), as shown in Figure 4.7b. There is a small reduction peak located at 0.16 V in the first cycle, which could be attributed to the formation of Li-Ge phase.[195-198] This peak disappears, however, after the first cycle, and a new peak appears at 0.36 V, suggesting the phase transition from lithiated Li_xGe to amorphous Ge.[199] In the case of Ge/N-CNTs, there is an obvious reduction peak centered at 1.3 V, which could be assigned to the formation of a solid electrolyte interphase (SEI) film between the Ge nanoparticles and the electrolyte (**Figure 4.8**). Figure 4.7c presents the cycling stability of the Ge@N-CNTs and Ge/N-CNTs composites at a constant current density of 100 mA g^{-1} in the potential range of 0.01-1.5 V. Clearly, the Ge@N-CNTs presents an enhanced cycling stability and higher reversible capacity compared to the Ge/N-CNTs. Specifically, the Ge@N-CNTs composite still delivers a high discharge capacity of 892 mAh g^{-1} beyond 200 cycles. Moreover, it demonstrates better coulombic efficiency compared to the Ge/N-CNTs, showing the better reversibility of the Ge@N-CNTs (Figure 4.7c and **Figure 4.9**). The rapid capacity fading is due to the huge volume changes during the cycling process, which would not only lead to the pulverization and loss of active material but also the continuous regeneration of the SEI film. As for the Ge@N-CNTs, the enhanced cycling stability demonstrates the advantages of the unique 1D structure, which could preserve the stable SEI films by accommodating the large volume expansion. The rate capabilities of the Ge@N-CNTs and Ge/N-CNTs composites were also investigated at various current densities. The Ge@N-CNTs shows considerably improved rate

performance when compared with the Ge/N-CNTs at all high current densities (Figure 4.7d). The specific capacities of the Ge@N-CNTs composite at the current densities of 3200 mA g^{-1} and 6400 mA g^{-1} were still 850 and 770 mAh g^{-1}, respectively. The Ge@N-CNTs still delivers a reversible capacity of 725 mAh g^{-1}, even at the high current rate of 8000 mA g^{-1}, whereas the Ge/N-CNTs only exhibits an average capacity of 220 mAh g^{-1} at the current rate of 8000 mA g^{-1}. In addition, the Ge@N-CNTs composite shows very good cycling stability at high current density. As shown in **Figure 4.10**, Ge@N-CNTs still delivers a reversible capacity of 715 mAh g^{-1} over 180 cycles at the current density of 8000 mA g^{-1}. The enhanced electrochemical performance of the Ge@N-CNTs composite could be attributed to the unique Ge nanoparticles encapsulated in the N-CNTs shells. Specifically, the Ge nanoparticles could facilitate Li^+ ion transport through reducing the diffusion distance. Furthermore, the void spaces and the N-CNTs could effectively suppress the huge volume expansion during cycling processes. In addition, the interconnected network of the N-CNTs could afford good electrical conductivity of the electrode and prevent electrical isolation after prolonged cycling. Therefore, when investigated as anode material, the Ge@N-CNTs composite manifests high specific capacity, enhanced cycling stability, and excellent rate capacity. The structural stability of the Ge@N-CNTs and Ge/N-CNTs was also investigated with *ex situ* TEM after alloying and dealloying. As can be seen from the TEM image (**Figure 4.11**a), the 1D structure of the Ge@N-CNTs is well preserved after full alloying. Li_xGe completely fills the inner hollow cavity and the diameter of the nanotube increases from 300 nm to about 500 nm, indicating that the void spaces and N-CNTs could effectively accommodate the volume expansion. Moreover, the structure recovered well after the dealloying process, and the Ge nanoparticles became porous after the extraction of Li during the recharge process (Figure 4.11b), which is consistent with previous reports.[39, 200] For the Ge/N-CNTs composite, on the other

hand, the bare Ge nanoparticles aggregated together after full lithiation, with the diameter of the N-CNTs slightly increased from 300 to 330 nm (Figure 4.11c). Furthermore, after dealloying, the size of the Ge particles became significantly smaller after the extraction of Li (Figure 4.11d), which would lead to the continuous regeneration of SEI film in the following cycles. As shown in **Figure 4.12**, even after 200 cycles, the unique 1D structure of the Ge@N-CNTs could be well preserved. These results imply enhanced structural stability of the unique 1D structure, with Ge nanoparticles uniformly distributed in the N-CNTs during cycling, which results in the enhanced electrochemical performance of the Ge@N-CNTs.

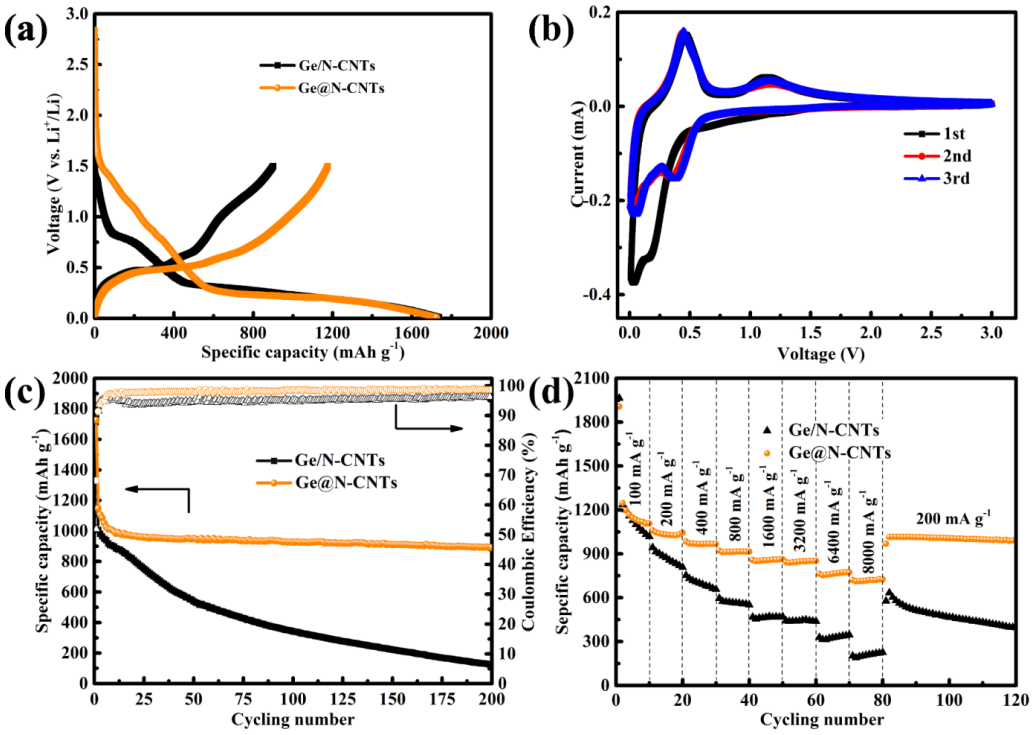

Figure 4.7. (a) First cycle discharge/charge voltage curves of Ge/N-CNTs and Ge@N-CNTs composites cycled at a current density of 100 mA g-1 between 0.01-1.5 V. (b) Cyclic voltammetry profiles of Ge@N-CNTs at a scan rate of 0.1 mV s^{-1} for the first three cycles. (c) Cycling stability of the Ge/N-CNTs and Ge@N-CNTs composites at a constant current density of 100 mA g^{-1} between 0.01-1.5 V. (d) Rate capabilities of Ge/N-CNTs and Ge@N-CNTs at different current densities.

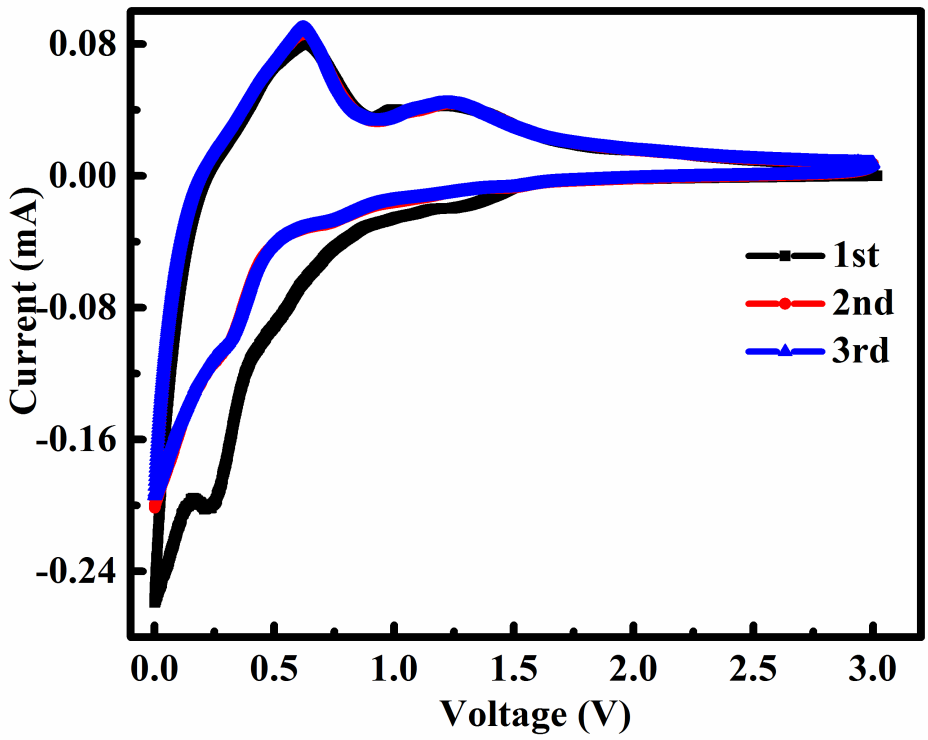

Figure 4.8. Cyclic voltammograms for the first 3 cycles of Ge/N-CNTs at the scan rate of 0.1 mV s^{-1}.

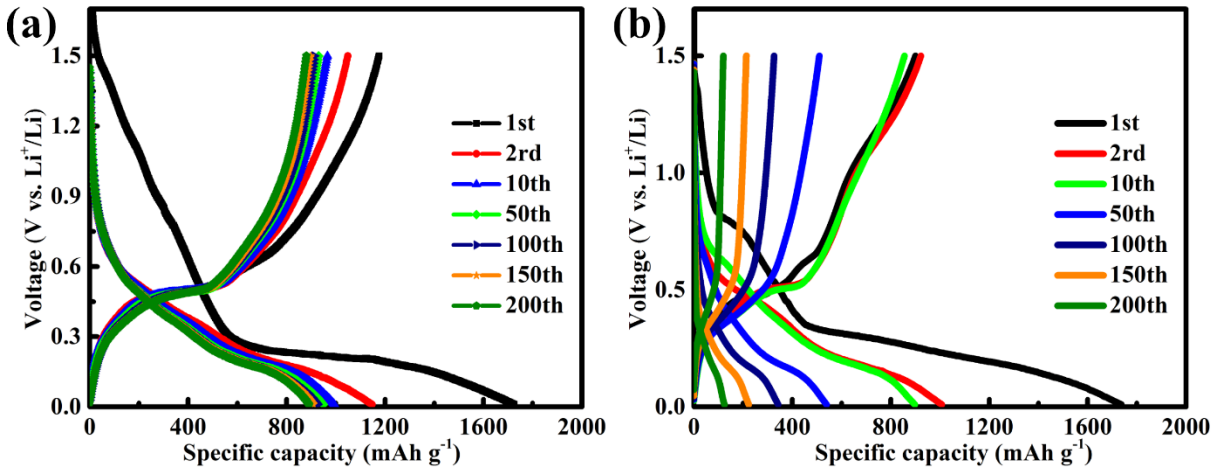

Figure 4.9. Galvanostatic discharge/charge curves for selected cycles of the (a) Ge@N-CNTs and (b) Ge/N-CNTs at a current density of 100 mA g^{-1}.

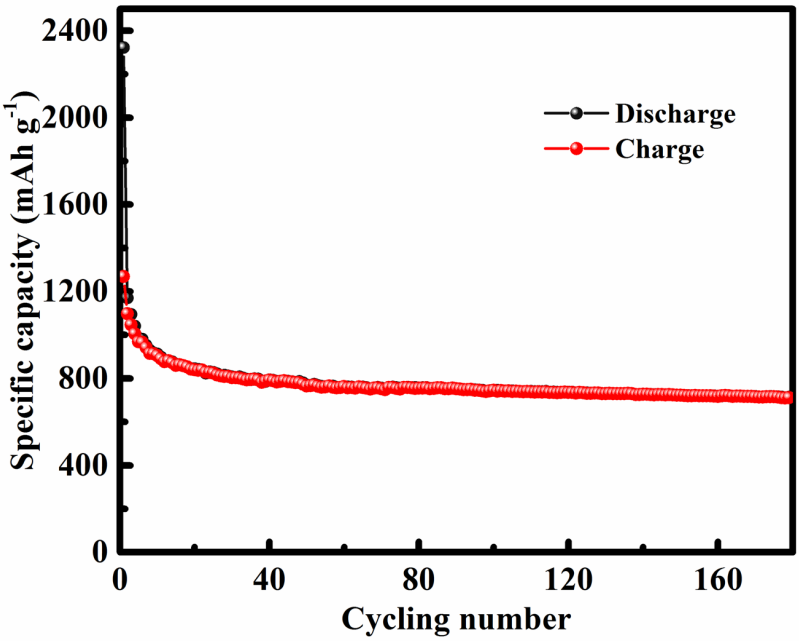

Figure 4.10. The cycling performance of Ge@N-CNTs at a current density of 8000 mA g^{-1}.

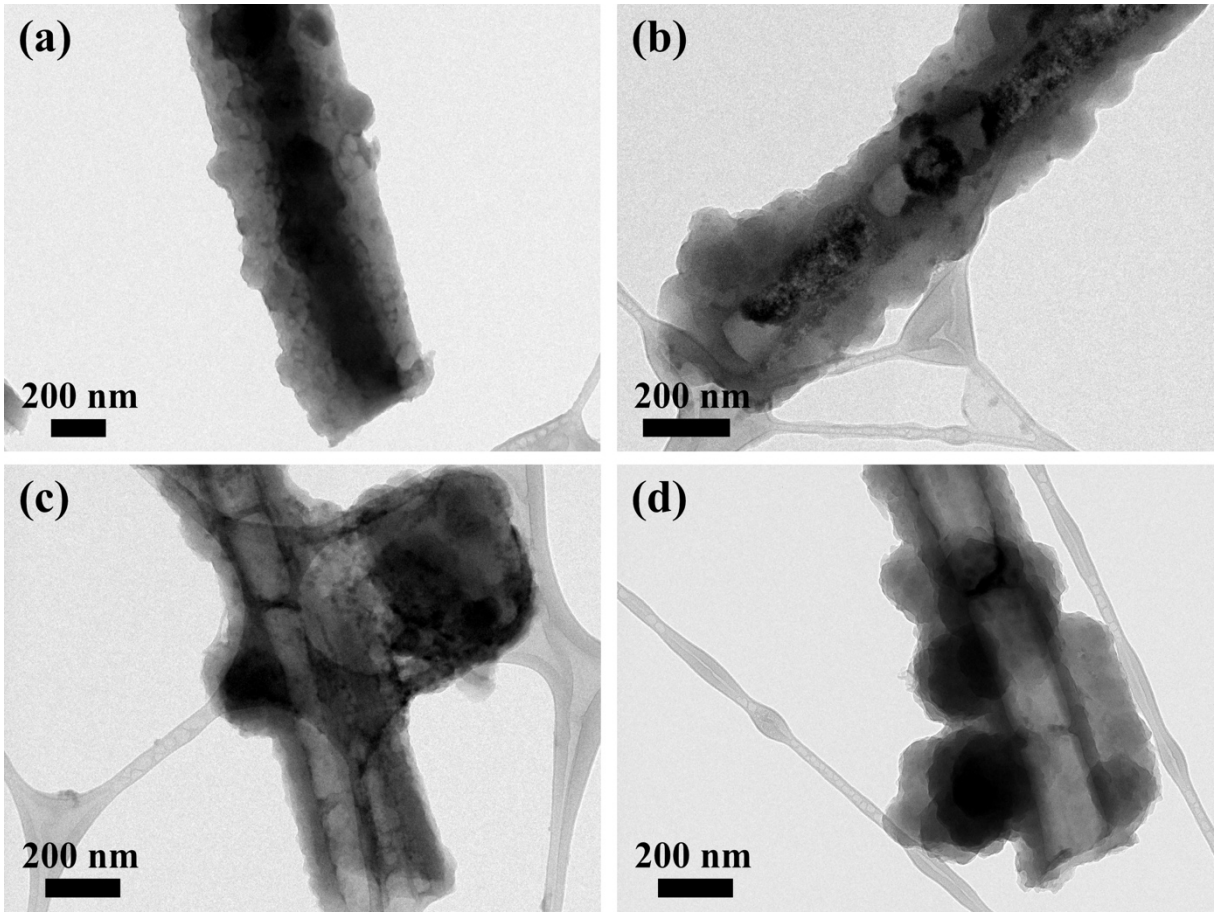

Figure 4.11. (a) Full lithiation and (b) delithiation TEM images of Ge@N-CNTs. (c) Full lithiation and (d) delithiation TEM images of Ge/N-CNTs.

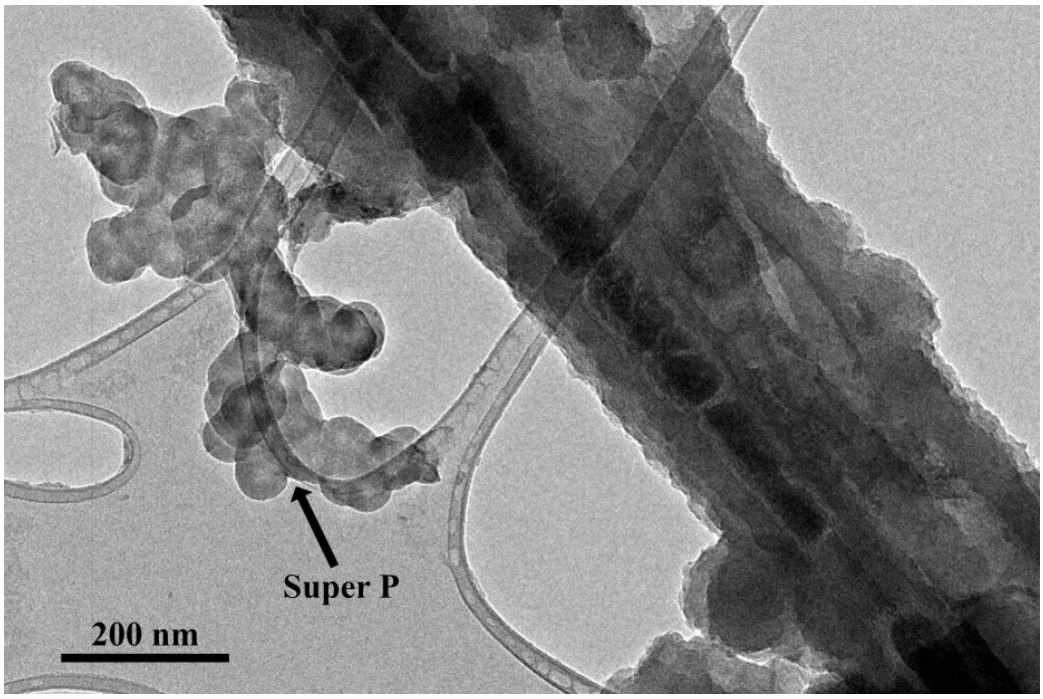

Figure 4.12. TEM image of Ge@N-CNTs after 200 cycles.

The excellent electrochemical performance of Ge@N-CNTs could be attributed to the unique structure properties. The successful synthesis of Ge nanoparticles uniformly distributed in N-CNTs lies in two key aspects. First, the surface tension of GeO_2 could be decreased through adding PVP, and then the solution could be induced into the robust PPy nanotubes by utilizing capillary action. Second, through further annealing and centrifuging treatment, GeO_2 could be reduced to Ge and NaCl also been removed, and a composite of Ge nanoparticles uniformly distributed in the N-CNTs could be obtained. Therefore, the uniformly distributed active materials nanoparticles could effectively utilize the void spaces provided by the unique 1D structure during cycling and prevent the agglomeration of active materials, which could preserve the original structure of the Ge@N-CNTs and achieve prolonged cycling stability when used as anode material for LIBs.

4.4 Summary

In this Chapter, we have presented a novel strategy to fabricate Ge@N-CNTs composite with Ge nanoparticles uniformly encapsulated in N-CNTs shells by using capillary action. Through adding PVP, the high-surface-tension GeO_2/NaCl solution could be induced into the inner hollow cavities of the PPy nanotubes to form a core-shell GeO_2/NaCl@PPy nanotubes composite. After further reducing GeO_2 to Ge and removing NaCl, the unique Ge@N-CNTs composite with Ge nanoparticles uniformly distributed in the N-CNTs could be obtained. The Ge@N-CNTs demonstrates enhanced cycling stability and excellent rate capability in comparison with Ge/N-CNTs, which could be attributed to the efficiently utilization of the void spaces provided by the uniformly distributed Ge nanoparticles. Moreover, the present strategy could be a general method to fabricate other 1D structured materials with enhanced electrochemical performance.

Chapter 5 Yolk-shell Silicon-carbon Nanospheres with Interior Core-shell Structure for High Performance Lithium Storage

5.1 Introduction

Yolk-shell structures have attracted considerable interests because of their unique electrical, mechanical, and optical properties and their potential technological applications in many different areas such as energy conversion and storage, catalysis, and drug delivery.[201-207] The most absorbing feature of yolk-shell structures, which offers exciting possibilities for future research, is that their outer shell can protect the inner yolk for different applications.[207, 208] Until now, many efforts have been devoted to the synthesis of yolk-shell structured materials. The most common methods normally involve the use of sacrificial templates such as SiO_2 with selective etching by hydrofluoric acid, which is not only tedious but also toxic.[209, 210] Therefore, it is still a big challenge to fabricate yolk-shell structures by an easy and environmental friendly strategy.

As the most promising anode material for lithium ion batteries (LIBs), silicon has attracted great attention due to its outstanding theoretical capacity (4200 mAh g^{-1}) and low cost.[211-213] Si suffers, however, from rapid capacity decay caused by the huge volume expansion (> 300 %) during alloying and dealloying processes.[214-217] In addition, Si also exhibits very unsatisfactory rate performance due to its poor electrical conductivity. To overcome these challenges, many approaches have been used to accommodate the volume expansion and enhance its electrical conductivity, such as yolk-shell structures and core-shell structures.[214, 217-221] Yolk-shell structures could

efficiently accommodate the volume changes and preserve the solid electrolyte interphase (SEI) during the alloying and dealloying processes, resulting in excellent cycling stability.[222-225] The core-shell structure is also considered as an attractive structure, which could significantly improve the rate capacity of Si by coating a conductive shell on the Si core.[226-230] Unfortunately, the current method normally needs a tedious procedure.[231-235] For example, a layer of SiO_2 is first formed on the surface of an Si core, and another layer of carbon-based shell formed is on the SiO_2 layer, and then the SiO_2 is selectively etched with using hazardous chemicals (HF or NaOH). Therefore, it is highly desirable to develop a novel strategy to fabricate Si-based composites with yolk-shell or core-shell structures to enhance its electrochemical performance.

This Chapter shows a facile strategy to tunably fabricate yolk-shell Si@SiO_2/C@carbon nanospheres as anode material for LIBs with interior core-shell structured Si@SiO_2/C as yolk by engineering the compositional chemistry. Due to the nonuniform composition inside polymeric phenolic resin coated on Si nanoparticles, the inner phenolic resin could be selectively removed to form a yolk-shell structure with the interior core-shell structure of Si@SiO_2/C. Benefiting from the unique structure, the yolk-shell Si@SiO_2/C@carbon nanospheres have the following merits. First, the exterior carbon on the nanospheres could accommodate the volume changes during the alloying and dealloying processes, which could suppress the drastic capacity decay of Si and preserve the SEI film. Second, the SiO_2/C layer on the surface of Si could significantly improve the electrical conductivity of the Si nanoparticles, resulting in excellent rate performance. In addition, the unique structure could prevent the aggregation of the active materials and increasing the cycling stability. Therefore, the yolk-shell Si@SiO_2/C@carbon nanospheres are expected to exhibit excellent

electrochemical performance when evaluated as anode material for LIBs.

5.2 Experimental Section

Synthesis of Yolk-shell Si@SiO_2/C@carbon nanospheres: 3-aminophenol (0.1 g) and cetyltrimethylammonium bromide (CTAB) (0.03 g) were first dispersed into deionized (DI) water (20 mL) and ethanol (10 mL). Then, Si nanoparticles (5 mg) was added into the solution. After ultrasonication for 1 h, formaldehyde solution (0.1 mL) and ammonia solution (0.1 mL) were dissolved into the above solution. After reacting for 30 min, acetone (20 mL) was added to selectively etch the interior part of the nanospheres. The products were obtained after washing with ethanol and DI water for several times. After carbonization at 1000 ºC for 6 h in N_2 atmosphere, yolk-shell Si@SiO_2/C@carbon nanospheres (YSCS@Si-30) were obtained. The diameter of the carbon nanospheres could be easily tuned through changing the reaction time, and YSCS@Si-60 and YSCS-120 were obtained through increasing the reaction time to 60 min and 120 min, respectively.

Materials characterization: Powder X-ray diffraction (XRD, GBC MMA) with Cu Kα radiation was utilized to study the crystalline structures of the samples. Raman spectra were collected on a JOBIN YVON HR800 Confocal system. Thermogravimetric analysis (TGA) measurements were performed from room temperature to 900 °C at a rate of 10 °C min^{-1} in air with a TGA instrument (Mettler-Toledo, Switzerland). The morphologies of the materials were characterized by transmission electron microscopy (JEM-2010, JEOL) and scanning transmission electron microscopy (JEM-ARM200F, JEOL).

Electrochemical measurement: 2032-type coin-cells were utilized to test the electrochemical performance. The electrodes were prepared through mixing the active material, Super P, and sodium carboxymethyl cellulose in a ratio of 8:1:1. The slurry was casted on Cu foil and dried at 80 ºC for 12 h in a vacuum oven. The electrodes were prepared by punching the Cu foil into discs with a diameter of 0.78 cm, and the loading mass of the active material for all the electrodes was at least 0.3 mg cm^{-2}. The cells were assembled with the prepared active material on Cu foil as working electrode, lithium foil as counter electrode, microporous polyethylene (Celgard 2400) as the separator, and 1 M $LiPF_6$ in a mixture of ethylene carbonate (EC), diethylcarbonate (DEC), and dimethyl carbonate (DMC) (3:4:4 v/v/v) as electrolyte. The assembly process was carried out in an argon-filled glove box with the oxygen and humidity levels both under 0.1 ppm (Mbraun, Germany). Galvanostatic discharge and charge processes were carried out on a Land battery tester between 0.01-2 V vs. Li^+/Li. Cyclic voltammetry and electrochemical impedance spectroscopy were conducted with a Biologic VMP-3 electrochemical workstation.

5.3 Results and Discussion

5.3.1 Structure and morphology

The synthesis strategy for the yolk-shell $Si@SiO_2/C@$carbon nanospheres with interior core-shell structured $Si@SiO_2/C$ as yolk is illustrated in **Figure 5.1**. First, cetyltrimethylammonium bromide (CTAB) and 3-aminophenol were added into a mixture of DI water and ethanol. Then, Si nanoparticles were dispersed uniformly in the solution by ultrasonication. A formaldehyde solution was then added to form phenolic resins through chemical polymerization with ammonia solution as catalyst,

which could combine with the -OH groups on the surfaces of Si nanoparticles. Owing to the step-growth polymerization process of the phenolic resins, the distribution of polymeric components inside the polymer-coated nanoparticles was inhomogeneous. Therefore, acetone was added to selectively remove the interior part of the phenolic resin forming the outer coating of the nanospheres after reacting for 30 min. The yolk-shell Si@SiO_2/C@carbon nanospheres with interior core-shell structured Si@SiO_2/C as yolk (YSCS@Si-30) were obtained after carbonization at 1000 ºC for 6 h under N_2 atmosphere. In addition, the phenolic resin could serve not only as the carbon source for the shell but also as sacrificial template for the yolk-shell structure. Therefore, YSCS@Si-30 with interior core-shell structured Si@SiO_2/C as yolk could be easily fabricated through this novel strategy. In addition, YSCS@Si-60 and YSCS@Si-120 with different diameters of nanospheres could be obtained by increasing the reaction time to 60 min or 120 min, respectively.

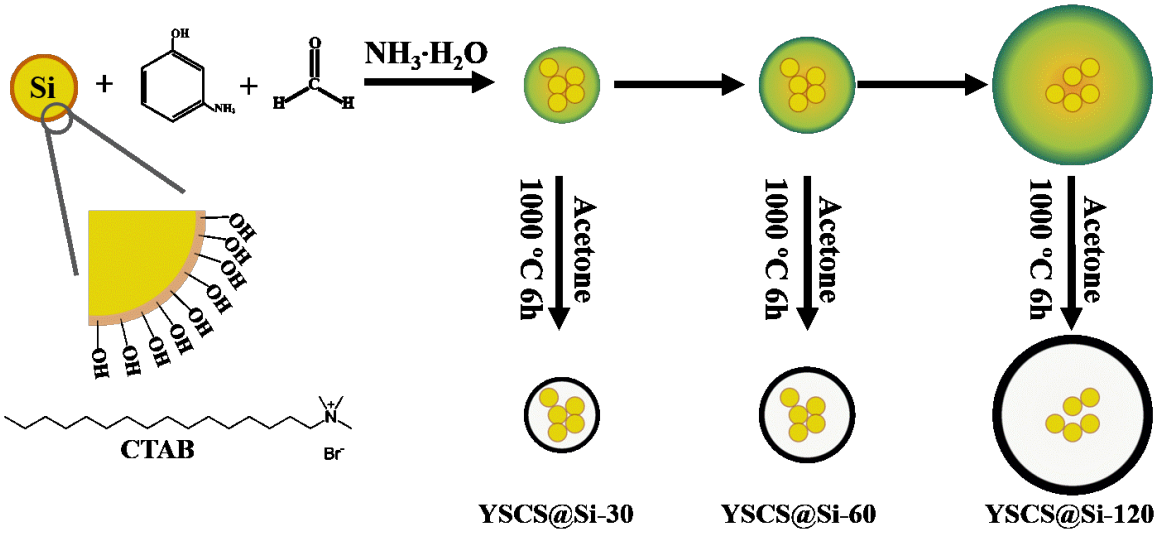

Figure 5.1. Illustration of the synthesis processes for the YSCS@Si-30, YSCS@Si-60, and YSCS@Si-120 composites.

As shown in the scanning transmission electron microscope (STEM) images (**Figure**

5.2), the YSCS@Si-30 particles have a sphere-like structure with the diameter around 260 nm, and the thickness of the exterior shell is about 25 nm. Normally, there are several Si nanoparticles dispersed in the carbon spheres as the yolk of the yolk-shell structure. In addition, the yolk of the YSCS@Si-30 also has a core-shell structure, with an extra shell about 5-10 nm in thickness on the surfaces of Si nanoparticles (Figure 5.2c). Figure 5.2d-I demonstrates that the YSCS@Si-60 and YSCS@Si-120 also possess similar structures to YSCS@Si-30 with an interior core-shell structure. As shown in Figure 5.2d-f, the YSCS@Si-60 has spheres about 330 nm in diameter, and the thickness of the shell is about 40 nm. On further increasing the reaction time to 120 min, the diameter of the spheres grows to 550 nm, and the thickness of the shell increases to 50 nm. Even though the large hollow cavity is beneficial for accommodating the volume changes during the alloying and dealloying processes, it may be not desirable for the electrochemical reactions because the poor contact between the carbon shell and the interior yolk. **Figure 5.3a** presents the high-angle annular dark-field STEM (HAADF-STEM) images of YSCS@Si-30 and the element distribution of YSCS@Si-30 was also investigated by energy dispersive spectroscopy (EDS). As shown in the EDS elemental mapping (Figure 5.3b-d), it is revealed that the Si is mainly distributed inside the nanospheres and signals of oxygen atoms also could be detected. In addition, the EDS spectra (Figure 5.3e) demonstrate that the YSCS@Si-30 only has Si, C, and O elements. In order to investigate the interior core-shell structure of the YSCS@Si-30, high resolution HAADF-STEM and corresponding EDS elemental mapping were investigated, as shown in **Figure 5.4**. It is clear that there is an amorphous shell outside Si nanoparticle with a thickness of about 5 nm. The corresponding EDS mapping images demonstrate that signals of oxygen and carbon could be detached from the outside of the Si nanoparticle, which indicates that the amorphous shell coating the Si nanoparticle consists of SiO_2 and C (Figure 5.4b-d).

The EDS spectra also prove the presence of Si, oxygen, and carbon. The C shell could significantly increase the electrical conductivity of the Si nanoparticles, leading to enhanced electrochemical performance. The contents of carbon in the three samples were also measured through using TGA in air. As shown in **Figure 5.5**, the residual mass of YSCS@Si-30, YSCS@Si-60, and YSCS@Si-120 at 800 ºC is around 52, 37, and 15 wt. %, respectively, indicating their Si (SiO_x) contents. The weight is also slightly increased above 800 ºC, reflecting the oxidation of Si at high temperature.

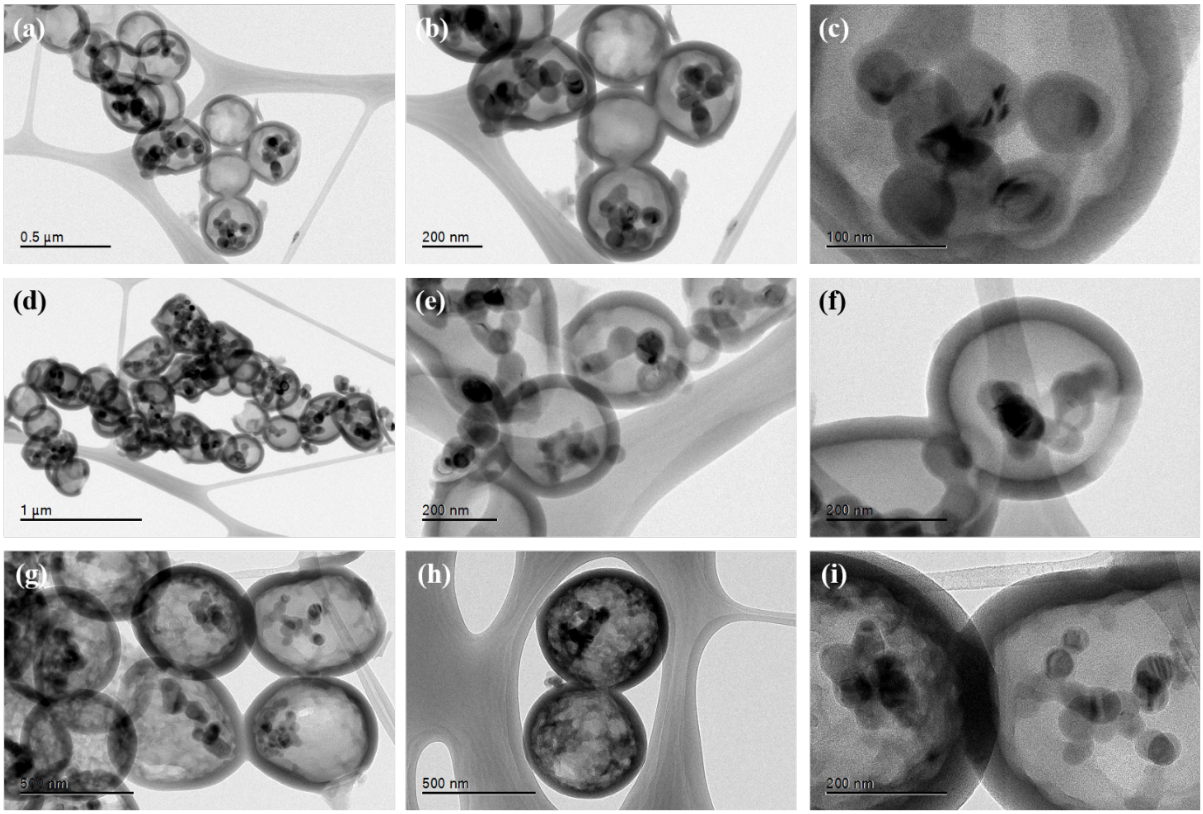

Figure 5.2. STEM images (a-c) YSCS@Si-30, (d-f) YSCS@Si-60, and (g-i) YSCS@Si-120.

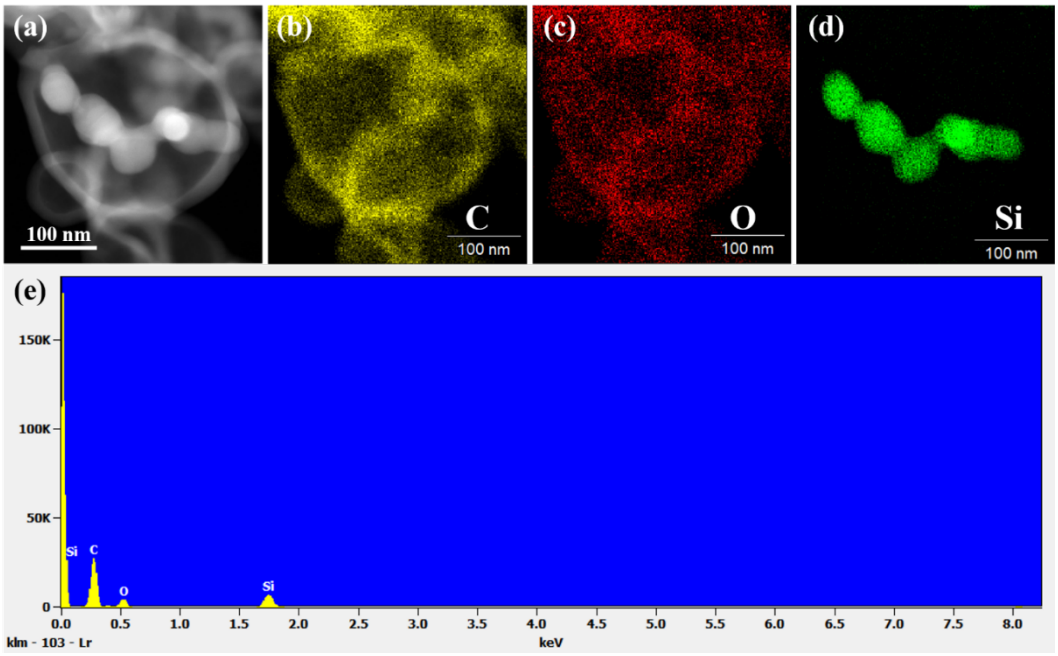

Figure 5.3. (a) HAADF-STEM image of YSCS@Si-30, with (b) C, (c) O, and (d) Si elemental mapping images, and (e) the corresponding EDS spectrum of YSCS@Si-30.

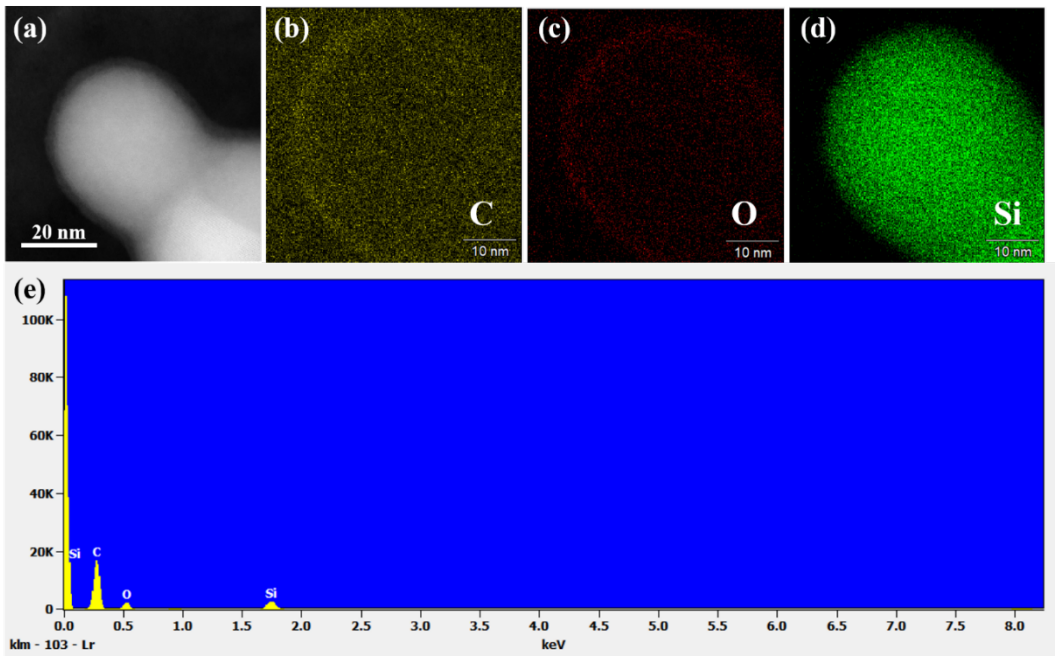

Figure 5.4. (a) High resolution HAADF-STEM image of an individual Si nanoparticle inside the YSCS@Si-30, with corresponding (b) C, (c) O, and (d) Si elemental mapping images and (e) the corresponding EDS spectrum of an individual Si nanoparticle inside the YSCS@Si-30.

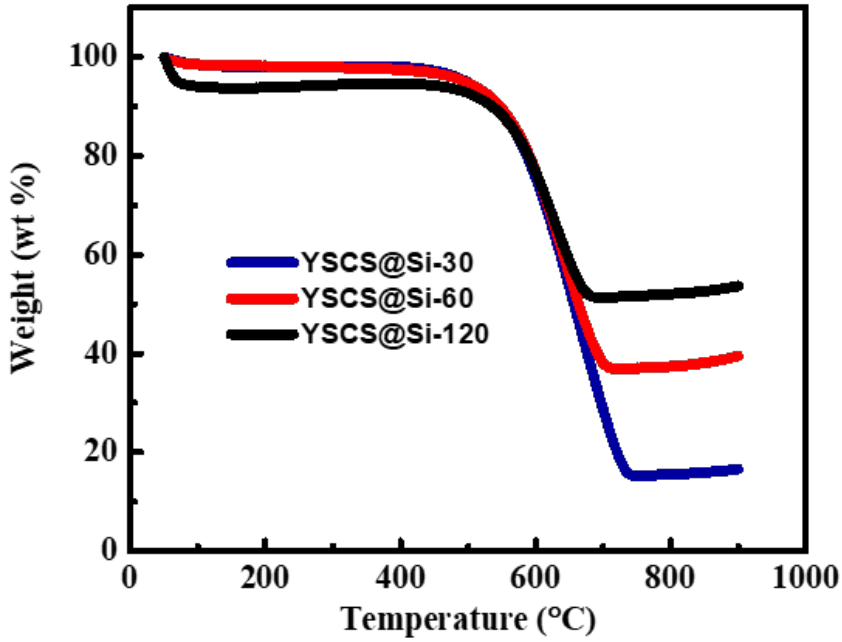

Figure 5.5. TGA curves of YSCS@Si-30, YSCS@Si-60, and YSCS@Si-120 in air under a heating rate of 10 °C min^{-1}.

The X-ray diffraction (XRD) patterns are presented in **Figure 5.6**a. The XRD peaks of the YSCS@Si-30, YSCS@Si-60, and YSCS@Si-120 could be assigned to silicon (JCPDS No. 27-1402) without any impurity. The diffraction peaks at 28.4º, 47.3º, 56.1º, 69.1º, and 76.3º could be assigned to the (111), (220), (311), (400), and (331) planes, respectively. In addition, no obvious carbon diffraction peak can be detected because of the amorphous nature of the carbon, which corresponds to the STEM observations (Figure 5.4). Raman spectra are presented in Figure 5.6b. All three samples have a peak centered at 504 cm^{-1}, which could be assigned to Si. The peaks located at 1350 and 1580 cm^{-1} can be indexed to the D and G bands of carbon, respectively. In addition, the relatively high intensity of D-band compared to the G band indicates the presence of amorphous carbon. For YSCS@Si-30, the peak centered

at 930 cm^{-1} could be assigned to the –OH groups on the surfaces of the Si nanoparticles, but with increasing of the thickness of the shell, it could not be observed in YSCS@Si-60 and YSCS@Si-120.

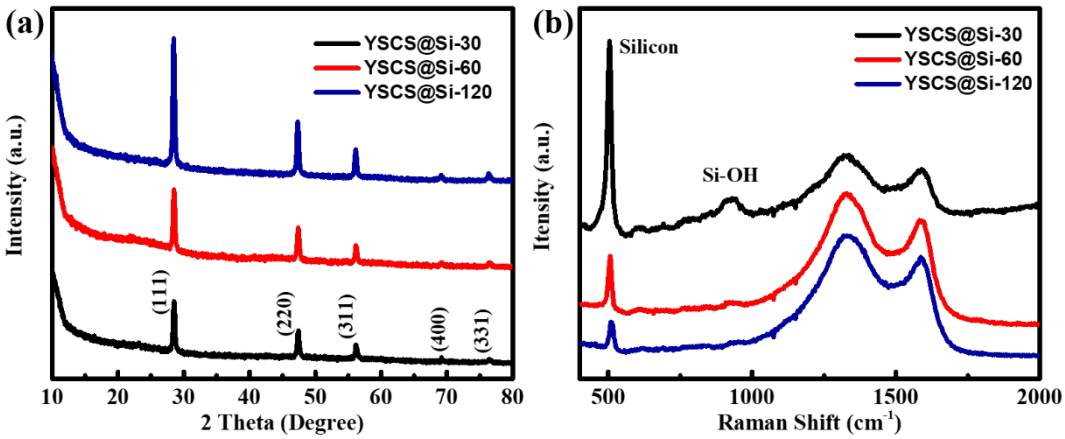

Figure 5.6. (a) XRD patterns and (b) Raman spectra of YSCS@Si-30, YSCS@Si-60, and YSCS@-120.

5.3.2 Electrochemical characterization

The electrochemical performances of YSCS@Si-30, YSCS@Si-60, and YSCS@-120 were investigated to demonstrate the structural advantages of the yolk-shell Si@SiO_2/C@carbon nanospheres with interior core-shell structured Si@SiO_2/C as yolk. The specific capacity was calculated based on the weight of the total active materials. **Figure 5.7**a presents the cyclic voltammetry (CV) curves of the three samples. During the cathodic scans, the broad peaks at around 0.7 V could be attributed to the formation of SEI films. The increasing currents below 0.5 V could be assigned to the insertion of Li ions into Si and carbon. During the anodic scan, the peak centered at 0.57 V could be attributed to the delithiation of Li-Si alloy. YSCS@Si-30 also exhibits excellent cycling stability, reflected by almost overlapping CV curves from

the 2nd to the 10th cycle (**Figure 5.8**). A new anodic peak also appears at 0.37 V, which could be attributed to dealloying process of the amorphous Si formed during alloying. In addition, the current of both cathodic and anodic peaks increased with the cycling number, indicating the formation of stable SEI film on the electrode. As shown in Figure 5.7b, YSCS@Si-30 reveals the highest initial discharge and recharge capacity of 2977 and 2174 mAh g^{-1}, respectively, which means that it exhibits the best initial coulombic efficiency of 73 %. YSCS@Si-60 shows an initial discharge and recharge capacity of 2206 and 1516 mAh g^{-1}, respectively, with an initial coulombic efficiency of 68 %. YSCS@Si-120 shows an initial coulombic efficiency of 67 %, and its initial discharge and charge capacities are 1811 and 1211 mAh g^{-1}, respectively. The highest capacity of YSCS@Si-30 could be credited to its having the highest Si content compared with the YSCS@Si-60 and YSCS@Si-120. The discharge plateaus located below 0.2 V could be attributed to the insertion of Li ions, which is consistent with the CV results, and the recharge plateaus below 0.5 V could be assigned to the deinsertion of Li ions from the Li-Si alloys. The cycling performances of three samples are presented in Figure 5.7c with a current density of 2 A g^{-1} after the first 5 cycles (under the current density of 0.2 A g^{-1}). It is obvious that YSCS@Si-30 has the highest charge capacity at about 1300 mAh g^{-1}, and even after 500 cycles, the capacity is still as high as 1000 mAh g^{-1}. YSCS@Si-60 and YSCS@Si-120 also exhibit good cycling stability after 500 cycles with the charge capacity of about 700 and 400 mAh g^{-1}, respectively. Due to their low silicon contents, however, their capacities are lower than for YSCS@Si-30. The rate capabilities of the three samples were also investigated under various current densities. YSCS@Si-30 exhibits the best rate performance when compared with the YSCS@Si-60 and YSCS@Si-120. Even under the current density of 4 and 6 A g^{-1}, the YSCS@Si-30 could still deliver a capacity of 860 and 670 mAh g^{-1}, respectively. The electrochemical impedance spectroscopy (EIS) was also

conducted on the three samples. As shown in **Figure 5.9**, YSCS@Si-30 has the smallest resistance compared to the other two samples. This may be because that the carbon spheres could not remain in intimate contact with each other with the increased diameter, leading to lower electrical conductivity compared to the small but intimately contacted carbon spheres. The excellent electrochemical performances of these materials could be attributed to their unique yolk-shell Si@SiO_2/C@carbon nanospheres with interior core-shell structured Si@SiO_2/C as the yolk structure. The exterior yolk-shell structure could efficiently accommodate the volume changes during the alloying and dealloying processes. The interior core-shell structure with its carbon layer could significantly increase the electrical conductivity of the Si nanoparticles.

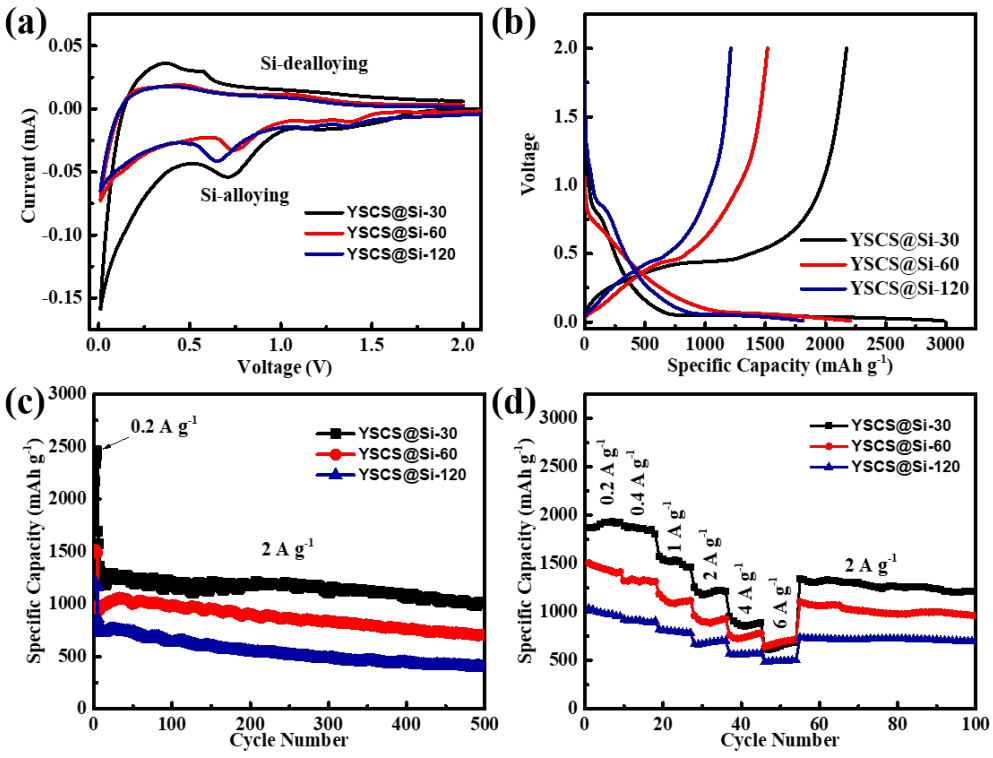

Figure 5.7. Electrochemical performances of YSCS@Si-30, YSCS@Si-60, and YSCS@Si-120: (a) Cyclic voltammetry curves at a scan rate of 0.1 mV s^{-1}, (b) initial discharge/charge voltage profiles at a current density of 0.2 A g^{-1}, (c) cycling stability, and (d) rate capabilities under different current densities.

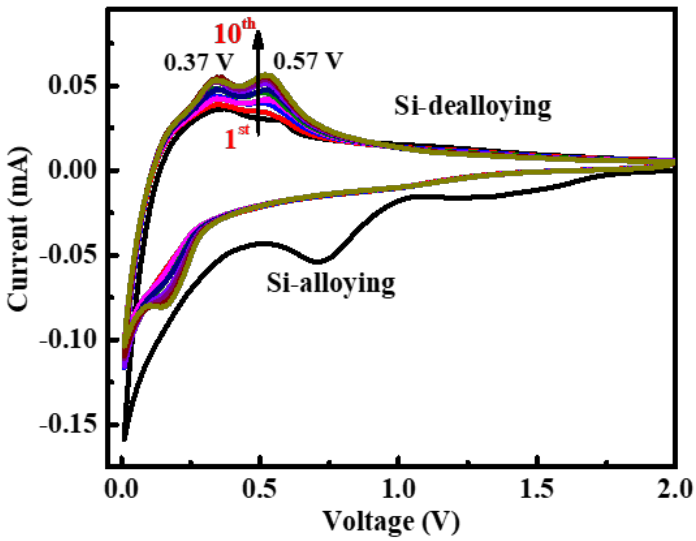

Figure 5.8. Cyclic voltammograms of the first 10 cycles for YSCS@Si-30 at a scan rate of 0.1 mV s^{-1}.

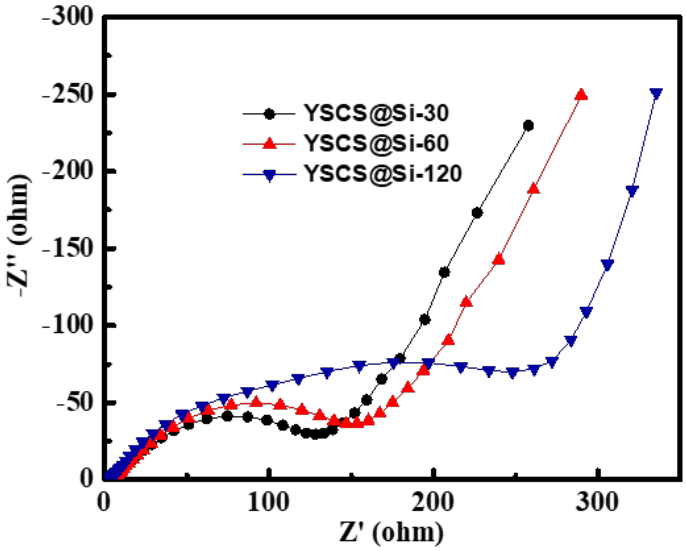

Figure 5.9. Electrochemical impedance spectra of YSCS@Si-30, YSCS@Si-60, and YSCS@Si-120.

The outstanding electrochemical performance of the as-prepared YSCS@Si-30 for LIBs are obtained due to the unique yolk-shell with core-shell structure through engineering the compositional chemistry. Specifically, the exterior carbon nanospheres

could accommodate the volume changes during the alloying and dealloying processes, which could suppress the drastic capacity decay of Si and preserve the SEI film. Besides, the SiO_2/C layer on the surface of Si could significantly improve the electrical conductivity of the Si nanoparticles, resulting in excellent rate performance. Additionally, the unique structure could prevent the aggregation of the active materials and increasing the cycling stability. Therefore, all of these features improve structure stability and electrons conductivity, which is supported by the outstanding electrochemical performance of the as-prepared materials for LIBs.

5.4 Summary

In this Chapter, a facile strategy was developed for the tunable fabrication of yolk-shell Si@SiO_2/C@carbon nanospheres with interior core-shell structured Si@SiO_2/C as yolk for anode material for LIBs by engineering the compositional chemistry. Due to the step-growth polymerization process of the phenolic resin, the distribution of polymeric components inside the phenolic resin coating the nanoparticles is non-unifrom, and the inner part could be selectively removed by using acetone to form a yolk-shell structure with interior core-shell structured Si@SiO_2/C. The phenolic resin could serve not only as the carbon source for the shell, but also as a sacrificial template for the yolk-shell structure. The exterior yolk-shell structure could efficiently accommodate the volume changes during the alloying and dealloying processes, while the interior core-shell structure with the carbon layer coating the Si nanoparticles could significantly increase their electrical conductivity. Among the different composites, the YSCS@Si-30 exhibited excellent electrochemical performance when evaluated as anode material for LIBs. Moreover, the present strategy could be a general method to fabricate other core-shell@yolk-shell structured materials for different applications.

Chapter 6 Phosphorous and Nitrogen Dual-Doped Carbon as Efficient Electrocatalyst for Sodium-Oxygen Batteries

6.1 Introduction

Lithium-oxygen batteries have received great attention during the past several years because of their high energy density and power density.[236-238] Unfortunately, there are still many problems that need to be resolved before practical application, such as high overpotential and poor cycling stability.[239-243] The main reason for these problems could be attributed to the formation of an extremely unstable superoxide intermediate (O_2^-), which could not be stabilized by small Li^+ ions due to the mismatch according to the hard and soft acid base (HSAB) theory and can react with non-aqueous electrolyte or carbon-based air cathodes.[117, 136, 244] By contrast, as a soft Lewis acid compared with Li^+, Na^+ could effectively stabilize the soft Lewis base O_2^- ions. Therefore, sodium-oxygen batteries have been considered as a more promising system due to the formation of a more stable product, leading to low overpotential and high reversibility.[126, 245, 246] As in the lithium-oxygen batteries, electrocatalysts with different catalytic activities also could significantly affect the catalytic performance and cycling stability of sodium-oxygen batteries through modulating the morphology and composition of discharge products.[77, 85, 86, 127, 129, 130, 247-249] To date, several different kinds of electrocatalysts have been explored as air cathodes for sodium-oxygen batteries with distinct discharge products such as sodium superoxide (NaO_2)[106, 250-253], sodium peroxide (Na_2O_2)[76, 77, 83], or sodium peroxide dihydrate ($Na_2O_2 \cdot 2H_2O$)[78, 135]. For example, Wang and co-workers fabricated hierarchical porous carbon spheres as an air cathode with high reversibility through forming film like NaO_2 discharge products.[130] Sun et al. synthesized CNT@Co_3O_4 catalysts with

micron-sized box-shaped NaO_2, which demonstrated good performance and long cycle life.[85] Zhou et al. reported the formation of $Na_2O_2 \cdot 2H_2O$ particles as discharge products by using the carbon nanotube paper as the air cathode.[78] Sun and co-workers found that Na_2O_2 was generated on the surface of nitrogen doped graphene cathodes.[77] In addition, Kang et al. demonstrated that NaO_2 could be transformed into $Na_2O_2 \cdot 2H_2O$ with spontaneous dissolution and ionization.[254] As the morphology and composition of discharge products of the sodium-oxygen batteries could greatly affect the electrochemical performance in such aspects as energy efficiency and cycling stability, it is important to achieve an in-depth understanding of the influence of electrocatalysts on the morphology and composition of discharge products and to prevent the transformation of sodium superoxide into other sodium oxides, which is a prerequisite for developing high performance and longlife sodium-oxygen batteries.[255] It is, however, still a big challenge to develop an efficient catalyst for sodium-oxygen batteries with high performance and long life at the current stage. Owing to the tunability of their structure and surface properties, carbonaceous materials have been extensively studied as efficient catalysts for various catalytic reactions.[256-259] The catalytic performance of carbon based materials could also be improved through doping with different elements, such as phosphorus, sulfur, and boron.[260-264] In addition, the catalytic performance could be further improved through dual doping with synergistic effects.[256] Thus, it is considered that carbonaceous materials with tunable structure and surface properties are one of the most promising types of catalytic materials for Na-O_2 chemistry.

In this Chapter, a heteroatom-doped carbon based cathode has been designed, and the influence of carbon catalysts doped with different heteroatoms has been studied with respect to the discharge products, cycling stability, and electrocatalytic performance of

sodium-oxygen batteries. Carbon materials with different doping, namely, phosphorus and nitrogen dual-doped carbon (PNDC) and nitrogen solely doped carbon (NSDC), were fabricated and studied as electrocatalysts for the sodium-oxygen battery. When the two different doped carbon materials were evaluated as air cathodes for the sodium-oxygen batteries, different electrocatalytic performance were observed due to the distinct morphology and compositions of discharge products formed on the different cathodes. The PNDC based Na-O_2 battery demonstrated a quite low recharge overpotential of about 0.18 V with NaO_2 as discharge product, and excellent cycling stability over 120 cycles was obtained. As for NSDC, mixed NaO_2 and $Na_2O_2{\cdot}2H_2O$ were identified as the discharge products, and there was poor cycling stability for only 23 cycles.

6.2 Experimental Section

Synthesis of polypyrrole: Polypyrrole was fabricated by a previously reported method.[193] Generally, 81.8 mg methyl orange and 1350 mg $FeCl_3$ were dissolved in 100 mL deionized water. Then, 33.5 mg pyrrole monomer was added into the above solution. After stirring at room temperature for 24 h, the polypyrrole was washed with ethanol and deionized water several times.

Synthesis of phosphorus and nitrogen dual-doped carbon: Polypyrrole was placed on a porcelain boat in a tube furnace under argon atmosphere. Another porcelain boat with NaH_2PO_2 was put on the upstream side. Then, the sample was annealed at 300 °C for 2 h with a heating rate of 5 °C min^{-1}. Finally, the sample was washed with ethanol and deionized water several times after cooling down to room temperature. To synthesize nitrogen solely doped carbon, the polypyrrole alone was put into the tube furnace with the same annealing conditions.

Materials Characterization: Raman spectra were investigated with a JOBIN YVON HR800 Confocal system. A Phoibos 100 Analyzer XPS with Al Kα X-rays was used to determine the surface chemical states of the samples. A JSM-7500FA scanning electron microscope and JEM-ARM200F transmission electron microscope were utilized to measure the structures and morphologies of the materials.

Electrochemical Measurements of Na-O_2 Batteries: The electrochemical properties were measured using CR2032-type coin cells with holes in the cathode part. To prepare the oxygen cathodes, the active materials and poly(tetrafluoroethylene) solution were mixed in the ratio of 90:10 in isopropyl alcohol as catalyst slurry. The slurry was then pasted onto carbon paper and dried in a vacuum oven at 120 °C for 12 h. The typical loading of cathode active materials was 0.3 mg cm^{-2}. Tetraethylene glycol dimethyl ether (TEGDME) solvent was purified by rotary evaporation and stored with 4 Å activated molecular sieves for two weeks before use. Sodium trifluoromethanesulfonate (sodium triflate, $NaSO_3CF_3$) was dried at 120 °C for 24 h under vacuum. The electrolyte, consisting of 0.5 m sodium triflate in TEGDME, was prepared in an argon-filled glovebox. The cells were assembled in an argon-filled MBRAUN glove box (H_2O level < 0.1 ppm and O_2 level < 0.1 ppm). A piece of sodium cut from a sodium cube served as the anode, and glass microfiber was used as the separator. All the measurements were carried out on Neware battery testers at room temperature in dry oxygen atmosphere with our designed facility. Cyclic voltammetry was measured on a Biologic VMP-3 electrochemical workstation with a scan rate of 0.1 mV/s. Electrochemical impedance spectroscopy curves were collected in the frequency range of 100 kHz to 0.1 Hz.

6.3 Results and Discussion

6.3.1 Structure and morphology

Polypyrrole (PPy) hollow nanotubes were first synthesized through a template method using methyl orange as the precursor. Afterwards, PNDC was prepared by using PPy as the main precursor and NaH_2PO_2 as the P precursor at 300 ºC in Ar, as illustrated in **Figure 6.1**a.[193] NSDC was also prepared through direct heating PPy at 300 ºC in Ar. The surface chemistries of PNDC and NSDC are different due to their differences in element doping. The structure and morphology of the samples were studied by scanning electron microscopy (SEM) and scanning transmission electron microscopy (STEM), as shown in Figure 6.1b-h, **Figure 6.2**, and **Figure 6.3**. The as-prepared polypyrrole has a tubular structure with the tube diameter around 400 nm and length up to 10 μm (Figure 6.2). After the doping process, the tubal structures are well preserved for both PNDC and NSDC (Figure 6.1 b-d and Figure 6.3). EDS mapping was then conducted to study the element distributions within the tubal carbon (Figure 6.1, Figure 6.3, and **Figure 6.4**). As shown in Figure 6.1e-g, the doping elements (P and N) are homogeneously distributed in the carbon tubal structures of the PNDC. In the NSDC, nitrogen is also evenly distributed throughout the whole tubal structure (Figure 6.3). In addition, the high resolution TEM images reveal that the PNDC is amorphous without any obvious crystalline structure (**Figure 6.5**).

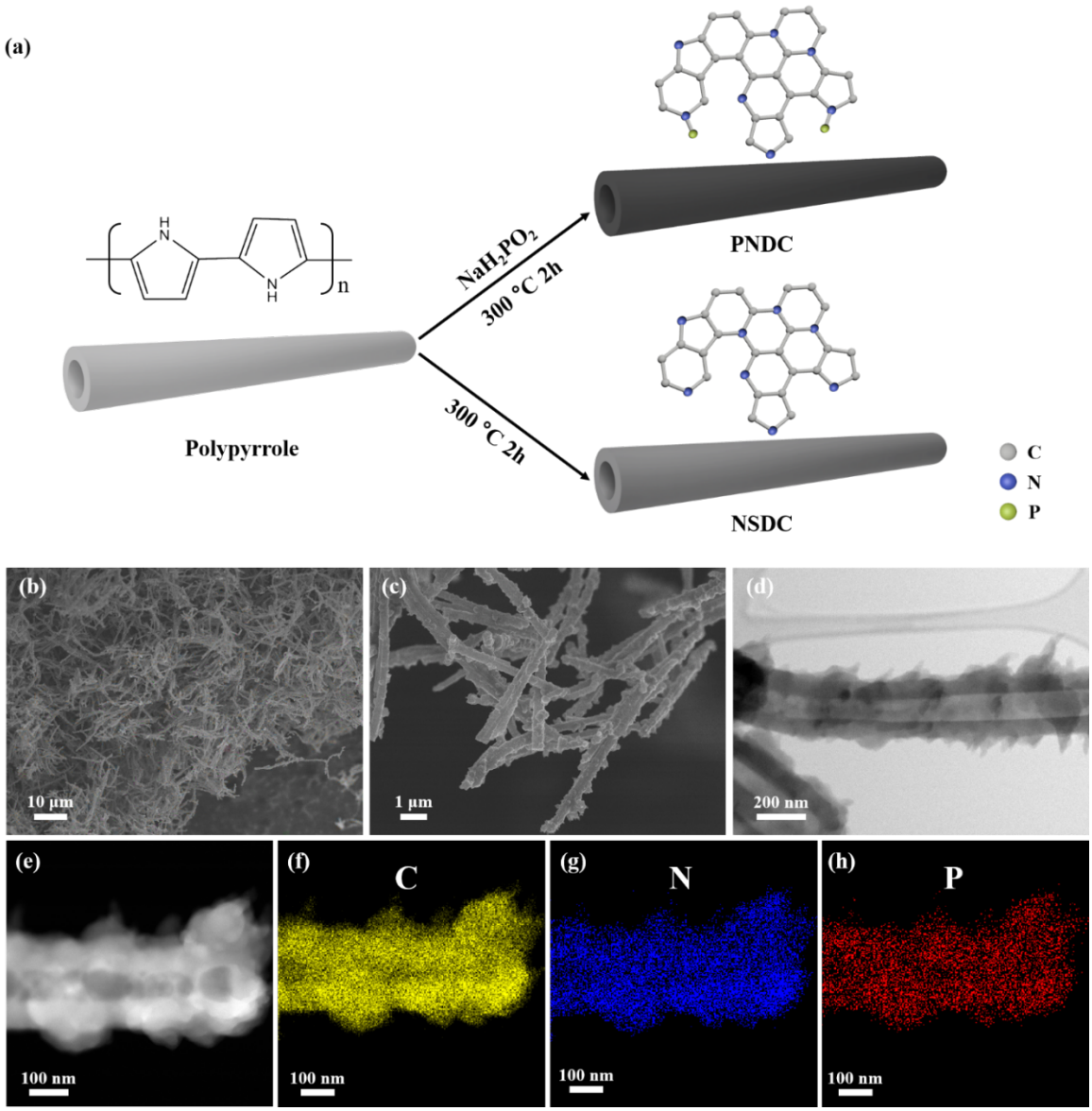

Figure 6.1. Structural characterization of the PNDC. (a) Schematic illustration of the preparation process for PNDC and NSDC; (b) Low magnification SEM image of the PNDC; (c) high magnification SEM image of the PNDC; (d) STEM image of an individual PNDC tube; (e) high-angle annular dark-field STEM image of the PNDC; (f-h) corresponding element mappings of various elements of an individual PNDC tube.

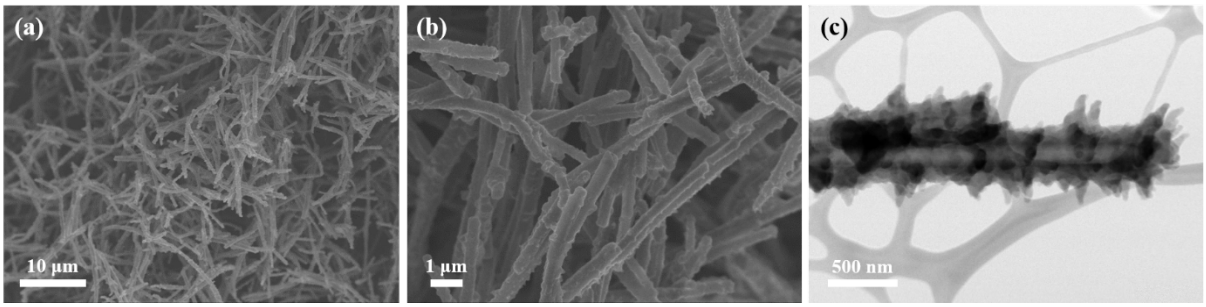

Figure 6.2. (a) Low magnification SEM image of the polypyrrole; (b) high magnification SEM image of the polypyrrole; (c) STEM image of an individual polypyrrole tube.

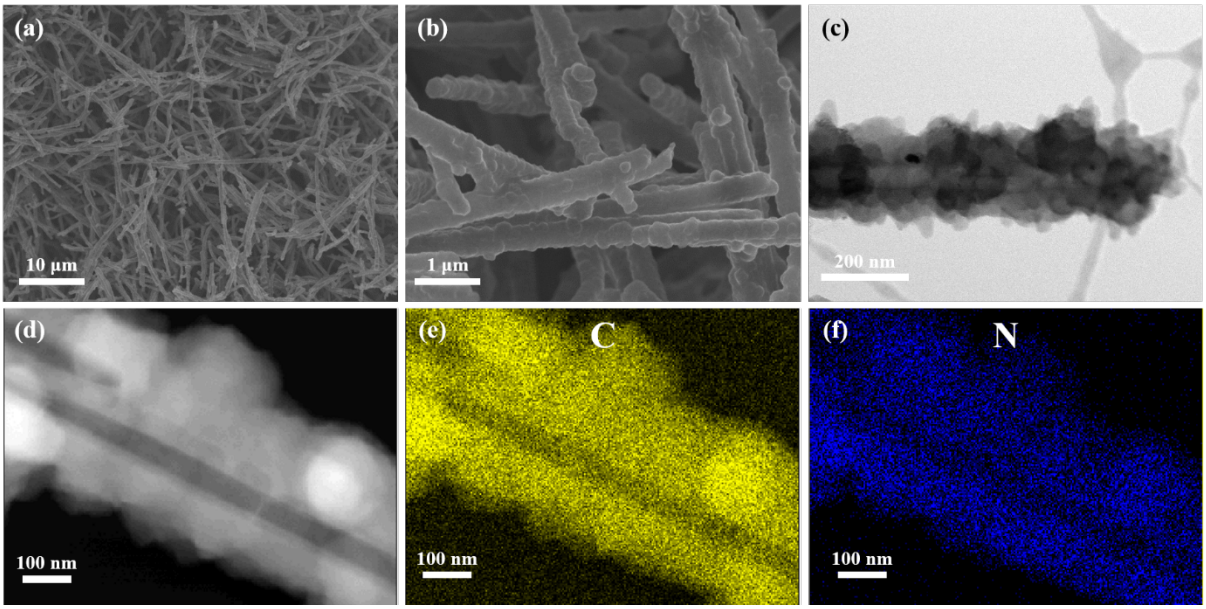

Figure 6.3. (a) Low magnification SEM image of the NSDC; (b) high magnification SEM image of the NSDC; (c) STEM image of an individual NSDC tube; (d) high-angle annular dark-field STEM image of an individual NSDC tube; (e-f) corresponding element mappings.

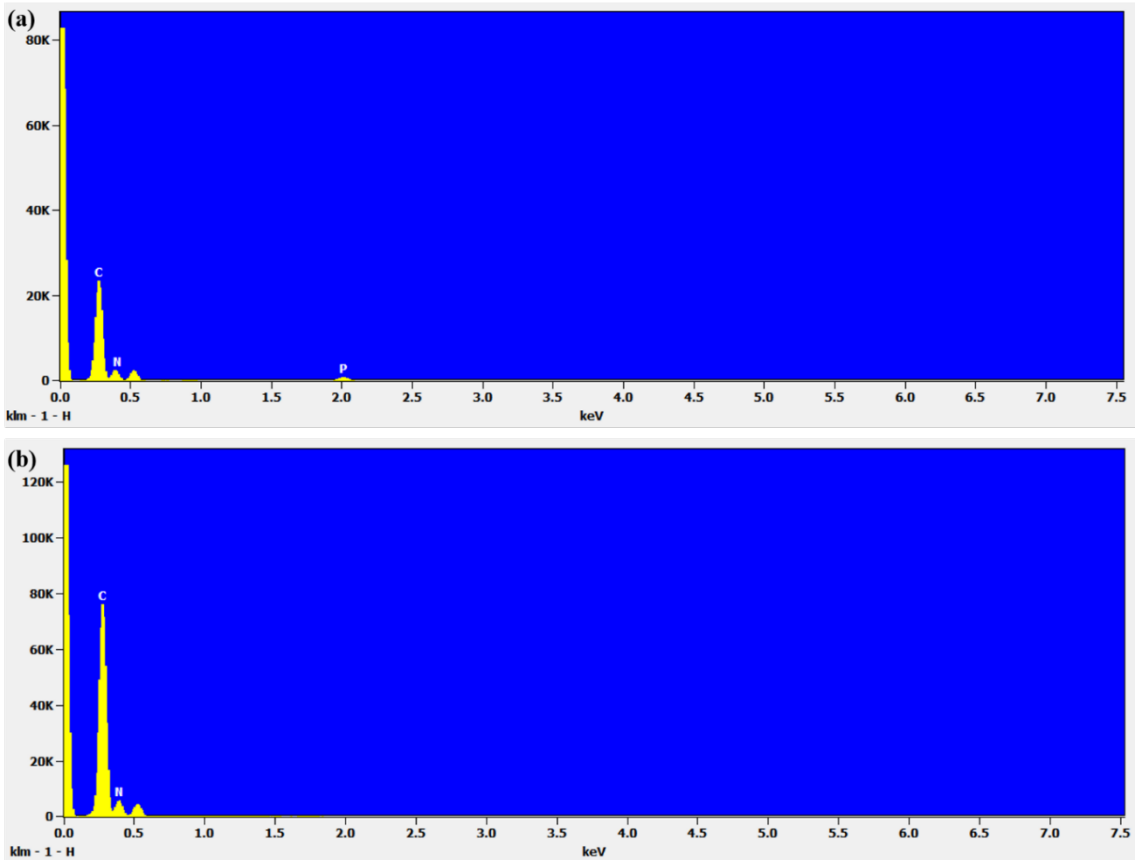

Figure 6.4. (a) EDS spectrum of PNDC; (b) EDS spectrum of NSDC.

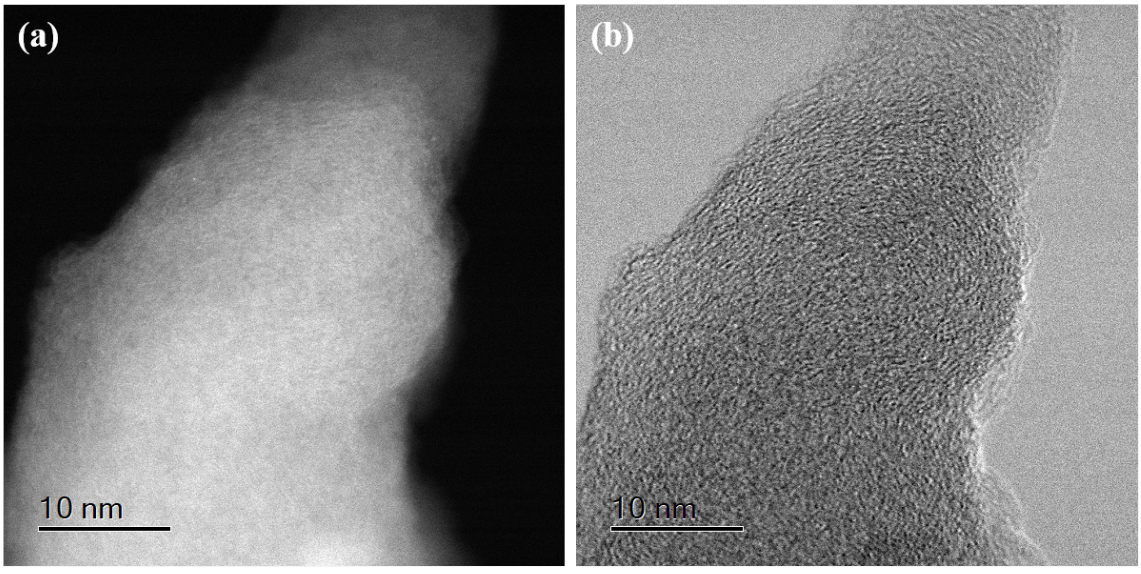

Figure 6.5. (a) High resolution high-angle annular dark-field STEM image of PNDC; (b) high resolution high-angle annular bright-field STEM image of PNDC.

Further information on the structural and surface chemical status of the samples were obtained from Raman spectroscopy and X-ray photoelectron spectroscopy (XPS) (**Figure 6.6** and **Figure 6.7**). As shown in Figure 6.7 a, the XPS survey scan of PNDC demonstrates the presence of P, N, and C without any impurities on the surface, which is consistent with the EDS results. The P and N elemental content is 2.36 atom % and 8.26 atom %, respectively. NSDC also has similar N content of about 8.50 atom % (Figure 6.7 b). The high-resolution C 1s spectra of PNDC (Figure 6.6 a) and NSDC (Figure 6.6 d) can be deconvoluted into three component peaks, corresponding to C-C/C=C, C-N, and C=O. The only difference is that the C=O peak of PNDC (288.6 eV) is shifted to higher binding energy compared with that of NSDC (287.9 eV), which may be caused by the doping with P atoms. On the other hand, the high-resolution N1s spectra of PNDC and NSDC show three nitrogen species (pyridinic-N, pyrrolic-N, and graphitic-N), implying that part of the pyrrolic-N atoms within the polypyrrole rings are transformed to pyridinic-N and graphitic-N. Compared with NSDC, the graphitic-N peak of PNDC is shifted to lower binding energy (from 402.4 to 401.7 eV). In addition, when compared with NSDC, the content of graphitic-N for PNDC decreased from 17.0 % to 10.1 %, while the content of pyrrolic-N increased from 64.9 % to 67.3 % and the content of pyridinic-N increased from 18.1 % to 22.6 %. The higher content of pyrrolic-N at the edges could improve the charge mobility and electrocatalytic activity of PNDC. The P doping in PNDC was also confirmed by XPS with a typical P-N coordination peak centered at 133.3 eV, indicating that P most probably replaces C to form P-N bonds.[265] As shown in Figure 6.6f, both PNDC and NSDC have the typical carbon D band and G band. The D band located at 1350 cm^{-1} could be attributed to disordered carbon atoms, while the G band observed at 1580 cm^{-1} can be ascribed to sp^2-hybridized graphitic carbon atoms. In addition, the I_D/I_G intensity ratio decreases from NSDC to PNDC, indicating that the defects are reduced after introducing P atoms.

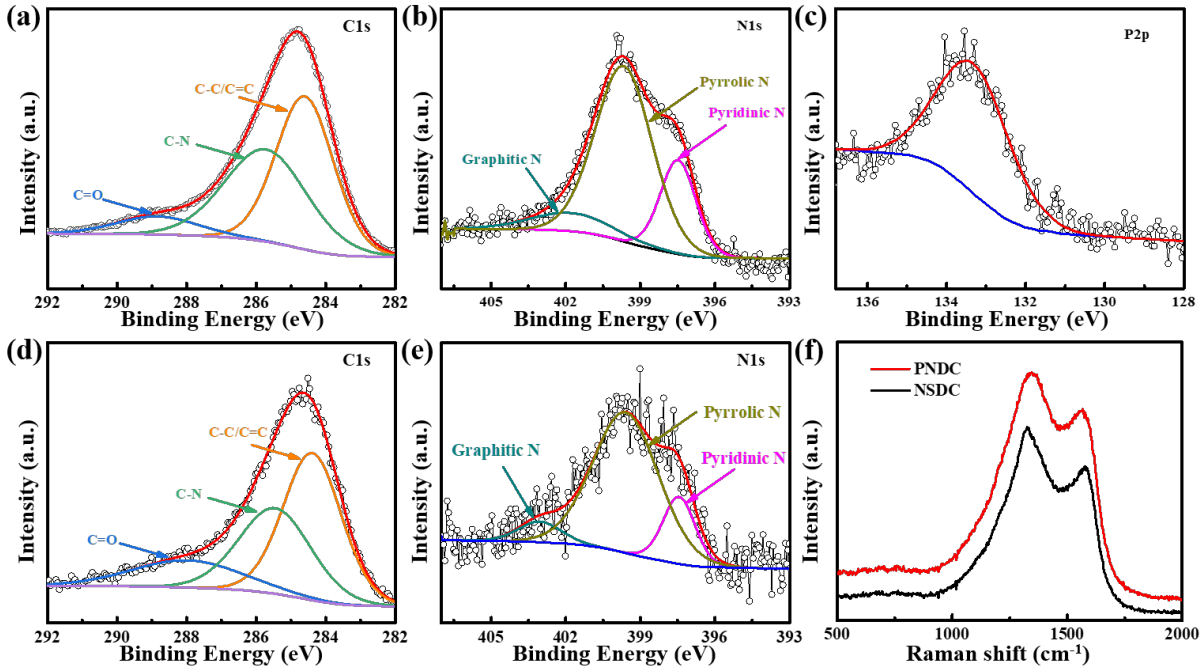

Figure 6.6. Chemical analysis of the PNDC and NSDC. (a) High resolution C 1s XPS spectrum, (b) high resolution N 1s XPS spectrum, and (c) high resolution P 2p XPS spectrum of PNDC; (d) high resolution C 1s XPS spectrum and (e) high resolution N 1s XPS spectrum of NSDC; (f) Raman spectra of PNDC and NSDC.

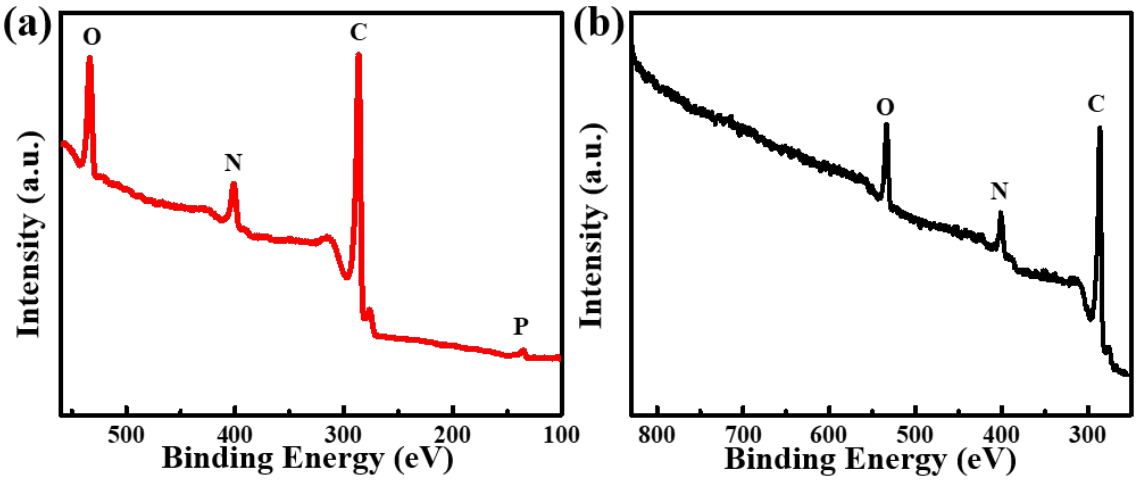

Figure 6.7. (a) XPS survey spectrum of PNDC; (b) XPS survey spectrum of NSDC.

6.3.2 Electrochemical characterization

In order to investigate the electrochemical properties of the as-prepared PNDC and NSDC, Na-O_2 batteries were then tested using PNDC and NSDC as air cathodes. The specific capacities were calculated based on the mass of active materials in the cathodes. Cyclic voltammetry curves of the two electrodes were collected to demonstrate their catalytic activities. As shown in **Figure 6.8**, the PNDC has higher anodic and cathodic peak current densities than the NSDC electrode, indicating that the PNDC exhibits superior catalytic activity. In addition, the PNDC electrode also has better conductivity compared with the NSDC electrode, as demonstrated by the Nyquist plots in **Figure 6.9**. The galvanostatic discharge/charge properties were investigated in the voltage range of 1.5-3.0 V at room temperature. The full discharge plot at current density of 200 mA g^{-1} is shown in **Figure 6.10**. The Na-O_2 batteries with the PNDC air cathode achieved a discharge capacity of 6216 mAh g^{-1}, which is much higher than that of the battery with the NSDC electrode (4975 mAh g^{-1}). **Figure 6.11**a presents the discharge/charge curves of Na-O_2 batteries with PNDC and NSDC cathode with a cut-off capacity of 1000 mAh g^{-1} at a current density of 400 mA g^{-1}. Compared with the NSDC electrode, the PNDC electrode exhibits much lower overpotential (0.18 V) and higher Coulombic efficiency. In addition, the PNDC also demonstrates outstanding rate capability. When the current density was increased from 100 to 200 or 400 mA g^{-1}, as shown in Figure 6.11b, the PNDC still exhibited a high discharge capacity and low overpotential. Meanwhile, the recharge capacity also increased from 593 to 797 mAh g^{-1}, which is consistent with other reports.[80, 129, 254, 266] In contrast, the NSDC electrode only delivered a recharge capacity of 389 mAh g^{-1}, even when the current density was increased to 400 mA g^{-1}. The excellent electrochemical performance and rate capability of the PNDC electrode are primarily attributable to its

high catalytic activity and the special one-dimensional (1D) nanotube structure. The 1D nanotubes could form an interconnected 3D network structure to further improve the electrical conductivity. Meanwhile, the PNDC can supply plentiful active sites and adequate space for gas diffusion and electrolyte impregnation as well as product accommodation, which could avoid blockage of diffusion pathways and coverage of the active sites. Figure 6.11d-f evaluates the cyclability of PNDC and NSDC electrodes at a current density of 200 mA g^{-1} with a fixed specific capacity of 1000 mA h g^{-1}. The NSDC electrode demonstrated unsatisfactory electrochemical performance when used as an air electrode in a Na-O_2 battery. Compared with NSDC, the recharge capacity of the PNDC was greater than 705 mAh g^{-1} at the first cycle, whereas its discharge and charge capacity was still as high as 1000 and 845 mAh g^{-1} for 120 cycles, respectively. Meanwhile, the charge overpotential of the PNDC air electrode at 120 cycles was still as low as 0.31 V, indicating the improved energy efficiency of the Na-O_2 battery based on PNDC cathode as compared to that based on NSDC cathode, as shown in Figure 6.11d. The PNDC electrode thus exhibits better cycling performance with stable discharge and charge capacities values. In comparison, the NSDC electrode only exhibited a recharge capacity of 216 mAh g^{-1} for the first cycle, while its discharge capacity decreased to 878 mAh g^{-1} for 23 cycles. The improved cycling performance of the PNDC air electrode is primarily attributed to its excellent catalytic activity and the utilization of stable nanotubes as supports for the *p* and *n* doping to avoid catalyst aggregation or detachment from the supports during a long cycling period. In addition, the different discharge/charge curves imply that distinct reaction mechanisms with different discharge products may take place on the two electrodes. Generally speaking, the PNDC air electrode exhibits better electrochemical performance, resulting from its highly efficient catalytic activity and the continuous 3D network consisting of 1D nanotubes.

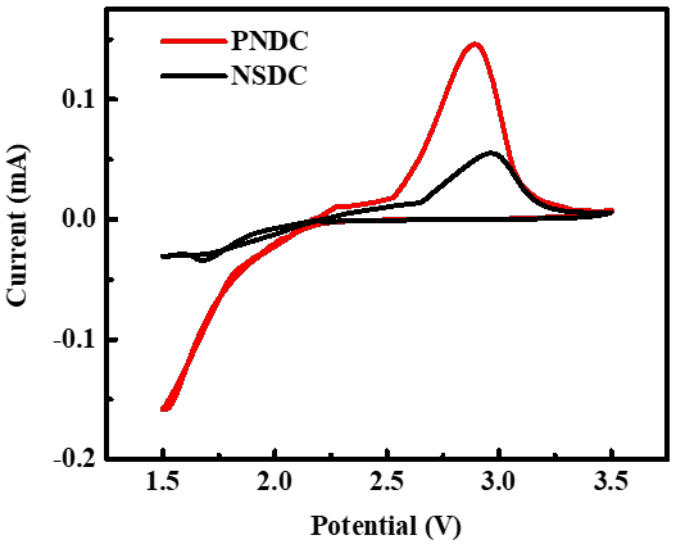

Figure 6.8. Cyclic voltammetry curves of the PNDC and NSDC.

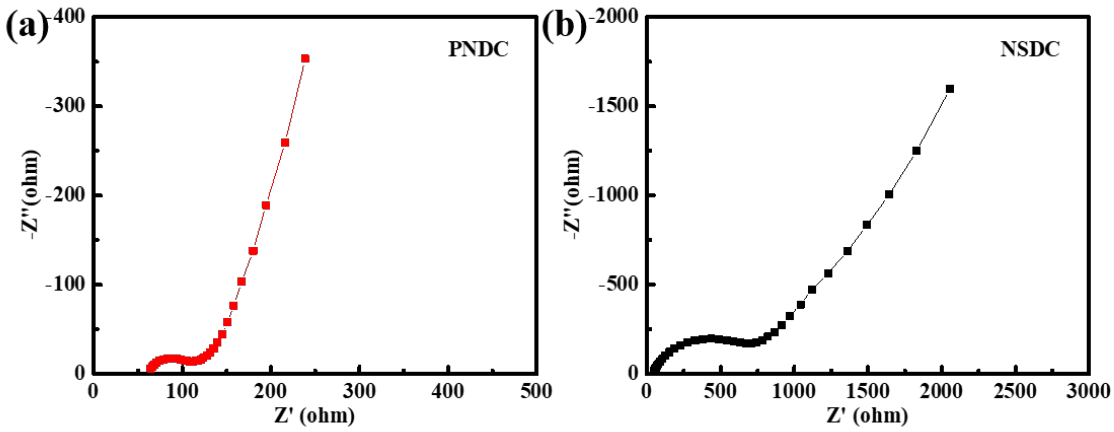

Figure 6.9. (a) Nyquist plot of PNDC, (b) Nyquist plot of NSDC.

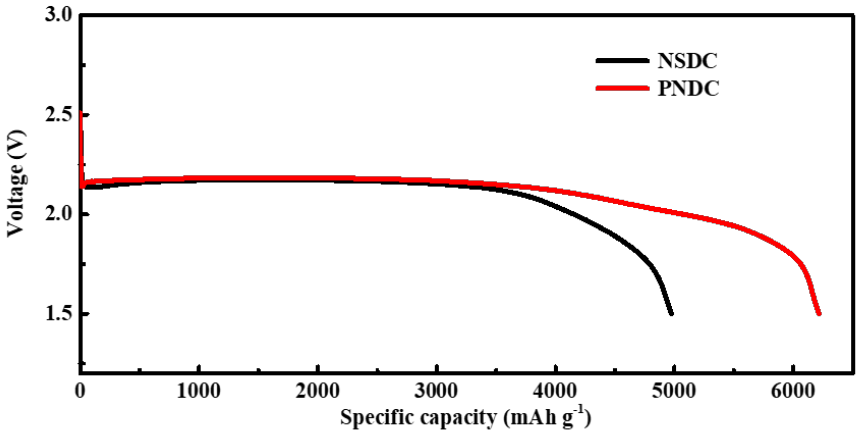

Figure 6.10. Comparison of PNDC and NSDC on full discharge.

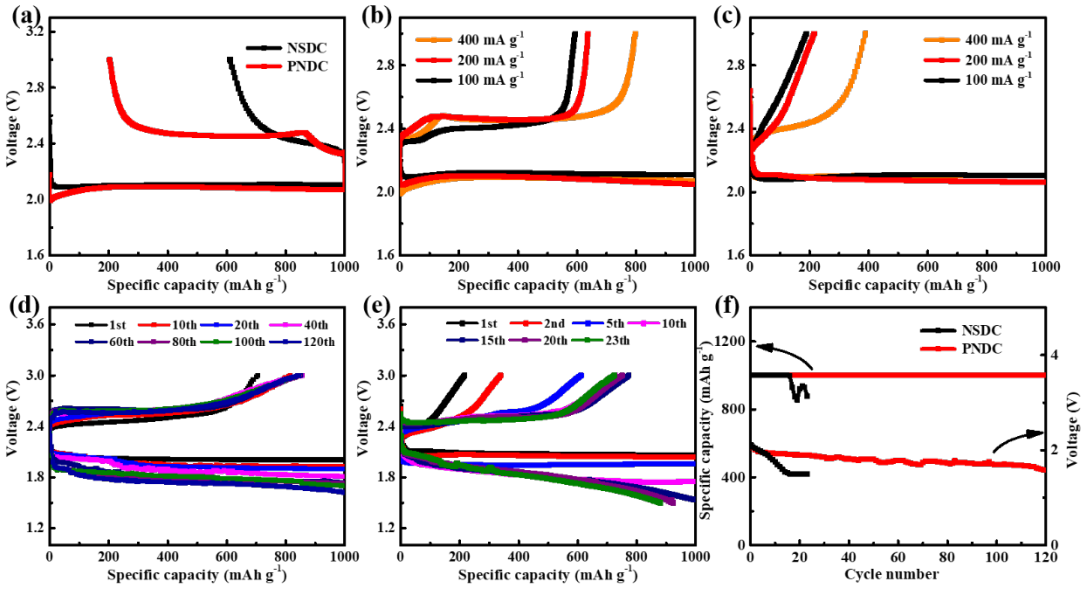

Figure 6.11. Electrochemical performances of the PNDC and NSDC. (a) Comparison of the discharge/charge plots of the PNDC and NSDC cathodes at a current density of 400 mA g^{-1}; (b) discharge/charge curves of the PNDC at different current densities; (c) discharge/charge curves of the NSDC at different current densities; (d) discharge/charge curves of the PNDC for selected cycles at a current density of 200 mA g^{-1} ; (e) discharge/charge curves of the NSDC for selected cycles at a current density of 200 mA g^{-1}; (f) comparison of cycling performance of the PNDC and NSDC electrodes at a current density of 200 mA g^{-1}.

In order to gain an in depth understanding of the reaction mechanism on the PNDC and NSDC electrodes, XRD and SEM were conducted on these electrodes after discharging at 200 mA g^{-1} to 1.5 V. As shown in **Figure 6.12**, the diffraction peaks of the PNDC electrode could be attributed to the crystalline NaO_2, indicating that NaO_2 was formed and well preserved on the PNDC electrode after discharging. For the NSDC electrode, however, the diffraction peaks can be assigned to NaO_2 and $Na_2O_2{\cdot}2H_2O$, implying that part of NaO_2 was transformed to $Na_2O_2{\cdot}2H_2O$ on the NSDC electrode after reacting with humidity (from the electrolyte or gas supply). As the PNDC and NSDC electrodes have quite similar morphology and structure, the diverse compositions of the discharge products on different electrodes could be attributed to the different reaction mechanisms driven by their different reaction activities with different elements doping. As shown in Figure 6.12 b and c, it is clear that an abundance of NaO_2 nanoparticles within the size range of 150-200 nm were formed on the surface of PNDC electrode. A film-like mix of discharge products (NaO_2 and $Na_2O_2{\cdot}2H_2O$) covered the NSDC electrode, however, instead of the nanoparticles (Figure 6.12 d and e). As illustrated in Figure 6.12 f, the PNDC electrodes could show better electrochemical performance not only because NaO_2 exhibits lower overpotential but also because the nanoparticle discharge products could be easily decomposed compared with the film-like discharge products. Therefore, the PNDC electrodes could provide more active sites for the reactions and exhibit better electrochemical performance.

The above results clearly demonstrate that the PNDC possesses excellent electrocatalytic performance for Na-O_2 batteries, which could be attributed to its surface properties and catalytic activities. Through homogeneously doping P and N in the carbon tubal structures of the PNDC, the defects could be reduced than NSDC. Besides, the PNDC exhibits superior catalytic activity with higher anodic and cathodic

peaks current densities compared to the NSDC electrode. Therefore, the PNDC electrode could accelerate the formation and stabilization of NaO_2 discharge product with a quite low charge overpotential, higher coulombic efficiency, and long cycling stability.

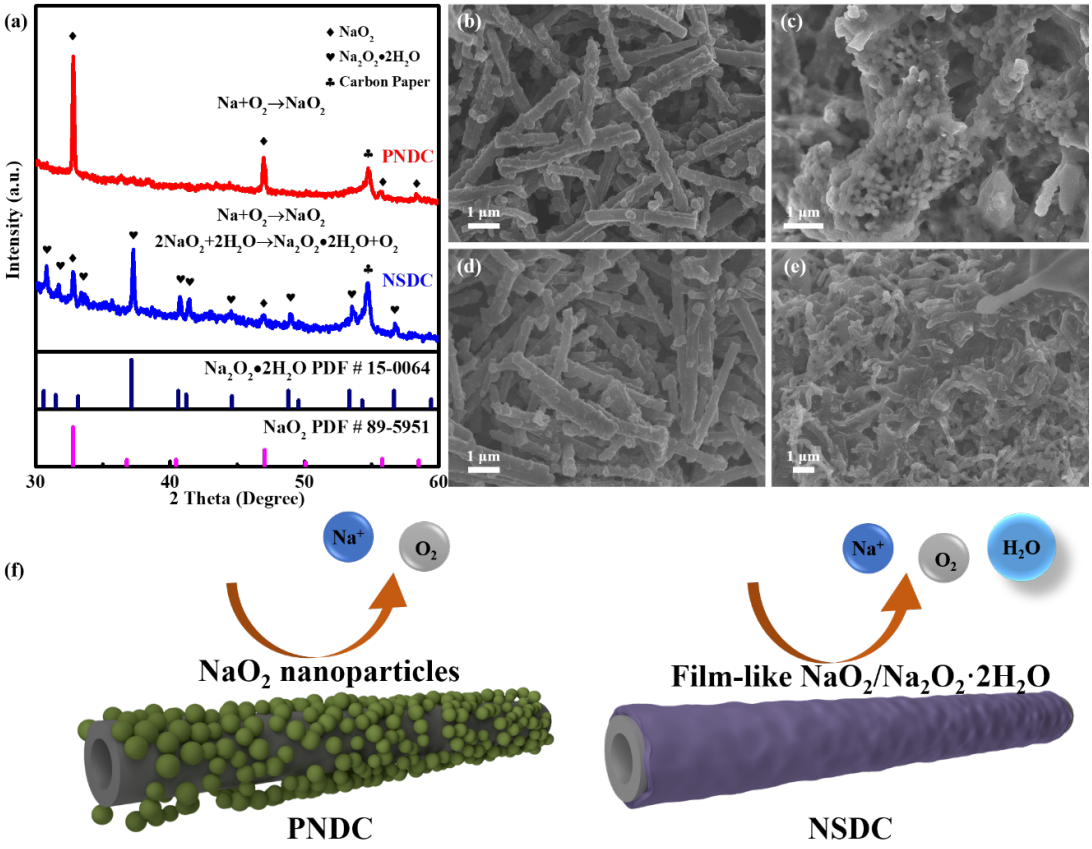

Figure 6.12. Characterization of the discharged electrodes. (a) XRD patterns of the PNDC and NSDC electrodes after discharge; SEM images of (b) the pristine PNDC electrode; (c) the PNDC electrode after discharge; (d) the pristine NSDC electrode; (e) the NSDC electrode after discharge; (f) schematic illustration of the PNDC and NSDC electrodes with different discharge products.

6.4 Summary

In this Chapter, the phosphorus and nitrogen dual-doped carbon (PNDC) and nitrogen solely doped carbon (NSDC) were synthesized and employed as electrocatalysts for the sodium-oxygen battery. Even though they have similar structures and morphology, the PNDC and NSDC electrodes exhibit different electrochemical behavior due to their different surface properties and catalytic activities. The PNDC electrode could facilitate the formation and stabilization of NaO_2 nanoparticles as discharge product with a quite low charge overpotential (0.18 V) and long cycling stability for 120 cycles. The NSDC electrode, however, is inclined to forming a mixture of film-like NaO_2 and $Na_2O_2 \cdot 2H_2O$ discharge products on the electrode surface with poor cycling stability for only 23 cycles. In addition, the NaO_2 nanoparticles deposited on the PNDC electrode could be easily decomposed when compared with the film-like discharge products formed on the surface of NSDC electrode. Therefore, the electrochemical performance of Na-O_2 batteries could be modulated by using different electrocatalysts with different reaction activities, leading to different reaction mechanisms with different discharge products and electrochemical performances.

Chapter 7 Ultrathin and Edge-Enriched Holey Nitride Nanosheets as Efficient Electrocatalysts for Sodium-Oxygen Batteries

7.1 Introduction

Ultrathin two-dimensional (2D) holey nanostructures have drawn significant research attention for energy storage, catalysis, electronics, and biomedical science because their unique feature could provide unprecedented chemical, electronic, and physical properties resulting from the electron confinement in two dimensions.[267-272] Due to their huge lateral surface area and atomic thickness, this special feature allows for direct correlation between the properties and the structure, giving superior atomic transport. They are frequently used as a bridge between microscale and nanoscale features to realize the fabrication of future microscale devices.[273-277] In contrast to the intact lateral surface, the holes on the lateral surface will result in ultrahigh specific surface area and a continuously connected integrated network, while maintaining atomic thickness, because the reaction intermediates can easily be transferred and diffuse throughout the whole porous system, not only along the large lateral surface direction, but also through holes on the surface, which can be considered as channels among numerous nanosheets.[241, 278-283] 2D holey nanosheets have inherent advantages for surface-related applications such as catalysis. For example, owing to the complete exposure of the large lateral surface atoms and the much greater number of catalytic active atoms in the hole area, it will dramatically accelerate the reaction kinetics, which would be much more favorable for achieving outstanding electrocatalytic performance towards the oxygen evolution reaction (OER).[274, 284] Meanwhile, this ultrathin holey 2D structure also presents excellent properties through accelerating the diffusion of the

evaluated gases and electrolyte accessibility.[268, 285] Moreover, because of the excellent mechanical strength from the strong in-plane covalent bonds, this 2D porous nanostructured catalyst can also alleviate or even solve many of physical issues regarding state-of-the-art nanoparticle catalysts, such as aggregation or peeling off during the reaction, resulting in significant descent of the electrocatalytic performance.[273, 286-291] A number of 2D structured materials are employed as catalysts to facilitate the sluggish evolution reaction kinetics, for example precious metals, metal hydroxides/oxides, and metal sulfides.[287, 292-303] Among these, transition metal nitrides have the inherent advantages of high catalytic activity, economic efficiency, and superior electrical conductivity due to the introduction of nitrogen atoms into the metal hosts, which exhibit a metallic state with continuous conductivity near the Fermi level according to the computer calculations.[297, 304-308]

Among various types of metal-oxygen batteries, sodium-oxygen batteries (Na-O_2 batteries) have been considered as the most promising energy storage devices due to their low charge overpotential and high energy density.[75, 246] However, it is still a big challenge to decrease the charge overpotential, which could affect the electrochemical performance of the batteries.[85, 86, 309, 310] Because the recharge performance of the Na-O_2 batteries mainly relays on the OER activity of the air cathode electrode materials, it is highly desirable to develop good electrocatalysts with excellent OER activity as air cathode for Na-O_2 batteries.

Therefore, in this Chapter, a strategy is proposed to develop ultrathin 2D holey structured bimetallic nitride materials with a strong high-orientation crystalline texture. A series of ultrathin 2D holey nickel-based nitrides (Ni_3M nitride, M = Fe, Co, Mn) has been designed and successfully synthesized, with a satisfactory specific surface

area (189.6 m^2 g^{-1}), maintaining 0.6-0.8 nm nanosheet thickness. The hierarchical porous continuously conductive architecture caused by the holey nitride nanosheets is much more beneficial to transport of reaction intermediates and gas diffusion throughout the entire electrode. The faster electron transportation along the ultrathin 2D direction can be further enhanced by their nearly single-crystalline structure, while the superior electrocatalytic performance could be ascribed to the highly exposed atoms on the large lateral surfaces, resulting from the vast surface area and plentiful exposed catalytically active atoms or lattice planes in the hole area. Furthermore, the influence of lattice spacing on the catalytic activities was investigated by comparing three different nickel-based nitrides which have different lattice spacing after introducing nitrogen. These ultrathin 2D holey nickel-based nitrides were also evaluated as air cathode materials for Na-O_2 batteries.

7.2 Experimental Section

Synthesis of Ni_3Fe-LDH: The Ni_3Fe-LDH nanosheets were synthesized based on previous procedures.[311] In general, $Fe(NO_3)_3 \cdot 9H_2O$ (140 mg) and $NiCl_2$ (188 mg) were dispersed into deionized (DI) water (80 mL) under severely stirring for 10 min, followed by adding urea (168 mg) and $Na_3C_6H_5O_7$ (5.16 mg). After another 10 min, the reaction proceeded for 24 h with a Teflon-lined autoclave under 150 ˚C. The Ni_3Fe-LDH was obtained after washing three times by ethanol and DI water.

Synthesis of Ni_3Co-LDH: The Ni_3Co-LDH nanosheets were fabricated based on previous procedures.[312] In general, $Ni(NO_3)_2 \cdot 6H_2O$ (727 mg), $CO(NH_2)_2$ (2.25 g), and $Co(NO_3)_2 \cdot 6H_2O$ (1153 mg) were dispersed into DI water to form a mixture (50 mL) with a volume ratio of $V_{(ethylene\ glycol)}/V_{(DI\ water)}$ = 3:1. After refluxing 3 h under 90 ˚C,

the product was collected after washing three times by ethanol and DI water.

Synthesis of Ni_3Mn-LDH: The Ni_3Mn-LDH nanosheets were synthesized with previous procedures.[313] In general, $Ni(NO_3)_2 \cdot 6H_2O$ (245 mg), $NaNO_3$ (153 mg), NH_4F (185 mg), and $Mn(NO_3)_2 \cdot 4H_2O$ (50 mg) were added into DI water (250 mL) under severely stirring with N_2 atmosphere. After 30 min, H_2O_2 (30 wt. %, 25 μL) was added dropwise into the solution. NaOH solution (50 mL, 0.12 M) was then dispersed dropwise into the solution. After stirring 12 h under room temperature, the product was collected after washing three times by ethanol and DI water.

Synthesis of holey 2D nitride nanosheets. To synthesize holey 2D Ni_3Fe nitride, Ni_3Co nitride, and Ni_3Mn nitride nanosheets, Ni_3Fe LDH, Ni_3Co LDH, and Ni_3Mn LDH nanosheets were calcined 1 min at NH_3 atmosphere at 500 ˚C (ramp rate about 10 ℃ min^{-1}).

Materials characterizations: The crystalline structures were analyzed with GBC MMA powder X-ray diffraction. As for the morphologies, JEOL JSM-7500FA scanning electron microscopy and JEM-ARM200F transmission electron microscopy were utilized. Atomic force microscopy was from Asylum AFM facility. The specific surface areas were investigated through Quantachrome Instruments Autosorb iQ2 through N_2 adsorption at -196 °C with Brunauer-Emmett-Teller (BET) method. The vacuum pressure was kept under 10^{-4} Pa to degas the samples at 100 °C. The mean value was calculated after obtaining three measurements for each sample.

Electrochemical measurements: A three-electrode glasscell with an Ag/AgCl reference electrode and a graphite rod counter electrode on Princeton 2273 and 616

workstations were employed to test electrochemical performance.[314] In order to make the catalyst inks, sample (5 mg) was added in mixed solution (1100 μL) with 5 % Nafion® solution (100 μL), isopropanol (250 μL), and DI water (750 μL). The working electrodes were obtained through dripping the catalyst ink (5 μL) on the pre-polished glassy carbon disk electrodes and drying for 20 min at 80 °C oven. Linear sweep voltammetry were performed use 1 M KOH. Electrochemical impedance spectroscopy tests were conducted at 0.607 V. To determine the active surface areas, electrochemical double-layer capacitance measurements was performed between 0.2 and 0.3 V at various scan rates. All potentials were referenced to reversible hydrogen electrode (RHE) with the following calculation: $E_{RHE} = 0.059\ pH + 0.197 + E_{Ag/AgCl}$.

Electrochemical Measurements of Na-O_2 Batteries: The electrochemical properties were measured using CR2032-type coin cells with holes in the cathode part. To prepare the oxygen cathodes, the active materials, super P, and poly(tetrafluoroethylene) solution were mixed in the ratio of 8:1:1 in isopropyl alcohol as catalyst slurry. The slurry was then pasted onto carbon paper and dried in a vacuum oven at 120 °C for 12 h. The typical loading of cathode active materials was 0.3 mg cm^{-2}. Tetraethylene glycol dimethyl ether (TEGDME) solvent was purified by rotary evaporation and stored with 4 Å activated molecular sieves for two weeks before use. Sodium trifluoromethanesulfonate (sodium triflate, $NaSO_3CF_3$) was dried at 120 °C for 24 h under vacuum. The electrolyte, consisting of 0.5 m sodium triflate in TEGDME, was prepared in an argon-filled glovebox. The cells were assembled in an argon-filled MBRAUN glove box (H_2O level < 0.1 ppm and O_2 level < 0.1 ppm). A pieces of sodium cut from a sodium cube served as the anode, and glass microfiber was used as the separator. All the measurements were carried out on Neware battery testers at room temperature in dry oxygen atmosphere with our designed facility.

7.3 Results and Discussion

7.3.1 Structure and morphology

The synthesis strategy for the ultrathin 2D holey nitride materials is illustrated in **Figure 7.1a**. The morphology and structure are characterized with scanning electron microscopy (SEM) and X-ray diffraction (XRD). A series of nickel-based layered double hydroxide (LDH) nanosheets were synthesized as precursors, including Ni_3Fe LDH, Ni_3Co LDH, and Ni_3Mn LDH, as illustrated in transmission electron microscopy (TEM) images (**Figure 7.2a**, **d**, and **g)**. All the LDH samples showed a uniform, silk-like, 2D nanosheet structure with big lateral size about several micrometers. In the following nitridation by annealing in an NH_3 atmosphere, the corresponding nitride products were obtained with numerous holes on the in-plane surface, as revealed in Figure 7.1(b, c, d) and Figure 7.2(b, e, h), but the products still maintained the 2D nanosheet structure. All the nitride materials exhibit a standard cubic diffraction pattern corresponding to (111), (200), and (220) planes as shown in Figure 7.1(e, f).[297, 298, 305] The distances of corresponding lattice spacing of Ni_3Fe nitride is much larger than those of Ni_3Co nitride and Ni_3Mn nitride, which could modify the distance of surface atoms with varying the surface electronic structure and catalytic activity.[315, 316] As can be seen from **Figure 7.3**, compared with metallic state samples, the peaks of three samples have been shifted to the left after introducing nitrogen, indicating that the nitrogen could increase the lattice spacing of the metallic state materials. The peak shifts of Ni_3Fe is much larger than the Ni_3Co and Ni_3Mn as well, implying that the lattice spacing of Ni_3Fe nitride is significantly increased after the induction of nitrogen. The morphology of the nitride materials is much more uniform than that of the oxide

materials, indicating that the nitrogen also could assist the form of uniform nanopores on the nanosheets, as can be seen from **Figure 7.4**.

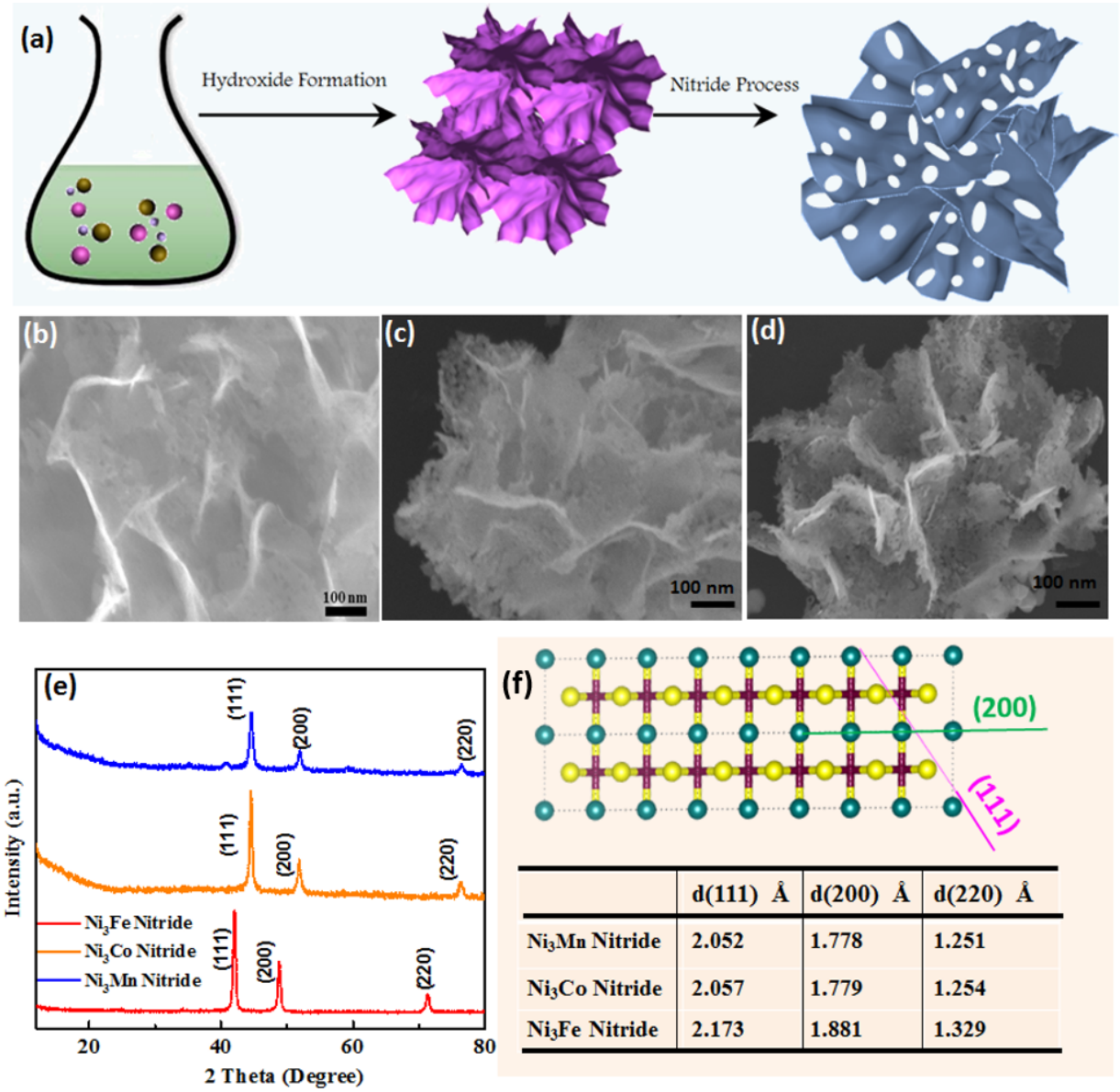

	d(111) Å	d(200) Å	d(220) Å
Ni_3Mn Nitride	2.052	1.778	1.251
Ni_3Co Nitride	2.057	1.779	1.254
Ni_3Fe Nitride	2.173	1.881	1.329

Figure 7.1. (a) Fabrication process of 2D holey Ni_3M nitride; SEM images of (b) 2D holey Ni_3Fe nitride; (c) 2D holey Ni_3Co nitride; (d) 2D holey Ni_3Mn nitride; (e) XRD pattern and (f) the corresponding distance of lattice plate.

The variations of the surface area and pore size range before and after nitridation process were further characterized, as shown in Figure 7.2. Taking Ni_3Fe nitride for

example, after the nitridation process, the specific surface area was dramatically enlarged from 114.9 to 189.6 m^2 g^{-1}, while numerous nanopores were generated, with the process primarily driven by the phase transformation and Kirkendall effect.[241, 279, 317] Meanwhile, the specific surface area of Ni_3Co nitride, and Ni_3Mn nitride were dramatically increased from 125.6 to 197.2, and from 108.5 to 168.3m^2 g^{-1}, respectively. Compared to those deposited on porous substrate, such as nickel foam, a remarkable enhancement of specific surface area was got because the high weight ratio of the substrate will decrease the whole electrode specific surface area to some extent.[318, 319] It is concluded that designed ultrathin holey 2D structured nitrides can be successfully obtained by annealing the corresponding LDH precursors, and the surface area can be dramatically increased by the generation of numerous holes on the large lateral surface.

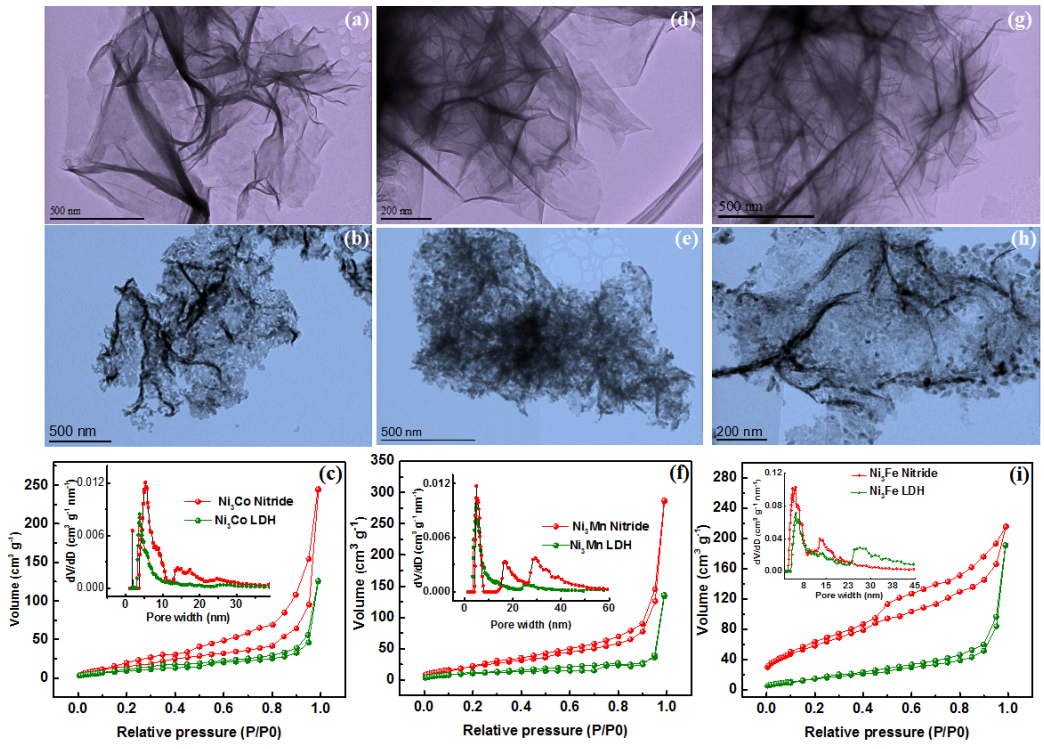

Figure 7.2. TEM images of 2D holey Ni_3M (M = Co, Mn, Fe) LDH nanosheets; 2D holey Ni_3M (M = Co, Mn, Fe) nitride nanosheets and Specific surface area of 2D Ni_3M (M = Co, Mn, Fe) LDH nanosheets and 2D holey Ni_3M nitride nanosheets (c); inset: pore size distributions; (a - c) M = Co; (d - f) M = Mn; (g - i) M = Fe.

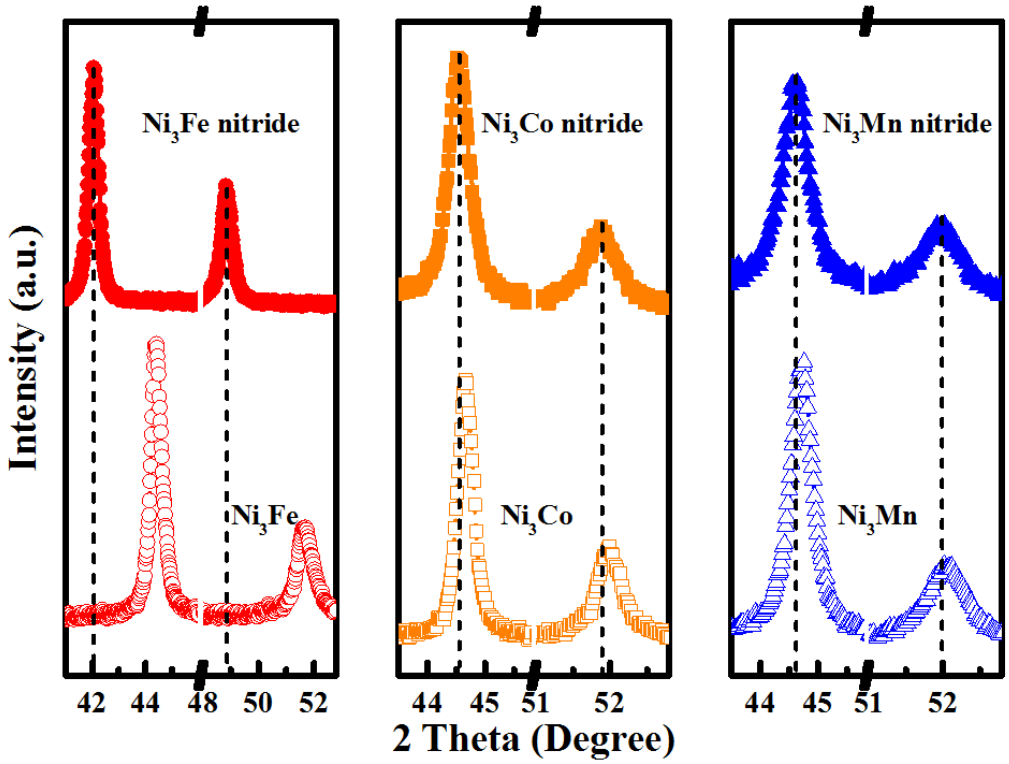

Figure 7.3. XRD comparison of nitride materials with metallic materials.

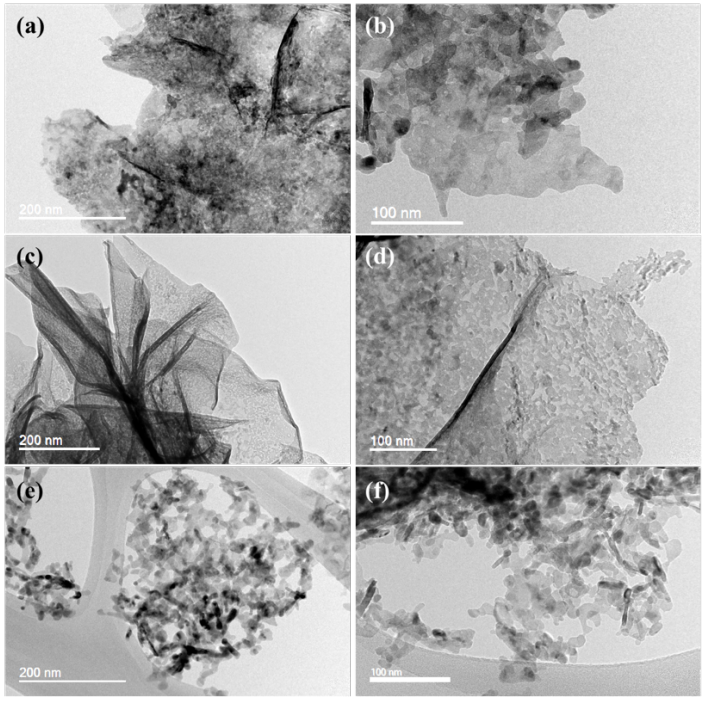

Figure 7.4. TEM images of (a), (b) 2D Ni_3Fe oxide nanosheets; (c), (d) 2D Ni_3Co oxide nanosheets; (e), (f) 2D Ni_3Mn oxide nanosheets.

Morphological characterization of the as-fabricated materials was studied by scanning TEM energy-dispersive X-ray spectroscopy (STEM-EDS) and atomic force microscopy (AFM), as shown in **Figure 7.5**, **Figure 7.6**, and **Figures 7.7**. Compatible with the conclusions on the surface area and pore distribution, nitride materials present an obvious holey structure with pore size ~ 15 nm. Meanwhile, all the elements demonstrate a homogenous distribution over the whole area and maintain similar molar ratios (**Figure 7.8** and **Table 7.1)**. Furthermore, after the nitridation process, a solo phase component distribution still exists, which is compatible with the XRD. The AFM was employed to estimate the thickness and surface structure of the as-synthesized 2D holey Ni_3Fe nitride nanosheets. As revealed in Figure 7.5g-j, the thickness of 2D holey Ni_3Fe nitride nanosheets is within the range of 0.6-0.8 nm, a thickness of approximately 3 atomic layers of (001) lattice planes. The trend in the curves also indicates the holey structure on the lateral 2D surfaces. High-angle annular dark-field STEM (HAADF-STEM) was utilized to characterize the structure of the ultrathin nitride nanosheets. As indicated in Figure 7.5k, l and **Figures 7.9** and **Figure 7.10**, in contrast to the intact surfaces, these holey nanosheets generate numerous edge areas and expose abundant lattice plates, which can thereby provide abundant catalytically active sites. More importantly, the ultrathin nanosheets show a nearly single-crystal structure with a strong high-orientation pattern, which can significantly increase the electrical conductivity. It is well acknowledged that there is a definite link between electrical conductivity and catalytic activity. High electrical conductivity can dramatically accelerate the kinetic rate of the catalytic reaction.[244, 304, 311] Generally, the integration of the huge surface area, abundant defects the exposed catalytic sites near the edges, and the ultrahigh electrical conductivity resulting from the nearly single-crystal structure, as well as the connected holey architecture will make this type of nitride

nanosheet a satisfactory electrocatalyst, particularly for gas generation processes.

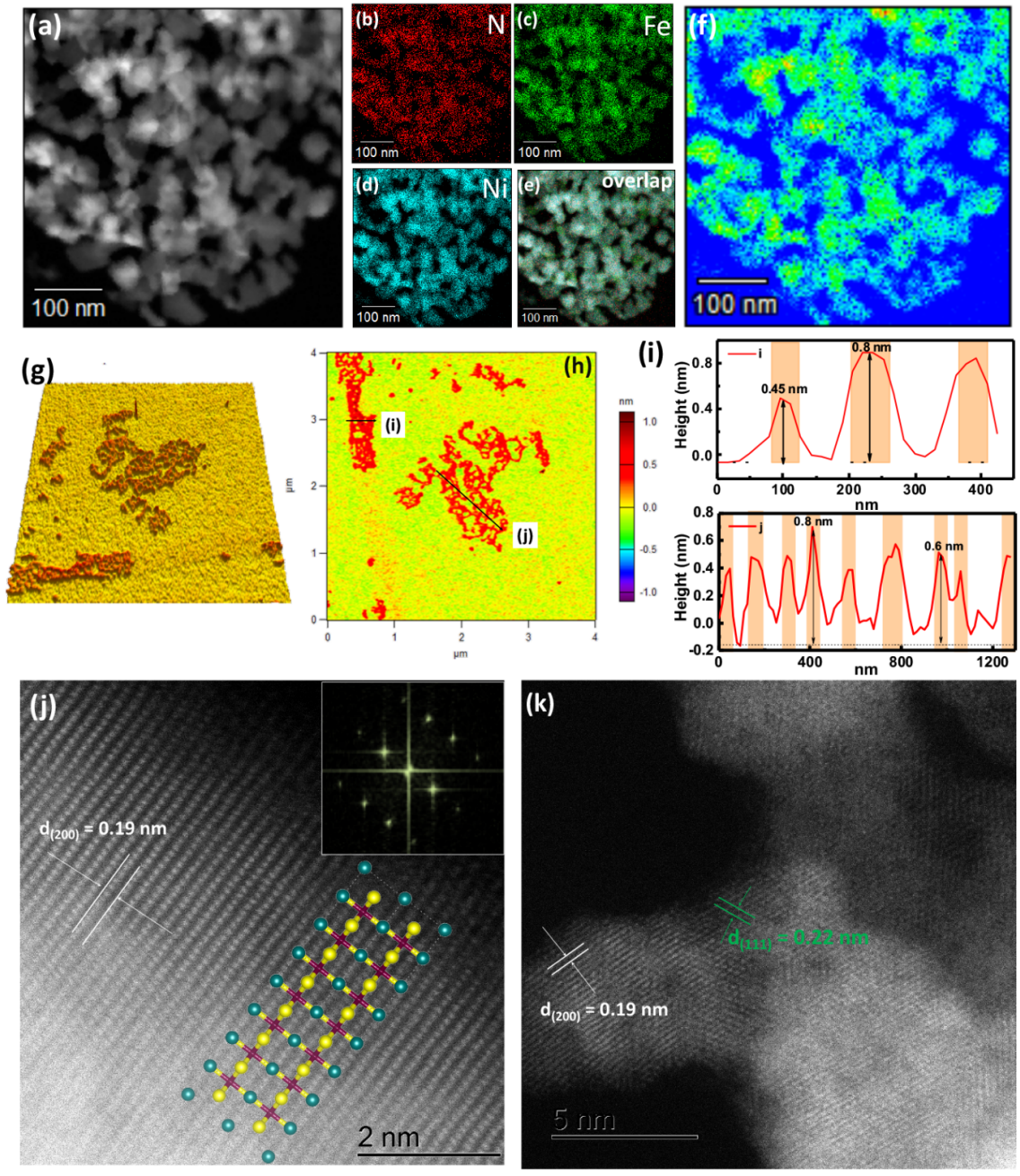

Figure 7.5. (a) HAADF-STEM image of holey Ni_3Fe nitride nanosheets; (b-e) STEM-EDS mapping of (a); (f) the phase distribution in (a); (g-j) AFM results for the holey Ni_3Fe nitride nanosheets; (k, l) HAADF-STEM images of holey Ni_3Fe nitride nanosheets; molecular diagram with fast Fourier transform (FFT) pattern as inset image in (k).

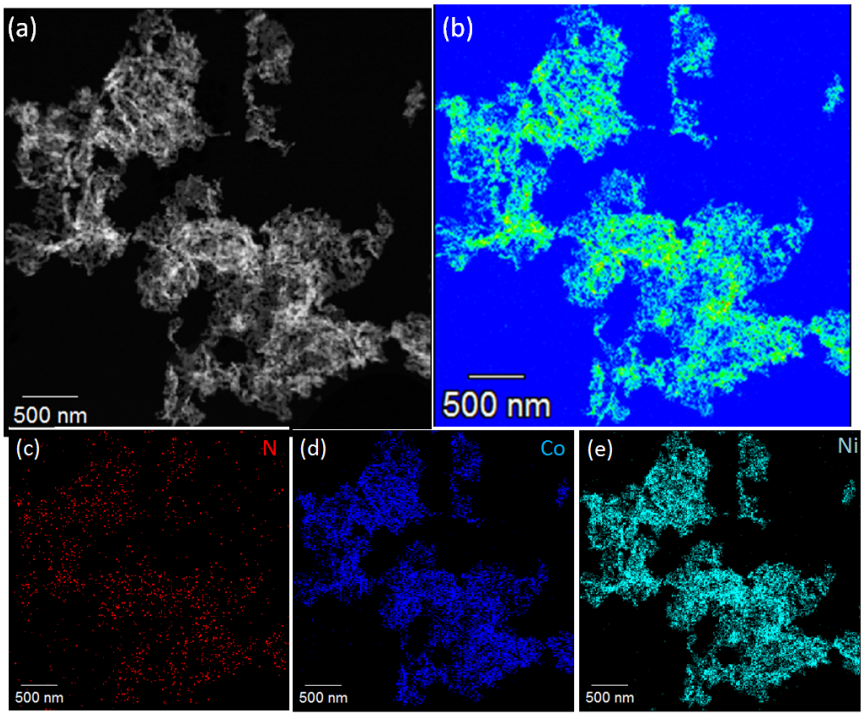

Figure 7.6. (a) HAADF-STEM image of holey 2D Ni_3Co nitride nanosheets; (b) the corresponding phase distribution; (c) N, (d) Co, and (e) Ni element distribution.

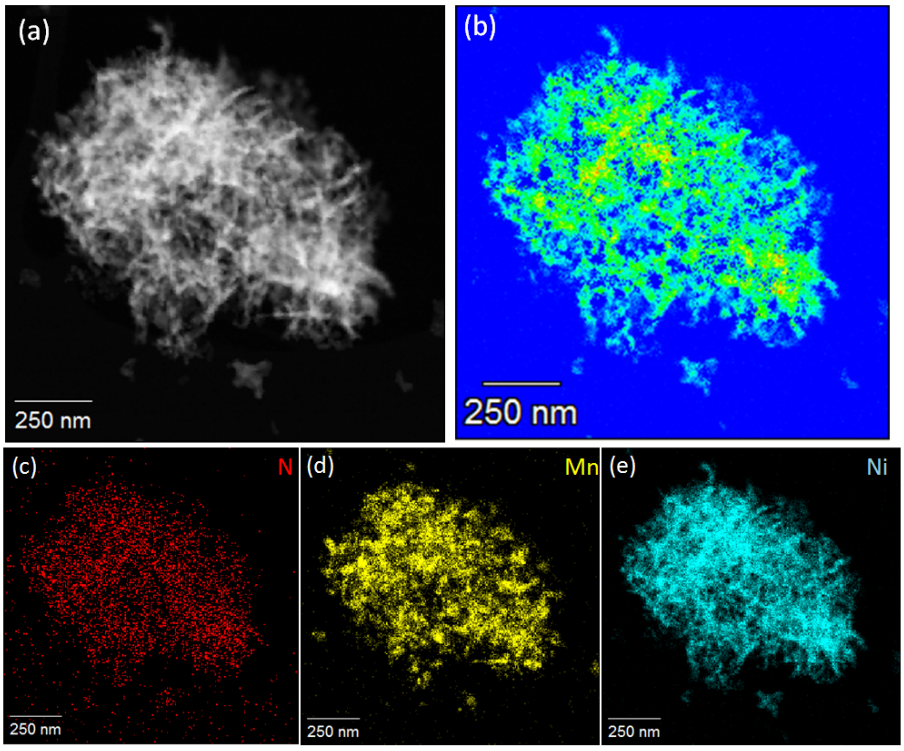

Figure 7.7. (a) HAADF-STEM image of holey 2D Ni_3Mn nitride nanosheets; (b) the corresponding phase distribution; (c) N, (d) Mn, and (e) Ni element distribution.

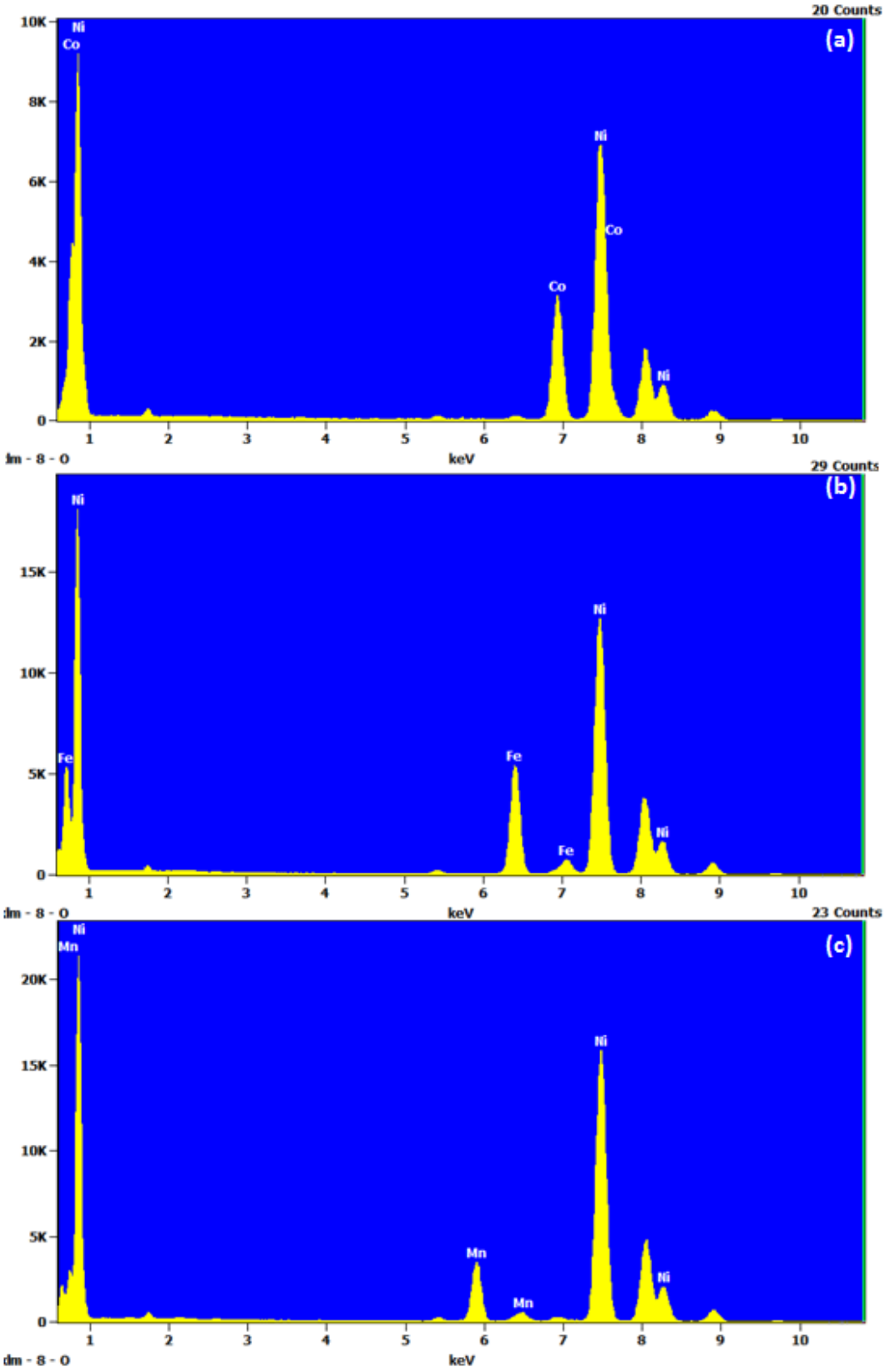

Figure 7.8. EDS spectra of (a) holey 2D Ni_3Co nitride nanosheets; (b) holey 2D Ni_3Fe nitride nanosheets; (c) holey 2D Ni_3Mn nitride nanosheets.

Table 7.1. The elements contents before and after nitridation treatment.

	Before (Atom %)		After (Atom %)		
Ni_3Fe	Ni (70.34)	Fe (29.66)	Ni (61.28)	Fe (21.43)	N (17.29)
Ni_3Co	Ni (68.72)	Co (31.28)	Ni (57.49)	Co (23.16)	N (19.35)
Ni_3Mn	Ni (72.15)	Mn (27.85)	Ni (61.12)	Mn (18.66)	N (20.22)

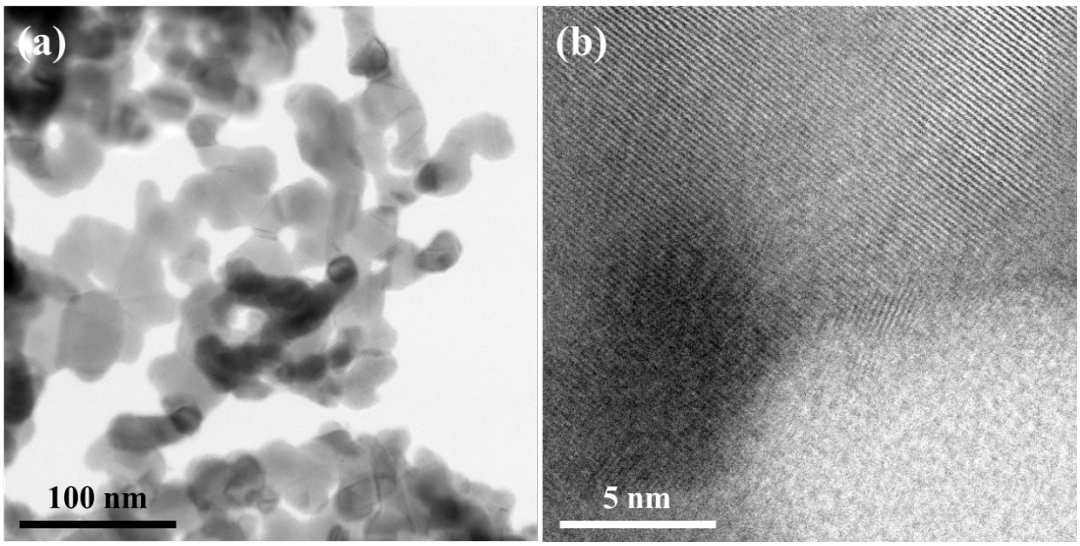

Figure 7.9. (a)TEM and (b) HAADF-STEM images of holey 2D Ni_3Co nitride nanosheets.

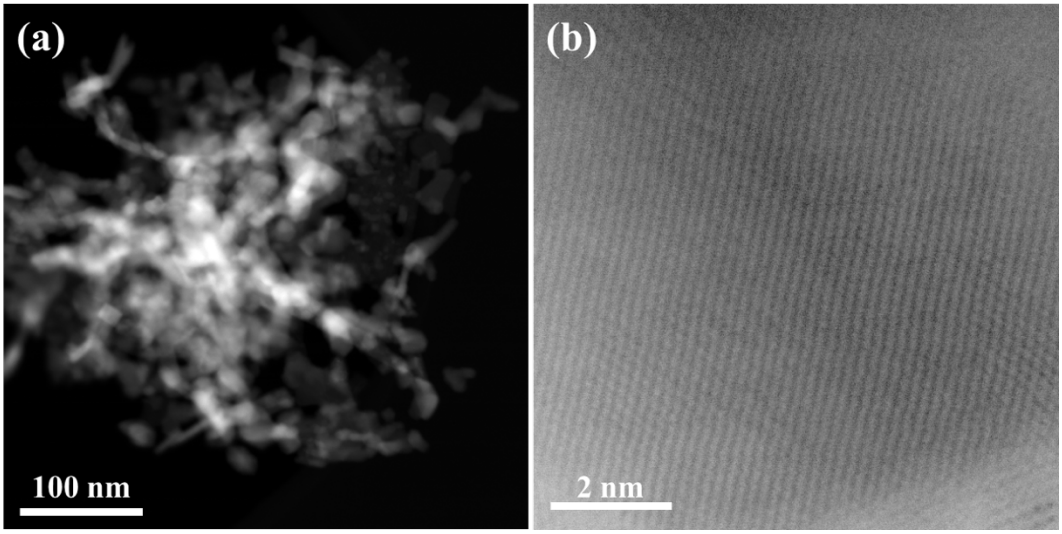

Figure 7.10. (a)TEM and (b) HAADF-STEM images of holey 2D Ni_3Mn nitride nanosheets.

7.3.2 Electrochemical characterizaiton

A rotating disk electrode (RDE) was utilized to explore the electrocatalytic properties of these 2D structured materials, including LDH and holey nitride nanosheets and commercial IrO_2 with 1.0 M KOH. Commercial IrO_2 was purchased from Sigma. The OER curves were investigated to determine each sample's OER catalytic activity based on mass-normalized current density (**Figure 7.11-15**). It is obvious that the 2D holey Ni_3Fe nitride nanosheets exhibit the highest current density compared with Ni_3Co nitride, Ni_3Mn nitride, and IrO_2. A quite small overpotential (300 mV) is required for the 2D holey Ni_3Fe nitride nanosheets to deliver the current density about 100 A g^{-1}, which is smaller than those of 2D holey Ni_3Co nitride nanosheets (340 mV), 2D holey Ni_3Mn nitride nanosheets (429 mV), and IrO_2 (465 mV). The small peak at 1.46 V of the Ni_3Fe nitride could be ascribed to the redox reaction of $Ni^{2+}/Ni^{3+}/Ni^{4+}$.[320] The 2D nickel-based LDH and 2D nickel-based oxides nanosheets were also investigated for comparison (**Figure 7.12 and Figure 7.13**). To generate 100 A g^{-1}, 2D Ni_3Fe LDH nanosheets, 2D Ni_3Co LDH nanosheets, and 2D Ni_3Mn LDH nanosheets required the overpotential of 413, 430, and 423 mV, respectively. Meanwhile, 2D Ni_3Fe oxide nanosheets, 2D Ni_3Co oxide nanosheets, and 2D Ni_3Mn oxide nanosheets required the overpotential of 357, 369, and 386 mV, respectively. It is clear that those 2D Ni_3M LDH nanosheet composites have higher overpotentials than their corresponding holey 2D nickel-based nitride nanosheet counterparts, which can be attributed to the excellent electrical conductivity, the architecture, and the numerous highly catalytically active sites. As revealed in Figure 7.11b and c, the excellent OER activities of the 2D holey Ni_3Fe nitride nanosheets were further confirmed by using Tafel plots and overpotential. The 2D porous Ni_3Fe nitride nanosheets has the smallest Tafel slope (51 mV dec^{-1}),

indicating more enhanced OER kinetic activity for the holey 2D Ni_3Fe nitride electrode when comparing with Ni_3Co nitride (55 mV dec^{-1}), Ni_3Mn nitride (64 mV dec^{-1}), and IrO_2 (69 mV dec^{-1}). As revealed in Figure 7.11d, the holey 2D Ni_3M nitride nanosheets exhibit huge activity enhancements over the commercial IrO_2, which could be due to excellent conductivity of the Ni_3M nitrides and the holey nanosheets structure. In particular, the holey 2D Ni_3Fe nitride nanosheets reveals the highest performance compared with IrO_2. With overpotential of 300 mV, the 2D porous Ni_3Fe nitride nanosheet sample shows an improvement over IrO_2 by a factor of nearly 25 times. Moreover, we investigated the long-term electrocatalytic stability of these 2D holey Ni_3M nitride nanosheets with high current density (100 A g^{-1}), as revealed in Figure 7.11e. Obviously, the holey 2D Ni_3Fe nitride nanosheet electrode requires the lowest overpotential compared to the holey 2D Ni_3Co nitride nanosheets and holey 2D Ni_3Mn nitride nanosheets, indicating its excellent stability and electrocatalytic activity. The excellent OER activities of the holey 2D Ni_3Fe nitride nanosheets could be ascribed to its excellent electrical conductivity and the numerous catalytically active sites provided by the newly formed in-plane nanopores. Moreover, the metallic nitride products exhibit excellent electrical conductivity (Figure 7.11f, **Figure 7.14**, and **Table 7.2)**, resulting from their metallic properties, highly-orientated crystalline texture, and large lattice spacing, which is also superior to those of reported nitride and other types of materials, such as sulfides, oxides and phosphates, primarily resulting from the highly orientated crystal structure.[293, 297, 304] In addition, the highest conductivity of Ni_3Fe nitride could be attributed to its larger crystal lattice, which could significantly facilitate the electron transport and leading to excellent conductivity.

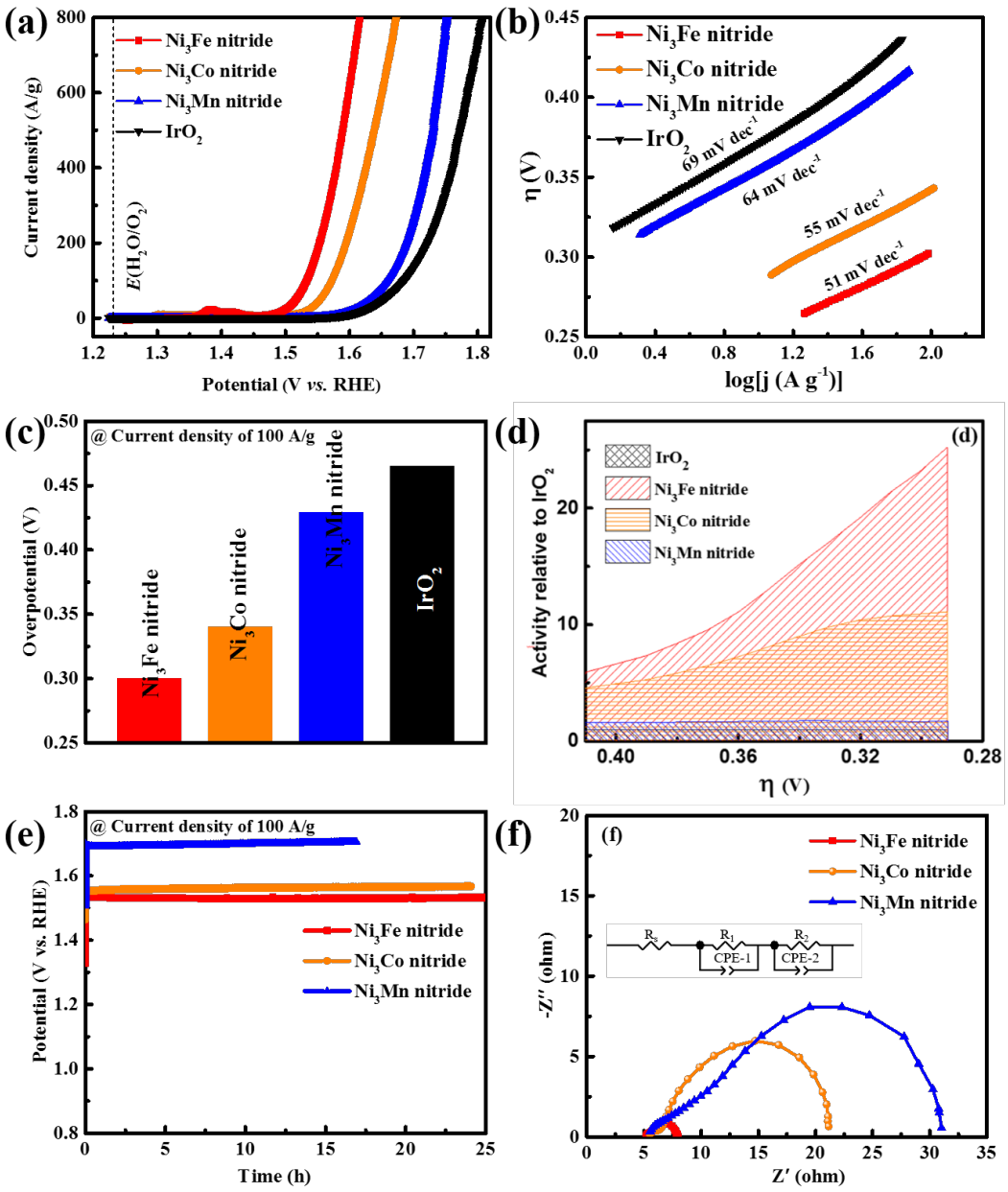

Figure 7.11. (a) Linear sweep voltammetrys (LSVs) of 2D holey Ni_3M Nitride nanosheets and IrO_2 with for the OER based on mass-normalized current density (scan rate of 10 mV s^{-1}); (b) Tafel plots of 2D holey Ni_3M Nitride nanosheets and IrO_2; (c) The overpotential required to realize the current density of 100 A g^{-1}; (d) Corresponding activity enhancement of 2D holey Ni_3M Nitride nanosheets relative to IrO_2; (e) Stability curves of the 2D porous Ni_3M nitride nanosheets; (f) Electrochemical impedance spectroscopy (EIS) curves of holey Ni_3M nitride nanosheets, the equivalent circuit diagram as inset. RHE: reversible hydrogen electrode.

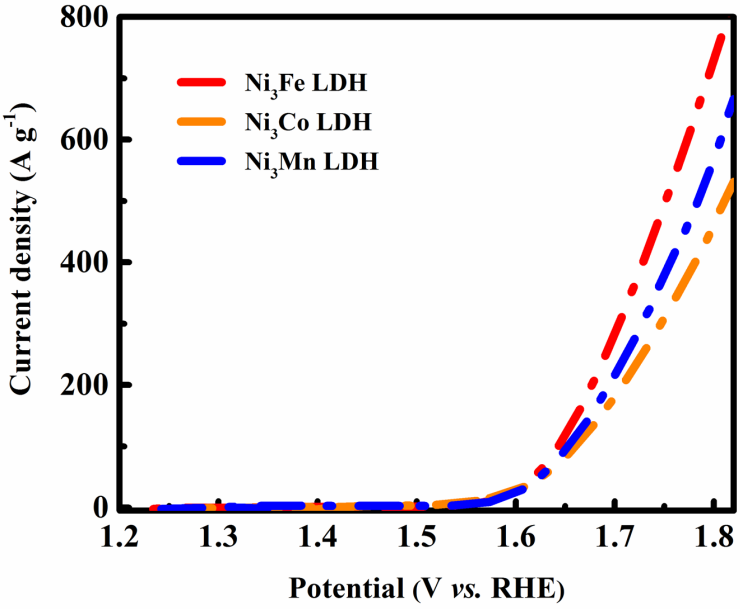

Figure 7.12. Linear sweep voltammetry (LSV) curves of the 2D Ni_3Fe LDH, Ni_3Co LDH, and Ni_3Mn LDH nanosheets based on mass-normalized current density. RHE: reversible hydrogen electrode.

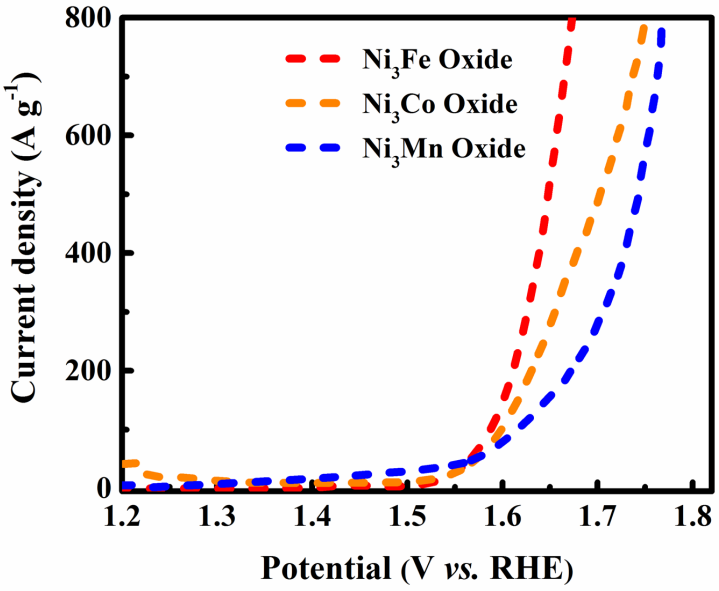

Figure 7.13. Linear sweep voltammetry (LSV) curves of the 2D Ni_3Fe oxide, Ni_3Co oxide, and Ni_3Mn oxide nanosheets based on mass-normalized current density. RHE: reversible hydrogen electrode.

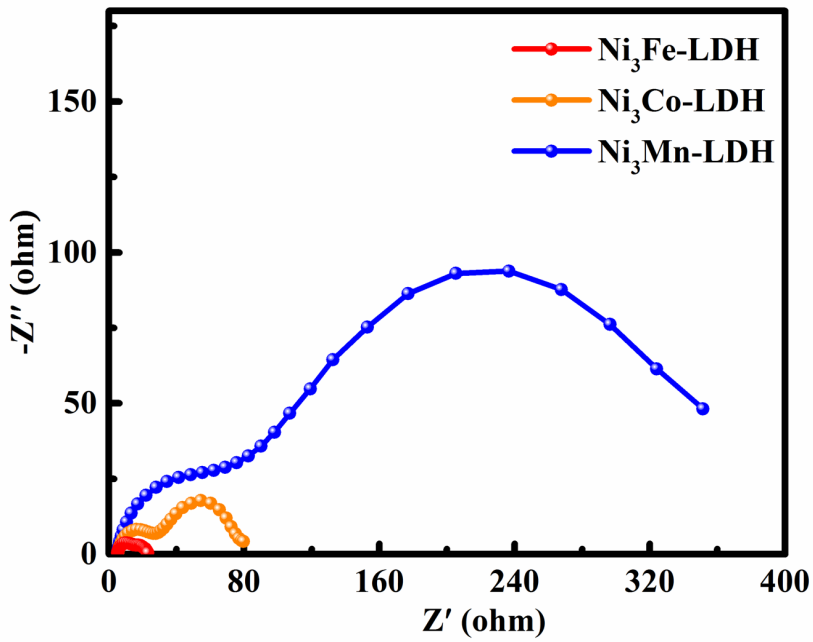

Figure 7.14. EIS curves of the 2D Ni_3Fe LDH, Ni_3Co LDH, and Ni_3Mn LDH nanosheets.

Table 7.2. The fitting results for Ni_3Fe, Ni_3Co, and Ni_3Mn nitride. Rs is the electrolyte transfer resistance. R1 and R2 are the electron transfer resistance. CPE-1 and CPE-2 are the constant phase element, which also represents the double layer capacitance.

	Rs (Ω cm^{-2})	R1 (Ω cm^{-2})	R2 (Ω cm^{-2})	CPE1-T (F cm^{-2})	CPE1-P	CPE2-T (F cm^{-2})	CPE2-P
Ni_3Fe nitride	5.15	0.56	2.30	0.0020	0.63	0.0023	0.73
Ni_3Co nitride	5.252	2.027	14.6	0.0035	0.49	0.0019	0.85
Ni_3Mn nitride	5.033	5.96	20.12	0.0022	0.56	0.0045	0.82

It is well known that there is a definite link between catalytic performance and active surface area, therefore, the electrochemical surface area (ECSA) was calculated through the corresponding electrochemical double-layer capacitance (C_{dl}) to demonstrate the advantages of the 2D holey nanosheets structure in determining the catalytic activity.[321-324] The slope of capacitive current density ($\Delta j = j_{anode} - j_{cathode}$) at 1.273 V against different scan rates is twice of the C_{dl}, utilized to stand for the corresponding ECSA. Typical CV curves of Ni_3Fe nitride, Ni_3Co nitride, Ni_3Mn nitride, and nickel-based LDH in different scan rates are shown in **Figure 7.15(a-c)** and **Figure 7.16**. As can be seen in **Figure 7.15d**, 2D holey Ni_3Fe nitride exhibits the largest C_{dl} compared with those of the other catalysts. From LDH to 2D holey nitride, the ECSA values increased by around twice. This increase is mainly assigned to the formation of abundant defects and uniform nanopores on the nanosheets during the nitridation process. More importantly, compared with 2D holey Ni_3Co nitride and Ni_3Mn nitride nanosheets, 2D holey Ni_3Fe nitride nanosheets has 104.2 % and 128.8 % higher ECSA, more than 9 - fold and 64 - fold times of OER current density at η = 320 mV achieved, respectively. Such enhancement of the electrocatalytic activity can not only be ascribed to the larger surface area, but also due to the higher intrinsic catalytic activity due to the significantly enlarged lattice spacing after introducing nitrogen, leading to much more electrochemically accessible inner layer surface.

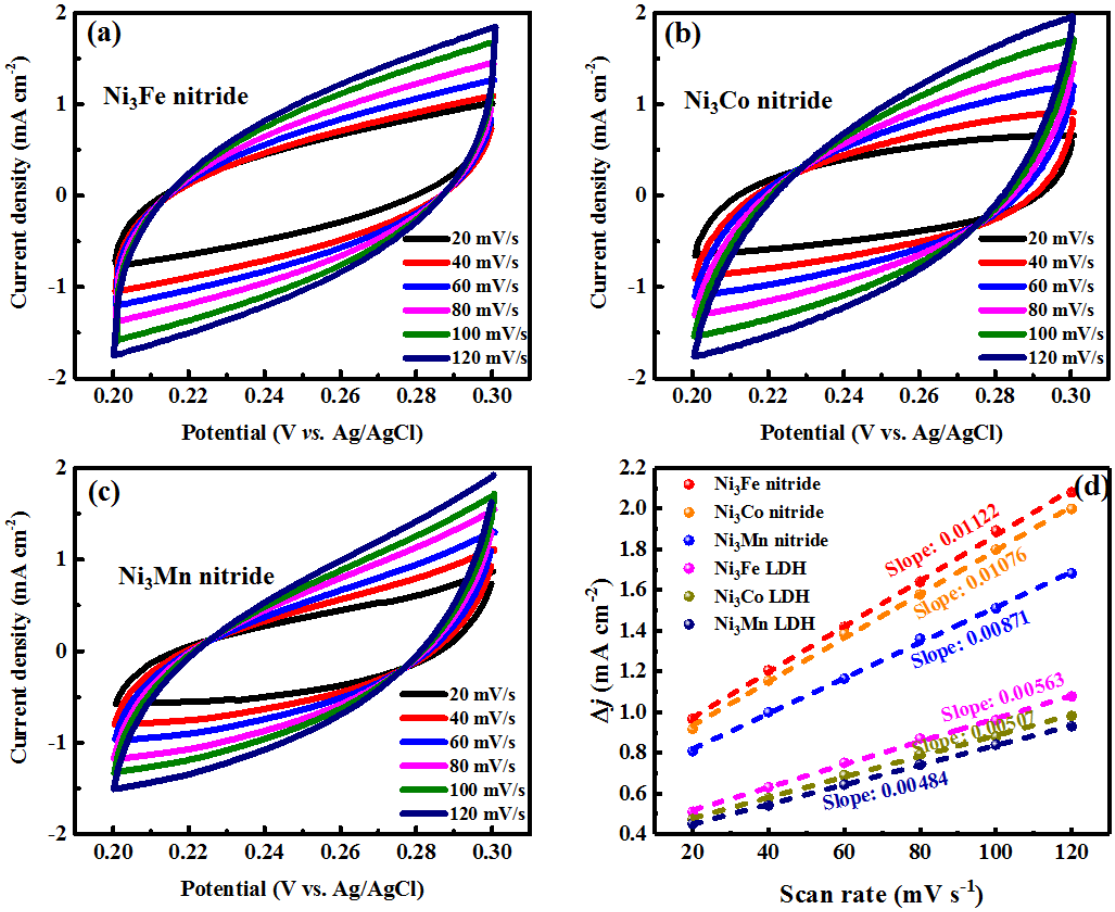

Figure 7.15. Typical CV curves of (a) Ni_3Fe nitride, (b) Ni_3Co nitride, and (c) Ni_3Mn nitride in 1M KOH with various scan rates. (d) Differences of current density ($\Delta j = j_{anode} - j_{cathode}$) at 1.273 V plotted vs. the scan rates. The C_{dl} is half of the slope.

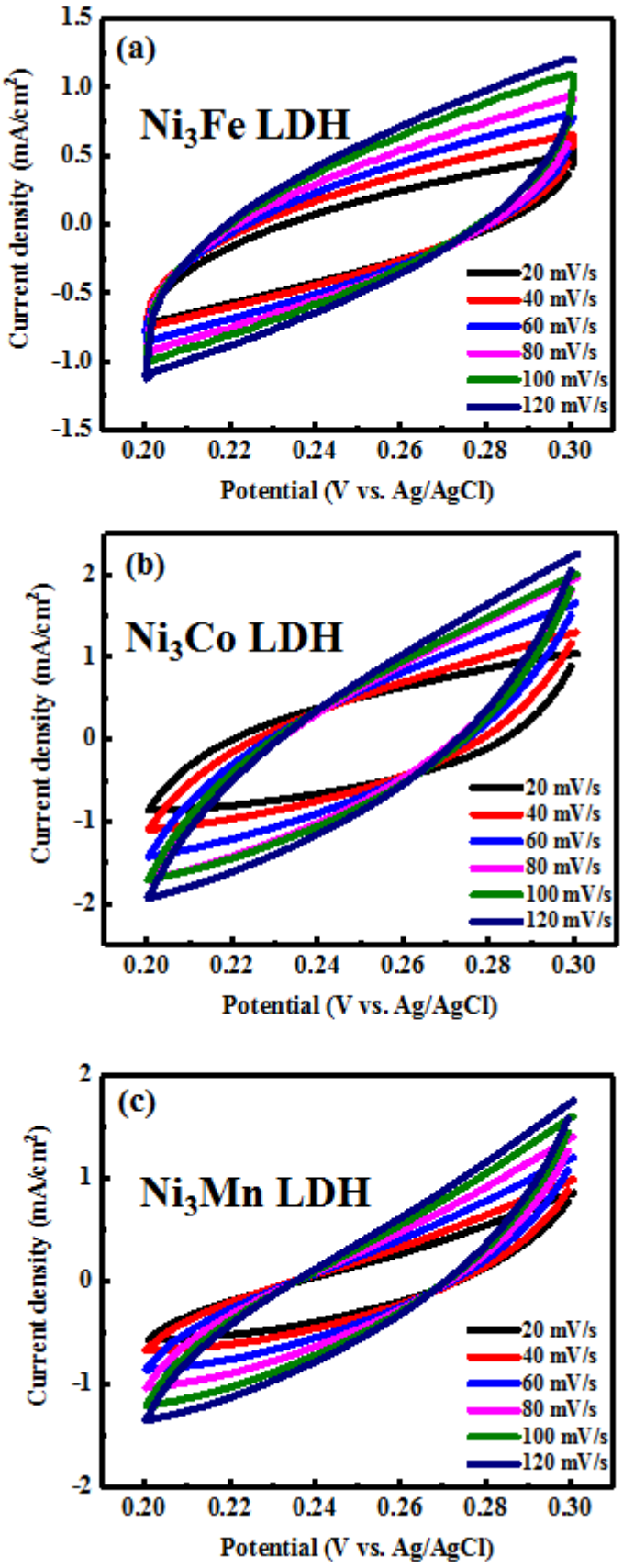

Figure 7.16. Typical cyclic voltammetry curves of (a) Ni_3Fe-LDH, (b) Ni_3Co-LDH, and (c) Ni_3Mn-LDH in 1M KOH with different scan rates.

Even after 1000 CV cycles, the Ni_3Fe nitride nanosheets still preserve the 2D holey morphology (**Figure 7.17a)**. HRTEM image indicates that there is a quite thin oxides layer about 1-2 nm on the Ni_3Fe nitride nanosheets (Figure 7.17b), suggesting the oxidization of Ni_3Fe nitride nanosheets. The composition changes of the 2D holey Ni_3Fe nitride nanosheets after 1000 CV cycles were explored with X-ray photoelectron spectroscopy (XPS), as revealed in Figure 7.17d-f. The peaks of Ni^{2+} and Fe^{3+} indicate that the existence of surface oxidation in Ni_3Fe nitride nanosheets into NiFe oxide/hydroxide. However, there is no NiFe oxide/hydroxide diffraction peak, indicating the main phase was still Ni_3Fe nitride (Figure 7.17c). In addition, there is no significant changes of elements contents before and after CV cycles (**Table 7.3**). All of the above characterizations provide solid evidence that the major phases are Ni_3Fe nitride with a very thin oxide layer during the catalytic process.

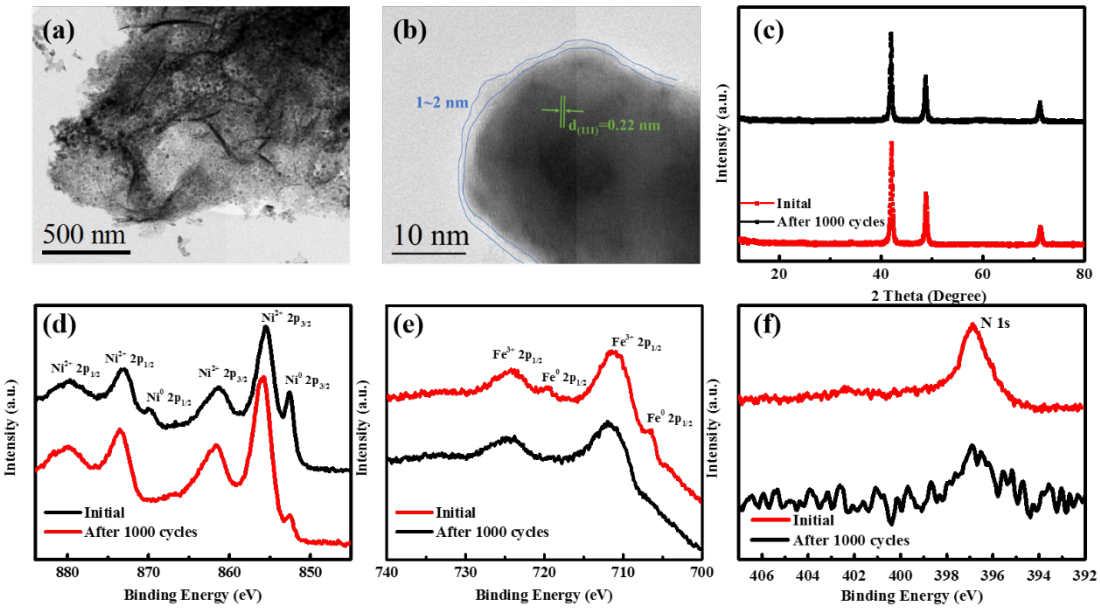

Figure 7.17. (a) TEM and (b) HRTEM images of the 2D holey Ni_3Fe nitride nanosheets after 1000 CV cycles. (c) XRD, (d) Ni 2p, (e) Fe 2p, and (f) N 1s XPS spectras of 2D holey Ni_3Fe nitride nanosheets before and after 1000 CV cycles.

Table 7.3. The elements contents before and after stability test.

	Before (Atom %)			After (Atom %)		
Ni_3Fe	Ni (61.28)	Fe (21.43)	N(17.29)	Ni (62.87)	Fe (20.45)	N (16.68)
Ni_3Co	Ni (57.49)	Co (23.16)	N(19.35)	Ni (59.60)	Co (22.86)	N (17.54)
Ni_3Mn	Ni (61.12)	Mn (18.66)	N(20.22)	Ni (60.99)	Mn (19.64)	N (19.37)

In order to study the electrocatalytic activities of these holey 2D Ni_3M nitride nanosheets, they were tested as air cathodes for Na-O_2 batteries. The galvanostatic discharge/charge properties were carried out in the voltage range of 1.5-3.0 V at room temperature. **Figure 7.18** demonstrates their discharge/charge curves with a limited capacity of 400 mAh g^{-1} under a current density of 200 mA g^{-1}. As shown in Figure 7.18a, the holey 2D Ni_3Fe nitride nanosheet electrode exhibited a quite stable discharge plateau at about 1.9 V for over 20 cycles. However, the discharge plateau of the holey 2D Ni_3Co nitride nanosheets and the holey 2D Ni_3Mn nitride nanosheets dramatically dropped after 10 and 5 cycles, respectively. Also, the holey 2D Ni_3Fe nitride nanosheets deliver a recharge capacity about 242 mAh g^{-1} at the 2^{nd} cycle, which is higher than the holey 2D Ni_3Co nitride nanosheets (136 mAh g^{-1}) and the holey 2D Ni_3Mn nitride nanosheets (209 mAh g^{-1}), as shown in Figure 7.18b and c. It demonstrates that the holey 2D Ni_3Fe nitride nanosheets could more efficiently decompose the discharge product compared with the holey 2D Ni_3Co nitride nanosheets and the holey 2D Ni_3Mn nitride nanosheets, owing to its excellent OER activity. Moreover, the holey 2D Ni_3Fe nitride nanosheets reveal an excellent cycling stability than those of the holey 2D Ni_3Co nitride nanosheets and the holey 2D Ni_3Mn nitride nanosheets (Figure 7.18d). For instance the 2D holey Ni_3Fe nitride nanosheets could deliver a discharge capacity of 400 mAh g^{-1} even after 50 cycles. On basis of the above results, it is clear that the holey 2D nickel-based nitride nanosheets derived from

2D nickel-based LDH nanosheets could be used as air cathodes for the Na-O_2 batteries due to their excellent electrocatalytic activities. The improved catalytic activities can be due to the excellent conductivity of the Ni_3M nitrides, abundant active sites, and huge surface area provided by the 2D holey nanosheet structure. It is clear that the 2D holey Ni_3Fe nitride nanosheets with holey nanostructure exhibit the best electrochemical performance when evaluated as air cathode for Na-O_2 batteries.

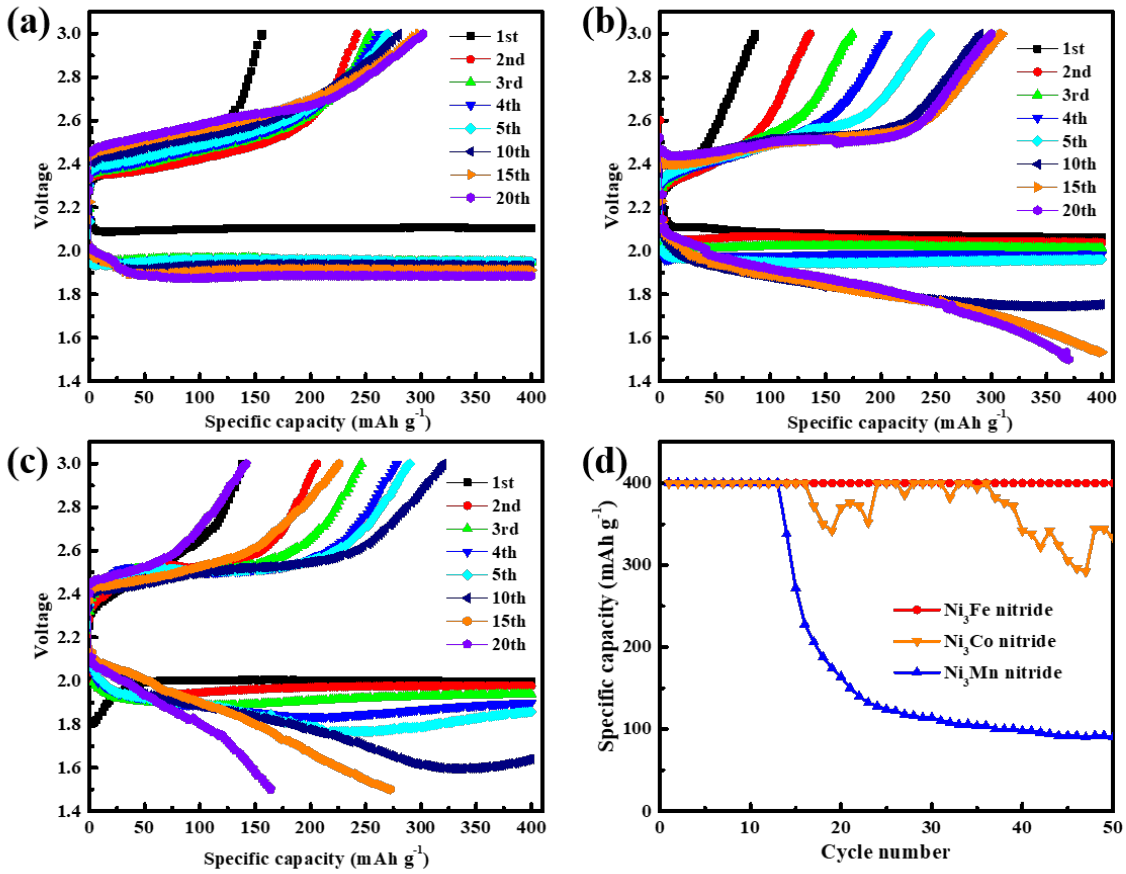

Figure 7.18. Discharge/charge profiles of the (a) Ni_3Fe nitride, (b) Ni_3Co nitride, and (c) Ni_3Mn nitride, (d) cycling stability of the Ni_3Fe nitride, Ni_3Co nitride, and Ni_3Mn nitride.

The excellent electrochemical performance of the ultrathin holey 2D nickel-based lateral nanosheets are observed because of the unique structure. Specifically, holey nitride nanosheets could accelerate the transport and diffusion of reaction intermediates

and gas within the electrode. Besides, their nearly single-crystalline structure could further enhance the electron transportation along the ultrathin 2D direction. Additionally, the highly exposed atoms on the large lateral surfaces could provide vast surface area and plentiful exposed catalytically active atoms or lattice planes. Therefore, the integration of the vast surface area, abundant exposed catalytic sites, and the ultrahigh electrical conductivity resulting, as well as the connected holey architecture will make this type of nitride nanosheet an excellent electrocatalyst with superior electrocatalytic performance for Na-O_2 batteries.

7.4 Summary

In this Chapter, ultrathin holey 2D nickel-based nitride lateral nanosheets (less than 1 nm thick) were designed and successfully synthesized by nitridation treatment of the corresponding hydroxide precursors. Owing to the highly-orientated crystalline texture, large lattice spacing, abundant exposed catalytically active sites resulting both from the atoms on the large lateral surfaces and the areas near the edges of the generated holes, as well as the hierarchical porous continuously conductive architecture suitable for transport of intermediate reaction products and diffusion of generated gases, these metallic nitride holey nanosheets showed excellent electrocatalytic property. Among them, the ultrathin holey 2D Ni_3Fe nitride nanosheets demonstrated a quite lower overpotential (300 mV) towards oxygen evolution to deliver a current density of 100 A g^{-1}, a large enhancement over commercial IrO_2 by a factor of nearly 25 times. Meanwhile, the ultrathin holey 2D Ni_3Fe nitride nanosheets demonstrated excellent electrocatalytic performance when evaluated as air cathode for Na-O_2 batteries with a stable discharge capacity of 400 mAh g^{-1} for over 50 cycles. The robust electrocatalytic activity of 2D Ni_3Fe nitride nanosheets is largely ascribed to the

enhanced electrochemical surface area, owing to the larger surface area and excellent intrinsic electrocatalytic property due to the significantly enlarged lattice spacing after introducing nitrogen, leading to much more electrochemically accessible inner layer surface.

Chapter 8 CONCLUSIONS AND OUTLOOK

8.1 General Conclusions

In this doctoral thesis, four different kinds of electrode materials were fabricated for rechargeable batteries: Ge@N-CNTs and yolk-shell Si@SiO_2/C@carbon nanospheres for lithium ion batteries, and the phosphorus and nitrogen dual-doped carbon (PNDC) and ultrathin 2D holey nickel-based nitrides for sodium-oxygen batteries. The physical and electrochemical properties of these materials were thoroughly investigated. These materials demonstrated excellent electrochemical performance, such as high specific capacities, outstanding cycling stability and high rate capabilities. These enhancements could be attributed to the rational design of the electrode materials, including increased electrical conductivity, efficiently accommodated volume expansion, sufficient active sites, and enlarged the surface areas.

Ge@N-CNTs composite with Ge nanoparticles uniformly encapsulated in N-CNTs shells has been fabricated as anode electrode material for LIBs by using capillary action. The Ge@N-CNTs composite could deliver a high discharge capacity of 892 mAh g^{-1} beyond 200 cycles under the current density of 100 mA g^{-1}. The Ge nanoparticles could facilitate Li^+ ion transport through reducing the diffusion distance. The void spaces and the N-CNTs could effectively suppress the huge volume expansion during cycling processes. In addition, the interconnected network of the N-CNTs could afford good electrical conductivity of the electrode and prevent electrical isolation after prolonged cycling. Therefore, the Ge@N-CNTs composite manifests high specific capacity, enhanced cycling stability, and excellent rate capacity as anode material for LIBs.

A facile strategy has been developed to tunable fabricate yolk-shell Si@SiO_2/C@carbon nanospheres with interior core-shell structured Si@SiO_2/C as yolk as anode material for LIBs by engineering the compositional chemistry. Owing to the step-growth polymerization process of the phenolic resin, the distribution of polymeric components inside the phenolic resin coating the Si nanoparticles is non-unifrom, and the inner part could be selectively removed by using acetone to form a yolk-shell structure with the interior core-shell structure consisting of Si@SiO_2/C. The phenolic resin could serve not only as the carbon source of the shell but also as sacrificial template for the yolk-shell structure. In addition, yolk-shell structured composites with different diameters of nanospheres could be obtained with different reaction times. Among these materials, YSCS@Si-30 reveals the highest charge capacity of about 1300 mAh g^{-1}, and even after 500 cycles, the capacity is still as high as 1000 mAh g^{-1} with a current density of 2 A g^{-1}. The excellent electrochemical performance of these materials could be attributed to their unique yolk-shell Si@SiO_2/C@carbon nanospheres with interior core-shell structured Si@SiO_2/C as the yolk. The exterior yolk-shell structure could efficiently accommodate the volume changes during the alloying and dealloying processes. Moreover, the interior core-shell structure with the carbon layer could significantly increase the electrical conductivity of the Si nanoparticles.

In order to study the influence of carbon catalysts doped with different heteroatoms on the discharge products, cycling stability, and electrocatalytic performance of sodium-oxygen batteries, two different carbon based electrocatalysts were synthesized: phosphorus and nitrogen dual-doped carbon (PNDC) and nitrogen solely doped carbon (NSDC). Even though they have similar structures and morphology, the PNDC and

NSDC electrodes exhibit different electrochemical behavior due to their different surface properties and catalytic activities. The PNDC electrode could facilitate the formation and stabilization of NaO_2 nanoparticles as the discharge product with a quite low charge overpotential (0.18 V) and long cycling stability for 120 cycles. The NSDC electrode, however, is inclined to forming a mixture of film-like NaO_2 and $Na_2O_2 \cdot 2H_2O$ discharge products on the electrode surface with poor cycling stability for only 23 cycles. In addition, the NaO_2 nanoparticles deposited on the PNDC electrode could be easily decomposed when compared with the film-like discharge products formed on the surface of the NSDC electrode. Therefore, the electrochemical performance of Na-O_2 batteries could be modulated by using different electrocatalysts with different reaction activities, leading to different reaction mechanisms with different discharge products and electrochemical performances.

Ultrathin holey 2D nickel-based nitride lateral nanosheets (Ni_3M nitride, M = Fe, Co, Mn) with a satisfactory specific surface area (189.6 $m^2\ g^{-1}$) and thickness of about 0.6-0.8 nm were designed and successfully synthesized by nitridation treatment of the corresponding hydroxide precursors. Among them, the ultrathin holey 2D Ni_3Fe nitride nanosheets demonstrated a quite low overpotential (300 mV) towards oxygen evolution an could deliver a current density of 100 A g^{-1}, a large enhancement over commercial IrO_2 by a factor of nearly 25 times. Meanwhile, the ultrathin holey 2D Ni_3Fe nitride nanosheets demonstrated excellent electrocatalytic performance when evaluated as air cathode for Na-O_2 batteries, with a stable discharge capacity of 400 mAh g^{-1} for over 50 cycles. The robust electrocatalytic activity of 2D Ni_3Fe nitride nanosheets is largely ascribed to their enhanced electrochemical surface area, owing to their larger surface area and excellent intrinsic electrocatalytic properties due to the significantly enlarged lattice spacing after introducing nitrogen, leading to much more electrochemically

accessible inner layer surface. Therefore, the concept of designing 2D ultrathin highly-orientated and holey nitride nanosheets has been explored for electrocatalyst application.

8.2 Outlook

Even through great achievements have been realized in developing high energy density and high performance rechargeable batteries, they still have many challenges before practical application, such as high cost, safety concerns, and cycling stability. Therefore, manufacturing electrode materials with excellent electrochemical properties, good cycling stability, low cost, and high safety is highly desirable for the future development of rechargeable batteries with high energy density and long cycle life. More research work on the development of high energy density rechargeable batteries could be conducted based on the strategies in this thesis.

Capillary action is a very powerful method to synthesize electrode materials. In this thesis, by utilizing capillary action, one-dimensional Ge@N-CNTs was successfully fabricated and exhibited excellent electrochemical performance when evaluated as anode material for LIBs. More work could be carried out to enhance the electrochemical performance of Ge@N-CNTs, such as tuning the void spaces between Ge nanoparticles, increasing the electrical conductivity of the composite through decreasing the thickness of the N-CNTs, and decreasing the size of the Ge nanoparticles to improve the ionic conductivity. In addition, other materials with similar structures could also be synthesized by the same method to enhance their electrochemical properties as electrode materials for rechargeable batteries.

Through engineering the compositional chemistry inside the polymer-coated nanoparticles, yolk-shell Si@SiO_2/C@carbon nanospheres with interior core-shell structured Si@SiO_2/C as yolk were synthesized as anode material for LIBs. In order to improve the electrochemical performance of the composite, the structure of the Si@SiO_2/C@carbon nanospheres could be precisely controlled, including the diameter, shell thickness, cavity, and architecture. This strategy also could be utilized to synthesize other composites with similar yolk-shell structures, such as metal oxides, metal alloys, metal sulfides, and metal phosphides.

The discharge products, cycling stability, and electrocatalytic performance of sodium-oxygen batteries could be influenced by the air cathode. The diverse compositions of discharge products on different electrodes could be attributed to the different reaction mechanisms driven from their different reaction activities with different elements doping. Although the characterizations of the reaction mechanisms and discharge products were carried out with ex-situ techniques, including ex-situ XRD, SEM, and XPS, in-situ techniques, such as in-situ synchrotron XRD, Raman spectroscopy, and TEM are necessary for a deeper understanding of the reaction mechanisms of sodium-oxygen batteries.

The ultrathin holey 2D nickel-based nitride lateral nanosheets (Ni_3M nitride, M = Fe, Co, Mn) demonstrated excellent electrocatalytic activity and were evaluated as air cathode materials for sodium-oxygen batteries. This method could be adopted to fabricate other ultrathin holey 2D nanosheet materials, which could be utilized as electrode materials for various rechargeable batteries, such as lithium-ion batteries, sodium-ion batteries, lithium-oxygen batteries, and sodium-ion batteries. In addition, computational calculations are essential for the investigation of the reaction

mechanisms of sodium-oxygen batteries.

With continuous endeavors to solve the above-mentioned challenges, the commercialization of rechargeable batteries with high energy density, low cost, good safety, and long cycle life is expected in the near future.

REFERENCES

[1] B. Dunn, H. Kamath, J. M. Tarascon, Electrical energy storage for the grid: a battery of choices, Science, 2011, 334, 928.

[2] B. Scrosati, J. Hassoun, Y. K. Sun, Lithium-ion batteries. A look into the future, Energy Environ. Sci., 2011, 4, 3287.

[3] M. Armand, J. M. Tarascon, Building better batteries, Nature, 2008, 451, 652.

[4] Y. Wang, G. Z. Cao, Developments in nanostructured cathode materials for high-performance lithium-ion batteries, Adv. Mater., 2008, 20, 2251.

[5] J. B. Goodenough, Y. Kim, Challenges for Rechargeable Li Batteries, Chem. Mater., 2010, 22, 587.

[6] K. Ozawa, Lithium-Ion Rechargeable Batteries with LiCoO2 and Carbon Electrodes - the LiCoO2/C System, Solid State Ionics, 1994, 69, 212.

[7] S. Luo, K. Wang, J. Wang, K. Jiang, Q. Li, S. Fan, Binder-free LiCoO2/carbon nanotube cathodes for high-performance lithium ion batteries, Adv. Mater., 2012, 24, 2294.

[8] Y. S. Jung, P. Lu, A. S. Cavanagh, C. Ban, G. H. Kim, S. H. Lee, S. M. George, S. J. Harris, A. C. Dillon, Unexpected Improved Performance of ALD Coated LiCoO2/Graphite Li-Ion Batteries, Adv. Energy Mater., 2013, 3, 213.

[9] P. F. Yan, J. M. Zheng, M. Gu, J. Xiao, J. G. Zhang, C. M. Wang, Intragranular cracking as a critical barrier for high-voltage usage of layer-structured cathode for lithium-ion batteries, Nat. Commun., 2017, 8, 14101.

[10] W. Sun, L. Suo, F. Wang, N. Eidson, C. Yang, F. Han, Z. Ma, T. Gao, M. Zhu, C. Wang, “Water-in-Salt” electrolyte enabled LiMn2O4/TiS2 Lithium-ion batteries, Electrochem. Commun., 2017, 82, 71.

[11] G. Zampardi, C. Batchelor-McAuley, E. Katelhon, R. G. Compton, Lithium-Ion-Transfer Kinetics of Single LiMn2O4 Particles, Angew. Chem., Int. Ed.,

2017, 56, 641.

[12] L. X. Yuan, Z. H. Wang, W. X. Zhang, X. L. Hu, J. T. Chen, Y. H. Huang, J. B. Goodenough, Development and challenges of LiFePO4 cathode material for lithium-ion batteries, Energy Environ. Sci., 2011, 4, 269.

[13] X. F. Wang, Z. J. Feng, J. T. Huang, W. Deng, X. B. Li, H. S. Zhang, Z. H. Wen, Graphene-decorated carbon-coated LiFePO4 nanospheres as a high-performance cathode material for lithium-ion batteries, Carbon, 2018, 127, 149.

[14] A. M. Cao, J. S. Hu, H. P. Liang, L. J. Wan, Self-assembled vanadium pentoxide (V2O5) hollow microspheres from nanorods and their application in lithium-ion batteries, Angew. Chem., Int. Ed., 2005, 44, 4391.

[15] L. W. Ji, Z. Lin, M. Alcoutlabi, X. W. Zhang, Recent developments in nanostructured anode materials for rechargeable lithium-ion batteries, Energy Environ. Sci., 2011, 4, 2682.

[16] R. McMillan, H. Slegr, Z. X. Shu, W. D. Wang, Fluoroethylene carbonate electrolyte and its use in lithium ion batteries with graphite anodes, J. Power Sources, 1999, 81, 20.

[17] M. C. Smart, Irreversible Capacities of Graphite in Low-Temperature Electrolytes for Lithium-Ion Batteries, J. Electrochem. Soc., 1999, 146, 3963.

[18] B. J. Landi, M. J. Ganter, C. D. Cress, R. A. DiLeo, R. P. Raffaelle, Carbon nanotubes for lithium ion batteries, Energy Environ. Sci., 2009, 2, 638.

[19] S. S. Li, Y. H. Luo, W. Lv, W. J. Yu, S. D. Wu, P. X. Hou, Q. H. Yang, Q. B. Meng, C. Liu, H. M. Cheng, Vertically Aligned Carbon Nanotubes Grown on Graphene Paper as Electrodes in Lithium-Ion Batteries and Dye-Sensitized Solar Cells, Adv. Energy Mater., 2011, 1, 486.

[20] E. Yoo, J. Kim, E. Hosono, H. S. Zhou, T. Kudo, I. Honma, Large reversible

Li storage of graphene nanosheet families for use in rechargeable lithium ion batteries, Nano Lett., 2008, 8, 2277.

[21] Z. S. Wu, W. Ren, L. Xu, F. Li, H. M. Cheng, Doped graphene sheets as anode materials with superhigh rate and large capacity for lithium ion batteries, ACS Nano, 2011, 5, 5463.

[22] B. Wang, J. Ryu, S. Choi, G. Song, D. Hong, C. Hwang, X. Chen, B. Wang, W. Li, H. K. Song, S. Park, R. S. Ruoff, Folding Graphene Film Yields High Areal Energy Storage in Lithium-Ion Batteries, ACS Nano, 2018, 12, 1739.

[23] Q. B. Zhang, H. X. Chen, L. L. Luo, B. T. Zhao, H. Luo, X. Han, J. W. Wang, C. M. Wang, Y. Yang, T. Zhu, M. L. Liu, Harnessing the concurrent reaction dynamics in active Si and Ge to achieve high performance lithium-ion batteries, Energy Environ. Sci., 2018, 11, 669.

[24] S. Choi, T. W. Kwon, A. Coskun, J. W. Choi, Highly elastic binders integrating polyrotaxanes for silicon microparticle anodes in lithium ion batteries, Science, 2017, 357, 279.

[25] S. Chen, L. Shen, P. A. van Aken, J. Maier, Y. Yu, Dual-Functionalized Double Carbon Shells Coated Silicon Nanoparticles for High Performance Lithium-Ion Batteries, Adv. Mater., 2017, 29, 1605650.

[26] C. M. Park, J. H. Kim, H. Kim, H. J. Sohn, Li-alloy based anode materials for Li secondary batteries, Chem. Soc. Rev., 2010, 39, 3115.

[27] G. R. Goward, N. J. Taylor, D. C. S. Souza, L. F. Nazar, The true crystal structure of Li17M4 (M=Ge, Sn, Pb)–revised from Li22M5, J. Alloys Compd., 2001, 329, 82.

[28] L. F. Cui, Y. Yang, C. M. Hsu, Y. Cui, Carbon-silicon core-shell nanowires as high capacity electrode for lithium ion batteries, Nano Lett., 2009, 9, 3370.

[29] C. K. Chan, H. Peng, G. Liu, K. McIlwrath, X. F. Zhang, R. A. Huggins, Y.

Cui, High-performance lithium battery anodes using silicon nanowires, Nat. Nanotechnol., 2007, 3, 31.

[30] S. H. Ng, J. Z. Wang, D. Wexler, K. Konstantinov, Z. P. Guo, H. K. Liu, Highly reversible lithium storage in spheroidal carbon-coated silicon nanocomposites as anodes for lithium-ion batteries, Angew. Chem., Int. Ed., 2006, 45, 6896.

[31] H. Kim, J. Choi, H. J. Sohn, T. Kang, The Insertion Mechanism of Lithium into Mg2Si Anode Material for Li-Ion Batteries, J. Electrochem. Soc., 1999, 146, 4401.

[32] J. Yang, M. Wachtler, M. Winter, J. O. Besenhard, Sub-Microcrystalline Sn and Sn-SnSb Powders as Lithium Storage Materials for Lithium-Ion Batteries, Electrochem. Solid-State Lett., 1999, 2, 161.

[33] A. R. Kamali, D. J. Fray, Review on Carbon and Silicon Based Materials as Anode Materials for Lithium Ion Batteries, J. New Mater. Electrochem. Syst., 2010, 13, 147.

[34] M. Stjerndahl, H. Bryngelsson, T. Gustafsson, J. T. Vaughey, M. M. Thackeray, K. Edstrom, Surface chemistry of intermetallic AlSb-anodes for Li-ion batteries, Electrochim. Acta, 2007, 52, 4947.

[35] J. M. Tarascon, M. Morcrette, L. Dupont, Y. Chabre, C. Payen, D. Larcher, V. Pralong, On the electrochemical reactivity mechanism of CoSb3 vs. lithium, J. Electrochem. Soc., 2003, 150, A732.

[36] H. Li, L. H. Shi, W. Lu, X. J. Huang, L. Q. Chen, Studies on capacity loss and capacity fading of nanosized SnSb alloy anode for Li-ion batteries, J. Electrochem. Soc., 2001, 148, A915.

[37] Q. Wang, H. Li, L. Q. Chen, X. J. Huang, Novel spherical microporous carbon as anode material for Li-ion batteries, Solid State Ionics, 2002, 152, 43.

[38] H. Li, X. J. Huang, L. Q. Chen, G. W. Zhou, Z. Zhang, D. P. Yu, Y. J. Mo, N.

Pei, The crystal structural evolution of nano-Si anode caused by lithium insertion and extraction at room temperature, Solid State Ionics, 2000, 135, 181.

[39] T. Kennedy, E. Mullane, H. Geaney, M. Osiak, C. O'Dwyer, K. M. Ryan, High-performance germanium nanowire-based lithium-ion battery anodes extending over 1000 cycles through in situ formation of a continuous porous network, Nano Lett., 2014, 14, 716.

[40] K. H. Seng, M. H. Park, Z. P. Guo, H. K. Liu, J. Cho, Self-assembled germanium/carbon nanostructures as high-power anode material for the lithium-ion battery, Angew. Chem., Int. Ed., 2012, 51, 5657.

[41] C. Yan, W. Xi, W. Si, J. Deng, O. G. Schmidt, Highly conductive and strain-released hybrid multilayer Ge/Ti nanomembranes with enhanced lithium-ion-storage capability, Adv. Mater., 2013, 25, 539.

[42] L. Wang, K. Bao, Z. Lou, G. Liang, Q. Zhou, Chemical synthesis of germanium nanoparticles with uniform size as anode materials for lithium ion batteries, Dalton Trans., 2016, 45, 2814.

[43] M. Ge, S. Kim, A. Nie, R. Shahbazian-Yassar, M. Mecklenburg, Y. Lu, X. Fang, C. Shen, J. Rong, S. Yi Park, D. Suk Kim, J. Young Kim, C. Zhou, Capacity retention behavior and morphology evolution of SixGe1-x nanoparticles as lithium-ion battery anode, Nanotechnology, 2015, 26, 255702.

[44] S. Fang, L. F. Shen, H. Zheng, Z. K. Tong, G. Pang, X. G. Zhang, Confined germanium nanoparticles in an N-doped carbon matrix for high-rate and ultralong-life lithium ion batteries, RSC Adv., 2015, 5, 85256.

[45] S. Ling, Z. Cui, G. She, X. Guo, L. Mu, W. Shi, A novel type of Ge nanotube arrays for lithium storage material, J Nanosci Nanotechnol, 2012, 12, 213.

[46] M. H. Park, Y. Cho, K. Kim, J. Kim, M. L. Liu, J. Cho, Germanium Nanotubes

Prepared by Using the Kirkendall Effect as Anodes for High-Rate Lithium Batteries, Angew. Chem., Int. Ed., 2011, 50, 9647.

[47] T. Kennedy, M. Bezuidenhout, K. Palaniappan, K. Stokes, M. Brandon, K. M. Ryan, Nanowire Heterostructures Comprising Germanium Stems and Silicon Branches as High-Capacity Li-Ion Anodes with Tunable Rate Capability, ACS Nano, 2015, 9, 7456.

[48] Y. Sun, S. Jin, G. Yang, J. Wang, C. Wang, Germanium Nanowires-in-Graphite Tubes via Self-Catalyzed Synergetic Confined Growth and Shell-Splitting Enhanced Li-Storage Performance, ACS Nano, 2015, 9, 3479.

[49] J. S. Kim, A. Y. Kim, Y. W. Byeon, J. P. Ahn, D. Byun, J. K. Lee, Porous Zn2GeO4 nanowires with uniform carbon-buffer layer for lithium-ion battery anodes with long cycle life, Electrochim. Acta, 2016, 195, 43.

[50] D. Li, H. Wang, H. K. Liu, Z. Guo, A New Strategy for Achieving a High Performance Anode for Lithium Ion Batteries-Encapsulating Germanium Nanoparticles in Carbon Nanoboxes, Adv. Energy Mater., 2016, 6, 1501666.

[51] S. Yoon, S. H. Jung, K. N. Jung, S. G. Woo, W. Cho, Y. N. Jo, K. Y. Cho, Preparation of nanostructured Ge/GeO2 composite in carbon matrix as an anode material for lithium-ion batteries, Electrochim. Acta, 2016, 188, 120.

[52] P. Kitschke, M. Walter, T. Ruffer, A. Seifert, F. Speck, T. Seyller, S. Spange, H. Lang, A. A. Auer, M. V. Kovalenko, M. Mehring, Porous Ge@C materials via twin polymerization of germanium(II) salicyl alcoholates for Li-ion batteries, J. Mater. Chem. A, 2016, 4, 2705.

[53] M. H. Seo, M. Park, K. T. Lee, K. Kim, J. Kim, J. Cho, High performance Ge nanowire anode sheathed with carbon for lithium rechargeable batteries, Energy Environ. Sci., 2011, 4, 425.

[54] D.-J. Xue, S. Xin, Y. Yan, K.-C. Jiang, Y.-X. Yin, Y.-G. Guo, L.-J. Wan,

Improving the electrode performance of Ge through Ge@ C core–shell nanoparticles and graphene networks, J. Am. Chem. Soc., 2012, 134, 2512.

[55] P. Poizot, S. Laruelle, S. Grugeon, L. Dupont, J. M. Tarascon, Nano-sized transition-metal oxides as negative-electrode materials for lithium-ion batteries, Nature, 2000, 407, 496.

[56] H. Wang, L. F. Cui, Y. Yang, H. Sanchez Casalongue, J. T. Robinson, Y. Liang, Y. Cui, H. Dai, Mn3O4-graphene hybrid as a high-capacity anode material for lithium ion batteries, J. Am. Chem. Soc., 2010, 132, 13978.

[57] W. Y. Li, L. N. Xu, J. Chen, Co3O4 nanomaterials in lithium-ion batteries and gas sensors, Adv. Funct. Mater., 2005, 15, 851.

[58] Z. S. Wu, W. Ren, L. Wen, L. Gao, J. Zhao, Z. Chen, G. Zhou, F. Li, H. M. Cheng, Graphene anchored with co(3)o(4) nanoparticles as anode of lithium ion batteries with enhanced reversible capacity and cyclic performance, ACS Nano, 2010, 4, 3187.

[59] G. M. Zhou, D. W. Wang, F. Li, L. L. Zhang, N. Li, Z. S. Wu, L. Wen, G. Q. Lu, H. M. Cheng, Graphene-Wrapped Fe3O4 Anode Material with Improved Reversible Capacity and Cyclic Stability for Lithium Ion Batteries, Chem. Mater., 2010, 22, 5306.

[60] X. Zhou, L. J. Wan, Y. G. Guo, Binding SnO2 nanocrystals in nitrogen-doped graphene sheets as anode materials for lithium-ion batteries, Adv. Mater., 2013, 25, 2152.

[61] X. Zhu, Y. Zhu, S. Murali, M. D. Stoller, R. S. Ruoff, Nanostructured reduced graphene oxide/Fe2O3 composite as a high-performance anode material for lithium ion batteries, ACS Nano, 2011, 5, 3333.

[62] Y. Li, B. Tan, Y. Wu, Mesoporous Co3O4 nanowire arrays for lithium ion batteries with high capacity and rate capability, Nano Lett., 2008, 8, 265.

[63] X. W. Lou, D. Deng, J. Y. Lee, J. Feng, L. A. Archer, Self-Supported Formation of Needlelike Co3O4 Nanotubes and Their Application as Lithium-Ion Battery Electrodes, Adv. Mater., 2008, 20, 258.

[64] J. Chen, L. Xu, W. Li, X. Gou, α-Fe2O3 Nanotubes in Gas Sensor and Lithium-Ion Battery Applications, Adv. Mater., 2005, 17, 582.

[65] M. V. Reddy, T. Yu, C. H. Sow, Z. X. Shen, C. T. Lim, G. V. Subba Rao, B. V. R. Chowdari, α-Fe2O3 Nanoflakes as an Anode Material for Li-Ion Batteries, Adv. Funct. Mater., 2007, 17, 2792.

[66] X. H. Wang, X. W. Li, X. L. Sun, F. Li, Q. M. Liu, Q. Wang, D. Y. He, Nanostructured NiO electrode for high rate Li-ion batteries, J. Mater. Chem., 2011, 21, 3571.

[67] B. Varghese, M. V. Reddy, Z. Yanwu, C. S. Lit, T. C. Hoong, G. V. S. Rao, B. V. R. Chowdari, A. T. S. Wee, C. T. Lim, C. H. Sow, Fabrication of NiO nanowall electrodes for high performance lithium ion battery, Chem. Mater., 2008, 20, 3360.

[68] B. Qiu, M. Xing, J. Zhang, Mesoporous TiO2 nanocrystals grown in situ on graphene aerogels for high photocatalysis and lithium-ion batteries, J. Am. Chem. Soc., 2014, 136, 5852.

[69] Y. Ren, Z. Liu, F. Pourpoint, A. R. Armstrong, C. P. Grey, P. G. Bruce, Nanoparticulate TiO2(B): an anode for lithium-ion batteries, Angew. Chem., Int. Ed., 2012, 51, 2164.

[70] M. S. Park, G. X. Wang, Y. M. Kang, D. Wexler, S. X. Dou, H. K. Liu, Preparation and electrochemical properties of SnO2 nanowires for application in lithium-ion batteries, Angew. Chem., Int. Ed., 2007, 46, 750.

[71] X. Wang, X. Q. Cao, L. Bourgeois, H. Guan, S. M. Chen, Y. T. Zhong, D. M. Tang, H. Q. Li, T. Y. Zhai, L. Li, Y. Bando, D. Golberg, N-Doped Graphene-

SnO2 Sandwich Paper for High-Performance Lithium-Ion Batteries, Adv. Funct. Mater., 2012, 22, 2682.

[72] E. Peled, D. Golodnitsky, H. Mazor, M. Goor, S. Avshalomov, Parameter analysis of a practical lithium- and sodium-air electric vehicle battery, J. Power Sources, 2011, 196, 6835.

[73] Q. Sun, Y. Yang, Z.-W. Fu, Electrochemical properties of room temperature sodium–air batteries with non-aqueous electrolyte, Electrochem. Commun., 2012, 16, 22.

[74] H. Yadegari, X. Sun, Recent Advances on Sodium-Oxygen Batteries: A Chemical Perspective, Acc. Chem. Res., 2018, 51, 1532.

[75] H. Yadegari, Q. Sun, X. Sun, Sodium-Oxygen Batteries: A Comparative Review from Chemical and Electrochemical Fundamentals to Future Perspective, Adv. Mater., 2016, 28, 7065.

[76] W. Liu, Q. Sun, Y. Yang, J. Y. Xie, Z. W. Fu, An enhanced electrochemical performance of a sodium-air battery with graphene nanosheets as air electrode catalysts, Chem. Commun., 2013, 49, 1951.

[77] Y. Li, H. Yadegari, X. Li, M. N. Banis, R. Li, X. Sun, Superior catalytic activity of nitrogen-doped graphene cathodes for high energy capacity sodium-air batteries, Chem. Commun., 2013, 49, 11731.

[78] Z. Jian, Y. Chen, F. Li, T. Zhang, C. Liu, H. Zhou, High capacity Na–O2 batteries with carbon nanotube paper as binder-free air cathode, J. Power Sources, 2014, 251, 466.

[79] N. Zhao, C. Li, X. Guo, Long-life Na-O2 batteries with high energy efficiency enabled by electrochemically splitting NaO2 at a low overpotential, Phys. Chem. Chem. Phys., 2014, 16, 15646.

[80] H. Yadegari, M. N. Banis, B. W. Xiao, Q. Sun, X. Li, A. Lushington, B. Q.

Wang, R. Y. Li, T. K. Sham, X. Y. Cui, X. L. Sun, Three-Dimensional Nanostructured Air Electrode for Sodium-Oxygen Batteries: A Mechanism Study toward the Cyclability of the Cell, Chem. Mater., 2015, 27, 3040.

[81] W.-M. Liu, W.-W. Yin, F. Ding, L. Sang, Z.-W. Fu, NiCo2O4 nanosheets supported on Ni foam for rechargeable nonaqueous sodium–air batteries, Electrochem. Commun., 2014, 45, 87.

[82] S. Rosenberg, A. Hintennach, In situ formation of α-MnO 2 nanowires as catalyst for sodium-air batteries, J. Power Sources, 2015, 274, 1043.

[83] Y. X. Hu, X. P. Han, Q. Zhao, J. Du, F. Y. Cheng, J. Chen, Porous perovskite calcium-manganese oxide microspheres as an efficient catalyst for rechargeable sodium-oxygen batteries, J. Mater. Chem. A, 2015, 3, 3320.

[84] N. Parveen, Z. Khan, S. A. Ansari, S. Park, S. T. Senthilkumar, Y. Kim, H. Ko, M. H. Cho, Feasibility of using hollow double walled Mn2O3 nanocubes for hybrid Na-air battery, Chem. Eng. J., 2019, 360, 415.

[85] Q. Sun, J. Liu, X. Li, B. Q. Wang, H. Yadegari, A. Lushington, M. N. Banis, Y. Zhao, W. Xiao, N. Chen, J. Wang, T. K. Sham, X. L. Sun, Atomic Layer Deposited Non-Noble Metal Oxide Catalyst for Sodium-Air Batteries: Tuning the Morphologies and Compositions of Discharge Product, Adv. Funct. Mater., 2017, 27, 1606662.

[86] J. Wang, R. Gao, L. Zheng, Z. Chen, Z. Wu, L. Sun, Z. Hu, X. Liu, CoO/CoP Heterostructured Nanosheets with an O–P Interpenetrated Interface as a Bifunctional Electrocatalyst for Na–O2 Battery, ACS Catal., 2018, 8, 8953.

[87] Q. Liu, L. Geng, T. Yang, Y. Tang, P. Jia, Y. Li, H. Li, T. Shen, L. Zhang, J. Huang, In-situ imaging electrocatalysis in a Na-O2 battery with Au-coated MnO2 nanowires air cathode, Energy Storage Materials, 2018.

[88] S. A. Freunberger, Y. Chen, N. E. Drewett, L. J. Hardwick, F. Barde, P. G.

Bruce, The lithium-oxygen battery with ether-based electrolytes, Angew. Chem., Int. Ed., 2011, 50, 8609.

[89] D. Sun, Y. Shen, W. Zhang, L. Yu, Z. Yi, W. Yin, D. Wang, Y. Huang, J. Wang, D. Wang, J. B. Goodenough, A solution-phase bifunctional catalyst for lithium-oxygen batteries, J. Am. Chem. Soc., 2014, 136, 8941.

[90] H. D. Lim, H. Song, J. Kim, H. Gwon, Y. Bae, K. Y. Park, J. Hong, H. Kim, T. Kim, Y. H. Kim, X. Lepro, R. Ovalle-Robles, R. H. Baughman, K. Kang, Superior rechargeability and efficiency of lithium-oxygen batteries: hierarchical air electrode architecture combined with a soluble catalyst, Angew. Chem., Int. Ed., 2014, 53, 3926.

[91] Z. Liang, Y. C. Lu, Critical Role of Redox Mediator in Suppressing Charging Instabilities of Lithium-Oxygen Batteries, J. Am. Chem. Soc., 2016, 138, 7574.

[92] X. Gao, Y. Chen, L. Johnson, Peter G. Bruce, Promoting solution phase discharge in Li–O2 batteries containing weakly solvating electrolyte solutions, Nat. Mater., 2016, 15, 882.

[93] B. J. Bergner, A. Schurmann, K. Peppler, A. Garsuch, J. Janek, TEMPO: a mobile catalyst for rechargeable Li-O(2) batteries, J. Am. Chem. Soc., 2014, 136, 15054.

[94] W. W. Yin, Z. Shadike, Y. Yang, F. Ding, L. Sang, H. Li, Z. W. Fu, A long-life Na-air battery based on a soluble NaI catalyst, Chem. Commun., 2015, 51, 2324.

[95] W.-W. Yin, J.-L. Yue, M.-H. Cao, W. Liu, J.-J. Ding, F. Ding, L. Sang, Z.-W. Fu, Dual catalytic behavior of a soluble ferrocene as an electrocatalyst and in the electrochemistry for Na–air batteries, J. Mater. Chem. A, 2015, 3, 19027.

[96] N. Zhao, C. Li, X. Guo, Long-life Na-O(2) batteries with high energy efficiency enabled by electrochemically splitting NaO(2) at a low

overpotential, Phys. Chem. Chem. Phys., 2014, 16, 15646.

[97] P. Hartmann, C. L. Bender, J. Sann, A. K. Durr, M. Jansen, J. Janek, P. Adelhelm, A comprehensive study on the cell chemistry of the sodium superoxide (NaO2) battery, Phys. Chem. Chem. Phys., 2013, 15, 11661.

[98] X. Bi, X. Ren, Z. Huang, M. Yu, E. Kreidler, Y. Wu, Investigating dendrites and side reactions in sodium-oxygen batteries for improved cycle lives, Chem. Commun., 2015, 51, 7665.

[99] S. C. Wu, Y. Qiao, K. Z. Jiang, Y. B. He, S. H. Guo, H. S. Zhou, Tailoring Sodium Anodes for Stable Sodium-Oxygen Batteries, Adv. Funct. Mater., 2018, 28, 1706374.

[100] C. L. Bender, B. Jache, P. Adelhelm, J. Janek, Sodiated carbon: a reversible anode for sodium–oxygen batteries and route for the chemical synthesis of sodium superoxide (NaO2), J. Mater. Chem. A, 2015, 3, 20633.

[101] L. Johnson, C. Li, Z. Liu, Y. Chen, S. A. Freunberger, P. C. Ashok, B. B. Praveen, K. Dholakia, J. M. Tarascon, P. G. Bruce, The role of LiO2 solubility in O2 reduction in aprotic solvents and its consequences for Li-O2 batteries, Nat. Chem., 2014, 6, 1091.

[102] N. B. Aetukuri, B. D. McCloskey, J. M. García, L. E. Krupp, V. Viswanathan, A. C. Luntz, Solvating additives drive solution-mediated electrochemistry and enhance toroid growth in non-aqueous Li–O2 batteries, Nat. Chem., 2014, 7, 50.

[103] K. Xu, Electrolytes and interphases in Li-ion batteries and beyond, Chem. Rev., 2014, 114, 11503.

[104] K. Xu, Nonaqueous liquid electrolytes for lithium-based rechargeable batteries, Chem. Rev., 2004, 104, 4303.

[105] L. Suo, O. Borodin, T. Gao, M. Olguin, J. Ho, X. Fan, C. Luo, C. Wang, K.

Xu, "Water-in-salt" electrolyte enables high-voltage aqueous lithium-ion chemistries, Science, 2015, 350, 938.

[106] M. He, K. C. Lau, X. Ren, N. Xiao, W. D. McCulloch, L. A. Curtiss, Y. Wu, Concentrated Electrolyte for the Sodium-Oxygen Battery: Solvation Structure and Improved Cycle Life, Angew. Chem., Int. Ed., 2016, 55, 15310.

[107] I. M. Aldous, L. J. Hardwick, Solvent-Mediated Control of the Electrochemical Discharge Products of Non-Aqueous Sodium-Oxygen Electrochemistry, Angew. Chem., Int. Ed., 2016, 55, 8254.

[108] W. Xu, J. Xiao, J. Zhang, D. Y. Wang, J. G. Zhang, Optimization of Nonaqueous Electrolytes for Primary Lithium/Air Batteries Operated in Ambient Environment, J. Electrochem. Soc., 2009, 156, A773.

[109] H. Park, J. Kim, M. H. Lee, S. K. Park, D.-H. Kim, Y. Bae, Y. Ko, B. Lee, K. Kang, Highly Durable and Stable Sodium Superoxide in Concentrated Electrolytes for Sodium-Oxygen Batteries, Adv. Energy Mater., 2018, 8, 1801760.

[110] Abate, II, L. E. Thompson, H. C. Kim, N. B. Aetukuri, Robust NaO2 Electrochemistry in Aprotic Na-O2 Batteries Employing Ethereal Electrolytes with a Protic Additive, J. Phys. Chem. Lett., 2016, 7, 2164.

[111] N. Zhao, X. X. Guo, Cell Chemistry of Sodium-Oxygen Batteries with Various Nonaqueous Electrolytes, J. Phys. Chem. C, 2015, 119, 25319.

[112] W. B. Luo, S. L. Chou, Y. C. Zhai, H. K. Liu, Self-assembled graphene and LiFePO4 composites with superior high rate capability for lithium ion batteries, J. Mater. Chem. A, 2014, 2, 4927.

[113] S. L. Chou, J. Z. Wang, H. K. Liu, S. X. Dou, Rapid Synthesis of Li4Ti5O12 Microspheres as Anode Materials and Its Binder Effect for Lithium-Ion Battery, J. Phys. Chem. C, 2011, 115, 16220.

[114] X. W. Gao, J. Z. Wang, S. L. Chou, H. K. Liu, Synthesis and electrochemical performance of LiV3O8/polyaniline as cathode material for the lithium battery, J. Power Sources, 2012, 220, 47.

[115] J. T. Xu, S. L. Chou, Q. F. Gu, H. K. Liu, S. X. Dou, The effect of different binders on electrochemical properties of LiNi1/3Mn1/3C1/3O2 cathode material in lithium ion batteries, J. Power Sources, 2013, 225, 172.

[116] X. Gao, W. Luo, C. Zhong, D. Wexler, S. L. Chou, H. K. Liu, Z. Shi, G. Chen, K. Ozawa, J. Z. Wang, Novel germanium/polypyrrole composite for high power lithium-ion batteries, Sci. Rep., 2014, 4, 6095.

[117] Z. Peng, S. A. Freunberger, L. J. Hardwick, Y. Chen, V. Giordani, F. Barde, P. Novak, D. Graham, J. M. Tarascon, P. G. Bruce, Oxygen reactions in a non-aqueous Li+ electrolyte, Angew. Chem., Int. Ed., 2011, 50, 6351.

[118] F. Mizuno, S. Nakanishi, Y. Kotani, S. Yokoishi, H. Iba, Rechargeable Li-Air Batteries with Carbonate-Based Liquid Electrolytes, Electrochemistry, 2010, 78, 403.

[119] S. A. Freunberger, Y. Chen, Z. Peng, J. M. Griffin, L. J. Hardwick, F. Barde, P. Novak, P. G. Bruce, Reactions in the rechargeable lithium-O2 battery with alkyl carbonate electrolytes, J. Am. Chem. Soc., 2011, 133, 8040.

[120] Y. Marcus, The Properties of Organic Liquids That Are Relevant to Their Use as Solvating Solvents, Chem. Soc. Rev., 1993, 22, 409.

[121] W.-J. Kwak, Z. Chen, C. S. Yoon, J.-K. Lee, K. Amine, Y.-K. Sun, Nanoconfinement of low-conductivity products in rechargeable sodium–air batteries, Nano Energy, 2015, 12, 123.

[122] J. Kim, H. D. Lim, H. Gwon, K. Kang, Sodium-oxygen batteries with alkyl-carbonate and ether based electrolytes, Phys. Chem. Chem. Phys., 2013, 15, 3623.

[123] S. Zhang, Z. Wen, K. Rui, C. Shen, Y. Lu, J. Yang, Graphene nanosheets loaded with Pt nanoparticles with enhanced electrochemical performance for sodium–oxygen batteries, J. Mater. Chem. A, 2015, 3, 2568.

[124] N. Zhao, X. Guo, Cell Chemistry of Sodium–Oxygen Batteries with Various Nonaqueous Electrolytes, J. Phys. Chem. C, 2015, 119, 25319.

[125] R. Tatara, G. M. Leverick, S. Feng, S. Wan, S. Terada, K. Dokko, M. Watanabe, Y. Shao-Horn, Tuning NaO2 Cube Sizes by Controlling Na+ and Solvent Activity in Na–O2 Batteries, J. Phys. Chem. C, 2018, 122, 18316.

[126] L. Lutz, W. Dachraoui, A. Demortiere, L. R. Johnson, P. G. Bruce, A. Grimaud, J. M. Tarascon, Operando Monitoring of the Solution-Mediated Discharge and Charge Processes in a Na-O2 Battery Using Liquid-Electrochemical Transmission Electron Microscopy, Nano Lett., 2018, 18, 1280.

[127] L. Lutz, D. A. D. Corte, Y. H. Chen, D. Batuk, L. R. Johnson, A. Abakumov, L. Yate, E. Azaceta, P. G. Bruce, J. M. Tarascon, A. Grimaud, The Role of the Electrode Surface in Na-Air Batteries: Insights in Electrochemical Product Formation and Chemical Growth of NaO2, Adv. Energy Mater., 2018, 8, 1701581.

[128] Y. Liu, X. Chi, Q. Han, Y. Du, J. Yang, Y. Liu, Vertically self-standing C@NiCo2O4 nanoneedle arrays as effective binder-free cathodes for rechargeable Na−O2 batteries, J. Alloys Compd., 2019, 772, 693.

[129] F. Wu, Y. Xing, J. Lai, X. Zhang, Y. Ye, J. Qian, L. Li, R. Chen, Micrometer-Sized RuO2 Catalysts Contributing to Formation of Amorphous Na-Deficient Sodium Peroxide in Na-O2 Batteries, Adv. Funct. Mater., 2017, 27, 1700632.

[130] B. Sun, K. Kretschmer, X. Xie, P. Munroe, Z. Peng, G. Wang, Hierarchical Porous Carbon Spheres for High-Performance Na-O2 Batteries, Adv. Mater., 2017, 29.

[131] L. Schafzahl, N. Mahne, B. Schafzahl, M. Wilkening, C. Slugovc, S. M. Borisov, S. A. Freunberger, Singlet Oxygen during Cycling of the Aprotic Sodium-O2 Battery, Angew. Chem., Int. Ed., 2017, 56, 15728.

[132] C. Xia, R. Fernandes, F. H. Cho, N. Sudhakar, B. Buonacorsi, S. Walker, M. Xu, J. Baugh, L. F. Nazar, Direct Evidence of Solution-Mediated Superoxide Transport and Organic Radical Formation in Sodium-Oxygen Batteries, J. Am. Chem. Soc., 2016, 138, 11219.

[133] V. Gutmann, Solvent effects on the reactivities of organometallic compounds, Coord. Chem. Rev., 1976, 18, 225.

[134] V. S. Bryantsev, V. Giordani, W. Walker, M. Blanco, S. Zecevic, K. Sasaki, J. Uddin, D. Addison, G. V. Chase, Predicting solvent stability in aprotic electrolyte Li-air batteries: nucleophilic substitution by the superoxide anion radical (O2(*-)), J. Phys. Chem. A, 2011, 115, 12399.

[135] J. Kim, H. D. Lim, H. Gwon, K. Kang, Sodium-oxygen batteries with alkyl-carbonate and ether based electrolytes, Phys. Chem. Chem. Phys., 2013, 15, 3623.

[136] C. O. Laoire, S. Mukerjee, K. M. Abraham, E. J. Plichta, M. A. Hendrickson, Influence of Nonaqueous Solvents on the Electrochemistry of Oxygen in the Rechargeable Lithium−Air Battery, J. Phys. Chem. C, 2010, 114, 9178.

[137] D. Bresser, E. Paillard, S. Passerini, Ionic Liquid-based Electrolytes for Li Metal/Air Batteries: A Review of Materials and the New 'LABOHR' Flow Cell Concept, J. Electrochem. Sci. Technol., 2014, 5, 37.

[138] Y. Katayama, K. Sekiguchi, M. Yamagata, T. Miura, Electrochemical behavior of oxygen/superoxide ion couple in 1-butyl-1-methylpyrrolidinium bis(trifluoromethylsulfonyl) imide room-temperature molten salt, J. Electrochem. Soc., 2005, 152, E247.

[139] M. Hayyan, F. S. Mjalli, M. A. Hashim, I. M. AlNashef, An investigation of the reaction between 1-butyl-3-methylimidazolium trifluoromethanesulfonate and superoxide ion, J. Mol. Liq., 2013, 181, 44.

[140] H. Nakamoto, Y. Suzuki, T. Shiotsuki, F. Mizuno, S. Higashi, K. Takechi, T. Asaoka, H. Nishikoori, H. Iba, Ether-functionalized ionic liquid electrolytes for lithium-air batteries, J. Power Sources, 2013, 243, 19.

[141] S. Higashi, Y. Kato, K. Takechi, H. Nakamoto, F. Mizuno, H. Nishikoori, H. Iba, T. Asaoka, Evaluation and analysis of Li-air battery using ether-functionalized ionic liquid, J. Power Sources, 2013, 240, 14.

[142] N. Mozhzhukhina, A. Y. Tesio, L. P. M. De Leo, E. J. Calvo, In Situ Infrared Spectroscopy Study of PYR14TFSI Ionic Liquid Stability for Li–O2Battery, J. Electrochem. Soc., 2017, 164, A518.

[143] P. M. Radjenovic, L. J. Hardwick, Time-resolved SERS study of the oxygen reduction reaction in ionic liquid electrolytes for non-aqueous lithium-oxygen cells, Faraday Discuss., 2018, 206, 379.

[144] M. Piana, J. Wandt, S. Meini, I. Buchberger, N. Tsiouvaras, H. A. Gasteiger, Stability of a Pyrrolidinium-Based Ionic Liquid in Li-O2 Cells, J. Electrochem. Soc., 2014, 161, A1992.

[145] S. K. Das, S. Xu, L. A. Archer, Carbon dioxide assist for non-aqueous sodium–oxygen batteries, Electrochem. Commun., 2013, 27, 59.

[146] G. A. Elia, J. Hassoun, W. J. Kwak, Y. K. Sun, B. Scrosati, F. Mueller, D. Bresser, S. Passerini, P. Oberhumer, N. Tsiouvaras, J. Reiter, An advanced lithium-air battery exploiting an ionic liquid-based electrolyte, Nano Lett., 2014, 14, 6572.

[147] S. Wu, J. Tang, F. Li, X. Liu, Y. Yamauchi, M. Ishida, H. Zhou, A Synergistic System for Lithium–Oxygen Batteries in Humid Atmosphere Integrating a

Composite Cathode and a Hydrophobic Ionic Liquid-Based Electrolyte, Adv. Funct. Mater., 2016, 26, 3291.

[148] A. R. Neale, P. Li, J. Jacquemin, P. Goodrich, S. C. Ball, R. G. Compton, C. Hardacre, Effect of cation structure on the oxygen solubility and diffusivity in a range of bis{(trifluoromethyl)sulfonyl}imide anion based ionic liquids for lithium-air battery electrolytes, Phys. Chem. Chem. Phys., 2016, 18, 11251.

[149] L. Cecchetto, M. Salomon, B. Scrosati, F. Croce, Study of a Li-air battery having an electrolyte solution formed by a mixture of an ether-based aprotic solvent and an ionic liquid, J. Power Sources, 2012, 213, 233.

[150] S. Monaco, F. Soavi, M. Mastragostino, Role of Oxygen Mass Transport in Rechargeable Li/O2 Batteries Operating with Ionic Liquids, J. Phys. Chem. Lett., 2013, 4, 1379.

[151] C. J. Allen, J. Hwang, R. Kautz, S. Mukerjee, E. J. Plichta, M. A. Hendrickson, K. M. Abraham, Oxygen Reduction Reactions in Ionic Liquids and the Formulation of a General ORR Mechanism for Li-Air Batteries, J. Phys. Chem. C, 2012, 116, 20755.

[152] C. O. Laoire, S. Mukerjee, K. M. Abraham, E. J. Plichta, M. A. Hendrickson, Elucidating the Mechanism of Oxygen Reduction for Lithium-Air Battery Applications, J. Phys. Chem. C, 2009, 113, 20127.

[153] A. Khetan, A. Luntz, V. Viswanathan, Trade-Offs in Capacity and Rechargeability in Nonaqueous Li-O2 Batteries: Solution-Driven Growth versus Nucleophilic Stability, J. Phys. Chem. Lett., 2015, 6, 1254.

[154] J. S. Wang, K. Matyjaszewski, Controlled Living Radical Polymerization - Atom-Transfer Radical Polymerization in the Presence of Transition-Metal Complexes, J. Am. Chem. Soc., 1995, 117, 5614.

[155] G. Du, Nanostructured anode materials for lithium-ion batteries, 2011.

[156] S. Xin, Z. Chang, X. Zhang, Y.-G. Guo, Progress of Rechargeable Lithium Metal Batteries Based on Conversion Reactions, Natl. Sci. Rev., 2016, 4, 1759.

[157] J. R. Dahn, T. Zheng, Y. H. Liu, J. S. Xue, Mechanisms for Lithium Insertion in Carbonaceous Materials, Science, 1995, 270, 590.

[158] W. Xiao, J. Zhou, L. Yu, D. Wang, X. W. Lou, Electrolytic Formation of Crystalline Silicon/Germanium Alloy Nanotubes and Hollow Particles with Enhanced Lithium-Storage Properties, Angew. Chem., Int. Ed., 2016, 55, 7427.

[159] T. Kennedy, M. Brandon, K. M. Ryan, Advances in the Application of Silicon and Germanium Nanowires for High-Performance Lithium-Ion Batteries, Adv. Mater., 2016, 28, 5696.

[160] S. Wu, C. Han, J. Iocozzia, M. Lu, R. Ge, R. Xu, Z. Lin, Germanium-Based Nanomaterials for Rechargeable Batteries, Angew. Chem., Int. Ed., 2016, 55, 7898.

[161] K. H. Seng, M. H. Park, Z. P. Guo, H. K. Liu, J. Cho, Catalytic role of Ge in highly reversible GeO2/Ge/C nanocomposite anode material for lithium batteries, Nano Lett., 2013, 13, 1230.

[162] G. L. Cui, L. Gu, N. Kaskhedikar, P. A. van Aken, J. Maier, A novel germanium/carbon nanotubes nanocomposite for lithium storage material, Electrochim. Acta, 2010, 55, 985.

[163] D. J. Xue, S. Xin, Y. Yan, K. C. Jiang, Y. X. Yin, Y. G. Guo, L. J. Wan, Improving the electrode performance of Ge through Ge@C core-shell nanoparticles and graphene networks, J. Am. Chem. Soc., 2012, 134, 2512.

[164] X. Liu, J. Hao, X. Liu, C. Chi, N. Li, F. Endres, Y. Zhang, Y. Li, J. Zhao, Preparation of Ge nanotube arrays from an ionic liquid for lithium ion battery anodes with improved cycling stability, Chem. Commun., 2015, 51, 2064.

[165] W. Li, M. Li, Z. Yang, J. Xu, X. Zhong, J. Wang, L. Zeng, X. Liu, Y. Jiang, X.

Wei, L. Gu, Y. Yu, Carbon-Coated Germanium Nanowires on Carbon Nanofibers as Self-Supported Electrodes for Flexible Lithium-Ion Batteries, Small, 2015, 11, 2762.

[166] F. W. Yuan, H. J. Yang, H. Y. Tuan, Alkanethiol-passivated ge nanowires as high-performance anode materials for lithium-ion batteries: the role of chemical surface functionalization, ACS Nano, 2012, 6, 9932.

[167] J. Liu, K. Song, C. Zhu, C. C. Chen, P. A. van Aken, J. Maier, Y. Yu, Ge/C nanowires as high-capacity and long-life anode materials for Li-ion batteries, ACS Nano, 2014, 8, 7051.

[168] Z. Chen, Y. Yan, S. Xin, W. Li, J. Qu, Y. G. Guo, W. G. Song, Copper germanate nanowire/reduced graphene oxide anode materials for high energy lithium-ion batteries, J. Mater. Chem. A, 2013, 1, 11404.

[169] S. Xin, L. Yu, Y. You, H. P. Cong, Y. X. Yin, X. L. Du, Y. G. Guo, S. H. Yu, Y. Cui, J. B. Goodenough, The Electrochemistry with Lithium versus Sodium of Selenium Confined To Slit Micropores in Carbon, Nano Lett., 2016, 16, 4560.

[170] W. J. Yu, C. Liu, P. X. Hou, L. Zhang, X. Y. Shan, F. Li, H. M. Cheng, Lithiation of silicon nanoparticles confined in carbon nanotubes, ACS Nano, 2015, 9, 5063.

[171] J. Q. Hu, X. M. Meng, Y. Jiang, C. S. Lee, S. T. Lee, Fabrication of germanium-filled silica nanotubes and aligned silica nanofibers, Adv. Mater., 2003, 15, 70.

[172] A. Pandurangan, C. Morin, D. L. Qian, R. Andrews, M. Crocker, Single-step synthesis of germanium nanowires encapsulated within multi-walled carbon nanotubes, Carbon, 2009, 47, 1708.

[173] G. A. Domrachev, A. M. Ob'edkov, B. S. Kaverin, A. A. Zaitsev, S. N. Titova, A. I. Kirillov, A. S. Strahkov, S. Y. Ketkov, E. G. Domracheva, K. B. Zhogova,

MOCVD Synthesis of Germanium Filled “Diamondlike” Carbon Nanotubes and Microtubes from Organogermanium Precursors and Their Field-Emission Properties, Chem. Vap. Deposition, 2006, 12, 357.

[174] Y. Yu, L. Gu, C. Wang, A. Dhanabalan, P. A. van Aken, J. Maier, Encapsulation of Sn@carbon nanoparticles in bamboo-like hollow carbon nanofibers as an anode material in lithium-based batteries, Angew. Chem., Int. Ed., 2009, 48, 6485.

[175] X. S. Zhou, L. Yu, X. Y. Yu, X. W. Lou, Encapsulating Sn Nanoparticles in Amorphous Carbon Nanotubes for Enhanced Lithium Storage Properties, Adv. Energy Mater., 2016, 6, 1601177.

[176] S. Xin, Y. G. Guo, L. J. Wan, Nanocarbon networks for advanced rechargeable lithium batteries, Acc. Chem. Res., 2012, 45, 1759.

[177] B. Jiang, Y. He, B. Li, S. Zhao, S. Wang, Y. B. He, Z. Lin, Polymer-Templated Formation of Polydopamine-Coated SnO2 Nanocrystals: Anodes for Cyclable Lithium-Ion Batteries, Angew. Chem., Int. Ed., 2017, 56, 1869.

[178] B. Jiang, C. Han, B. Li, Y. He, Z. Lin, In-Situ Crafting of ZnFe(2)O(4) Nanoparticles Impregnated within Continuous Carbon Network as Advanced Anode Materials, ACS Nano, 2016, 10, 2728.

[179] S. Q. Zhao, Z. W. Wang, Y. J. He, B. B. Jiang, Y. W. Harn, X. Q. Liu, F. Q. Yu, F. Feng, Q. Shen, Z. Q. Lin, Interconnected Ni(HCO3)(2) Hollow Spheres Enabled by Self-Sacrificial Templating with Enhanced Lithium Storage Properties, ACS Energy Lett., 2017, 2, 111.

[180] K. F. Huo, L. Wang, C. J. Peng, X. Peng, Y. Y. Li, Q. W. Li, Z. Z. Jin, P. K. Chu, Crumpled N-doped carbon nanotubes encapsulated with peapod-like Ge nanoparticles for high-rate and long-life Li-ion battery anodes, J. Mater. Chem. A, 2016, 4, 7585.

[181] C. Wu, Y. Jiang, P. Kopold, P. A. van Aken, J. Maier, Y. Yu, Peapod-Like Carbon-Encapsulated Cobalt Chalcogenide Nanowires as Cycle-Stable and High-Rate Materials for Sodium-Ion Anodes, Adv. Mater., 2016, 28, 7276.

[182] C. Wu, P. Kopold, P. A. van Aken, J. Maier, Y. Yu, High Performance Graphene/Ni2P Hybrid Anodes for Lithium and Sodium Storage through 3D Yolk-Shell-Like Nanostructural Design, Adv. Mater., 2017, 29, 1604015.

[183] W. Li, Z. Yang, J. Cheng, X. Zhong, L. Gu, Y. Yu, Germanium nanoparticles encapsulated in flexible carbon nanofibers as self-supported electrodes for high performance lithium-ion batteries, Nanoscale, 2014, 6, 4532.

[184] S. C. Tsang, Y. K. Chen, P. J. F. Harris, M. L. H. Green, A Simple Chemical Method of Opening and Filling Carbon Nanotubes, Nature, 1994, 372, 159.

[185] R. Kreizman, S. Y. Hong, J. Sloan, R. Popovitz-Biro, A. Albu-Yaron, G. Tobias, B. Ballesteros, B. G. Davis, M. L. Green, R. Tenne, Core-shell PbI2@WS2 inorganic nanotubes from capillary wetting, Angew. Chem., Int. Ed., 2009, 48, 1230.

[186] G. Zheng, Q. Zhang, J. J. Cha, Y. Yang, W. Li, Z. W. Seh, Y. Cui, Amphiphilic surface modification of hollow carbon nanofibers for improved cycle life of lithium sulfur batteries, Nano Lett., 2013, 13, 1265.

[187] M. Haft, M. Gronke, M. Gellesch, S. Wurmehl, B. Buchner, M. Mertig, S. Hampel, Tailored nanoparticles and wires of Sn, Ge and Pb inside carbon nanotubes, Carbon, 2016, 101, 352.

[188] Y. Wu, X. Qiu, F. Liang, Q. Zhang, A. Koo, Y. Dai, Y. Lei, X. Sun, A metal-organic framework-derived bifunctional catalyst for hybrid sodium-air batteries, Appl. Catal., B, 2019, 241, 407.

[189] T. Prem Kumar, R. Ramesh, Y. Y. Lin, G. T.-K. Fey, Tin-filled carbon nanotubes as insertion anode materials for lithium-ion batteries, Electrochem.

Commun., 2004, 6, 520.

[190] D. Ugarte, A. Chatelain, W. A. de Heer, Nanocapillarity and Chemistry in Carbon Nanotubes, Science, 1996, 274, 1897.

[191] E. Dujardin, T. W. Ebbesen, H. Hiura, K. Tanigaki, Capillarity and wetting of carbon nanotubes, Science, 1994, 265, 1850.

[192] A. Mizev, A. Trofimenko, D. Schwabe, A. Viviani, Instability of Marangoni flow in the presence of an insoluble surfactant. Experiments, Eur. Phys. J.: Spec. Top., 2013, 219, 89.

[193] M. Li, W. G. Li, J. Liu, J. S. Yao, Preparation and characterization of PPy with methyl orange as soft template, J. Mater. Sci.: Mater. Electron., 2013, 24, 906.

[194] E. Kim, Y. Xia, G. M. Whitesides, Micromolding in Capillaries: Applications in Materials Science, J. Am. Chem. Soc., 1996, 118, 5722.

[195] Y. Xiao, M. Cao, Freeze-drying-assisted synthesis of hierarchically porous carbon/germanium hybrid for high-efficiency lithium-ion batteries, Chem. - Asian J., 2014, 9, 2859.

[196] C. Zhong, J.-Z. Wang, X.-W. Gao, D. Wexler, H.-K. Liu, In situ one-step synthesis of a 3D nanostructured germanium–graphene composite and its application in lithium-ion batteries, J. Mater. Chem. A, 2013, 1, 10798.

[197] S. Fang, L. Shen, H. Zheng, X. Zhang, Ge–graphene–carbon nanotube composite anode for high performance lithium-ion batteries, J. Mater. Chem. A, 2015, 3, 1498.

[198] Y. Xu, X. S. Zhu, X. S. Zhou, X. Liu, Y. X. Liu, Z. H. Dai, J. C. Bao, Ge Nanoparticles Encapsulated in Nitrogen-Doped Reduced Graphene Oxide as an Advanced Anode Material for Lithium-ion Batteries, J. Phys. Chem. C, 2014, 118, 28502.

[199] C. Yan, W. Xi, W. Si, J. Deng, O. G. Schmidt, Highly conductive and strain-

released hybrid multilayer Ge/Ti nanomembranes with enhanced lithium-ion-storage capability, Adv. Mater., 2013, 25, 539.

[200] X. H. Liu, S. Huang, S. T. Picraux, J. Li, T. Zhu, J. Y. Huang, Reversible Nanopore Formation in Ge Nanowires during Lithiation–Delithiation Cycling: An In Situ Transmission Electron Microscopy Study, Nano Lett., 2011, 11, 3991.

[201] D. S. Bin, Z. X. Chi, Y. Li, K. Zhang, X. Yang, Y. G. Sun, J. Y. Piao, A. M. Cao, L. J. Wan, Controlling the Compositional Chemistry in Single Nanoparticles for Functional Hollow Carbon Nanospheres, J. Am. Chem. Soc., 2017, 139, 13492.

[202] Y.-X. Wang, J. Yang, S.-L. Chou, H. K. Liu, W.-x. Zhang, D. Zhao, S. X. Dou, Uniform yolk-shell iron sulfide–carbon nanospheres for superior sodium–iron sulfide batteries, Nat. Commun., 2015, 6, 8689.

[203] J. Liu, P. Kopold, C. Wu, P. A. van Aken, J. Maier, Y. Yu, Uniform yolk-shell Sn4P3@C nanospheres as high-capacity and cycle-stable anode materials for sodium-ion batteries, Energy Environ. Sci., 2015, 8, 3531.

[204] N. Liu, H. Wu, M. T. McDowell, Y. Yao, C. Wang, Y. Cui, A yolk-shell design for stabilized and scalable li-ion battery alloy anodes, Nano Lett., 2012, 12, 3315.

[205] J. Liu, S. Z. Qiao, S. Budi Hartono, G. Q. M. Lu, Monodisperse Yolk-Shell Nanoparticles with a Hierarchical Porous Structure for Delivery Vehicles and Nanoreactors, Angew. Chem., Int. Ed., 2010, 49, 4981.

[206] J. Liu, S. Z. Qiao, J. S. Chen, X. W. Lou, X. Xing, G. Q. Lu, Yolk/shell nanoparticles: new platforms for nanoreactors, drug delivery and lithium-ion batteries, Chem. Commun., 2011, 47, 12578.

[207] L. Cao, D. Chen, R. A. Caruso, Surface-metastable phase-initiated seeding and

ostwald ripening: a facile fluorine-free process towards spherical fluffy core/shell, yolk/shell, and hollow anatase nanostructures, Angew. Chem., Int. Ed., 2013, 52, 10986.

[208] X. J. Wu, D. Xu, Soft template synthesis of yolk/silica shell particles, Adv. Mater., 2010, 22, 1516.

[209] L. Y. Yang, H. Z. Li, J. Liu, Z. Q. Sun, S. S. Tang, M. Lei, Dual yolk-shell structure of carbon and silica-coated silicon for high-performance lithium-ion batteries, Sci. Rep., 2015, 5, 10908.

[210] L. Liu, P. C. Du, X. B. Zhao, J. Zeng, P. Liu, Independent temperature and pH dual-stimuli responsive yolk/shell polymer microspheres for controlled release: Structural effect, Eur. Polym. J., 2015, 69, 540.

[211] H. Wu, G. Yu, L. Pan, N. Liu, M. T. McDowell, Z. Bao, Y. Cui, Stable Li-ion battery anodes by in-situ polymerization of conducting hydrogel to conformally coat silicon nanoparticles, Nat. Commun., 2013, 4, 1943.

[212] C. Wang, H. Wu, Z. Chen, M. T. McDowell, Y. Cui, Z. Bao, Self-healing chemistry enables the stable operation of silicon microparticle anodes for high-energy lithium-ion batteries, Nat. Chem., 2013, 5, 1042.

[213] J. Ma, J. Sung, J. Hong, S. Chae, N. Kim, S. H. Choi, G. Nam, Y. Son, S. Y. Kim, M. Ko, J. Cho, Towards maximized volumetric capacity via pore-coordinated design for large-volume-change lithium-ion battery anodes, Nat. Commun., 2019, 10, 475.

[214] L. Zhang, R. Rajagopalan, H. P. Guo, X. L. Hu, S. X. Dou, H. K. Liu, A Green and Facile Way to Prepare Granadilla-Like Silicon-Based Anode Materials for Li-Ion Batteries, Adv. Funct. Mater., 2016, 26, 440.

[215] Y. Son, S. Sim, H. Ma, M. Choi, Y. Son, N. Park, J. Cho, M. Park, Exploring Critical Factors Affecting Strain Distribution in 1D Silicon-Based

Nanostructures for Lithium-Ion Battery Anodes, Adv. Mater., 2018, 30, e1705430.

[216] J. Liu, Y. Yang, P. Lyu, P. Nachtigall, Y. Xu, Few-Layer Silicene Nanosheets with Superior Lithium-Storage Properties, Adv. Mater., 2018, 30, e1800838.

[217] Z. L. Li, H. L. Zhao, P. P. Lv, Z. J. Zhang, Y. Zhang, Z. H. Du, Y. Q. Teng, L. N. Zhao, Z. M. Zhu, Watermelon-Like Structured SiOx-TiO2@C Nanocomposite as a High-Performance Lithium-Ion Battery Anode, Adv. Funct. Mater., 2018, 28, 1605711.

[218] G. R. Zheng, Y. X. Xiang, L. F. Xu, H. Luo, B. L. Wang, Y. Liu, X. Han, W. M. Zhao, S. J. Chen, H. L. Chen, Q. B. Zhang, T. Zhu, Y. Yang, Controlling Surface Oxides in Si/C Nanocomposite Anodes for High-Performance Li-Ion Batteries, Adv. Energy Mater., 2018, 8, 1801718.

[219] T. Liu, L. Qu, K. Qian, J. Liu, Q. Zhang, L. Liu, S. Liu, Raspberry-like hollow carbon nanospheres with enhanced matrix-free peptide detection profiles, Chem. Commun., 2016, 52, 1709.

[220] P. Gao, X. Huang, Y. Zhao, X. Hu, D. Cen, G. Gao, Z. Bao, Y. Mei, Z. Di, G. Wu, Formation of Si Hollow Structures as Promising Anode Materials through Reduction of Silica in AlCl3-NaCl Molten Salt, ACS Nano, 2018, 12, 11481.

[221] J. P. Yang, Y. X. Wang, S. L. Chou, R. Y. Zhang, Y. F. Xu, J. W. Fan, W. X. Zhang, H. K. Liu, D. Y. Zhao, S. X. Dou, Yolk-shell silicon-mesoporous carbon anode with compact solid electrolyte interphase film for superior lithium-ion batteries, Nano Energy, 2015, 18, 133.

[222] N. Liu, H. Wu, M. T. McDowell, Y. Yao, C. Wang, Y. Cui, A yolk-shell design for stabilized and scalable li-ion battery alloy anodes, Nano Lett., 2012, 12, 3315.

[223] S. Guo, X. Hu, Y. Hou, Z. Wen, Tunable Synthesis of Yolk-Shell Porous

Silicon@Carbon for Optimizing Si/C-Based Anode of Lithium-Ion Batteries, ACS Applied Materials & Interfaces, 2017, 9, 42084.

[224] Y. Liu, Z. Tai, T. Zhou, V. Sencadas, J. Zhang, L. Zhang, K. Konstantinov, Z. Guo, H. K. Liu, An All-Integrated Anode via Interlinked Chemical Bonding between Double-Shelled-Yolk-Structured Silicon and Binder for Lithium-Ion Batteries, Adv. Mater., 2017, 29, 1703028.

[225] Y. Jin, S. Li, A. Kushima, X. Q. Zheng, Y. M. Sun, J. Xie, J. Sun, W. J. Xue, G. M. Zhou, J. Wu, F. F. Shi, R. F. Zhang, Z. Zhu, K. P. So, Y. Cui, J. Li, Self-healing SEI enables full-cell cycling of a silicon-majority anode with a coulombic efficiency exceeding 99.9%, Energy Environ. Sci., 2017, 10, 580.

[226] L. F. Cui, R. Ruffo, C. K. Chan, H. Peng, Y. Cui, Crystalline-amorphous core-shell silicon nanowires for high capacity and high current battery electrodes, Nano Lett., 2009, 9, 491.

[227] T. H. Hwang, Y. M. Lee, B. S. Kong, J. S. Seo, J. W. Choi, Electrospun core-shell fibers for robust silicon nanoparticle-based lithium ion battery anodes, Nano Lett., 2012, 12, 802.

[228] Y. H. Xu, G. P. Yin, Y. L. Ma, P. J. Zuo, X. Q. Cheng, Nanosized core/shell silicon@carbon anode material for lithium ion batteries with polyvinylidene fluoride as carbon source, J. Mater. Chem., 2010, 20, 3216.

[229] H. Yoo, J. I. Lee, H. Kim, J. P. Lee, J. Cho, S. Park, Helical silicon/silicon oxide core-shell anodes grown onto the surface of bulk silicon, Nano Lett., 2011, 11, 4324.

[230] G. Jeong, J.-G. Kim, M.-S. Park, M. Seo, S. M. Hwang, Y.-U. Kim, Y.-J. Kim, J. H. Kim, S. X. Dou, Core–Shell Structured Silicon Nanoparticles@TiO2–x/Carbon Mesoporous Microfiber Composite as a Safe and High-Performance Lithium-Ion Battery Anode, ACS Nano, 2014, 8, 2977.

[231] J. Xie, L. Tong, L. W. Su, Y. W. Xu, L. B. Wang, Y. H. Wang, Core-shell yolk-shell Si@C@Void@C nanohybrids as advanced lithium ion battery anodes with good electronic conductivity and corrosion resistance, J. Power Sources, 2017, 342, 529.

[232] Z. Cai, L. Xu, M. Yan, C. Han, L. He, K. M. Hercule, C. Niu, Z. Yuan, W. Xu, L. Qu, K. Zhao, L. Mai, Manganese oxide/carbon yolk-shell nanorod anodes for high capacity lithium batteries, Nano Lett., 2015, 15, 738.

[233] M.-H. Lin, S. Hy, C.-Y. Chen, J.-H. Cheng, J. Rick, N.-W. Pu, W.-N. Su, Y.-C. Lee, B.-J. Hwang, Resilient Yolk-Shell Silicon-Reduced Graphene Oxide/Amorphous Carbon Anode Material from a Synergistic Dual-Coating Process for Lithium-Ion Batteries, ChemElectroChem, 2016, 3, 1446.

[234] H. Zhang, L. Zhou, O. Noonan, D. J. Martin, A. K. Whittaker, C. Yu, Tailoring the Void Size of Iron Oxide@Carbon Yolk-Shell Structure for Optimized Lithium Storage, Adv. Funct. Mater., 2014, 24, 4337.

[235] J. Liu, H. Q. Yang, F. Kleitz, Z. G. Chen, T. Yang, E. Strounina, G. Q. M. Lu, S. Z. Qiao, Yolk-Shell Hybrid Materials with a Periodic Mesoporous Organosilica Shell: Ideal Nanoreactors for Selective Alcohol Oxidation, Adv. Funct. Mater., 2012, 22, 591.

[236] P. Zhang, Y. Zhao, X. Zhang, Functional and stability orientation synthesis of materials and structures in aprotic Li-O2 batteries, Chem. Soc. Rev., 2018, 47, 2921.

[237] L. Ma, T. Yu, E. Tzoganakis, K. Amine, T. Wu, Z. Chen, J. Lu, Fundamental Understanding and Material Challenges in Rechargeable Nonaqueous Li-O2 Batteries: Recent Progress and Perspective, Adv. Energy Mater., 2018, 8, 1800348.

[238] S. X. Yang, P. He, H. S. Zhou, Research progresses on materials and electrode

design towards key challenges of Li-air batteries, Energy Storage Materials, 2018, 13, 29.

[239] J. Wang, Y. Li, X. Sun, Challenges and opportunities of nanostructured materials for aprotic rechargeable lithium–air batteries, Nano Energy, 2013, 2, 443.

[240] H. Guo, W. Luo, J. Chen, S. Chou, H. Liu, J. Wang, Review of Electrolytes in Nonaqueous Lithium-Oxygen Batteries, Adv. Sustainable Syst., 2018, 2, 1700183.

[241] W. B. Luo, X. W. Gao, S. L. Chou, J. Z. Wang, H. K. Liu, Porous AgPd-Pd Composite Nanotubes as Highly Efficient Electrocatalysts for Lithium-Oxygen Batteries, Adv. Mater., 2015, 27, 6862.

[242] Z. Peng, S. A. Freunberger, Y. Chen, P. G. Bruce, A reversible and higher-rate Li-O2 battery, Science, 2012, 337, 563.

[243] Y. Chen, X. Gao, L. R. Johnson, P. G. Bruce, Kinetics of lithium peroxide oxidation by redox mediators and consequences for the lithium-oxygen cell, Nat. Commun., 2018, 9, 767.

[244] W. B. Luo, T. V. Pham, H. P. Guo, H. K. Liu, S. X. Dou, Three-Dimensional Array of TiN@Pt3Cu Nanowires as an Efficient Porous Electrode for the Lithium-Oxygen Battery, ACS Nano, 2017, 11, 1747.

[245] H. Yadegari, Q. Sun, X. Sun, Sodium-Oxygen Batteries: A Comparative Review from Chemical and Electrochemical Fundamentals to Future Perspective, Adv. Mater., 2016, 28, 7065.

[246] P. Hartmann, C. L. Bender, M. Vracar, A. K. Durr, A. Garsuch, J. Janek, P. Adelhelm, A rechargeable room-temperature sodium superoxide (NaO2) battery, Nat. Mater., 2013, 12, 228.

[247] N. Li, Y. Yin, F. Meng, Q. Zhang, J. Yan, Q. Jiang, Enabling Pyrochlore-Type

Oxides as Highly Efficient Electrocatalysts for High-Capacity and Stable Na–O2 Batteries: The Synergy of Electronic Structure and Morphology, ACS Catal., 2017, 7, 7688.

[248] H. Yadegari, C. J. Franko, M. N. Banis, Q. Sun, R. Li, G. R. Goward, X. Sun, How to Control the Discharge Products in Na-O2 Cells: Direct Evidence toward the Role of Functional Groups at the Air Electrode Surface, J. Phys. Chem. Lett., 2017, 8, 4794.

[249] H. Yadegari, Y. Li, M. N. Banis, X. Li, B. Wang, Q. Sun, R. Li, T.-K. Sham, X. Cui, X. Sun, On rechargeability and reaction kinetics of sodium–air batteries, Energy Environ. Sci., 2014, 7, 3747.

[250] N. Ortiz-Vitoriano, T. P. Batcho, D. G. Kwabi, B. Han, N. Pour, K. P. Yao, C. V. Thompson, Y. Shao-Horn, Rate-Dependent Nucleation and Growth of NaO2 in Na-O2 Batteries, J. Phys. Chem. Lett., 2015, 6, 2636.

[251] P. Hartmann, M. Heinemann, C. L. Bender, K. Graf, R. P. Baumann, P. Adelhelm, C. Heiliger, J. Janek, Discharge and Charge Reaction Paths in Sodium-Oxygen Batteries: Does NaO2 Form by Direct Electrochemical Growth or by Precipitation from Solution?, J. Phys. Chem. C, 2015, 119, 22778.

[252] R. Pinedo, D. A. Weber, B. Bergner, D. Schröder, P. Adelhelm, J. Janek, Insights into the Chemical Nature and Formation Mechanisms of Discharge Products in Na–O2 Batteries by Means of Operando X-ray Diffraction, J. Phys. Chem. C, 2016, 120, 8472.

[253] C. Xia, R. Black, R. Fernandes, B. Adams, L. F. Nazar, The critical role of phase-transfer catalysis in aprotic sodium oxygen batteries, Nat. Chem., 2015, 7, 496.

[254] J. Kim, H. Park, B. Lee, W. M. Seong, H. D. Lim, Y. Bae, H. Kim, W. K. Kim,

K. H. Ryu, K. Kang, Dissolution and ionization of sodium superoxide in sodium-oxygen batteries, Nat. Commun., 2016, 7, 10670.

[255] S. Kang, Y. Mo, S. P. Ong, G. Ceder, Nanoscale stabilization of sodium oxides: implications for Na-O2 batteries, Nano Lett., 2014, 14, 1016.

[256] S. Chen, J. Duan, M. Jaroniec, S. Z. Qiao, Nitrogen and oxygen dual-doped carbon hydrogel film as a substrate-free electrode for highly efficient oxygen evolution reaction, Adv. Mater., 2014, 26, 2925.

[257] S. Zhao, D. W. Wang, R. Amal, L. Dai, Carbon-Based Metal-Free Catalysts for Key Reactions Involved in Energy Conversion and Storage, Adv. Mater., 2019, 31, e1801526.

[258] J. Wang, H. X. Zhong, Z. L. Wang, F. L. Meng, X. B. Zhang, Integrated Three-Dimensional Carbon Paper/Carbon Tubes/Cobalt-Sulfide Sheets as an Efficient Electrode for Overall Water Splitting, ACS Nano, 2016, 10, 2342.

[259] L. Xia, Q. F. Zhang, C. Wu, Y. R. Liu, M. Ding, J. Y. Ye, Y. H. Cheng, C. K. Jia, Graphene coated carbon felt as a high-performance electrode for all vanadium redox flow batteries, Surf. Coat. Technol., 2019, 358, 153.

[260] J. Liang, Y. Jiao, M. Jaroniec, S. Z. Qiao, Sulfur and nitrogen dual-doped mesoporous graphene electrocatalyst for oxygen reduction with synergistically enhanced performance, Angew. Chem., Int. Ed., 2012, 51, 11496.

[261] J. Liang, X. Du, C. Gibson, X. W. Du, S. Z. Qiao, N-doped graphene natively grown on hierarchical ordered porous carbon for enhanced oxygen reduction, Adv. Mater., 2013, 25, 6226.

[262] Y. Zheng, Y. Jiao, L. Ge, M. Jaroniec, S. Z. Qiao, Two-step boron and nitrogen doping in graphene for enhanced synergistic catalysis, Angew. Chem., Int. Ed., 2013, 52, 3110.

[263] Y. Jiao, Y. Zheng, M. Jaroniec, S. Z. Qiao, Origin of the electrocatalytic

oxygen reduction activity of graphene-based catalysts: a roadmap to achieve the best performance, J. Am. Chem. Soc., 2014, 136, 4394.

[264] K. Gong, F. Du, Z. Xia, M. Durstock, L. Dai, Nitrogen-doped carbon nanotube arrays with high electrocatalytic activity for oxygen reduction, Science, 2009, 323, 760.

[265] K. Li, S. Chen, S. Chen, X. Liu, W. Pan, J. Zhang, Nitrogen, phosphorus co-doped carbon cloth as self-standing electrode for lithium-iodine batteries, Nano Res., 2018, 12, 549.

[266] Q. Sun, J. Liu, B. Xiao, B. Wang, M. Banis, H. Yadegari, K. R. Adair, R. Li, X. Sun, Visualizing the Oxidation Mechanism and Morphological Evolution of the Cubic-Shaped Superoxide Discharge Product in Na–Air Batteries, Adv. Funct. Mater., 0, 1808332.

[267] G. R. Bhimanapati, Z. Lin, V. Meunier, Y. Jung, J. Cha, S. Das, D. Xiao, Y. Son, M. S. Strano, V. R. Cooper, L. Liang, S. G. Louie, E. Ringe, W. Zhou, S. S. Kim, R. R. Naik, B. G. Sumpter, H. Terrones, F. Xia, Y. Wang, J. Zhu, D. Akinwande, N. Alem, J. A. Schuller, R. E. Schaak, M. Terrones, J. A. Robinson, Recent Advances in Two-Dimensional Materials beyond Graphene, ACS Nano, 2015, 9, 11509.

[268] C. Tan, X. Cao, X. J. Wu, Q. He, J. Yang, X. Zhang, J. Chen, W. Zhao, S. Han, G. H. Nam, M. Sindoro, H. Zhang, Recent Advances in Ultrathin Two-Dimensional Nanomaterials, Chem. Rev., 2017, 117, 6225.

[269] M. Chhowalla, Z. Liu, H. Zhang, Two-dimensional transition metal dichalcogenide (TMD) nanosheets, Chem. Soc. Rev., 2015, 44, 2584.

[270] Y. Dou, L. Zhang, X. Xu, Z. Sun, T. Liao, S. X. Dou, Atomically thin non-layered nanomaterials for energy storage and conversion, Chem. Soc. Rev., 2017, 46, 7338.

[271] A. H. Khan, S. Ghosh, B. Pradhan, A. Dalui, L. K. Shrestha, S. Acharya, K. Ariga, Two-Dimensional (2D) Nanomaterials towards Electrochemical Nanoarchitectonics in Energy-Related Applications, Bull. Chem. Soc. Jpn., 2017, 90, 627.

[272] P. Chen, Z. Zhang, X. Duan, X. Duan, Chemical synthesis of two-dimensional atomic crystals, heterostructures and superlattices, Chem. Soc. Rev., 2018, 47, 3129.

[273] S. Z. Butler, S. M. Hollen, L. Cao, Y. Cui, J. A. Gupta, H. R. Gutierrez, T. F. Heinz, S. S. Hong, J. Huang, A. F. Ismach, E. Johnston-Halperin, M. Kuno, V. V. Plashnitsa, R. D. Robinson, R. S. Ruoff, S. Salahuddin, J. Shan, L. Shi, M. G. Spencer, M. Terrones, W. Windl, J. E. Goldberger, Progress, challenges, and opportunities in two-dimensional materials beyond graphene, ACS Nano, 2013, 7, 2898.

[274] H. Zhang, Ultrathin Two-Dimensional Nanomaterials, ACS Nano, 2015, 9, 9451.

[275] Y. Shi, H. Li, L. J. Li, Recent advances in controlled synthesis of two-dimensional transition metal dichalcogenides via vapour deposition techniques, Chem. Soc. Rev., 2015, 44, 2744.

[276] C. Tan, H. Zhang, Two-dimensional transition metal dichalcogenide nanosheet-based composites, Chem. Soc. Rev., 2015, 44, 2713.

[277] F. M. Auxilia, S. Ishihara, S. Mandal, T. Tanabe, G. Saravanan, G. V. Ramesh, N. Umezawa, T. Hara, Y. Xu, S. Hishita, Y. Yamauchi, A. Dakshanamoorthy, J. P. Hill, K. Ariga, H. Abe, Low-temperature remediation of NO catalyzed by interleaved CuO nanoplates, Adv. Mater., 2014, 26, 4481.

[278] K. X. Wang, M. D. Wei, M. A. Morris, H. S. Zhou, J. D. Holmes, Mesoporous titania nanotubes: Their preparation and application as electrode materials for

rechargeable lithium batteries, Adv. Mater., 2007, 19, 3016.

[279] X. Xia, Y. Wang, A. Ruditskiy, Y. Xia, 25th anniversary article: galvanic replacement: a simple and versatile route to hollow nanostructures with tunable and well-controlled properties, Adv. Mater., 2013, 25, 6313.

[280] J. X. Feng, H. Xu, Y. T. Dong, S. H. Ye, Y. X. Tong, G. R. Li, FeOOH/Co/FeOOH Hybrid Nanotube Arrays as High-Performance Electrocatalysts for the Oxygen Evolution Reaction, Angew. Chem., Int. Ed., 2016, 55, 3694.

[281] J. X. Feng, S. H. Ye, H. Xu, Y. X. Tong, G. R. Li, Design and Synthesis of FeOOH/CeO2 Heterolayered Nanotube Electrocatalysts for the Oxygen Evolution Reaction, Adv. Mater., 2016, 28, 4698.

[282] X. F. Lu, L. F. Gu, J. W. Wang, J. X. Wu, P. Q. Liao, G. R. Li, Bimetal-Organic Framework Derived CoFe2 O4 /C Porous Hybrid Nanorod Arrays as High-Performance Electrocatalysts for Oxygen Evolution Reaction, Adv. Mater., 2017, 29, 1604437.

[283] S. H. Ye, Z. X. Shi, J. X. Feng, Y. X. Tong, G. R. Li, Activating CoOOH Porous Nanosheet Arrays by Partial Iron Substitution for Efficient Oxygen Evolution Reaction, Angew. Chem., Int. Ed., 2018, 57, 2672.

[284] Y. Sun, S. Gao, F. Lei, Y. Xie, Atomically-thin two-dimensional sheets for understanding active sites in catalysis, Chem. Soc. Rev., 2015, 44, 623.

[285] D. Chen, L. Peng, Y. Yuan, Y. Zhu, Z. Fang, C. Yan, G. Chen, R. Shahbazian-Yassar, J. Lu, K. Amine, G. Yu, Two-Dimensional Holey Co3O4 Nanosheets for High-Rate Alkali-Ion Batteries: From Rational Synthesis to in Situ Probing, Nano Lett., 2017, 17, 3907.

[286] X. Duan, C. Wang, A. Pan, R. Yu, X. Duan, Two-dimensional transition metal dichalcogenides as atomically thin semiconductors: opportunities and

challenges, Chem. Soc. Rev., 2015, 44, 8859.

[287] W. B. Luo, X. W. Gao, D. Q. Shi, S. L. Chou, J. Z. Wang, H. K. Liu, Binder-Free and Carbon-Free 3D Porous Air Electrode for Li-O2 Batteries with High Efficiency, High Capacity, and Long Life, Small, 2016, 12, 3031.

[288] P. Wang, Z. Pu, Y. Li, L. Wu, Z. Tu, M. Jiang, Z. Kou, I. S. Amiinu, S. Mu, Iron-Doped Nickel Phosphide Nanosheet Arrays: An Efficient Bifunctional Electrocatalyst for Water Splitting, ACS Appl. Mater. Interfaces, 2017, 9, 26001.

[289] Z. Pu, I. S. Amiinu, C. Zhang, M. Wang, Z. Kou, S. Mu, Phytic acid-derivative transition metal phosphides encapsulated in N,P-codoped carbon: an efficient and durable hydrogen evolution electrocatalyst in a wide pH range, Nanoscale, 2017, 9, 3555.

[290] Z. H. Pu, Y. Xue, W. Q. Li, I. S. Amiinu, S. C. Mu, Efficient water splitting catalyzed by flexible NiP2 nanosheet array electrodes under both neutral and alkaline solutions, New J. Chem., 2017, 41, 2154.

[291] Z. Pu, C. Zhang, I. S. Amiinu, W. Li, L. Wu, S. Mu, General Strategy for the Synthesis of Transition-Metal Phosphide/N-Doped Carbon Frameworks for Hydrogen and Oxygen Evolution, ACS Appl. Mater. Interfaces, 2017, 9, 16187.

[292] P. Chen, T. Zhou, L. Xing, K. Xu, Y. Tong, H. Xie, L. Zhang, W. Yan, W. Chu, C. Wu, Y. Xie, Atomically Dispersed Iron-Nitrogen Species as Electrocatalysts for Bifunctional Oxygen Evolution and Reduction Reactions, Angew. Chem., Int. Ed., 2017, 56, 610.

[293] B. Konkena, J. Masa, A. J. R. Botz, I. Sinev, W. Xia, J. Koßmann, R. Drautz, M. Muhler, W. Schuhmann, Metallic NiPS3@NiOOH Core–Shell Heterostructures as Highly Efficient and Stable Electrocatalyst for the Oxygen

Evolution Reaction, ACS Catal., 2016, 7, 229.

[294] W. B. Luo, S. L. Chou, J. Z. Wang, Y. C. Zhai, H. K. Liu, A Metal-Free, Free-Standing, Macroporous Graphene@g-C(3)N(4) Composite Air Electrode for High-Energy Lithium Oxygen Batteries, Small, 2015, 11, 2817.

[295] K. Xu, H. Ding, H. F. Lv, S. Tao, P. Z. Chen, X. J. Wu, W. S. Chu, C. Z. Wu, Y. Xie, Understanding Structure-Dependent Catalytic Performance of Nickel Selenides for Electrochemical Water Oxidation, ACS Catal., 2017, 7, 310.

[296] G.-F. Chen, T. Y. Ma, Z.-Q. Liu, N. Li, Y.-Z. Su, K. Davey, S.-Z. Qiao, Efficient and Stable Bifunctional Electrocatalysts Ni/NixMy (M = P, S) for Overall Water Splitting, Adv. Funct. Mater., 2016, 26, 3314.

[297] F. Yu, H. Q. Zhou, Z. Zhu, J. Y. Sun, R. He, J. M. Bao, S. Chen, Z. F. Ren, Three-Dimensional Nanoporous Iron Nitride Film as an Efficient Electrocatalyst for Water Oxidation, ACS Catal., 2017, 7, 2052.

[298] B. Zhang, C. Xiao, S. Xie, J. Liang, X. Chen, Y. Tang, Iron–Nickel Nitride Nanostructures in Situ Grown on Surface-Redox-Etching Nickel Foam: Efficient and Ultrasustainable Electrocatalysts for Overall Water Splitting, Chem. Mater., 2016, 28, 6934.

[299] J. Yu, Q. Q. Li, Y. Li, C. Y. Xu, L. Zhen, V. P. Dravid, J. S. Wu, Ternary Metal Phosphide with Triple-Layered Structure as a Low-Cost and Efficient Electrocatalyst for Bifunctional Water Splitting, Adv. Funct. Mater., 2016, 26, 7644.

[300] J. G. Chen, C. W. Jones, S. Linic, V. R. Stamenkovic, Best Practices in Pursuit of Topics in Heterogeneous Electrocatalysis, ACS Catal., 2017, 7, 6392.

[301] P. P. Lopes, D. Strmcnik, D. Tripkovic, J. G. Connell, V. Stamenkovic, N. M. Markovic, Relationships between Atomic Level Surface Structure and Stability/Activity of Platinum Surface Atoms in Aqueous Environments, ACS

Catal., 2016, 6, 2536.

[302] L. Yang, Y. L. Lv, D. P. Cao, Co,N-codoped nanotube/graphene 1D/2D heterostructure for efficient oxygen reduction and hydrogen evolution reactions, J. Mater. Chem. A, 2018, 6, 3926.

[303] M. Y. Gao, J. R. Zeng, Q. B. Zhang, C. Yang, X. T. Li, Y. X. Hua, C. Y. Xu, Scalable one-step electrochemical deposition of nanoporous amorphous S-doped NiFe2O4/Ni3Fe composite films as highly efficient electrocatalysts for oxygen evolution with ultrahigh stability, J. Mater. Chem. A, 2018, 6, 1551.

[304] K. Xu, P. Chen, X. Li, Y. Tong, H. Ding, X. Wu, W. Chu, Z. Peng, C. Wu, Y. Xie, Metallic nickel nitride nanosheets realizing enhanced electrochemical water oxidation, J. Am. Chem. Soc., 2015, 137, 4119.

[305] S. W. Li, Y. C. Wang, S. J. Peng, L. J. Zhang, A. M. Al-Enizi, H. Zhang, X. H. Sun, G. F. Zheng, Co-Ni-Based Nanotubes/Nanosheets as Efficient Water Splitting Electrocatalysts, Adv. Energy Mater., 2016, 6, 1501661.

[306] Y. Yang, H. L. Fei, G. D. Ruan, Y. L. Li, J. M. Tour, Vertically Aligned WS2 Nanosheets for Water Splitting, Adv. Funct. Mater., 2015, 25, 6199.

[307] D. Q. Gao, J. Y. Zhang, T. T. Wang, W. Xiao, K. Tao, D. S. Xue, J. Ding, Metallic Ni3N nanosheets with exposed active surface sites for efficient hydrogen evolution, J. Mater. Chem. A, 2016, 4, 17363.

[308] S. Jin, Are Metal Chalcogenides, Nitrides, and Phosphides Oxygen Evolution Catalysts or Bifunctional Catalysts?, ACS Energy Lett., 2017, 2, 1937.

[309] K. Song, D. A. Agyeman, M. Park, J. Yang, Y. M. Kang, High-Energy-Density Metal-Oxygen Batteries: Lithium-Oxygen Batteries vs Sodium-Oxygen Batteries, Adv. Mater., 2017, 29.

[310] L. Ma, D. Zhang, Y. Lei, Y. Yuan, T. Wu, J. Lu, K. Amine, High-Capacity Sodium Peroxide Based Na–O2 Batteries with Low Charge Overpotential via

a Nanostructured Catalytic Cathode, ACS Energy Lett., 2018, 3, 276.

[311] X. Long, G. Li, Z. Wang, H. Zhu, T. Zhang, S. Xiao, W. Guo, S. Yang, Metallic Iron-Nickel Sulfide Ultrathin Nanosheets As a Highly Active Electrocatalyst for Hydrogen Evolution Reaction in Acidic Media, J. Am. Chem. Soc., 2015, 137, 11900.

[312] R. Li, Z. Hu, X. Shao, P. Cheng, S. Li, W. Yu, W. Lin, D. Yuan, Large Scale Synthesis of NiCo Layered Double Hydroxides for Superior Asymmetric Electrochemical Capacitor, Sci. Rep., 2016, 6, 18737.

[313] F. Song, X. Hu, Ultrathin cobalt-manganese layered double hydroxide is an efficient oxygen evolution catalyst, J. Am. Chem. Soc., 2014, 136, 16481.

[314] P. P. Lopes, D. Tripkovic, P. F. B. D. Martins, D. Strmcnik, E. A. Ticianelli, V. R. Stamenkovic, N. M. Markovic, Dynamics of electrochemical Pt dissolution at atomic and molecular levels, J. Electroanal. Chem., 2018, 819, 123.

[315] H. Wang, S. Xu, C. Tsai, Y. Li, C. Liu, J. Zhao, Y. Liu, H. Yuan, F. Abild-Pedersen, F. B. Prinz, J. K. Norskov, Y. Cui, Direct and continuous strain control of catalysts with tunable battery electrode materials, Science, 2016, 354, 1031.

[316] M. C. Luo, S. J. Guo, Strain-controlled electrocatalysis on multimetallic nanomaterials, Nat. Rev. Mater., 2017, 2, 17059.

[317] D. Zhang, W. P. Sun, Y. Zhang, Y. H. Dou, Y. Z. Jiang, S. X. Dou, Engineering Hierarchical Hollow Nickel Sulfide Spheres for High-Performance Sodium Storage, Adv. Funct. Mater., 2016, 26, 7479.

[318] T. V. Pham, H. P. Guo, W. B. Luo, S. L. Chou, J. Z. Wang, H. K. Liu, Carbon- and binder-free 3D porous perovskite oxide air electrode for rechargeable lithium-oxygen batteries, J. Mater. Chem. A, 2017, 5, 5283.

[319] W. M. Liu, T. T. Gao, Y. Yang, Q. Sun, Z. W. Fu, A hierarchical three-dimensional NiCo2O4 nanowire array/carbon cloth as an air electrode for nonaqueous Li-air batteries, Phys. Chem. Chem. Phys., 2013, 15, 15806.

[320] M. Gong, Y. Li, H. Wang, Y. Liang, J. Z. Wu, J. Zhou, J. Wang, T. Regier, F. Wei, H. Dai, An advanced Ni-Fe layered double hydroxide electrocatalyst for water oxidation, J. Am. Chem. Soc., 2013, 135, 8452.

[321] F. Song, X. Hu, Exfoliation of layered double hydroxides for enhanced oxygen evolution catalysis, Nat. Commun., 2014, 5, 4477.

[322] Y. Dou, L. Zhang, J. Xu, C. T. He, X. Xu, Z. Sun, T. Liao, B. Nagy, P. Liu, S. X. Dou, Manipulating the Architecture of Atomically Thin Transition Metal (Hydr)oxides for Enhanced Oxygen Evolution Catalysis, ACS Nano, 2018, 12, 1878.

[323] C. C. McCrory, S. Jung, J. C. Peters, T. F. Jaramillo, Benchmarking heterogeneous electrocatalysts for the oxygen evolution reaction, J. Am. Chem. Soc., 2013, 135, 16977.

[324] B. Konkena, K. Junge Puring, I. Sinev, S. Piontek, O. Khavryuchenko, J. P. Durholt, R. Schmid, H. Tuysuz, M. Muhler, W. Schuhmann, U. P. Apfel, Pentlandite rocks as sustainable and stable efficient electrocatalysts for hydrogen generation, Nat. Commun., 2016, 7, 12269.

APPENDIX A: LIST OF PUBLICATIONS

1. ***Haipeng Guo**, Boyang Ruan, Wenbin Luo*, Jianqiu Deng, Jiazhao Wang*, Huakun Liu, Shixue Dou, Ultrathin and Edge-Enriched Holey Nitride Nanosheets as Bifunctional Electrocatalysts for the Oxygen and Hydrogen Evolution Reactions. *ACS Catalysis*, **2018**, *8* (10), 9686–9696. (IF:11.384)
2. ***Haipeng Guo**, Boyang Ruan, Lili Liu, Zhanliang, Tao, Shulei Chou, Jiazhao Wang*, Huakun Liu*, Capillary-Induced Ge Uniformly Distributed in N-Doped Carbon Nanotubes with Enhanced Li-Storage Performance, *Small*, **2017**, 13, 1700920. (IF:9.59)
3. ***Haipeng Guo**[†], Wenbin Luo[†], Jun Chen, Shulei Chou, Huakun Liu, Jiazhao Wang*, Review of Electrolytes in Nonaqueous Lithium–Oxygen Batteries, *Advanced Sustainable Systems*, **2018**, 1700183. ([†] These authors contributed equally to this work.)
4. ***Haipeng Guo**, Zhi Zheng, Chaozhu Shu, Wenbin Luo, Shulei Chou, Jiazhao Wang*, Huakun Liu, Phosphorus and Nitrogen Dual Doped Carbon as Efficient Cathode for Sodium Oxygen Batteries, (To be submitted)
5. ***Haipeng Guo**, Lei Zhang, Shulei Chou, Jiazhao Wang*, Huakun Liu*, Yolk-shell Silicon-carbon Nanospheres with Interior Core-shell Structure for High Performance Lithium Storage, (To be submitted)
6. **Haipeng Guo**, Zhi Zheng, Nengfei Yu, Wenbin Luo, Shulei Chou, Jiazhao Wang*, Huakun Liu, Ultrathin 2D Holey Wrinkle CoFe Nitride Nanosheets as Air Cathodes for the Zinc Air Batteries, (To be submitted)
7. Xiaowei Wang[†], **Haipeng Guo**[†], Ji Liang*, Jiafeng Zhang*, Bao Zhang, Jiazhao Wang, Wenbin Luo*, Huakun Liu, Shixue Dou, Integrated Free-standing Flexible Electrode with Holey Structured Two-dimensional Bimetallic Phosphide

Nanosheets for Sodium Ion Batteries, *Advanced Functional Materials*, **2018**, 28, 1801016. († These authors contributed equally to this work.) (IF:13.325)

8. Chaozhu Shu, Chang Wu, Jianping Long, **Haipeng Guo**, Shixue Dou, Jiazhao Wang*, Highly reversible Li-O_2 battery induced by modulating local electronic structure via synergistic interfacial interaction between ruthenium nanoparticles and hierarchically porous carbon, *Nano Energy*, 2019, 166-175. (IF:13.120)
9. Enhui Wang, Mingzhe Chen, Xiaohong Liu, Yumei Liu, **Haipeng Guo**, Zhenguo Wu, Wei Xiang, Benhe Zhong, Xiaodong Guo*, Shulei Chou*, Shixue Dou, Organic Cross-Linker Enabling a 3D Porous Skeleton–Supported $Na_3V_2(PO_4)_3$/Carbon Composite for High Power Sodium-Ion Battery Cathode, *Small Methods*, **2018**, 1800169.
10. Boyang Ruan, **Haipeng Guo**, Yuyang Hou, Qiannan Liu, Yuanfu Deng, Guohua Chen, Shulei Chou, Huakun Liu, Jiazhao Wang*, Carbon-Encapsulated Sn@N-Doped Carbon Nanotubes as Anode Materials for Application in SIBs, *ACS Applied Materials & Interfaces*, **2017**, 9(43), 37682-37693. (IF:8.097)
11. Lei Zhang, Xianluo Hu*, Chaoji Chen, **Haipeng Guo**, Xiaoxiao Liu, Gengzhao Xu, Haijian Zhong, Shuang Cheng, Peng Wu, Jiashen Meng, Yunhui Huang*, Shixue Dou, Huakun Liu*, In Operando Mechanism Analysis on Nanocrystalline Silicon Anode Material for Reversible and Ultrafast Sodium Storage, *Advanced Materials*, **2017**, 29, 1604708. (IF:21.95)
12. Lili Liu, **Haipeng Guo**, Yuyang Hou, Jun Wang, Lijun Fu, Jun Chen, Huakun Liu, Jiazhao Wang*, Yuping Wu*, A 3D hierarchical porous Co_3O_4 nanotube network as an efficient cathode for rechargeable lithium–oxygen batteries, *Journal of Materials Chemistry A*, **2017**, 5, 14673-14681. (IF:9.931)
13. Lei Zhang, Yuhai Dou, **Haipeng Guo**, Binwei Zhang, Xiaoxiao Liu, Min Wan, Weijie Li, Xianluo Hu*, Shixue Dou, Yunhui Huang, Huakun Liu*, A facile way

to fabricate double-shell pomegranate-like porous carbon microspheres for high-performance Li-ion batteries, *Journal of Materials Chemistry A*, **2017**, 5, 12073-12079. (IF:9.931)

14. Lei Zhang, Ranjusha Rajagopalan, **Haipeng Guo**, Xianluo Hu, Shixue Dou*, Huakun Liu*, A Green and Facile Way to Prepare Granadilla-Like Silicon-Based Anode Materials for Li-Ion Batteries, *Advanced Functional Materials*, **2016**, 26, 440-446. (IF:13.325)
15. Lei Zhang, **Haipeng Guo**, Ranjusha Rajagopalan, Xianluo Hu, Yunhui Huang, Shixue Dou, Huakun Liu*, One-step synthesis of a silicon/hematite@carbon hybrid nanosheet/silicon sandwich-like composite as an anode material for Li-ion batteries, *Journal of Materials Chemistry A*, **2016**, 4, 4056-4061. (IF:9.931)
16. Wenbin Luo*, Thien Viet Pham, **Haipeng Guo**, Huakun Liu, Shixue Dou, Three-Dimensional Array of TiN@ Pt_3Cu Nanowires as an Efficient Porous Electrode for the Lithium–Oxygen Battery, *ACS Nano*, **2017**, 11(2), 1747-1754. (IF:13.709)
17. Thien Viet Pham, **Haipeng Guo**, Wenbin Luo*, Shulei Chou, Jiazhao Wang*, Huakun Liu, Carbon- and binder-free 3D porous perovskite oxide air electrode for rechargeable lithium–oxygen batteries, *Journal of Materials Chemistry A*, **2017**, 5, 5283-5289. (IF:9.931)
18. Boyang Ruan, **Haipeng Guo**, Qiannan Liu, Dongqi Shi, Shulei Chou, Huakun Liu, Guohua Chen, Jiazhao Wang*, 3-D structured SnO_2–polypyrrole nanotubes applied in Na-ion batteries, *RSC Advances*, **2016**, 6, 103124-103131. (IF:2.936)
19. Yuyang Hou, Yuqing Liu, Zhen Zhou, Lili Liu, **Haipeng Guo**, Huakun Liu, Jiazhao Wang*, Jun Chen*, Metal-oxygen bonds: Stabilizing the intermediate species towards practical Li-air batteries, *Electrochimica Acta*, **2018**, 313-320. (IF:5.116)
20. Weibo Hua, Zhenguo Wu, Mingzhen Chen, Michael Knapp, Xiaodong Guo*,

Sylvio Indris*, Joachim R. Binder*, Natalia N. Bramnik, Benhe Zhong, **Haipeng Guo**, Shulei Chou*, Yong-Mook Kang*, Helmut Ehrenberg*, Shape-controlled synthesis of hierarchically layered lithium transition-metal oxide cathode materials by shear exfoliation in continuous stirred-tank reactors, *Journal of Materials Chemistry A*, **2017**, 5, 25391-25400. (IF:9.931)

Papers listed were all written during my PhD study.

The publications marked with an asterisk are exclusively related to this thesis.

APPENDIX B: CONFERENCES

1. The 2016 International Symposium on Next-Generation Batteries, North Wollongong, Australia, August. 9th to 12th, 2016.
2. The 2nd International Symposium on Renewable Energy Technologies, Sydney, Australia, 30 November to 04 December, 2016.
3. The 5th BAJC Annual Conference 2017, Gold Coast, Australia, February 21, 2017.
4. The 6th BAJC Annual Conference 2018, Wollongong, January 29, 2018.
5. The 19th International Meeting on Lithium Batteries (IMLB2018), Kyoto, Japan, June 17 to 22, 2018.
6. The 2019 International Symposium of Future Materials in conjunction of 25th anniversary of ISEM, North Wollongong, Australia, 31 January to 03 February, 2019.

APPENDIX C: SCHOLARSHIPS & AWARDS

1. 2015 International Postgraduate Research Scholarship, 03/2015.
2. 2015 University Postgraduate Award, 03/2015.
3. 2017 Faculty Top-up Scholarship, 08/2017.
4. International Postgraduate Tuition Award, 07/2018.
5. 2017 Postgraduate Student Merit Award of ISEM.